

University of New Hampshire

## University of New Hampshire Scholars' Repository

---

Doctoral Dissertations

Student Scholarship

---

Spring 1996

### Development of Q-band EPR/ENDOR spectrometer and EPR/ENDOR studies of dinitrosyl iron model complexes

Wenge Wang

*University of New Hampshire, Durham*

Follow this and additional works at: <https://scholars.unh.edu/dissertation>

---

#### Recommended Citation

Wang, Wenge, "Development of Q-band EPR/ENDOR spectrometer and EPR/ENDOR studies of dinitrosyl iron model complexes" (1996). *Doctoral Dissertations*. 1902.

<https://scholars.unh.edu/dissertation/1902>

This Dissertation is brought to you for free and open access by the Student Scholarship at University of New Hampshire Scholars' Repository. It has been accepted for inclusion in Doctoral Dissertations by an authorized administrator of University of New Hampshire Scholars' Repository. For more information, please contact [Scholarly.Communication@unh.edu](mailto:Scholarly.Communication@unh.edu).

## INFORMATION TO USERS

This manuscript has been reproduced from the microfilm master. UMI films the text directly from the original or copy submitted. Thus, some thesis and dissertation copies are in typewriter face, while others may be from any type of computer printer.

**The quality of this reproduction is dependent upon the quality of the copy submitted.** Broken or indistinct print, colored or poor quality illustrations and photographs, print bleedthrough, substandard margins, and improper alignment can adversely affect reproduction.

In the unlikely event that the author did not send UMI a complete manuscript and there are missing pages, these will be noted. Also, if unauthorized copyright material had to be removed, a note will indicate the deletion.

Oversize materials (e.g., maps, drawings, charts) are reproduced by sectioning the original, beginning at the upper left-hand corner and continuing from left to right in equal sections with small overlaps. Each original is also photographed in one exposure and is included in reduced form at the back of the book.

Photographs included in the original manuscript have been reproduced xerographically in this copy. Higher quality 6" x 9" black and white photographic prints are available for any photographs or illustrations appearing in this copy for an additional charge. Contact UMI directly to order.

# UMI

A Bell & Howell Information Company  
300 North Zeeb Road, Ann Arbor MI 48106-1346 USA  
313/761-4700 800/521-0600



DEVELOPMENT OF Q-BAND EPR/ENDOR SPECTROMETER AND EPR/ENDOR  
STUDIES OF DINITROSYL IRON MODEL COMPLEXES

BY

WENGE WANG  
B.S. BEIJING UNIVERSITY, 1990

DISSERTATION

Submitted to the University of New Hampshire  
in Partial Fulfillment of  
the Requirements for the Degree of

Doctor of Philosophy

in

Chemistry

May, 1996

**UMI Number: 9627169**

---

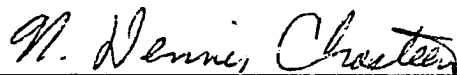
**UMI Microform 9627169**  
**Copyright 1996, by UMI Company. All rights reserved.**

**This microform edition is protected against unauthorized  
copying under Title 17, United States Code.**

---

**UMI**  
**300 North Zeeb Road**  
**Ann Arbor, MI 48103**


This dissertation has been examined and approved.



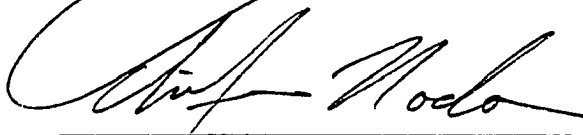
\_\_\_\_\_  
Dissertation director, N. Dennis Chasteen  
Professor of Chemistry



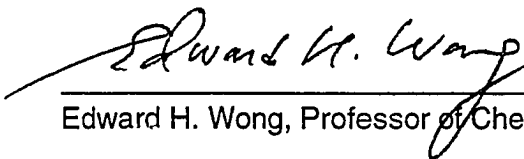
\_\_\_\_\_  
Olof E. Echt, Associate Professor of Physics



\_\_\_\_\_  
Howard R. Mayne, Professor of Chemistry



\_\_\_\_\_  
Chifuru Noda, Assistant Professor of Chemistry



\_\_\_\_\_  
Edward H. Wong, Professor of Chemistry

18 December, 1995

Date

## DEDICATION

This dissertation is dedicated to my parents, Qi-Hou Wang and Yue-Qing Li, my sister, Shu-Qin Wang, and brother, Wei-Feng Wang.

## ACKNOWLEDGEMENTS

I am deeply indebted to my advisor, N. Dennis Chasteen, for his inspiration, guidance and patience, without which my graduate career would not have been as challenging and rewarding. I'd also like to thank John Grady and Xiaoke Yang for helping me with the liquid helium temperature experiment operation and numerous other things which are too many to mention, and Pam Proulx Curry who has patiently helped me with my English writing any time I needed. Special thanks to Shujun Sun for her friendship and many helpful advises on my research as well as life in general. My thanks also goes to the rest of the group for their support and encouragement, which have helped me through many hardships. Meanwhile, it is a pleasure to acknowledge the UNH machine shop for machining the parts for the Q-band cavities and helpful discussion in improving the design of the cavities.

I also wish to thank Dr. Robert B. Clarkson of the University of Illinois EPR Research Center for helpful discussions and for the use of his wire-wound cavity and Q-band waveguide/coupler assembly in the early stage of this work, Dr. James S. Hyde of the National Biomedical ESR Center for helpful discussions regarding the Varian Q-band system and Dr. Paul Cope of Wilmad Glass for providing some of the capillaries used in this work.

Above all, I'd like to express my deepest appreciation



to my parents, Qi-Hou Wang and Yue-Qing Li, for their love,  
understanding and support throughout the years.

## TABLE OF CONTENTS

	Page
<b>DEDICATION.....</b>	<b>iii</b>
<b>ACKNOWLEDGEMENTS.....</b>	<b>iv</b>
<b>LIST OF FIGURES.....</b>	<b>ix</b>
<b>LIST OF SYMBOLS.....</b>	<b>xiv</b>
<b>ABSTRACT.....</b>	<b>xvi</b>
<b>CHAPTER</b>	
<b>1. INTRODUCTION</b>	
EPR and ENDOR Spectroscopy.....	1
Q-Band EPR and ENDOR.....	8
Cavities.....	11
Coupling of Microwave Energy into Cavities and Cavity Tuning.....	15
CavityQ.....	17
Absorption and Dispersion Mode.....	18
<b>2. CONSTRUCTION AND PERFORMANCE OF "RIBBON-WOUND" TE011 CYLINDRICAL EPR CAVITIES.....</b>	
Introduction.....	22
Materials and Methods.....	24
Cavity Wall Construction.....	24
EPR Silver Wall Cavity Construction.....	28
Epoxy and Epoxy/quartz Formulation.....	29
Sample Preparations.....	30
EPR and ENDOR Measurements.....	31
RESULTS AND DISCUSSION.....	31
CONCLUSION.....	42
<b>3. Q-BAND ENDOR COIL, RF CIRCUIT CONSTRUCTION AND PERFORMANCE.....</b>	
	<b>43</b>

	Introduction.....	43
	ENDOR Cavity Construction.....	44
	SamplePreparation.....	48
	InstrumentDescription.....	48
	Results and Discussion.....	51
<b>4</b>	<b>EPR AND ENDOR STUDIES OF DINITROSYL IRON MODEL COMPOUNDS.....</b>	<b>72</b>
	Introduction.....	72
	Experimentalmethods.....	76
	Results and discussion.....	78
	EPR studies of dinitrosyl iron complexes.....	78
	Fe-NO-Cys complex.....	79
	Fe-NO-Mer, Fe-NO-Eth and Fe-NO-TGA complexes.....	85
	Fe-NO-Pen complex.....	96
	Fe-NO-Im complex.....	100
	Proton ENDOR of dinitrosyl iron model complexes..	104
	Fe-NO-Mer, Fe-NO-TGA and Fe-NO-Cys complexes.....	106
	Fe-NO-Pen complex.....	120
	Fe-NO-Im complex.....	131
	Conclusions.....	137
	<b>REFERENCES.....</b>	<b>141</b>
	<b>APPENDIX.....</b>	<b>147</b>
<b>A</b>	<b>HELIUM FLOW CRYOSTAT OPERATION.....</b>	<b>147</b>
<b>B</b>	<b>CAVITY Q MEASUREMENTS.....</b>	<b>153</b>
<b>C</b>	<b>OPTIMUM DIMENSION FOR CYLINDRICAL TE<sub>011</sub> CAVITIES.....</b>	<b>156</b>
<b>D</b>	<b>SILVERPLATING.....</b>	<b>159</b>
<b>E</b>	<b>OPERATION OF Q-BAND EPR SPECTROMETER.....</b>	<b>168</b>
<b>F</b>	<b>CAVITY P<sub>12</sub> AND S/N MEASUREMENT ON WEAK PITCH SAMPLE.....</b>	<b>173</b>
<b>G</b>	<b>Q-BAND MODULATION COIL CONSTRUCTION.....</b>	<b>180</b>

H	POINT DIPOLE DIPOLE INTERACTION APPROXIMATION.....	183
I	EPR/ENDOR STUDIES OF DINITROSYL IRON AMINOETHANETHIOL COMPLEX.....	186

## LIST OF FIGURES

FIGURE	PAGE
1.1	Energy levels for an electron coupled to one nucleus in magnetic field, $S=1/2$ , $I=1/2$ .....5
1.2	A rectangular $TE_{102}$ microwave cavity.....13
1.3	Cylindrical cavity operating in the $TE_{011}$ mode. (a) Cavity (b) Electric ( $\bullet \times$ ) and (c) magnetic field (---) distributions.....14
1.4	(a) Cavity tuning by inductance. (b) Cavity tuning by capacitance. (c) Cavity tuning by volume.....16
1.5	Schematic diagram of klystron power mode. $\nu_0$ is the resonant frequency of the cavity and $\nu_1-\nu_2$ is the half-power bandwidth of the cavity.....19
2.1	(a) Ribbon-wound cavity (b) Brass or aluminum mandrel (c) Teflon mold.....25
2.2	Power saturation curves of weak pitch sample. Data scaled to relative Signal/Noise of each cavity (Table 2.1).....36
2.3	Signal amplitude of 3 mM $CuCl_2$ in 2:1 $H_2O$ /glycerol vs cavity dimensions.....38
2.4	Dispersion mode rapid-passage EPR spectrum of 20 mM $VO(Im)_4^{2+}$ in a 2:1 $H_2O$ /glycerol solution at pH = 7 in a silver plated brass ribbon-wound cavity.....40
2.5	Q-band EPR spectrum of 1 mM $VOSO_4$ in $H_2O$ /glycerol (2:1 by volume) solution under rapid-passage condition (a) and 20 mM $VO(Im)_4^{2+}$ in $H_2O$ /glycerol solution (b).....41
3.1	Schematic drawing of the ENDOR cavity piston assembly. (a) RF coil (b) Aluminum piston (c) Piston holder...45
3.2	Sketch of cylindrical $TE_{011}$ Q-band ENDOR cavity configuration. Left: $TE_{011}$ ENDOR cavity with single silver wire loop as RF coil.....47
3.3	Diagram of ENDOR RF circuit setup. (a) Field modulation ENDOR RF circuit (solid line), (b) Frequency modulation ENDOR RF circuit (dashed line).....49

3.4	Equivalent circuit of RF coil in $TE_{011}$ resonant cavity. $C_1$ , coil capacitance; $C_2$ , coil-cavity capacitance; $R, L$ , resistance and inductance of the RF coil, respectively.....	53
3.5	Frequency dependence of RF power output. Cavity: silver plated brass ribbon-wound cavity with silver hairpin RF coil.....	55
3.6	Q-band EPR absorption spectrum of irradiated sucrose sample.....	57
3.7	Q-band EPR dispersion spectrum of irradiated sucrose sample.....	58
3.8	Field modulation Q-band $^1H$ ENDOR of irradiated sucrose radical with the magnetic field set on the peak marked by arrow in Figure 3.7.....	59
3.9	Field modulation ENDOR background signal from 0-40 MHz.....	60
3.10	Field modulation ENDOR background signal from 60 to 100 MHz.....	61
3.11	Frequency modulation Q-band $^1H$ ENDOR of irradiated sucroseradical.....	63
3.12	Field modulation Q-band $^1H$ ENDOR of irradiated sucrose radical 50:1 diluted in KCl.....	65
3.13	Field modulation Q-band $^1H$ ENDOR of 20 mM $VO(Im)_4^{2+}$ in $H_2O$ /glycerol solution at pH = 7 with the magnetic field set on the peak marked xy (a), z (b) of Figure 2.3 and off resonance.....	66
3.14	20 mM $VO(Im)_4^{2+}$ (pH = 7) $^1H$ ENDOR signal amplitude vs. RF power.....	68
3.15	20 mM $VO(Im)_4^{2+}$ $^1H$ ENDOR signal amplitude vs. Microwave power.....	69
3.16	20 mM $VO(Im)_4^{2+}$ $^1H$ ENDOR signal amplitude vs. Temperature .....	70
4.1	Schematic diagram of the structures for the ligands indinitrosyl iron complexes.....	75
4.2	(a) Saturation curves of $Fe-^{14}NO$ -Pen at different concentrations. (b) Saturation curves of $Fe-^{14}NO$ -Pen after correction for concentration differences.....	80

4.3	Proposed structure of dinitrosyl ion cysteine.....	81
4.4	X-ray structure of Roussin's red ethyl ester.....	82
4.5	Experimental (a) and computer simulation of room temperature EPR spectrum of 20 mM dinitrosyl ion cysteine complex at pH = 6. Inset: EPR spectrum of the same sample at 100 K.....	84
4.6	Room temperature EPR spectrum of Fe- <sup>14</sup> NO-Mer (a) and Fe- <sup>15</sup> NO-Mer (b) (pH =6).....	86
4.7	Computer simulation (a) and experimental (b) EPR spectrum of Fe- <sup>14</sup> NO-Mer complex at room temperature..	87
4.8	Computer simulation (a) and experimental (b) EPR spectrum of Fe- <sup>15</sup> NO-Mer complex at room temperature..	88
4.9	EPR spectrum of Fe- <sup>14</sup> NO-Mer (a) and Fe- <sup>15</sup> NO-Mer (b) (pH = 6) at 77 K.....	90
4.10	EPR spectrum of Fe- <sup>14</sup> NO-Eth (pH = 6) at 77 K.....	93
4.11	Room temperature EPR spectrum of 20 mM Fe- <sup>14</sup> NO-TGA at pH=6.....	94
4.12	Proposed structure of Fe-NO-TGA.....	95
4.13	Room temperature EPR spectrum of 20 mM Fe- <sup>14</sup> NO-Pen at pH = 6.....	97
4.14	Room temperature EPR spectrum of 20 mM Fe- <sup>15</sup> NO-Pen complex at pH = 6.....	99
4.15	Room temperature EPR spectrum of 20 mM Fe- <sup>14</sup> NO-Im complex at pH = 6.....	101
4.16	Computer simulation (a) and experimental (b) EPR spectrum of Fe- <sup>15</sup> NO-Im complex.....	102
4.17	Frequency modulation X-band <sup>1</sup> H ENDOR of 20 mM Fe- <sup>14</sup> NO-Mer complex at pH = 6.....	107
4.18	EPR spectrum of Fe- <sup>14</sup> NO-Mer (pH = 6) at 77 K.....	108
4.19	Molecular modeling structure of Fe-NO-Mer.....	110
4.20	Frequency modulation X-band <sup>1</sup> H ENDOR of 20 mM Fe- <sup>14</sup> NO-TGA complex at pH = 6.....	112
4.21	Molecular modeling structure of Fe-NO-TGA.....	113

4.22	Frequency modulation X-band $^1\text{H}$ ENDOR of 20 mM $\text{Fe-}^{14}\text{NO-Cys}$ complex.....	115
4.23	EPR spectrum of $\text{Fe-}^{14}\text{NO-Cys}$ (pH = 6) at 77K.....	116
4.24	Molecular modeling structure of $\text{Fe-NO-Cys}$ complex...	117
4.25	EPR spectrum of $\text{Fe-}^{14}\text{NO-Pen}$ (pH = 6) at 77 K.....	121
4.26	Frequency modulation X-band $^1\text{H}$ ENDOR of 20 mM $\text{Fe-}^{14}\text{NO-Pen}$ complex at pH = 6.....	122
4.27	Molecular modeling structure of $\text{Fe-NO-Pen}$ complex...	124
4.28	X-band $^1\text{H}$ ENDOR of $\text{Fe-}^{14}\text{NO-Pen}$ in $\text{D}_2\text{O}$ (pD = 6.6)....	128
4.29	Field modulation Q-band $^1\text{H}$ ENDOR of 20 mM $\text{Fe-}^{14}\text{NO-Pen}$ pH = 6 with the magnetic field set at varies positions along the EPR envelope indicated in Figure 4.25.....	129
4.30	Q-band dispersion EPR spectrum of 20 mM $\text{Fe-}^{14}\text{NO-Pen}$ (pH = 6) at 7 K.....	132
4.31	Frequency modulation X-band $^1\text{H}$ ENDOR of 20 mM $\text{Fe-}^{14}\text{NO-Im}$ (pH = 6) with the magnetic field set at varies positions along the EPR envelope indicated in Figure 4.27.....	133
4.32	EPR spectrum of $\text{Fe-}^{14}\text{NO-Im}$ complex (pH = 6 ) at 100 K.....	134
4.33	X-band $^1\text{H}$ ENDOR of $\text{Fe-}^{14}\text{NO-Im}$ after 3:1 dilution with $\text{D}_2\text{O}$ at 30 K.....	136
4.34	Molecular modeling structure of $\text{Fe-NO-Im}$ complex.....	138
4.35	Summary of proton ENDOR hyperfine couplings in $\text{VO(Im)}_4^{2+}$ and the structure of $\text{VO(Im)}_4^{2+}$ complex....	139
A.1	Schematic drawing of the Cryo Industries 8CC Variable Temperature Helium Flow Cryostat.....	148
B.1	Klystron power mode.....	154
C.1	$Q_0\sigma/\lambda$ vs (d/z) for cylindrical $\text{TE}_{011}$ cavity.....	158
D.1	Apparatus for electro-silver plating (a) and polishing (b) of the cylindrical brass ribbon-wound cavity.....	160
E.1	Schematic drawing of the Q-band cavity coupler	



	(iris).....	171
F.1	Power saturation curve of weak pitch sample. Cavity: silver-plated brass ribbon wound cavity.....	175
F.2	Curve fitting of the power saturation data in Figure F.1. Inset: The linear part of the saturation curve.....	176
F.3	(a) Weak pitch spectrum at 0.01 mW power, (b) baseline trace at 63 mW (0 dB).....	177
F.4	Linear regression of the baseline in Figure F.3b....	178
G.1	Schematic diagram of the Q-band modulation coil.....	181
I.1	Structure of aminoethanethiol and ethylamine.....	187
I.2	Possible structure of Fe-NO-Cys at frozen state.....	188
I.3	Frequency modulation X-band $^1\text{H}$ ENDOR of Fe- $^{14}\text{NO}$ -AET complex made in $\text{H}_2\text{O}$ and $\text{D}_2\text{O}$ .....	189

## LIST OF SYMBOLS

<b>A</b>	electron nuclear hyperfine tensor
<b>a</b>	the isotropic coupling constant
$\beta$	Bohr magneton
$\beta_N$	nuclear magneton
$\delta(\text{cm})$	microwave skin depth
<b>f</b>	resonant frequency of the cavity
$ \psi(0) $	the amplitude of the electronic wave function at the nucleus
$\bar{g}$	electron g tensor
$g_{\perp}$	perpendicular g factor
$g_{\parallel}$	parallel g factor
$g_N$	the nuclear g-factor
$\mathcal{H}$	spin Hamiltonian
$\gamma$	the magnetogyric ratio
<b>H</b>	applied magnetic field
$H_1$	magnetic field strength of microwave
$H_2$	magnetic field strength of RF
$\epsilon$	dielectric constant
<b>I</b>	the nuclear spin angular momentum
$I_x, I_y, I_z$	the scalar components of <b>I</b> along X, Y, Z axes in the molecular frame
$\chi$	magnetic susceptibility
$\chi''$	the imaginary part of $\chi$
$\chi'$	the real part of $\chi$
$\lambda$	the wavelength of <b>f</b>

$m_s$	magnetic spin quantum number of the electron
$m_I$	magnetic spin quantum number of the nucleus
$\mu$	permeability of the sample
$\mu_e$	magnetic moments of the electron
$\mu_N$	magnetic moments of the nucleus
$\nu_n$	nuclear Larmor frequency
$\nu_0$	resonance frequency of the cavity
$\Delta\nu$	the difference of frequency values at the half-power points
$P_{1/2}$	microwave power at half saturation of the EPR signal
$Q$	the quadrupole tensor
$Q$	cavity quality factor
$Q_L$	overall or loaded $Q$
$Q_u$	unloaded $Q$ arises only from the ohmic losses in the cavity walls
$Q_e$	$Q$ due to dielectric losses
$Q_r$	$Q$ due to energy loss through the cavity coupling hole
$Q_x$	$Q$ due to the energy loss from the sample at resonance
$r$	radius vector from $\mu_e$ to $\mu_N$
$S$	spin angular momentum operator
$S_x, S_y, S_z$	the scalar components of $S$ along X, Y, Z axes in the molecular frame
$T_1$	the spin-lattice relaxation time
$T_2$	the spin-spin relaxation time

## ABSTRACT

### DEVELOPMENT OF A Q-BAND EPR/ENDOR SPECTROMETER AND EPR/ENDOR STUDIES OF DINITROSYL IRON MODEL COMPLEXES

By

Wenge Wang  
University of New Hampshire, May, 1996

A robust yet sensitive Q-band (35 GHz) cavity has been designed for routine variable temperature EPR (electron paramagnetic resonance) and ENDOR (electron nuclear double resonance) measurements down to 2 K. It consists of an aluminum or brass (plain, silver or gold plated) ribbon imbedded in a cylindrical epoxy or epoxy/quartz composite with a tunable piston at the bottom. The cavity has all the advantages of the traditional silver wire-wound cavity often used for Q-band measurements but is much more robust and easier to construct. The cavity suppresses degenerate resonant modes and minimizes wall eddy currents induced by field modulation. With standard Varian Q-band modulation coils, a 100-kHz modulation field of 27 G peak-to-peak is obtained at the sample. The cavity  $Q_L$  ( $\approx 2500$ ) and weak pitch signal/noise ( $\approx 1000:1$ ) with a Varian/E-110 microwave bridge are comparable to those obtained with either a traditional wire-wound cavity or a cavity constructed with a

thin silver wall on an epoxy/quartz substrate. A set of parallel posts along the axis of the cavity (bidirection) form the ENDOR coil.

Dinitrosyl iron model complexes with ligands of cysteine, mercaptoethanol, thioglycolic acid, ethanethiol, penicillamine and imidazole were studied by EPR and ENDOR spectroscopy. X-band and Q-band ENDOR measurements have been made at various fields across the EPR envelope at temperatures from 2 K to 100 K. We have assigned most of the  $^1\text{H}$  resonances with reasonable certainty. The data confirm the thiol groups binding in the complexes with mercaptan ligands at room temperatures, and suggest that a structural rearrangement occurs with dinitrosyl iron cysteine and penicillamine upon freezing the sample, in which case coordination of both the thiol and amino group takes place. The assignment of axial EPR spectra to thiol coordination in every instance has also been cast in doubt by our data.

## CHAPTER 1

### INTRODUCTION

#### EPR and ENDOR Spectroscopy

Electron paramagnetic resonance (EPR) has long been used as a powerful tool for the study of paramagnetic systems (1-8). EPR measures the interaction between electronic magnetic moments and a magnetic field. This interaction can be expressed quantum mechanically by the electronic Zeeman term in the Hamiltonian:

$$\mathcal{H}_{EZ} = \beta \mathbf{H} \cdot \mathbf{g} \cdot \mathbf{S} \quad (1.1)$$

where  $\beta$  is the Bohr magneton,  $\mathbf{H}$ , the applied magnetic field,  $\mathbf{S}$ , the electron spin angular momentum operator, and  $\mathbf{g}$ , a symmetric tensor. For isotropic samples or liquid solutions where the anisotropy is averaged out by fast molecular motion,  $\mathbf{g}$  becomes a number,  $g$ . The  $\mathbf{g}$  or  $g$  varies for different paramagnetic systems due to spin-orbit coupling and is different from that of a free electron ( $g_e = 2.0023$ ).

For paramagnetic systems also containing magnetic nuclei, at least two more terms need to be added to the above spin Hamiltonian: one is the nuclear Zeeman energy, resulting from the interaction between the magnetic nuclei

and the magnetic field. The Hamiltonian is given by:

$$\mathcal{H}_{\text{NZ}} = - g_N \beta_N \mathbf{H} \cdot \mathbf{I} \quad (1.2)$$

where  $g_N$  and  $\beta_N$  are the nuclear  $g$ -factor and nuclear magneton, respectively;  $\mathbf{I}$  is the nuclear spin angular momentum operator. Unlike the  $g$  values in EPR,  $g_N$  is a characteristic property of the nucleus.

Another term to be added to the Hamiltonian comes from the interaction of the unpaired electron with the surrounding magnetic nuclei. This interaction is known as the electron-nuclear hyperfine interaction, and its Hamiltonian is of the form

$$\mathcal{H}_{\text{HF}} = \mathbf{S} \cdot \mathbf{A} \cdot \mathbf{I} \quad (1.3)$$

where  $\mathbf{A}$  is the hyperfine tensor, which can be separated into two parts, the isotropic hyperfine and dipolar hyperfine interactions. The isotropic hyperfine coupling is caused by the interaction of the nuclear moment with the magnetic field produced at the nucleus by the electron spin. The Hamiltonian for this interaction is

$$\mathcal{H}_1 = a \mathbf{S} \cdot \mathbf{I} = a(S_x I_x + S_y I_y + S_z I_z) \quad (1.4)$$

where  $a$  is the isotropic coupling constant, given by

$$a = (8\pi/3)g\beta g_N\beta_N|\psi(0)|^2 \quad (1.5)$$

where  $|\psi(0)|$  is the amplitude of the electronic wave function at the nucleus.  $S_x, S_y, S_z$  and  $I_x, I_y, I_z$  are the scalar components of  $\mathbf{S}$  and  $\mathbf{I}$  along the X, Y, Z axes in the molecular frame. If the applied magnetic field is along the Z axis, then  $aS_z \cdot I_z$  becomes the dominant term, regarded as the first order hyperfine effect. The term  $a(S_x \cdot I_x + S_y \cdot I_y)$  is the second order hyperfine effect and can often be neglected at high magnetic fields.

The dipolar interaction, on the other hand, results from the dipolar coupling between the magnetic moments of the electron ( $\mu_e$ ) and the nucleus ( $\mu_N$ ). The Hamiltonian of this interaction has the form

$$\mathcal{H}_2 = -g\beta g_N\beta_N\{\mathbf{I} \cdot \mathbf{S}/r^3 - 3(\mathbf{I} \cdot \mathbf{r})(\mathbf{S} \cdot \mathbf{r})/r^5\} \quad (1.6)$$

where  $r$  and  $\mathbf{r}$  is the distance and radius vector from  $\mu_e$  to  $\mu_N$ , respectively. In contrast to the isotropic coupling, this dipolar interaction depends on the relative orientation of the paramagnetic molecule in the static magnetic field  $\mathbf{H}$ .

For systems containing magnetic nuclei with  $I > 1/2$ , a quadrupole term also needs to be taken into account. This term represents the energy of the magnetic nuclear quadrupole moment in the electric field gradient produced by



surrounding electrons and by other nuclei. The Hamiltonian of this interaction is

$$\mathcal{H}_Q = h\mathbf{I} \cdot \mathbf{Q} \cdot \mathbf{I} \quad (1.7)$$

where  $\mathbf{Q}$  is the quadrupole tensor.

In summary, the complete Hamiltonian for an electron spin coupled to a nucleus in the magnetic field is

$$\mathcal{H} = \mathcal{H}_{EZ} + \mathcal{H}_{NZ} + \mathcal{H}_{HF} + \mathcal{H}_Q = g\beta\mathbf{H} \cdot \mathbf{S} - g_N\beta_N\mathbf{H} \cdot \mathbf{I} + \mathbf{S} \cdot \mathbf{A} \cdot \mathbf{I} + h\mathbf{I} \cdot \mathbf{Q} \cdot \mathbf{I} \quad (1.8)$$

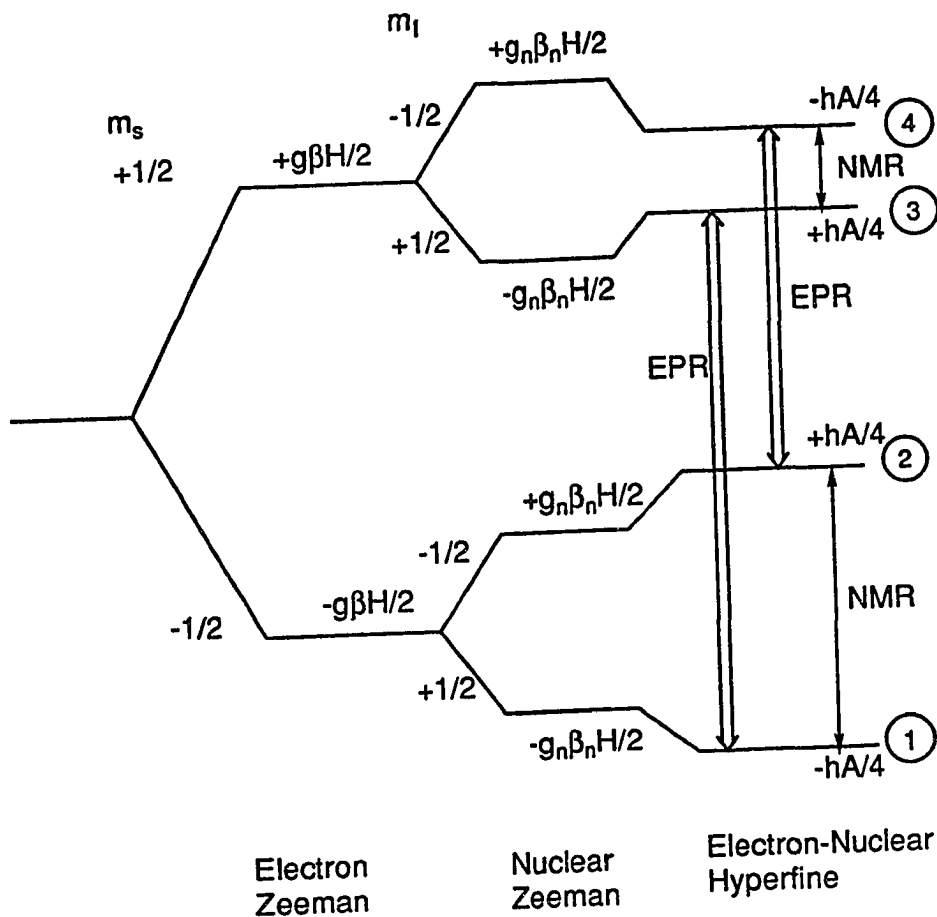
If we assume that  $I = 1/2$ , and both  $g$  and the hyperfine coupling are isotropic, the Hamiltonian reduces to

$$\mathcal{H} = g\beta\mathbf{H} \cdot \mathbf{S} - g_N\beta_N\mathbf{H} \cdot \mathbf{I} + a\mathbf{S} \cdot \mathbf{I} \quad (1.9)$$

and the corresponding energy levels (to the first order) are given by

$$E = g\beta H m_s - g_N\beta_N H m_I + a m_s m_I \quad (1.10)$$

where  $m_s$  and  $m_I$  are the magnetic spin quantum number of the electron and nucleus, respectively. The energy level diagram of such a system is shown in Figure 1.1 (9) (A corresponds to  $a$  in frequency units). According to the selection rules  $\Delta m_s = 1$  and  $\Delta m_I = 0$ , there are two allowed EPR transitions:  $1 \rightarrow 3$  and  $2 \rightarrow 4$ , resulting in two signals



$$\nu_{\text{ENDOR}} = \nu_n \pm A/2 \quad (\nu_n > A/2)$$

Figure 1.1: Energy levels for an electron coupled to one nucleus in magnetic field,  $S=1/2$ ,  $I=1/2$ . Here  $hA = a$ , where  $h$  is Planck constant;  $A$  and  $a$  are the hyperfine couplings in Hz and J, respectively (9).

in the EPR spectrum. Data obtained from the spectrum, namely  $g$  (from the center position of the signals) and  $a$  (from the separation of the peaks), provide a wealth of information about the paramagnetic species, including the identification and the geometry as well as the nuclear environment of the spin center. As in any spectroscopy, the applications of EPR is limited by its resolution, *i.e.* small nuclear hyperfine interactions cannot be resolved due to inhomogeneous broadening of the EPR lines; thus information about weakly coupled nuclei is lost. Fortunately, the missing details can be regained by means of electron-nuclear double resonance (ENDOR).

In an ENDOR experiment, the static magnetic field is first fixed on a particular EPR transition of interest, *e.g.* level 1 to 3 in Figure 1.1. (9) The microwave power is then increased so as to saturate this transition. Under these conditions, no EPR signal can be observed. A radio frequency (RF) is then introduced into the sample and swept in a particular frequency range. When the radio frequency matches the energy difference between nuclear spin levels, *e.g.* 3 and 4, or 1 and 2, an NMR transition occurs, which will produce an inequality in the populations between levels 1 and 3. As a result, the corresponding EPR transition is desaturated and the EPR signal is restored. This increase in the EPR signal versus the RF frequency constitutes an ENDOR spectrum. The ENDOR frequencies, in this case, are

given by

$$\nu_{\pm} = |\nu_n \pm A/2| \quad (1.11)$$

The spectrum consists of two lines, either centered at the nuclear Larmor frequency ( $\nu_n = g_N \beta_N H/h$ ) and separated by the hyperfine coupling (A) (Figure 1.1), or centered at A/2 and separated by  $2\nu_n$ , depending on the relative values of  $\nu_n$  and A/2.

The advantages of ENDOR come from the fact that it has both the capability of NMR in providing structural information about the surrounding nuclei and the sensitivity of EPR detection. Additionally, ENDOR can also be used to identify the interacting nuclei because of the dependence of the ENDOR frequencies on the nuclear g-factor. By combining both EPR and ENDOR techniques, one can obtain more complete chemical information about the paramagnetic system under investigation (10-15).

For a successful ENDOR experiment, two conditions regarding the saturation of the EPR and NMR lines must be satisfied (16):

$$\gamma_e^2 H_1^2 T_{1e}^2 T_{2c}^2 \geq 1 \quad (1.12)$$

$$\gamma_n^2 H_2^2 T_{1n}^2 T_{2n}^2 \geq 1 \quad (1.13)$$

where  $\gamma$  is the magnetogyric ratio;  $T_1$  is the spin-lattice

relaxation time and  $T_2$ , the spin-spin relaxation time. The subscripts e and n represent the electron and nuclear spin, respectively.  $H_1$  and  $H_2$  are the magnetic field strength of microwave and RF, respectively. In the case of transition metal complexes with large spin-orbit coupling, the relaxation times are very short at room temperatures. Therefore, most ENDOR experiments are run at very low temperatures to decrease the relaxation rates so that equation 1.13 is satisfied. Also for nuclei of low magnetic moment (e.g.  $^{14}\text{N}$ ) it can be difficult to achieve the saturation conditions, and therefore difficult to observe ENDOR. However, in most cases, the effective RF field at the nuclei can be enhanced by the electron nuclear hyperfine interaction (16). This enhancement, combined with low temperature operation and carefully-chosen experimental parameters, makes it possible to detect the ENDOR of these nuclei.

#### Q-band EPR and ENDOR

EPR and ENDOR experiment can be categorized as different "bands" according to the frequency ranges at which they are carried out (Table 1.1).

Table 1.1 Microwave frequency range for different "bands"

Band	L	S	C	X	K	Q	W	D
Frequency (GHz)	1-2	2-4	4-8	8-12	20-25	33-50	90	140

EPR measurement has been made from frequencies of a few MHz (3 MHz) (17) to frequencies as high as 140 GHz (18). The primary concern in the choice of the microwave frequency is the sensitivity. Good sensitivity requires the frequency to be as high as possible, since the sensitivity is proportional to  $\nu^2$ . In practice, however, there are a number of limitations to high frequency EPR/ENDOR experiments. One such limitation is the homogeneity of the magnetic field which is difficult to achieve with conventional magnets at fields higher than 25,000 G. Another is the size of the sample. Even though not critical, it is usually desirable to have a large sample size, since the EPR response is proportional to both the sensitivity of the spectrometer and the total number of spins in the active region of the cavity. Too small a sample volume may result in a weak signal, or loss of a signal. For these reasons, the microwave frequency most commonly used in the EPR experiment is X-band. Very often, however, one has to use a higher frequency in order to achieve higher sensitivity and more effective separation of species with different  $g$  values through increased spectral dispersion. The increased sensitivity is particularly important for biological samples, which are usually not available in large quantities. Furthermore, at high magnetic field, the second order hyperfine interactions are small compared with the electronic Zeeman term energy and

can be neglected or treated as a perturbation, thus simplifying the analysis of experimental results.

The benefits of using high microwave frequency are even more evident in ENDOR experiments. One such benefit comes from the better resolution of the EPR spectra at higher microwave frequencies. Consider a paramagnetic system having more than one EPR active species with similar  $g$  values, the EPR signals from different species will most likely overlap with one another at X-band, making it hard to selectively saturate one EPR signal without affecting another. This simultaneous saturation of multiple EPR species results in a complicated ENDOR spectrum as well. In this case, one is required to go to higher magnetic field to achieve better separation of EPR signals. In some other cases, one encounters complexity caused by the overlapping of ENDOR signals. A typical example is overlapping  $^1\text{H}$  ( $I = 1/2$ ) and  $^{14}\text{N}$  ( $I = 1$ ) ENDOR. The  $^1\text{H}$  ENDOR spectrum consists of two lines centered at  $\nu_{\text{H}}$  and separated by the hyperfine coupling constant  $A$ , and for  $^{14}\text{N}$ , the ENDOR lines are centered at  $A/2$  and separated by  $2\nu_{\text{N}}$ . At X-band, for sufficiently large  $A/2$  these two nuclear ENDOR signals tend to fall in the same region, making the assignment of the spectrum often difficult. This problem can be overcome by doing ENDOR at a higher magnetic field, in which the proton ENDOR lines move to a much higher frequency range, while the  $^{14}\text{N}$  ENDOR lines remain in the same spectral region;

separation of ENDOR lines from these two nuclei is thus achieved. In addition, better resolution of the ENDOR spectrum can also be achieved due to the increased RF range at higher microwave frequency.

At Q-band, magnetic fields used usually are no higher than 16,000 G, and the sample volume is about 30  $\mu$ L, small but still reasonable. Thus, Q-band is most frequently used for high frequency EPR/ENDOR spectroscopy. Increasingly, experiments are carried out at this frequency (19-25) or at a combination of Q-band and lower frequencies (26,27).

From an experimental point of view, two factors are very important for successful EPR/ENDOR: a good quality resonator and means of effectively introducing RF power to the sample. Chapter 2 describes the construction and performance of Q-band cylindrical EPR cavities. Configuration of an ENDOR coil and RF circuit for the Q-band spectrometer are presented in chapter 3. The experimental arrangement for low temperature operation is provided in Appendix A.

### **Cavities**

The resonator is the key component of all electron spin resonance spectrometers. It comes in many forms depending on the type of the resonator and its applications (28-30). The most commonly used resonator in EPR/ENDOR measurements is the so called "cavity", which is essentially a metallic



box or cylinder with dimensions comparable to that of the microwave wavelength so as to sustain microwave oscillation. Its function is to provide electromagnetic energy to the sample inside. The energy is stored in the cavity in the form of standing electromagnetic waves, the configuration of the standing waves (modes) is dictated by the size and shape of the cavities. Figure 1.2 (a) shows a rectangular  $TE_{102}$  microwave cavity(31) where TE stands for 'transverse electric' and the subscripts indicate the number of half-wavelengths along the several dimensions (A,B,C) (Fig. 1.2 (b),(c)). The microwave electric field ( $E_1$ ) and magnetic field ( $H_1$ ) distributions can be seen from Figure 1.2 (b),(c). The maximum microwave magnetic field is in a plane that bisects the cavity, where the electric field is a minimum.

Another type of commonly used cavity is the cylindrical cavity. Figure 1.3 (a) depicts such a cavity operating in the  $TE_{011}$  mode and its electric and magnetic field distributions are shown in Figure 1.3(b) and (c), respectively (31). Generally speaking, cylindrical cavities have higher energy density than rectangular cavities when operating in the  $TE_{011}$  mode.

To be useful for EPR measurements, a cavity should meet the following requirements: provide high energy density and a maximum microwave magnetic field ( $H_1$ ) at the sample and maintain  $H_1$  perpendicular to the external magnetic field ( $H_0$ ).

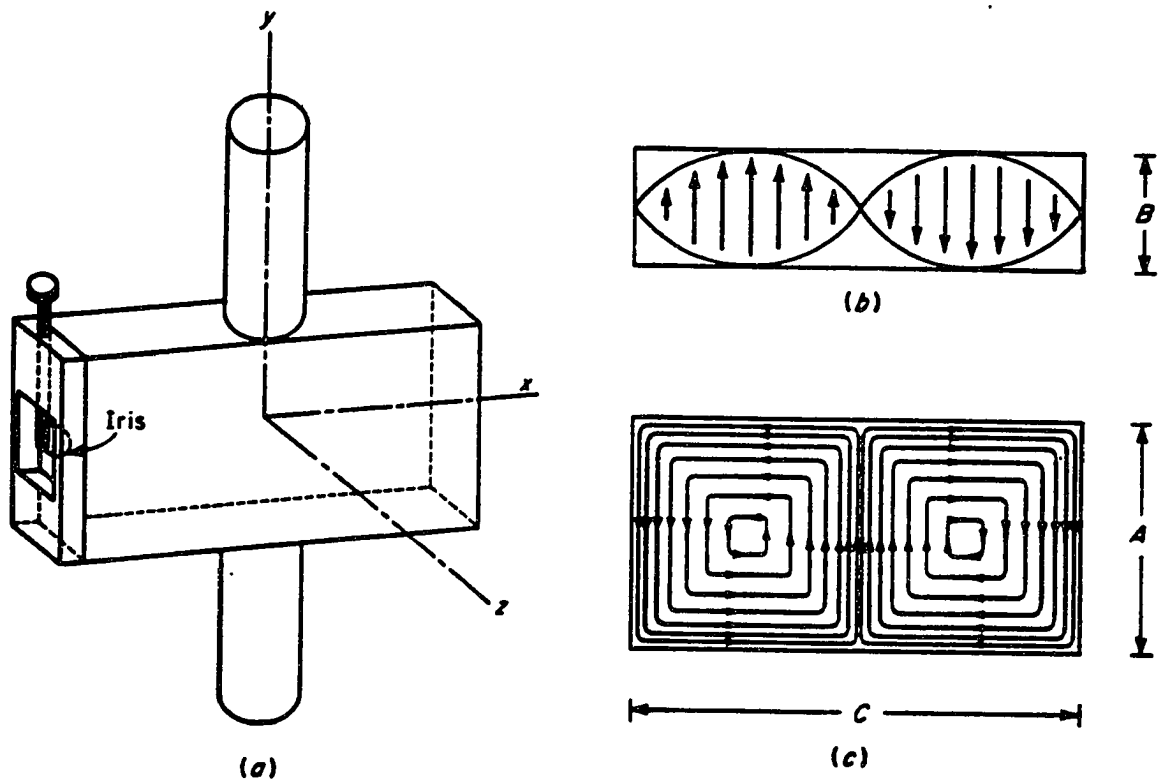
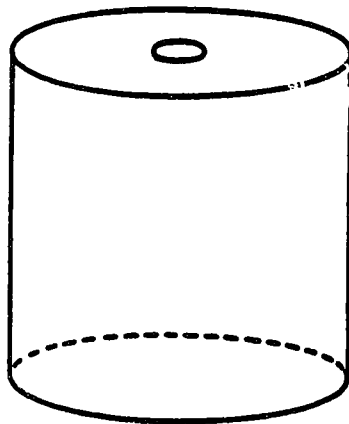
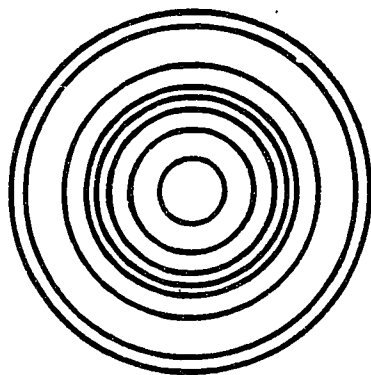


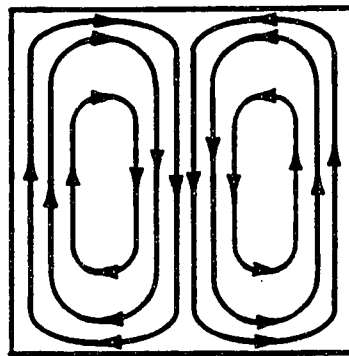
Figure 1.2: A rectangular  $TE_{102}$  microwave cavity. (a) Cylindrical extensions above and below the cavity prevent excessive leakage of microwave radiation out of the cavity and act as positioning guides for a sample. The microwave energy is coupled into the cavity through the iris hole at the left. (b) Electric field (—) distribution. (c) magnetic field (---) distribution. A is one half-wave length; C is two half-wavelengths; the B dimension is not critical, but should be less than one half-wavelength (31).



(a)



(b)



(c)

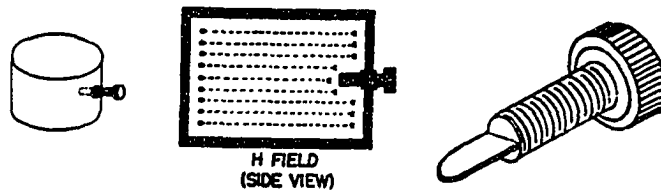
Figure 1.3: Cylindrical cavity operating in the  $TE_{011}$  mode. (a) Cavity: the resonant frequency is determined by the height and diameter of the cylinder. (b) Electric ( $\bullet \times$ ) and (c) magnetic field (---) distributions (31).

## Coupling of microwave energy into cavities and cavity tuning

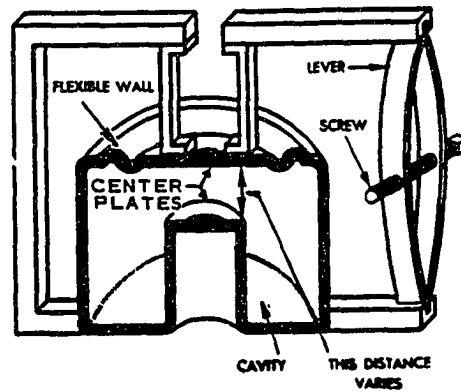
Microwave energy can be coupled into and out of the cavity by means of an iris (Fig. 1.2 (a)), which is a small hole in a plane perpendicular to the direction of the electromagnetic wave propagation. The coupling results from the penetration of the electromagnetic fields through the opening. It is essentially an impedance matching device between the waveguide and the cavity. It serves to reduce the reflection of microwave energy from the cavity. By adjusting the position of a metallic tip inserted in the hole, optimum impedance matching can be achieved, in which case, the reflection of the microwave from the cavity is solely due to the absorption of the microwave energy by the sample.

Tuning of a cavity may be accomplished by changing any of the following three parameters: cavity inductance, cavity capacitance and cavity volume (32). Figure 1.4 (a) illustrates the method for tuning a cavity by varying its inductance. A metallic screw is inserted into the cavity at a point where the  $H_1$  field is maximum. This will decrease the effective inductance of the cavity, and increase the resonance frequency. A second method for tuning a cavity, i.e. by varying its capacitance, is depicted in Figure 1.4 (b), where the E-field is contained in the gap between the center plates. Adjusting the distance between the center plates varies the capacitance of the cavity, hence the

(a)



(b)



(c)

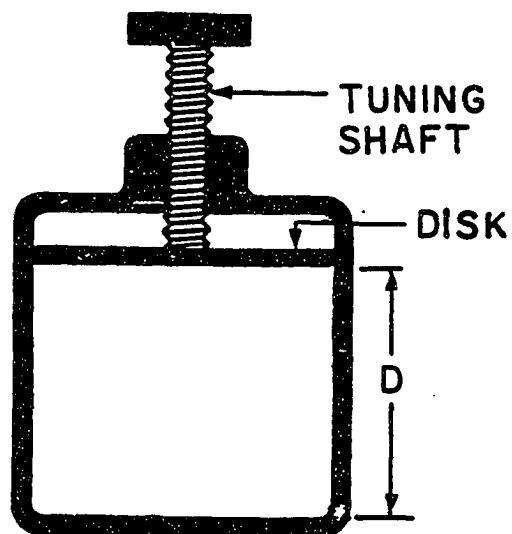


Figure 1.4: (a) Cavity tuning by inductance. (b) Cavity tuning by capacitance. (c) Cavity tuning by volume (32).

resonance frequency. A cylindrical cavity is commonly tuned by varying its volume, i.e. adjusting the vertical position of a piston fitted to one end of the cavity (Figure 1.4 (c)), the larger the distance, the lower the resonance frequency.

### Cavity Q

One important characteristic property of a cavity is its Quality factor (Q) which reflects how efficiently the microwave energy is stored in the cavity. One way to define Q is

$$Q = 2\pi(\text{energy stored})/(\text{energy dissipated}) \quad (1.14)$$

The overall or loaded Q ( $Q_L$ ) can be computed by the following equation (33):

$$1/Q_L = 1/Q_u + 1/Q_e + 1/Q_r + 1/Q_x \quad (1.15)$$

where  $Q_u$  is the unloaded Q, arising only from the ohmic losses in the cavity walls;  $Q_e$  is due to dielectric losses,  $Q_r$  to energy loss through the cavity coupling hole and  $Q_x$  to the energy loss from the sample at resonance. Equation (1.13) implies that the Q of the cavity can be increased by decreasing the resistance of the cavity wall and using samples with low dielectric constant.

An alternative definition for Q is the following (34):

$$Q = \nu_0 / \Delta\nu \quad (1.16)$$

where  $\nu_0$  is the resonance frequency of the cavity and  $\Delta\nu = \nu_2 - \nu_1$ , which is the difference of frequency values at which half the power is reflected back from the cavity. Based on this latter definition, the Q measurement can be made by using the mode pattern on the oscilloscope, which is a display of the klystron power output reflected from the microwave cavity as a function of the microwave frequency (Fig. 1.5). See Appendix B for details on measurements of the cavity Q.

#### **Absorption and dispersion mode**

Absorption and dispersion modes are essentially two methods of microwave detection in EPR. An important property of the sample which is responsible for EPR detection is the magnetic susceptibility  $\chi$ ,

$$\chi = \chi' + i\chi'' \quad (1.17)$$

At resonance, the sample interacts with the microwave magnetic field causing a change in both the real ( $\chi'$ ) and imaginary part ( $\chi''$ ) of  $\chi$ . The change in the imaginary part ( $\chi''$ ) causes a change of cavity  $Q_x$ , since (33)

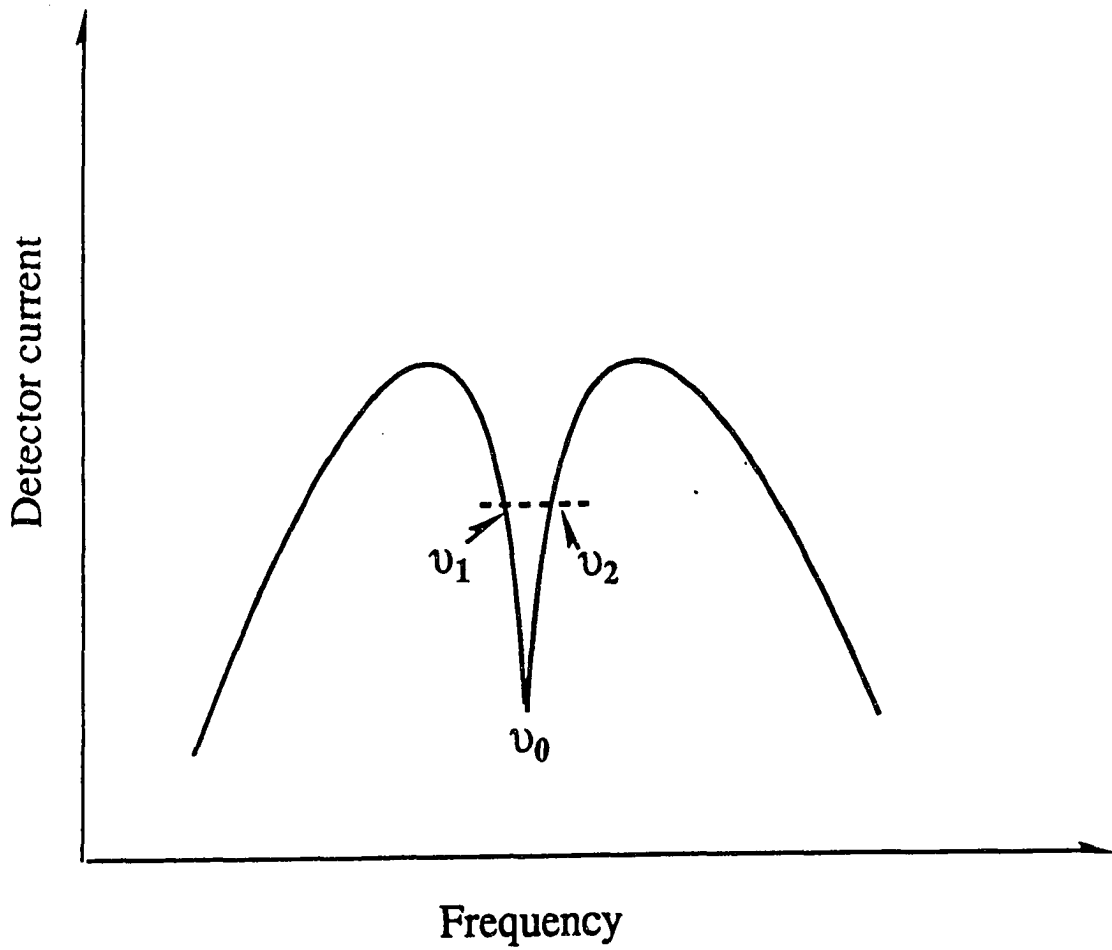


Figure 1.5: Schematic diagram of klystron power mode.  $\nu_0$  is the resonant frequency of the cavity and  $\nu_1 - \nu_2$  is the half-power bandwidth of the cavity. (mode.the)



$$Q_x = [(v_0/2) \int_{\text{cavity}} H_1^2 dV] / [(v_0/2) \int_{\text{sample}} H_1^2 \chi'' dV] \quad (1.18)$$

The numerator represents the energy stored in the cavity, whereas the denominator the energy absorbed by the sample. If  $\chi''$  is homogeneous over the sample volume, then

$$Q_x = [\int_{\text{cavity}} H_1^2 dV] / [\chi'' \int_{\text{sample}} H_1^2 dV] \quad (1.19)$$

The change of  $Q_x$  can cause the change of overall  $Q$  (eq. 1.15), hence the reflection of the microwave energy from the cavity, which can be detected by means of a crystal detector in the bridge, furnishing the absorption mode detection (33).

The dispersion mode, on the other hand, is related to the change in the real part of the magnetic susceptibility ( $\chi'$ ), which leads to a change in the resonant frequency of the cavity (33). To understand this frequency change, consider the velocity  $v$  of the electromagnetic radiation in a dielectric medium

$$v = 1/(\mu\varepsilon)^{1/2} = \lambda f \quad (1.20)$$

where  $\mu$  is the permeability of the sample,  $\mu = \mu_0 (1+\chi')$ ;  $\varepsilon$  is the dielectric constant of the sample;  $f$  is the resonant frequency of the cavity and  $\lambda$  is the wavelength of  $f$ . Since

the wavelength is fixed by the dimension of the cavity, if there is a change in  $\chi'$ , then the frequency will change. This frequency change can be detected by an AFC (automatic frequency control) detector when the microwave bridge is operating in dispersion mode.

The Varian E-110 Q-band microwave bridge can be operated in either the absorption or dispersion mode. Both modes have been used in the EPR and ENDOR measurements presented in the next two chapters.

**CHAPTER 2**  
**CONSTRUCTION AND PERFORMANCE OF "RIBBON-WOUND" TE<sub>011</sub>**  
**CYLINDRICAL EPR CAVITIES**

**Introduction**

Applications of Q-band (35 GHz) EPR and ENDOR spectroscopy have become increasingly widespread (19-25). Thus, the design of robust yet sensitive Q-band cavities for use in both EPR and ENDOR measurements at liquid helium temperatures are of considerable interest. However, construction of such cavities is challenging since they must withstand repeated temperature cycling as well as provide high microwave energy density and magnetic field modulation at the sample. With these considerations in mind, several methods of cavity construction have been developed and used in the past. The most straightforward approach is a solid metal wall cylindrical cavity, constructed from a thin metal layer deposited onto a rigid, nonconducting material such as glass, ceramic or plastic (28,29). Construction of this type of cavity is difficult since, not only must the metal layer withstand temperature cycling without cracking, but it must also be thinner than the skin depth of the 100 kHz field modulation frequency (200 - 400  $\mu\text{m}$ ), yet thicker than the 35 GHz microwave skin depth (0.5 - 1  $\mu\text{m}$ ). Moreover,

degenerate resonant modes cannot be avoided with this design. A loop-gap resonator (35-40), a low  $Q_L$  device which does not have degenerate modes, has also been used successfully for 35 GHz EPR spectroscopy (30).

Another type of cavity commonly used in the Q-band EPR experiment is the  $TE_{011}$  cylindrical silver wire-wound cavity in which the cavity wall is made of a silver wire embedded in an epoxy body (41). Cylindrical cavities in the  $TE_{011}$  mode are often used in EPR measurements because they usually have a higher microwave energy density at the sample than rectangular cavities (31). The major advantage of the wire-wound cavity over the solid metal wall cavity lies in the fact that it provides sufficient penetration of the modulation field, and also suppresses mode degeneracy since, among all the resonant modes in a cylindrical resonant cavity, only  $TE_{0mn}$  modes have pure azimuthal wall current distribution. Thus, a cavity having a spiral conductive wall as part of the cavity wall attenuates all modes except the  $TE_{0mn}$  family. Eddy currents caused by the field modulation are also greatly minimized. Apart from the difficulty in making the wire-wound cavity, it is not very durable since the silver wire (about 155 cm in full length in a Varian cavity) has the tendency to come loose from the epoxy body during repeated temperature cycling. To overcome these problems, a new  $TE_{011}$  cylindrical EPR Q-band cavity wall has been developed. The construction and the

performance of the newly designed  $TE_{011}$  cavity in both EPR and ENDOR spectroscopy are described here.

## Materials and methods

### *Cavity Wall Construction*

Figure 2.1(a) shows a schematic drawing of the cross section of the cavity wall. Bonded to the epoxy or epoxy/quartz composite is a thin metal (brass or aluminum) alloy layer with a spiral groove cut through the alloy along the entire length of the cavity except for one end. Since the structure resembles the silver wire-wound cavity, we call it a "ribbon-wound" cavity. The unloaded  $Q$  ( $Q_u$ ) critically depends on the cavity dimension and operating mode as well as the material of the cavity wall. For  $TE_{011}$  cylindrical cavities, the maximum  $Q_L$  is obtained when the diameter of the cavity is the same as the length of the cavity at resonance (Appendix C). At Q-band frequencies (34 - 36 GHz), the optimal diameter is about 11.3 mm, with the length of the cavity being adjusted using a piston which can be screwed in from the bottom. Coupling is achieved with a standard Varian "iris" arrangement at the top of the cavity.

A mandrel 12.3 mm in diameter and approximately 40 mm long is first made out of a whole piece of brass or aluminum

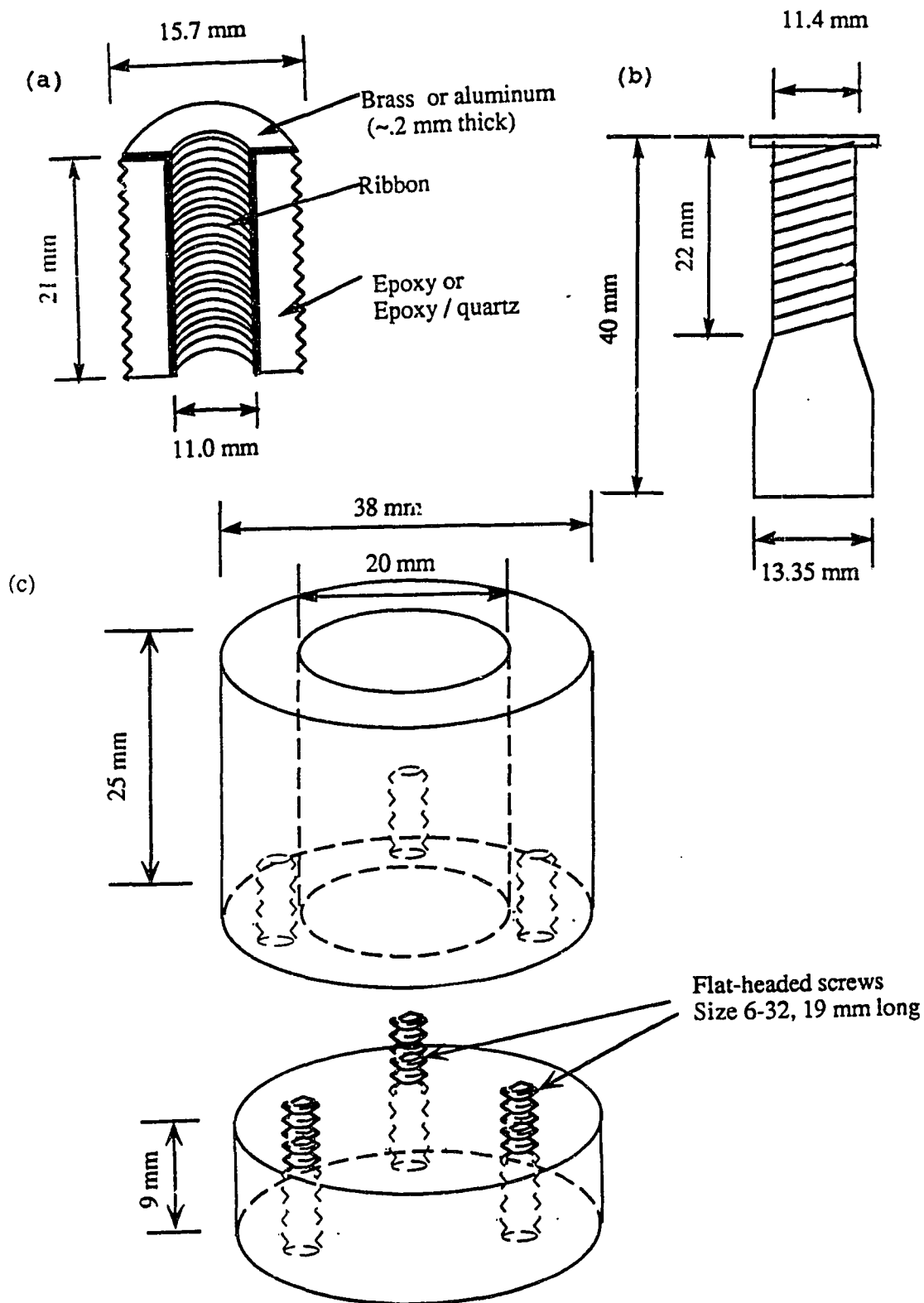


Figure 2.1: (a) Ribbon-wound cavity (b) Brass or aluminum mandrel (c) Teflon mold. (55) (File name: Cavity.the)

alloy (Fig. 2.1(b)). The mandrel is made 18 mm longer than the final desired length of the cavity to provide a handle for machining. The selection of the alloy is based on its metal content and machinability. For the brass cavity, Alloy 360 standard free-cutting brass (McMaster-Carr Supply Company, Dayton, NJ) is used. It contains 61.5% copper, 35.4% zinc and 3.1% lead, the lead content providing "lubrication" during high speed machining. To make the aluminum ribbon-wound cavity, alloy 6063-T5 (Central Steel & Wire Company, Chicago, Illinois), containing 99% Al, 0.35% Fe, 0.10 % each of Cu, Mn, Cr, Zn and Ti is used. Spiral grooves (24 threads/in.) are then cut into the alloy at a depth of about 0.0075" (~ 0.2 mm) from one end of the mandrel to the other as indicated in Figure 2.1(b). The grooved part of the mandrel, roughly 22 mm long, is then placed into a Teflon mold (38 mm o.d., 20 mm i.d.) (Fig. 2.1(c)) and cast with either epoxy or an epoxy/quartz composite (see below). The mandrel then is released from the mold and the brass (or aluminum) drilled out through the center until the spiral grooves emerge on the inside, giving a ribbon thickness of 0.2 mm and an inner diameter of 11.0 mm. The entire length of the outermost surface of the epoxy is threaded (40 threads/in.) for attaching one end of the cavity to the terminated waveguide with the coupling "iris" and the other end to the tuning piston. The excess brass (or aluminum), epoxy, and the end of the cavity wall are

then machined off. Finally the inner wall of the finished cavity is polished with a slurry of fine silica powder (38 - 45  $\mu\text{m}$  dia.) free of EPR signals in a water/glycerol (3:1 by volume) solution.

A thin layer of silver or gold is then electrically plated onto the brass ribbon to enhance the conductivity. The silver plating is done using a solution of analytical reagent grade KCN (Mallinckrodt Chemical Works, St. Louis, Missouri) (47 g/L),  $\text{AgNO}_3$  (Mallinckrodt) (31.7 g/L) and  $\text{K}_2\text{CO}_3$  (Aldrich Chemical Company, Inc.) (25 g/L). The detailed plating procedure is described in Appendix D. Stock solutions (103.7 g/L) were passed down a Chelex 100 (Sigma) column before mixing to reduce levels of Cu(II) and other divalent metal ion impurities giving rise to weak EPR signals at liquid helium temperatures from the cavity wall.  $\text{AgNO}_3$  salt with KCN was used instead of  $\text{AgCN}$  salt normally employed in traditional silver plating solution because of the lower Cu content of the resultant solution (0.6 ppm vs. 3.0 ppm respectively) as measured by atomic absorption spectrometry. About 30 minutes total plating time (2 minutes forward followed by 1 minute reverse plating in every 3 minute cycle) at a current density of 5  $\text{mA}/\text{cm}^2$  results in a silver layer of 5-10  $\mu\text{m}$ . The gold plating (2-5  $\mu\text{m}$  in thickness) was done by Exotic Plating Lab (North Chelmsford, Massachusetts).

Weak background signals from the cavity were further



attenuated 20 - 50 % by soaking the finished cavity wall in a solution of KCN (47 g/L) and  $\text{Na}_2\text{S}_2\text{O}_4$  (Aldrich Chemical Company, Inc.) (30 g/L) for 6 - 8 hours under an argon atmosphere. Weak signals from  $\text{Mn}^{2+}$  were eliminated by subsequent rinsing in household bleach (5.25 % sodium hypochlorite solution). In the case of the silver cavity, the cavity wall was polished afterwards with Tarn-X metal polishing detergent (Doman Products, Inc., Lincolnwood, Illinois) to remove the oxidized silver layer from the action of the bleach.

#### ***EPR Silver Wall Cavity Construction***

A solid thin silver wall cavity was also constructed by affixing layer of silver to an epoxy/quartz body using the method described by Cook et al. (42). Briefly, a thin silver layer (5-10  $\mu\text{m}$ ) was first electroplated onto an aluminum mandrel and the mandrel cast in the epoxy/quartz composite. After the Teflon mold was removed, the epoxy/quartz body was threaded and the aluminum mandrel dissolved away in a concentrated NaOH solution. The silver layer was polished with Simichrome Polish polishing paste (Imported by Competition Chemicals, Inc., Iowa Falls, Iowa) to smooth out any uneven parts of the surface caused by inhomogeneous plating and then finally polished with Tarn-X.

### *Epoxy and Epoxy/quartz Formulation*

The epoxy casting mixture consists of 22 parts (by weight) DER 331 Liquid Epoxy Resin and 26 parts Henkel Versamid 140 Curing Agent (Allied Resin Corp., East Weymouth, Massachusetts). In the case of the epoxy/quartz composite 52 parts silica powder are added. The cured resin is suitable for cryogenic applications and is free of EPR signals. The silica powder is obtained by grinding signal-free T08 quartz tubing (Heraeus-Amersil, Duluth, Georgia) in a ball mill, followed by sieving through standard testing sieves. Fine silica powder with diameters of 38-45  $\mu\text{m}$  and below 38  $\mu\text{m}$  are used 1:1 with the epoxy silica composite. To wash off the impurities introduced during the grinding and sieving processes, the powder is soaked in a concentrated HCl/HNO<sub>3</sub> (1:1 by volume) solution for approximately 5 minutes, heated to a boil for another 5 minutes, and then allowed to stand in the acid mixture at room temperature overnight. Finally the powder is rinsed with deionized water to remove the acid and annealed in a furnace at about 800°C for 8-10 hours to eliminate a residual weak EPR signal remaining in the quartz.

The addition of silica thickens the epoxy. To reduce the viscosity, the mixing and pouring must be done through the open door of an oven at about 150°C. In order to remove trapped air in the resin and thoroughly fill the space between the grooves on the mandrel, the Teflon mold is

vibrated with a hand held vibrator while pouring the epoxy mixture. The mixture is then cured for about 1 hour at 160°C followed by 16 hours at room temperature. More extensive curing at elevated temperature introduces EPR signals.

### *Sample preparations*

The weak pitch sample is made by adding appropriate amount of coal (Burbh blacksvill #2) into a powder of KCl to make a final percentage of 0.012 % coal by weight. The mixture is thoroughly grounded using a pestle and a mortar to obtain a homogeneous sample. Then the sample is pumped to below  $10^{-3}$  Torr in a standard EPR sample tube (3 mm i.d., 4 mm o.d.) and sealed under vacuum. Burbh Blacksvill #2 is used because it has a characteristic g-factor (2.003) and peak-to-peak line width (1.7 G) close to that of the pitch sample ( $g = 2.0028$  and EPR line width = 1.7 G). In a similar manner, the sample was also made in a capillary tube (1 mm i.d., 2 mm o.d. ) for Q-band cavities. To correct for the spin concentration, the final sample is tested on the Varian E-4 EPR spectrometer and is found to be 5 % higher in signal amplitude than a standard Varian weak pitch sample (0.0003 % pitch in KCl) under the same instrumental conditions. Neither line broadening nor deterioration of the signal has been observed over a period of about 12 months.

The vanadyl imidazole complex was prepared as described in reference 43.

#### ***EPR and ENDOR Measurements***

EPR measurements were done on a Varian E-9 EPR Spectrometer with the Varian E-110 Q-band microwave bridge in both absorption and dispersion mode (See Appendix E for operation procedure of the bridge). The spectra were taken by a computer data acquisition system using EW software (Philip D. Morse and Scientific Software Services, Bloomington, IL). Low temperature (liquid helium) measurements employed a MODEL 8CC Variable Temperature Helium Flow Cryostat (CRYO Industries of America, Inc., Atkinson, New Hampshire) fitted with an epoxy fiber glass tail which allows penetration of the modulation field from externally mounted coils. This external arrangement of the modulation coils permits high modulation fields to be achieved and avoids increased helium boil-off when the field modulation is turned on.

#### **RESULTS AND DISCUSSION**

Ribbon-wound cavities are more robust than the traditional silver wire-wound cavity because the large surface area of the wide, flat ribbon ( $\approx 70$  cm length) provides better bonding between the metal and epoxy. As a

consequence, the ribbon is less likely to separate from the epoxy as is the case with the thin 155 cm wire of a wire-wound cavity. The thermal coefficient of expansion of the epoxy/quartz composite more closely matches that of the alloy and in principle should result in a more thermally stable structure. This has been our experience. However, to date an aluminum ribbon-wound cavity constructed with a straight epoxy body has held up equally well during repeated temperature cycling between room temperature and 4 K provided that cooling or heating rates do not exceed 8 K/min.

The cavity  $Q_L$ , modulation field penetration (MFP), and signal to noise ratio (S/N) of standard Varian weak pitch for four different ribbon-wound cavities are summarized in Table 2.1. For comparative purposes, the corresponding measurements were also made on a commercial Varian silver wire-wound cavity and on the solid thin silver wall cavity (Table 2.1). The loaded  $Q$ 's for all cavities are very similar (2000 - 2600) with the silver cavities having slightly higher  $Q$ 's than the others, presumably due to their higher wall conductivities.

Table 2.1 Results of cavity performance testing.

Cavities	Wall thickness (mm)	$Q_L^b$	MFP <sup>c</sup> (G)	S/N <sup>d</sup>	$P_{1/2}^e$ (mW)	Background signal as percent of Cu <sup>2+</sup> EPR signal <sup>f</sup>	
						Peak-Peak	Double Integral
Brass ribbon-wound cavity	.2	2000	27	1000	.24	1.6	11
Silver-plated brass ribbon-wound cavity	.2	2600	27	1150	.24	.9	9
Gold-plated brass ribbon-wound cavity	.2	2000	27	800	.20	1.2	12.5
Aluminum ribbon-wound cavity	.2	2200	27	900	.19	1	4
Silver wire-wound cavity	.4 <sup>a</sup>	2300	20	1100	.20	---	---
Thin silver wall cavity	.01	2500	10	1150	.20	---	---

33

<sup>a</sup>The diameter of the silver wire.

<sup>b</sup> The  $Q_L$  values were measured with an empty capillary quartz tube (2.10 mm o.d., 0.99 mm i.d.) in the cavity, following the method described by Dalal et al. (34). Estimated error in  $Q$  is  $\pm 5\%$  or nominally  $\pm 100$ .

<sup>c</sup>Modulation field penetration was measured from the overmodulation broadening of the  $m_1 = 1/2$  line of Mn<sup>2+</sup> in CaO ( $\Delta H_{pp} = 0.7$  G).

<sup>d</sup>A time constant of 1 s and a modulation amplitude of 8 G were employed. The Signal-to-Noise ratio was calculated from  $S/N = (\text{Signal/Noise})\sqrt{P_0/P_1}$ . See Appendix F for more details.

Obtained from curve fitting the equation  $A = KP^{0.5}/(1+P/P_{1/2})^{.5b}$  (44), where A is the EPR signal amplitude, K a proportionality constant, P the microwave power,  $P_{1/2}$  the microwave power at half saturation of the EPR signal, and b the inhomogeneity parameter. Errors are nominally  $\pm 0.02$  mW (Appendix F).

EPR spectrum of 1mM  $\text{CuCl}_2$ ,  $\text{H}_2\text{O}$ /glycerol (2:1 by volume) taken at 4  $\mu\text{W}$  and 15 K with other instrument settings the same as those for cavity background measurements in Figure 2.4. The ratio (R) between Cu(II) signal amplitude and the background signals was calculated from the following equation:  $R = (\text{Cu-signal}/\text{Background})\sqrt{P_2/P_1}(T_1/T_2)$ , where  $P_1$ ,  $P_2$  and  $T_1$ ,  $T_2$  are the corresponding microwave powers and temperatures under which the spectra were taken for the 1 mM  $\text{CuCl}_2$  solution and the cavity background signals respectively.

The ribbon-wound cavities have superior peak-to-peak modulation penetration compared to the silver wire-wound cavity (27 G vs. 20 G, Table 2.1). Both the ribbon-wound and wire-wound cavities have greater modulation penetration than the thin silver wall cavity (10 G) since opposing fields from induced eddy currents are minimized in the spiral structures. Since for liquid helium temperature operations, the outer diameter of the fiber glass tail on the Cryostat is too big to fit into the Varian modulation coil holder, a homemade modulation coil (Appendix G) was used instead. The modulation penetration in this configuration is about half of that with the Varian coil in the absence of the Cryostat due to the close placement of the coils to the magnet pole faces. The signal-to-noise ratios with weak pitch are comparable for all the cavities (800 - 1100).

The power saturation curves of weak pitch in the various cavities are shown in Figure 2.2. The values of the microwave power at half saturation of the EPR signal,  $P_{1/2}$ , are relatively low ( $\approx 0.20 - 0.24$  mW) at room temperature (Table 2.1), reflecting the high microwave energy density at the sample in all the  $TE_{011}$  cavities. It is evident from Figure 2.2 that the silver plated brass ribbon-wound cavity performs best but the other cavities also work quite well.

In order to determine the optimum sample tube size for the ribbon-wound cavity, the EPR signal of a 3 mM  $CuCl_2$



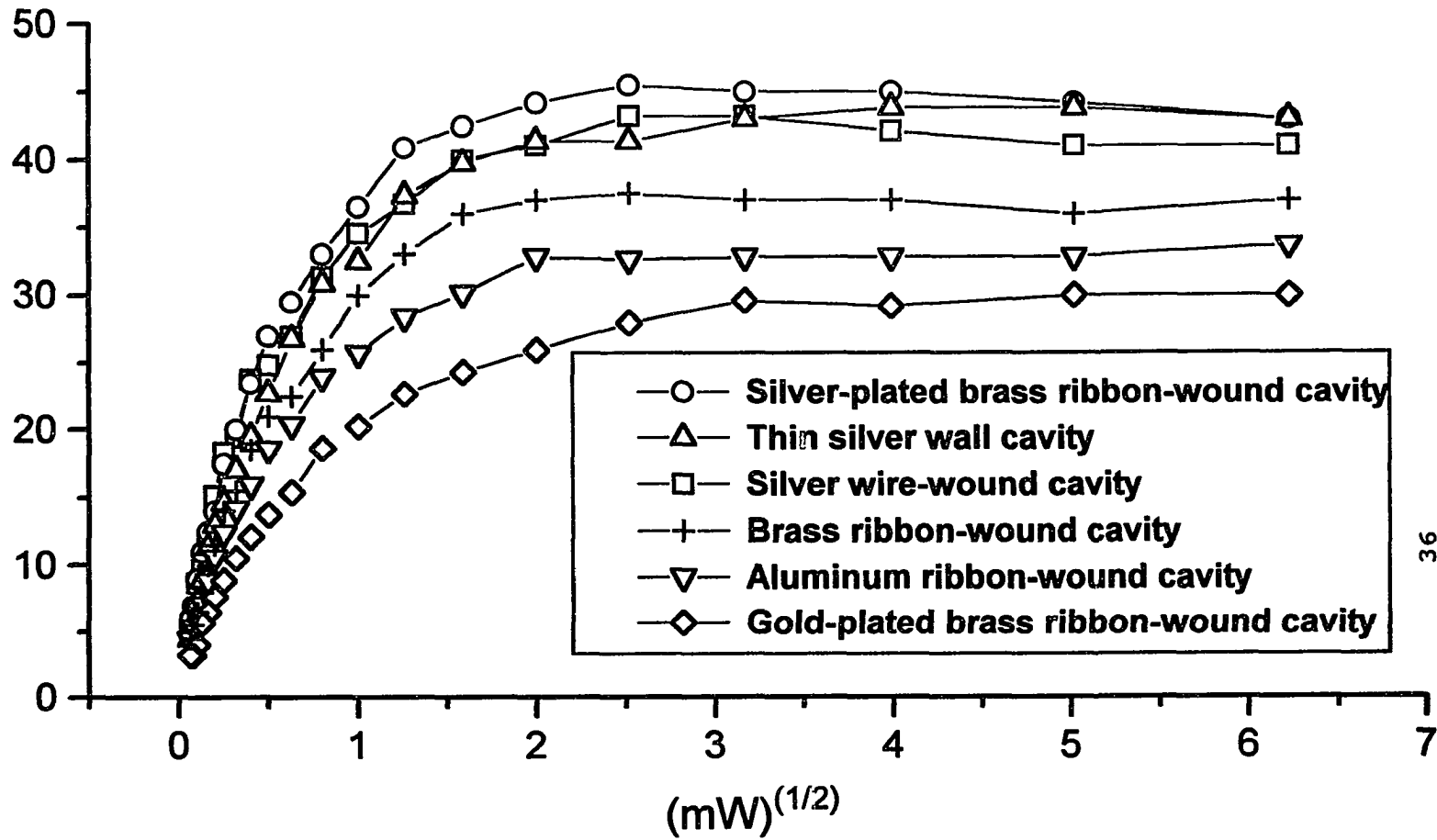


Figure 2.2: Power saturation curves of weak pitch sample. Data scaled to relative Signal/Noise of each cavity (Table 2.1). (File name: nat701.plt)

solution was measured in a series of capillary tubes (Wilmad Glass, Buena, New Jersey) with different inner and outer diameters. The results are listed in Table 2.2. A plot of the signal amplitudes as a function of tube dimensions is also provided (Fig. 2.3). Capillary tubes with 1.3 mm i.d. and 2.15 mm o.d. (Vitro Dynamics, Mountain Lakes, New Jersey) give the strongest EPR signal of all the tubes tested. Furthermore, the data in Table 2.2 show that capillary tubes of 1 mm i.d. or smaller sizes traditionally employed in Q-band work, give EPR signals a factor of two or more lower than that obtained with the 1.3 mm i.d. tube.

Table 2.2 Dependence of EPR Signal Amplitude on Capillary Tube Dimensions.

Capillary tubes No.	i.d. (mm)	o.d. (mm)	Relative EPR signal <sup>a</sup>
#1	0.50	.85	5.9
#2	0.50	2.10	17.6
#3	0.85	1.15	18.8
#4	.99	2.10	50.0
#5	1.00	1.55	45.3
#6	1.05	1.80	32.7
#7	1.20	1.85	69.1
#8	1.30	2.15	100
#9	1.35	2.2	86.4
#10	1.39	2.30	95.0

<sup>a</sup>EPR signal amplitude of 3 mM CuCl<sub>2</sub> in 2:1 H<sub>2</sub>O/glycerol normalized to 100. Instrument conditions: Field Set, 11500 G; Scan Range, 2000 G; Scan Time, 4 minutes; Modulation Amplitude, 5 G; Modulation Frequency, 100 kHz; Microwave Frequency, 35 GHz; Microwave Power, 1.6 mW; Receiver Gain, 100; Time Constant, 0.3 s; Temperature, 100 K.

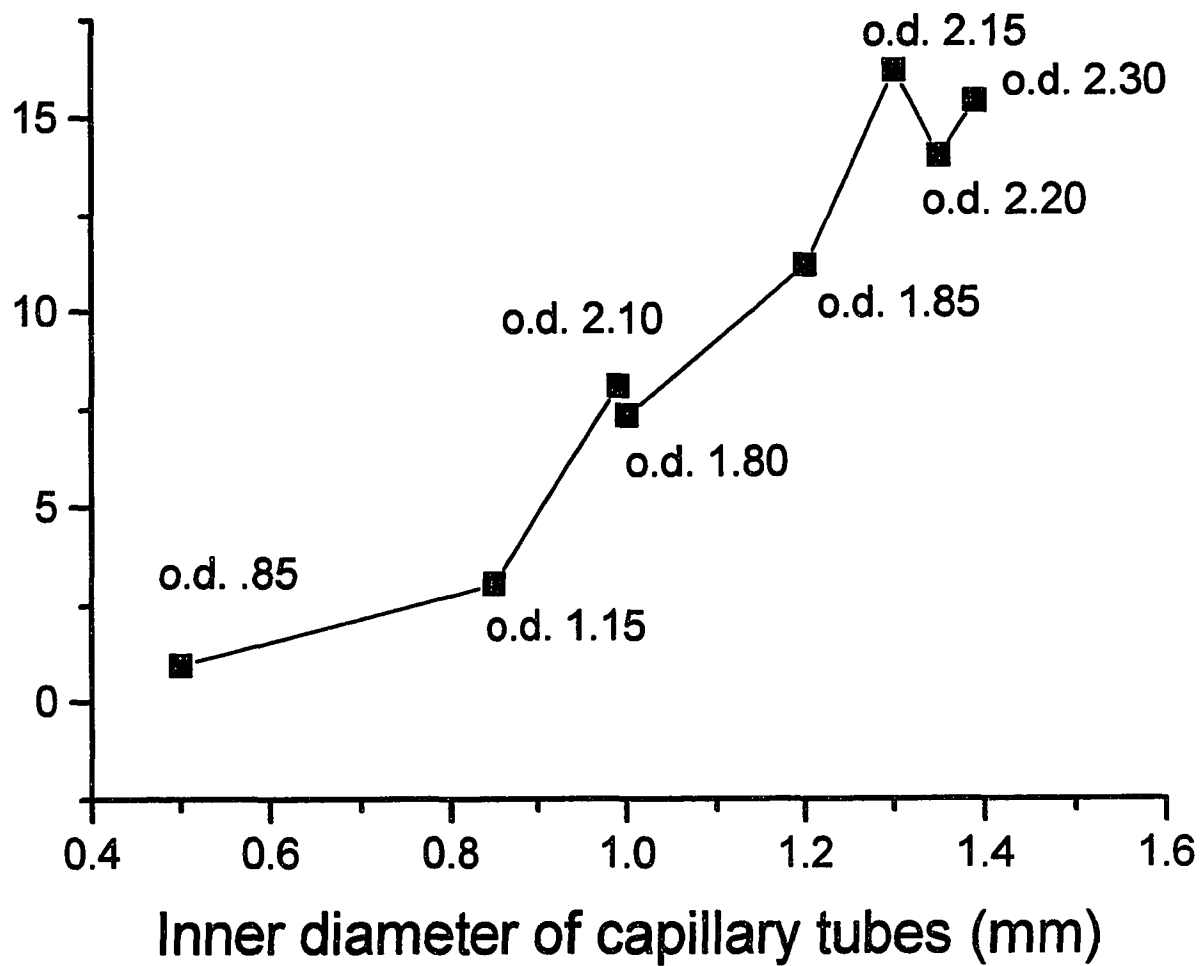


Figure 2.3: Signal amplitude of 3 mM CuCl<sub>2</sub> in 2:1 H<sub>2</sub>O/glycerol vs tube dimensions. Experiment conditions: same as in Table 2.2. (Filename: tubes.plt)

Figures 2.4 and 2.5 illustrate the quality of the EPR spectra obtained with the ribbon-wound cavity. Figure 2.4 shows the dispersion spectrum of a 20 mM  $\text{VO}(\text{Im})_4^{2+}$  ( $\text{Im} \equiv$  imidazole) solution at 4.5 K. The spectrum was measured at a modulation frequency of 100 kHz under rapid passage conditions using the silver plated brass ribbon-wound cavity. The steps in the wings of the spectrum from the 8 parallel hyperfine lines of the  $^{51}\text{V}$  ( $I = 7/2$ ) nucleus are clearly evident as are the more intense 8-line perpendicular features corresponding to the smaller  $^{51}\text{V}$  hyperfine coupling. For comparison, absorption spectra at 4.7 K of 1 mM  $\text{VOSO}_4$  solution at 1.6 mW and under rapid passage conditions, and of 20 mM  $\text{VO}(\text{Im})_4^{2+}$  solution at only 0.6  $\mu\text{W}$  power are shown in Figure 2.5. A 10 kHz modulation frequency was used for both of these spectra. The spectrum of  $\text{VO}(\text{Im})_4^{2+}$  at low power in Figure 5b shows minor rapid passage effects and more closely resembles Q-band EPR spectra of  $\text{VO}^{2+}$  measured at 100 K where saturation does not readily occur (45).

Cavity background signals are almost always a problem at liquid helium temperatures with immersion cavities since most materials contain trace amounts of EPR active impurities (e.g.  $\text{Cu}(\text{II})$ ,  $\text{Mn}(\text{II})$ , etc.) which become observable at low temperatures. While all the ribbon-wound cavities are free of background EPR signals at room temperature and show only very weak signals at 100 K (not shown), signals around  $g \approx 2$  become observable at liquid

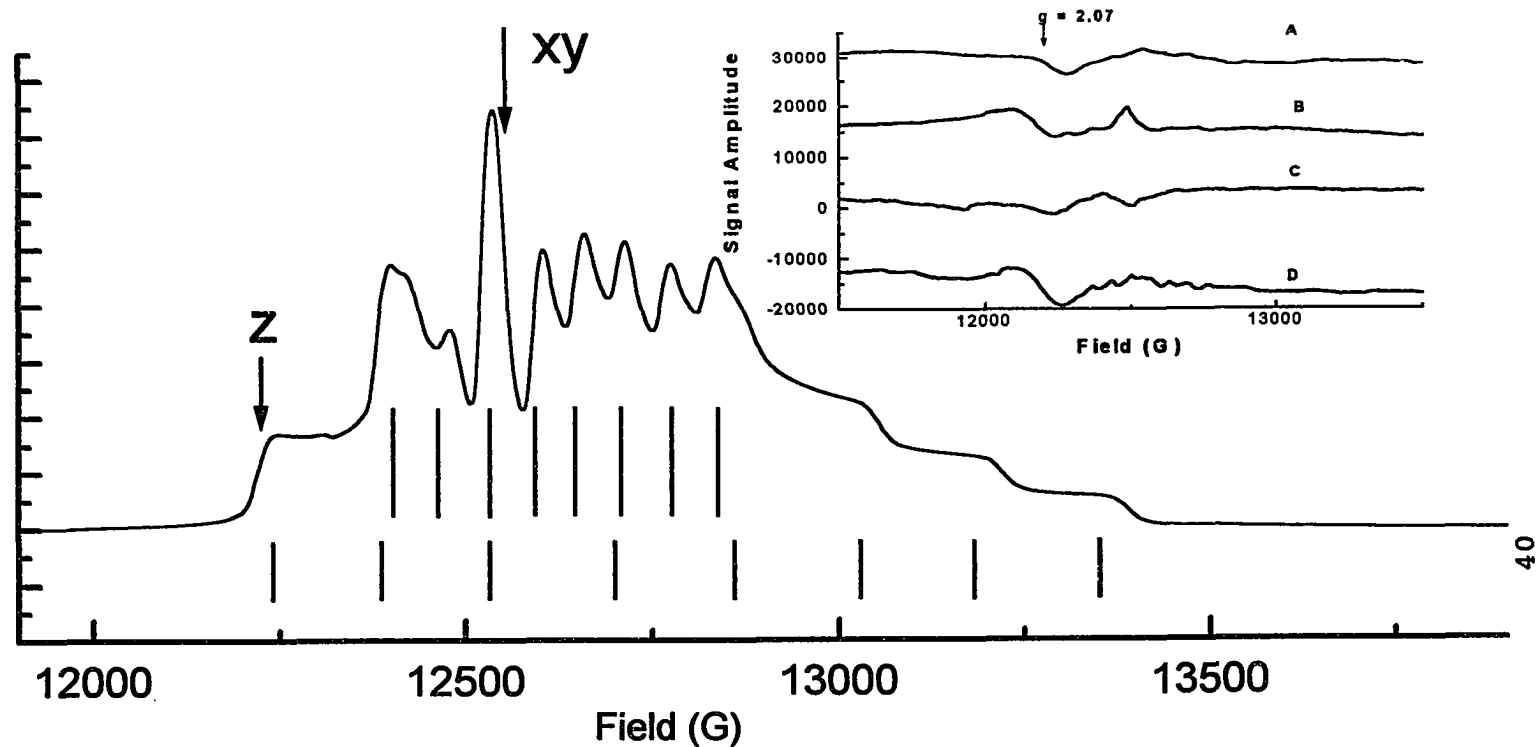


Figure 2.4: Dispersion mode rapid-passage EPR spectrum of  $20 \text{ mM VO(Im)}_2^{2+}$  in a  $2:1 \text{ H}_2\text{O/glycerol}$  solution at  $\text{pH} = 7$  in a silver plated brass ribbon-wound cavity. Instrument conditions: Field Set,  $12900 \text{ G}$ ; Scan Range,  $2000 \text{ G}$ ; Scan Time,  $8 \text{ minutes}$ ; Temperature,  $4.5 \text{ K}$ ; Microwave Frequency,  $34.905 \text{ GHz}$ ; Microwave Power,  $3.95 \text{ mW}$ ; Modulation Frequency,  $100 \text{ kHz}$ ; Modulation Amplitude,  $0.4 \text{ G}$ ; Receiver Gain,  $2.5$ ; Time Constant,  $0.3 \text{ s}$ . Inset: Weak cavity background signals at liquid helium temperature. A, Aluminum ribbon wound cavity; B, Gold-plated brass ribbon-wound cavity; C, Silver-plated brass ribbon-wound cavity; D, Brass ribbon-wound cavity. Instrument conditions: Field Set,  $12500 \text{ G}$ ; Scan Range,  $2000 \text{ G}$ ; Scan Time,  $4 \text{ minutes}$ ; Temperature,  $6 \text{ K}$ ; Microwave Frequency,  $35 \text{ GHz}$ ; Microwave power,  $1.6 \text{ mW}$ ; Modulation Frequency,  $100 \text{ kHz}$ ; Modulation Amplitude,  $5 \text{ G}$ ; Receiver Gain,  $1250$ ; Time Constant,  $1 \text{ s}$ . The measurements were taken with an empty capillary tube ( $0.99 \text{ mm i.d.}$ ,  $2.10 \text{ mm o.d.}$ ) inside the cavity. (File name: 032195b.plt)

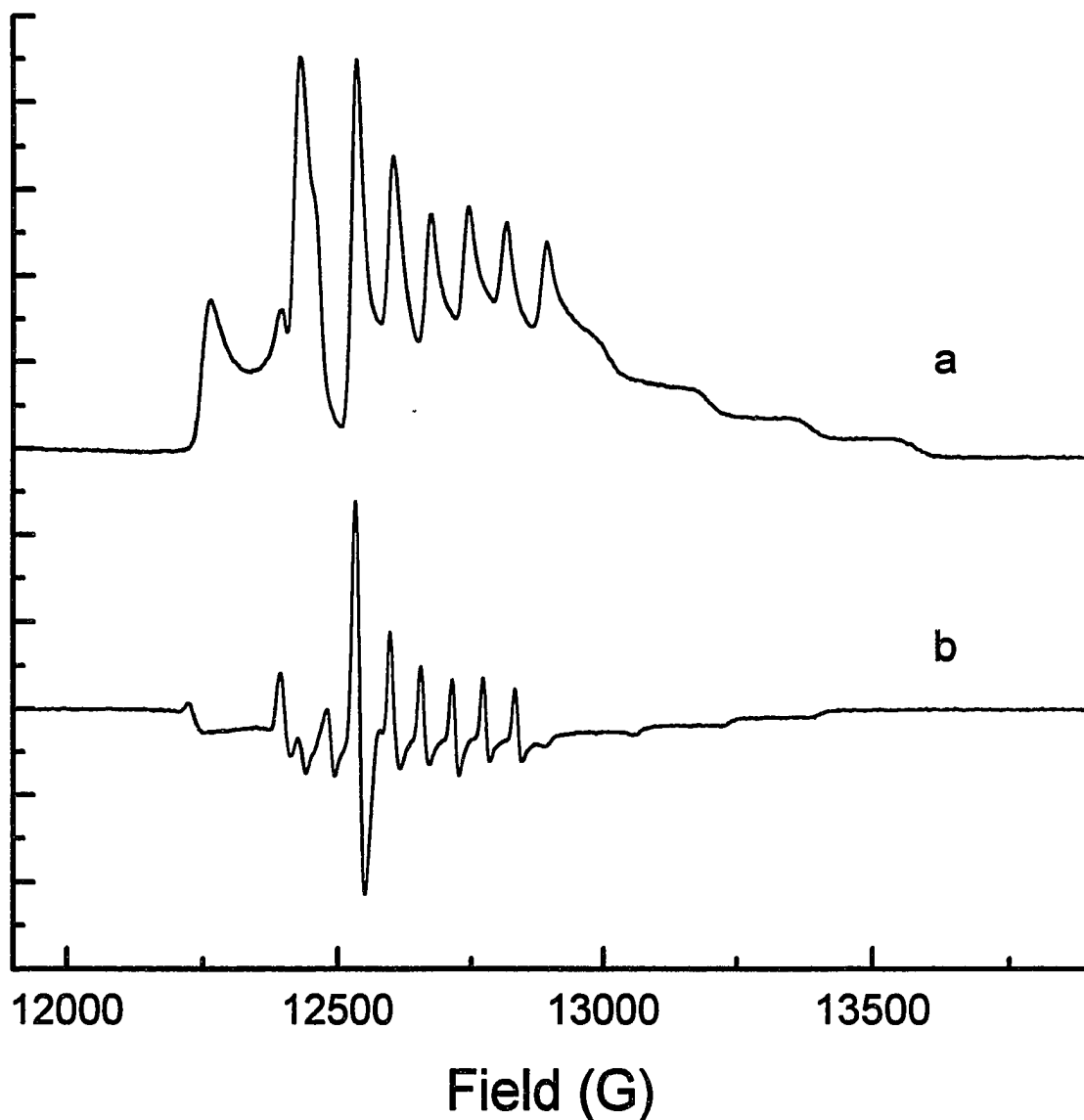


Figure 2.5: Q-band EPR spectrum of 1 mM  $\text{VOSO}_4$  in  $\text{H}_2\text{O}$ /glycerol (2:1 by volume) solution under rapid-passage condition (a) and 20 mM  $\text{VO}(\text{Im})_4^{2+}$  in  $\text{H}_2\text{O}$ /glycerol solution (b). Instrument conditions: Field Set, 12900 G; Scan Range, 2000 G; Scan Time, 8 minutes; Temperature, 4.7 K; Microwave Frequency, 34.885 GHz (a) and 34.910 GHz (b); Microwave power, 1.6 mW (a) and 0.6  $\mu\text{W}$  (b); Modulation Frequency, 10 kHz; Modulation Amplitude, 1 G; Receiver Gain, 500; Time Constant, 0.3 s. (File name: 032195c.plt)

helium temperatures (Fig. 2.4 inset). A signal at  $g = 2.07$  is consistently seen for all the cavities and is probably due to a Cu(II) impurity in the cavity wall. These background signals are inconsequential for most samples since their peak-to-peak amplitudes are typically only 0.9 - 1.6 % of that of a standard 1 mM CuCl<sub>2</sub> solution measured under the same conditions (Table 2.1).

### CONCLUSION

In conclusion, the ribbon-wound cavity is comparable to the commercial silver wire-wound cavity in terms of both cavity  $Q_L$  and weak pitch signal-to-noise ratio but has superior modulation field penetration. It is more robust against temperature cycling and easier to construct as well and can be readily modified for use in the ENDOR experiment (See Chapter 3). The basic design can be extended to frequencies other than the Q-band used in the present work. The silver-plated brass ribbon-wound cavity gave the best overall performance of all cavities tested. However, the aluminum ribbon-wound cavity also performs acceptably and is the easiest to construct since no electroplating is involved and the cavity body is made with epoxy alone rather than with the epoxy/quartz composite.

## CHAPTER 3

### Q-BAND ENDOR COIL, RF CIRCUIT CONSTRUCTION AND PERFORMANCE

#### Introduction

As has been mentioned previously, ENDOR experiments involve electron spin as well as nuclear spin transitions, which require the introduction of the radio frequency (RF) to the sample. To accomplish this, a coil needs to be incorporated into the cavity to generate the RF field. Design of ENDOR coils varies depending on cavity configuration as well as the type of ENDOR experiment (46-49). A good ENDOR coil should be able to deliver sufficient RF power while having minimal effect on the cavity Q. The construction of such a coil can be very challenging due to both theoretical considerations and practical concerns. For Q-band ENDOR applications, because of the limited cavity dimension and sample size, the problems associated with the placement and configuration of the RF coil as well as the tuning of the cavity become even more involved.

Technical details about the modification of the Q-band cylindrical EPR cavities into ENDOR cavities and the construction of the RF circuit as well as some remarks on the performance of the Q-band ENDOR spectrometer are discussed here. The ENDOR cavity along with the RF circuit has been tested with gamma- irradiated sucrose and vanadyl-



imidazole complex with satisfactory results.

### ENDOR Cavity Construction

Two modifications were made on the EPR cavity assembly, i.e. two holes was drilled at the end of waveguide and the cavity piston to accommodate the entry of the ENDOR coil, and the piston was reconstructed for ease of tuning. Figure 3.1 is a schematic drawing of the RF coil and piston assembly for the ENDOR cavity. This assembly inserts into ribbon-wound cavity wall of Figure 2.1(a). The hair pin RF coil (Fig. 3.1(a)) is formed by a single silver wire (0.5 mm diameter, 99.9985 % Ag) (Johnson Mathey, Ward Hill, Massachusetts), with two ends passing through the piston (Fig. 3.1(b), (c)) and the waveguide (not shown) where the cavity is attached. The wire is electrically insulated with Teflon from the main cavity body, the piston and the waveguide, thus forming a single RF loop. When tuning the cavity, the silver wire was first inserted into the cavity. The piston arrangement in Figure 3.1 (b) and (c) allows vertical, but not rotational movement of the piston, thus the cavity can be tuned without altering the parallel configuration of the silver wires. An appropriate number of brass washers is inserted between the cavity and the piston holder prior to tightening the piston in place. Since there is no need for the field modulation coil to be placed inside

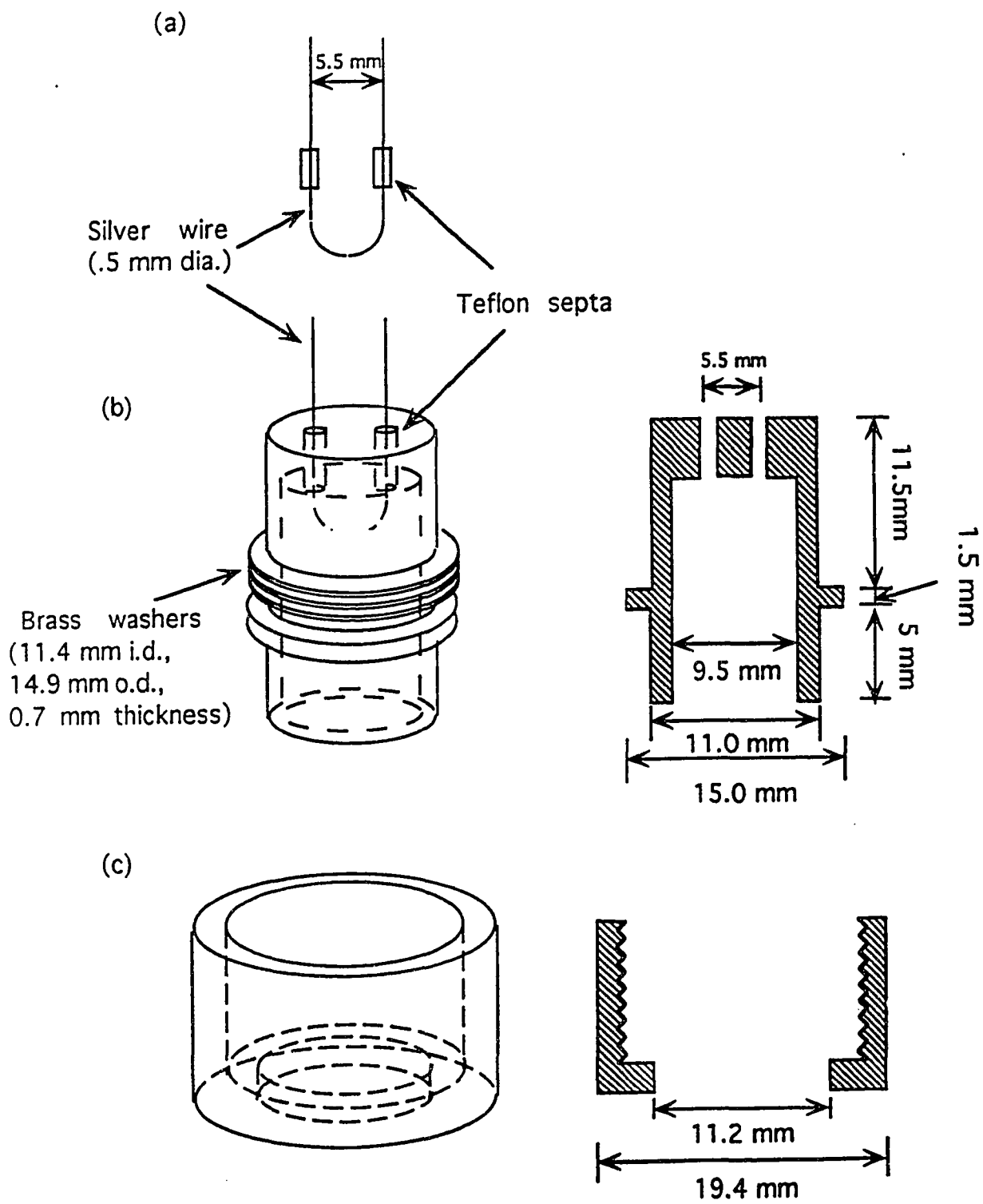


Figure 3.1: Schematic drawing of the ENDOR cavity piston assembly. (a) RF coil (b) Aluminum piston (c) Piston holder

the ribbon-wound cavity, as is the case for thick solid wall cavities, the ENDOR cavity configuration used here is simpler to construct.

During the ENDOR experiment, very high RF power is delivered into the ENDOR coil over a long period of time (usually hours). Part of the power is released in the form of heat which, in turn, can change the cavity dimensions and thus the resonance frequency. In addition, the cavity Q is lowered. For this reason, high purity silver wire, which has a very high electric conductivity, was used for the ENDOR coil to minimize RF heating. It is also free of EPR signals. An enamelled copper wire (0.5 mm dia.) was also used in place of silver in the sucrose radical ENDOR experiment, but no discernible difference in ENDOR performance was observed, except for background EPR signals observed near  $g = 2$ .

Figure 3.2 (left) shows the overall picture of the ENDOR cavity with RF coil inside. It is essential that the plane of the loop be perpendicular to the direction of the static magnetic field to avoid the induced current generated by the modulating magnetic field. The coil inside the cavity should be free of distortion to ensure this perpendicular orientation and also to minimize the reduction of the cavity Q. With this configuration, the magnetic field directions of microwave, RF and static magnet are perpendicular to one another, as is shown in Figure 3.2

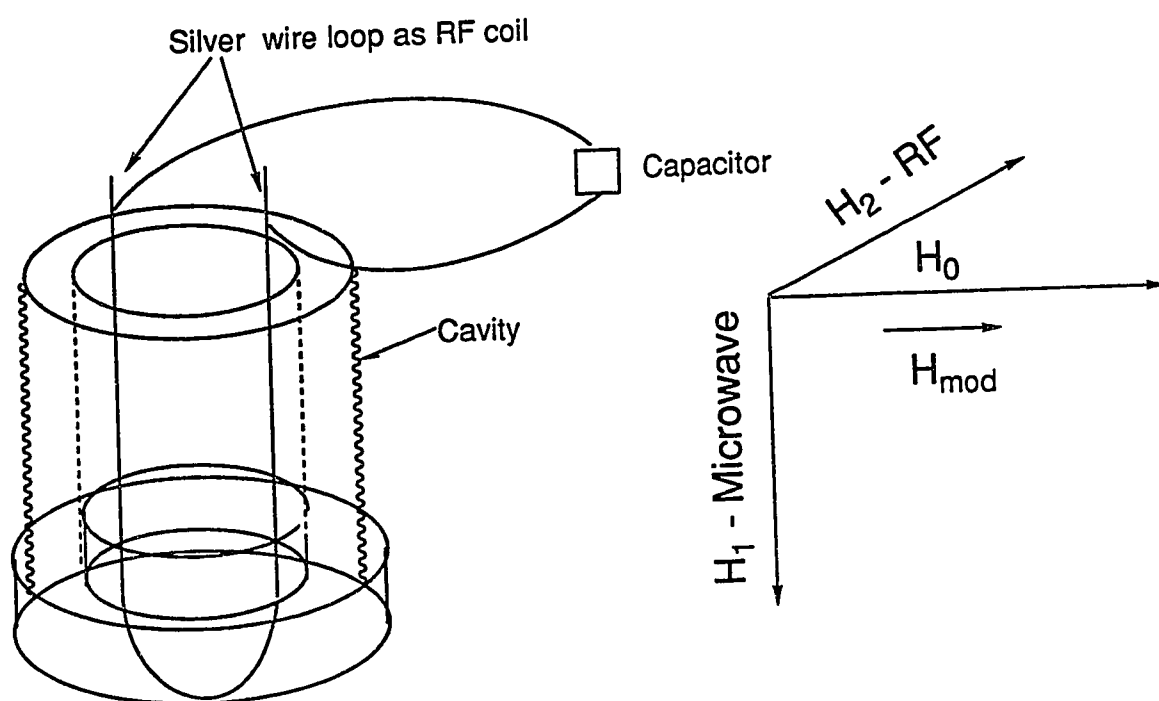


Figure 3.2: Sketch of cylindrical  $TE_{011}$  Q-band ENDOR cavity configuration. Left:  $TE_{011}$  ENDOR cavity with single silver wire loop as RF coil. Right: Magnetic field directions,  $H_1, H_2$  stands for magnetic field of microwave and RF, respectively;  $H_0$ , static magnetic field;  $H_{mod}$ , modulation field.

(right). It is necessary that the silver loop outside the cavity at the bottom be as short as possible to minimize RF leakage.

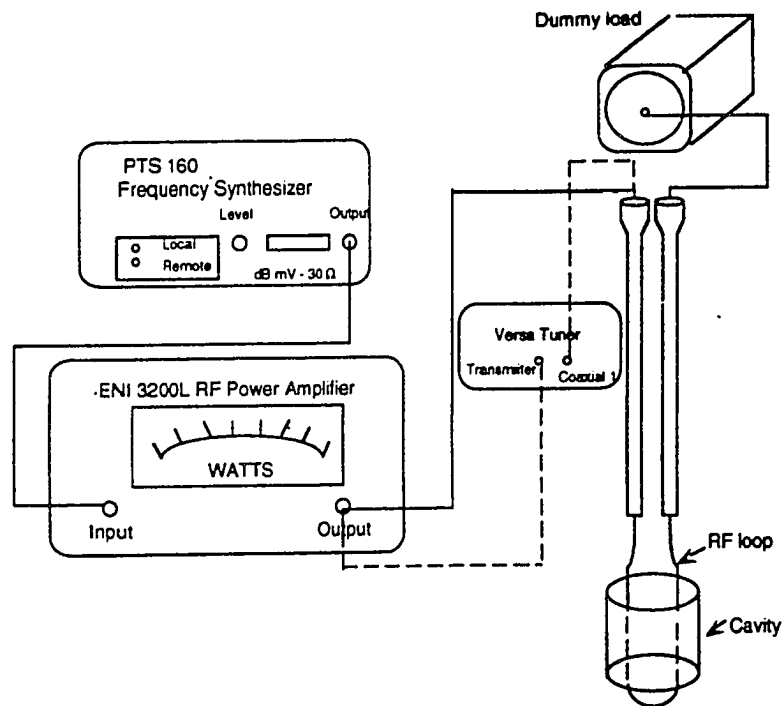
#### **Sample preparation**

A typical standard test sample for ENDOR spectroscopy is sucrose radical. It was obtained by irradiating on sucrose powder for approximately 72 hours with  $^{137}\text{Cs}$  gamma rays. The diluted sucrose sample is made by mixing the irradiated sucrose sample with reagent grade KCl (1:50 by weight).

#### **Instrument description**

Figure 3.3 is a block diagram of the apparatus in the RF circuit for field modulation (a) and frequency modulation (b) ENDOR measurements. The RF source was a PTS 160 frequency synthesizer (100 kHz - 159.999 MHz) (Programmed Test Sources, Inc., Littleton, Massachusetts) followed by an ENI Model 3200L Broadband Power Amplifier (Electronic Navigation Industries Inc., Rochester, New York) which has a flat frequency response from 250 kHz to 150 MHz and maximum power output of 300 W. In frequency modulation ENDOR (Fig. 3.3b), a surface acoustic wave (SAW) oscillator (Constructed by Electronic laboratory of the Department of Chemistry, University of Illinois, Urbana, Illinois) was added to the circuit as a source of frequency modulation. It is uniquely

a



b

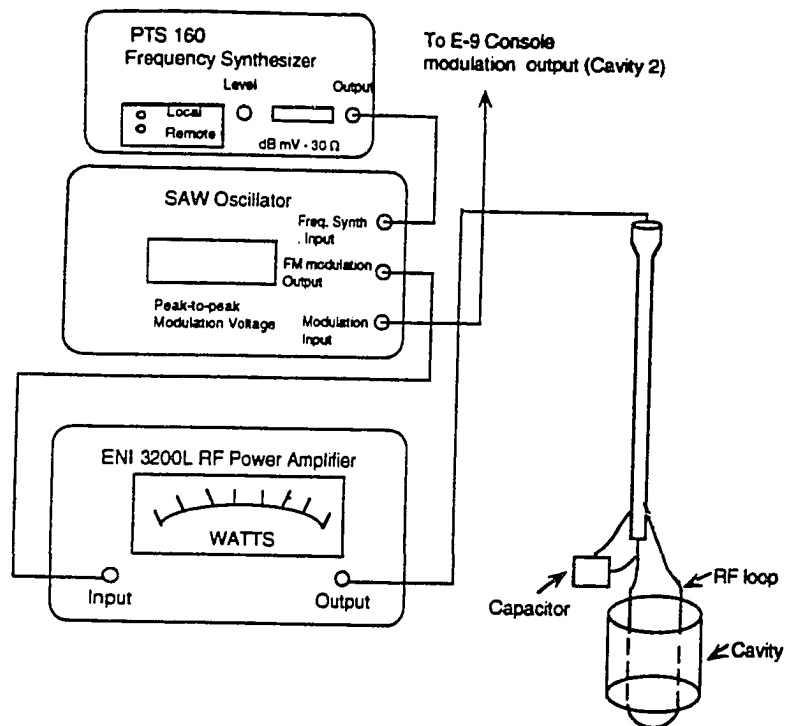


Figure 3.3: Diagram of ENDOR RF circuit setup. (a) Field modulation ENDOR RF circuit, (b) Frequency modulation ENDOR RF circuit. (51).

designed to produce sine wave FM RF without a switching transient, which usually occurs in digital frequency synthesizers when stepping frequency (50). An IBM S486SX/DX PC was used for both RF control and data acquisition using EW software (Philip D. Morse and Scientific Software Services, Bloomington, Illinois).

The connections between the RF source, ENDOR coil and the dummy load were made via two parallel 0.141" semirigid coaxial cables. Coaxial lines are used because of low radiation losses. Since the inner conductor is completely shielded by the outer one, little electric or magnetic field exist outside the shield. If properly terminated, the power loss in coaxial line is the sum of the ohmic losses of the conductors along the length of the cable and the dielectric losses of the spacer between the two conductors. And it has a characteristic impedance of about 50 ohm, which is a good match to that of the RF power supply. The top loop of the coil is soldered directly to the center conductor of the cables. To minimize RF power loss, this portion of RF circuit was wrapped with a sheet of aluminum foil, which was electrically connected to the outer shield of the cable. Since almost all ENDOR work needs to be done at temperatures lower than 30 K, it is desirable to use cables of low thermal conductive material in order to reduce the helium consumption rate. However, poor thermal conductive materials are also poor electric conductors use of which can

increase the RF power losses. A compromise solution is to use a combination of low and high conductive cables. The stainless steel coax cable with silver coated/copperclad/stainless steel wire as the inner conductor (70-01-0046-03, SSI Cable Corporation, Shelton, WA) is placed at the cavity end close to the helium flow valve. A 0.141" semirigid copper coaxial cable (Haverhill Cable & Manufacturing Corp., Haverhill, MA) is used for the rest of the cable line and the two cables are connected through an OSM JACK TO JACK adapter (M/A-COM Omni Spectra, Inc. Ronkonkoma, NY). The cables are fastened tightly against the waveguide by cotton strings to ensure mechanical stability. Due to the complexity in the cable configuration, sufficient caution needs to be taken in the connection and alignment of the cables. Failing to do so will result in severe base line artifacts and even loss of ENDOR signals. This has been confirmed experimentally. For best shielding effects, the outer conductors of the coax cables are cross connected at various places along the entire length of the cable by braided copper wires.

### **Results and discussion**

The Q of the ENDOR cavity is ~ 2300, only slightly lower than that without the RF coil (2600). This high Q certainly improves the overall sensitivity of the ENDOR spectrometer. Frequencies from 0 - 160 MHz, with power up



to 300 W has been applied to the coil, provided cooling is done with nitrogen or helium gas. In the liquid helium temperature experiment, no appreciable increase in the helium consumption rate has been observed suggesting that the RF heating effect is minimal. After equilibrium has been reached, no problems associated with thermal instability are encountered.

One of the major problems with the ENDOR experiment is the variation in RF power delivery caused by the impedance mismatch between the power supply and RF load. The ENDOR cavity assembly can be thought of as a RLC circuit (Figure 3.4). The total impedance of the structure varies as a function of the RF frequency and thus the efficiency of the RF power transfer.

Since little can be done with the hair-pin coil itself, the alternative way to match the impedance of the coil with that of the power supply is by connecting a capacitor in parallel with the ENDOR coil (Fig. 3.3b). Since it is almost impossible to match the impedance through the entire range of the frequency used, the best one can do is to match the impedance at the frequency range of interest. A 0.1  $\mu\text{F}$  capacitor was used for this purpose; it provided a good impedance match in the region of 53 MHz (proton Larmor frequency). The second approach is to attach a variable impedance device in series with the coil (Fig. 3.3a). Such a device is a MFJ-941 Versa Tuner (MFJ Enterprises, Inc.

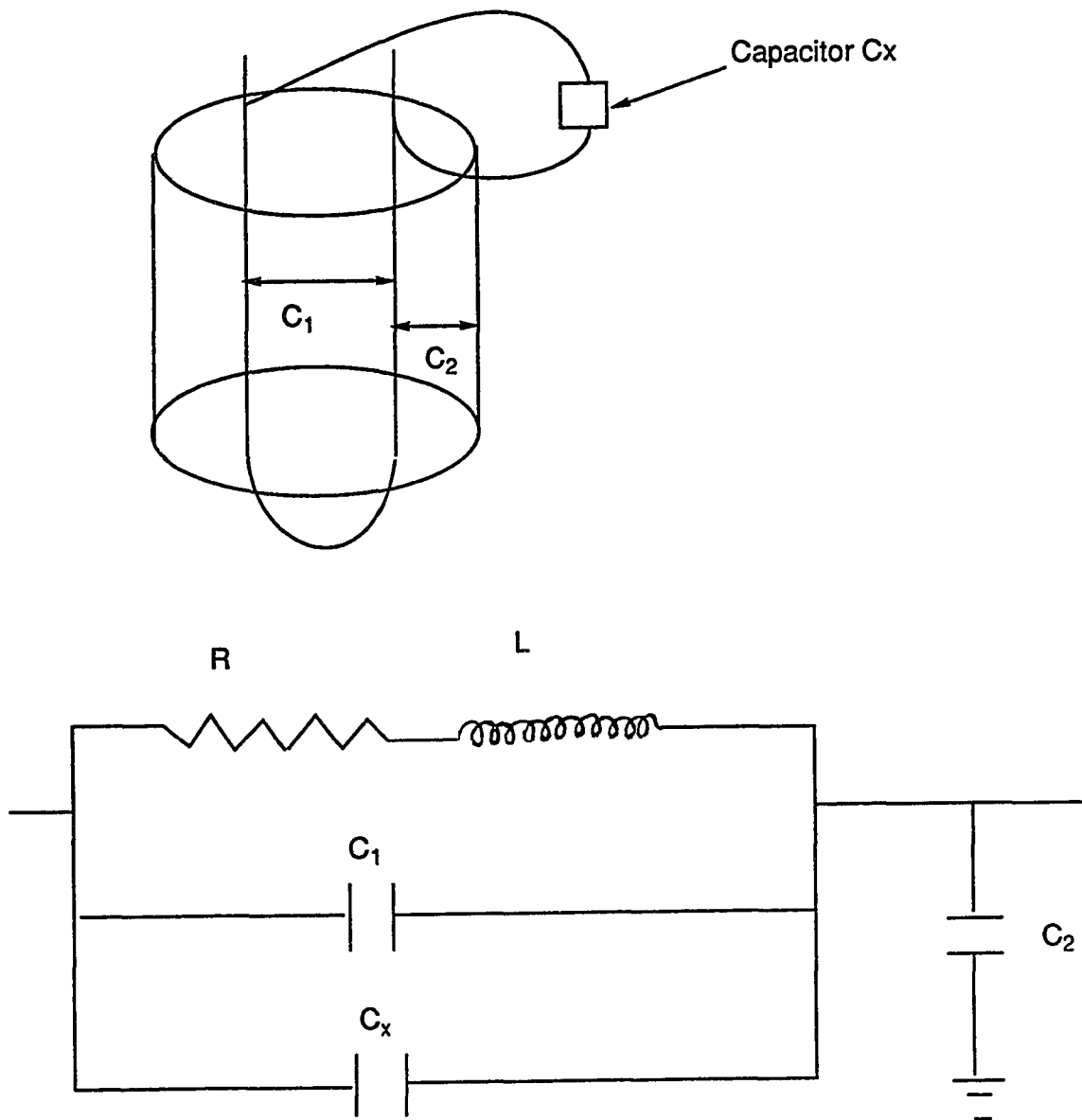


Figure 3.4: Equivalent circuit of RF coil in  $TE_{011}$  resonant cavity.  $C_1$ , coil capacitance;  $C_2$ , coil-cavity capacitance;  $R, L$ , resistance and inductance of the RF coil, respectively. (Filename: circuit.the)

Mississippi State, Mississippi), which is designed to match the impedance of any transmitters to virtually any loads connected by coax lines. It employs a cross-needle meter which allows forward and reflected power to be read simultaneously. The optimum settings will be those which give the maximum forward power and minimum reflected power. The chief advantage of using the Versa Tuner over the capacitor is that the former provides more experimental flexibility; one can choose and change the range of frequency where the impedance needs to be matched during the experiment without having to disassemble the circuit. A third approach is to terminate the circuit with a dummy load of 50 ohm impedance (Fig. 3.3a). The behavior of the RF power output is shown in Figure 3.5, for the circuit with capacitor, with Versa Tuner and with the 50 ohm dummy load. There are tremendous power fluctuations over the entire frequency range due to impedance mismatch. This situation is greatly improved when the RF circuit is terminated with the 50 ohm dummy load (Fig.3.5). Unlike the capacitor and Versa Tuner, the dummy load seems to provide a very good impedance match over the entire RF frequency range. The dummy load was employed in field modulation dispersion mode ENDOR experiments, while the capacitor matching configuration seemed to work best for frequency modulation ENDOR based on experimental observations of the baseline artifacts. The Versa Tuner could be used in combination

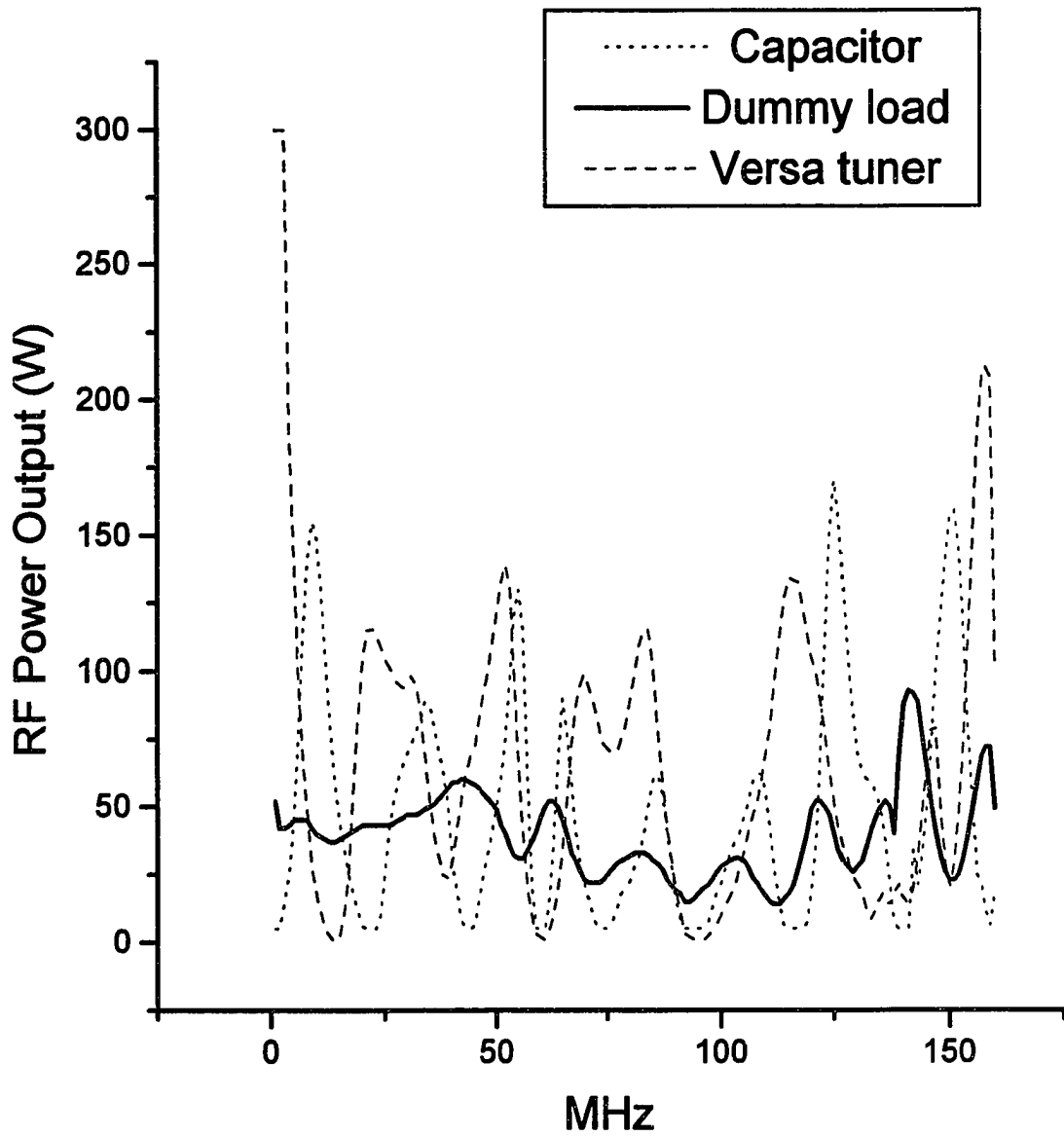


Figure 3.5 Frequency dependence of RF power output. Cavity: silver plated brass ribbon-wound cavity with silver hairpin RF coil. (File name: rfpow.sem)

with the dummy load if high RF power at a particular frequency range is desired. This has not been put into practice so far. Figures 3.6 and 3.7 show the Q-band EPR spectra of Gamma irradiated sucrose radical in absorption and dispersion mode, respectively. The fine structure in the absorption mode spectrum result from the interaction between the protons and the unpaired electron of the sample. Such interactions are not as apparent in the dispersion spectrum of Figure 3.7. Figure 3.8 is the field modulation Q-band dispersion mode ENDOR spectrum of this sample at 100 K. A matrix proton ENDOR signal is readily obtained around proton Larmor frequency (53 MHz) with a satisfactory S/N (~150). Background signals in other RF frequency ranges were tested as shown in Figures 3.9 and Figure 3.10. There is always a very large increase in the baseline level below 6 MHz. We attribute this to the abnormal behavior of the instrument at low frequency extreme. Similar phenomena, to a different degree, have been observed in X-band frequency modulation ENDOR measurements. No significant background signals in other parts of the RF frequency region up to about 100 MHz are observed.

As a further test, frequency modulation ENDOR in absorption mode has also been measured on the sucrose radical sample. Such a spectrum is shown in Figure 3.11 a. In this case, it is difficult to discriminate the ENDOR signal against the background (Fig. 3.11 b). After

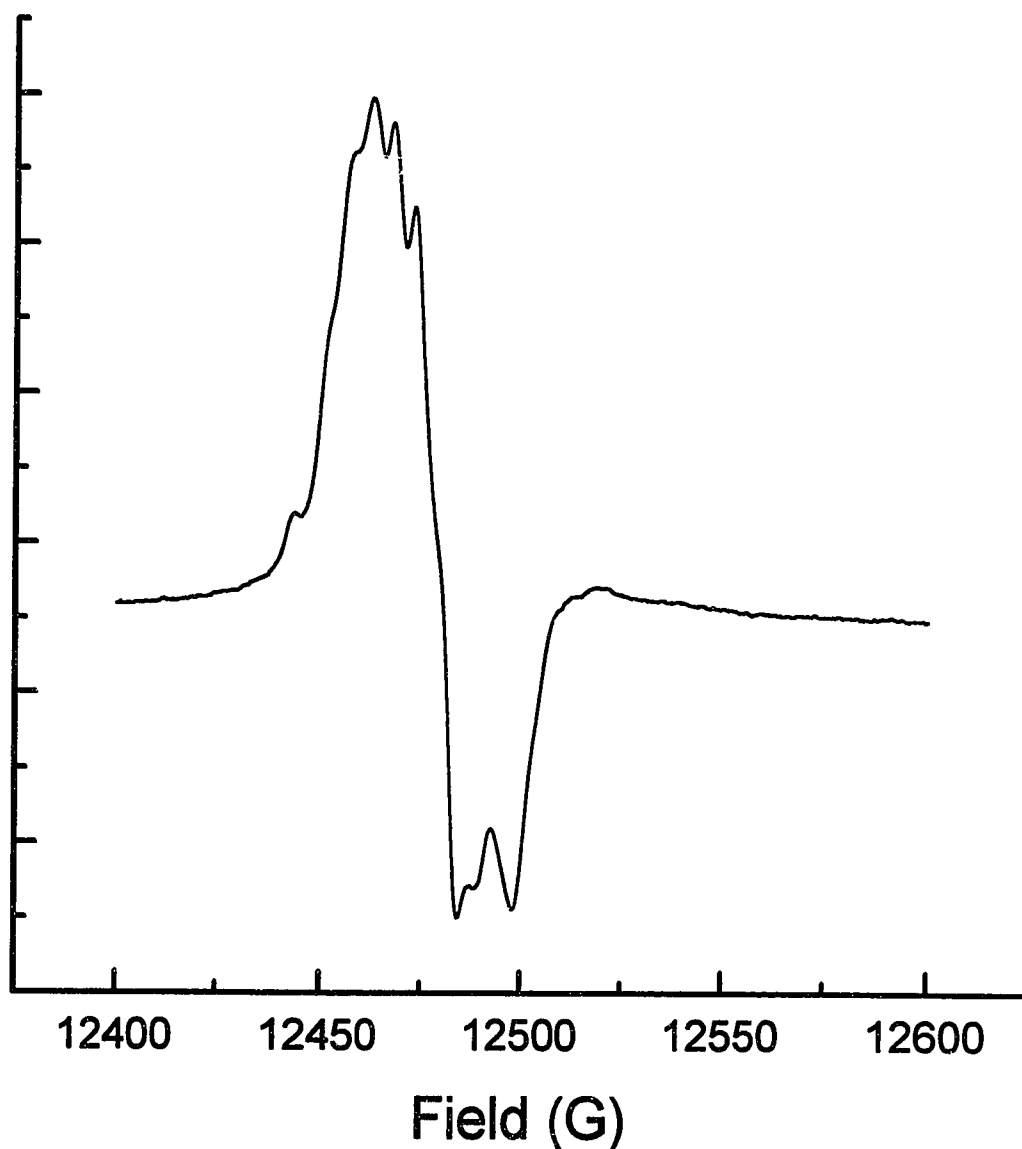


Figure 3.6 Q-band EPR absorption spectrum of irradiated sucrose sample. Instrument conditions: Field Set, 12500 G; Scan Range, 200 G; Scan Time, 4 minutes; Temperature, 298 K; Microwave Frequency, 34.905 GHz; Microwave Power, 0.063 mW; Modulation Frequency, 100 kHz; Modulation Amplitude, 5 G; Receiver Gain, 160; Time Constant, 1 s. (File name: 031894p5.plt)

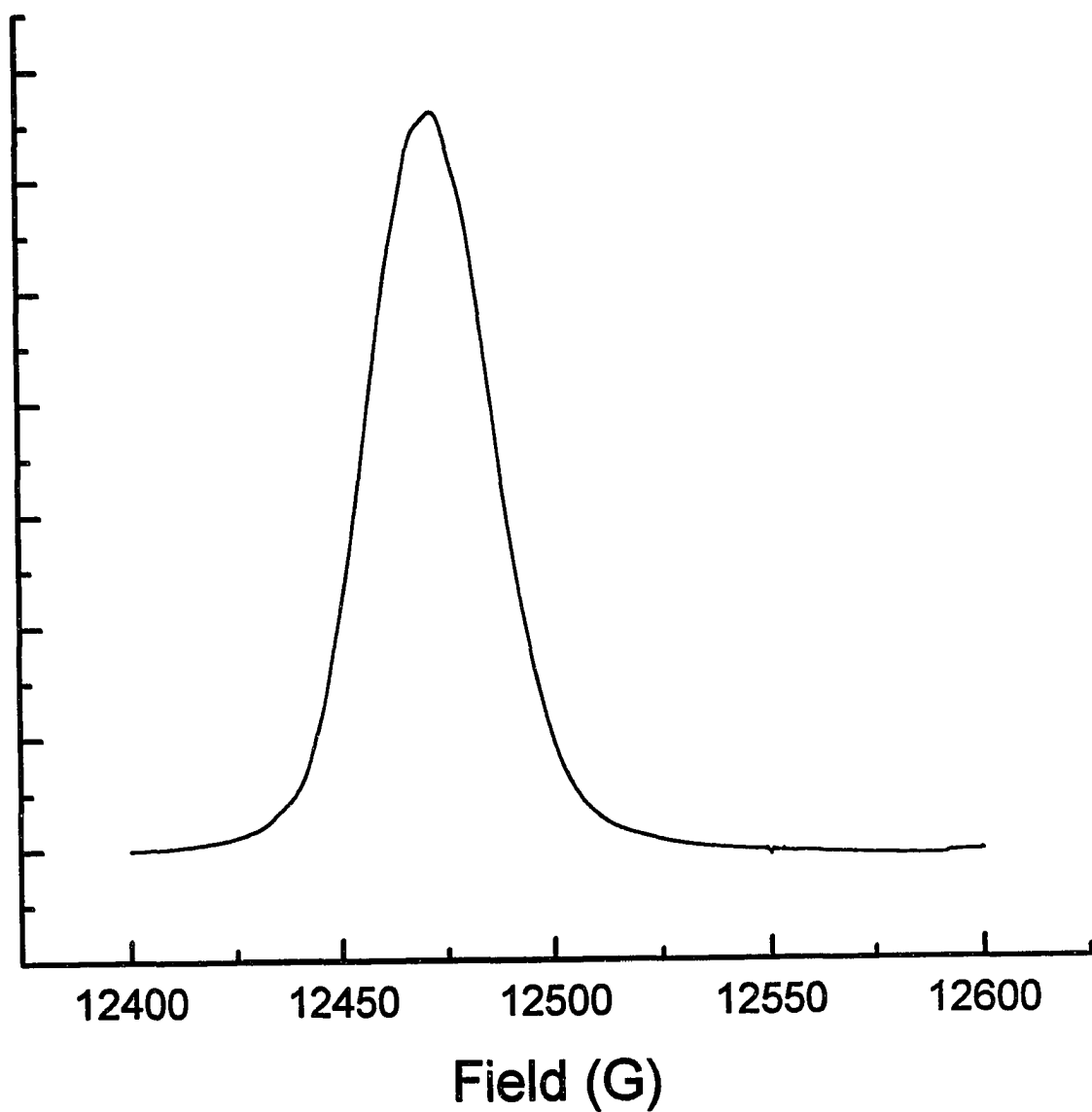


Figure 3.7: Q-band EPR dispersion spectrum of irradiated sucrose sample. Instrument conditions: Field Set, 12500 G; Scan Range, 200 G; Scan Time, 4 minutes; Temperature, 298 K; Microwave Frequency, 34.905 GHz; Microwave Power, 0.063 mW; Modulation Frequency, 100 kHz; Modulation Amplitude, 2 G; Receiver Gain, 2.5; Time Constant, 0.003 s. (File name: 040194a1.plt)

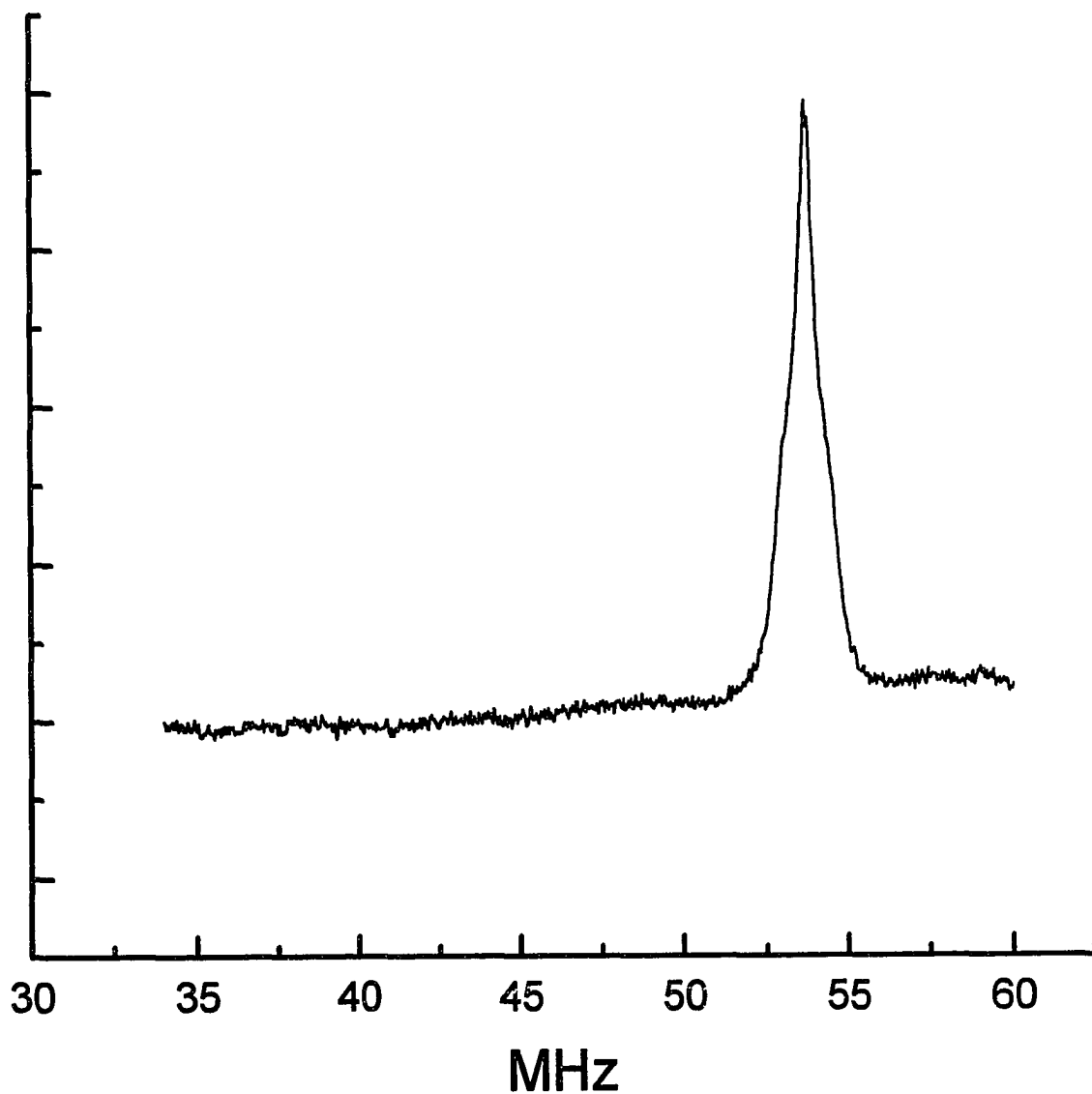


Figure 3.8: Field modulation Q-band  $^1\text{H}$  ENDOR of irradiated sucrose radical. Experimental conditions: Microwave Frequency, 34.905 GHz; Microwave power, 1.975 mW; Modulation Frequency, 100 kHz; Modulation Amplitude, 1 G; Receiver Gain, 12.5; Temperature, 100 K; Time Constant, 0.03 s; radio frequency power, 50 W; radio frequency scan rate, 0.5 MHz/s; number of scan(s) 1. (File name: 051795a1.plt)



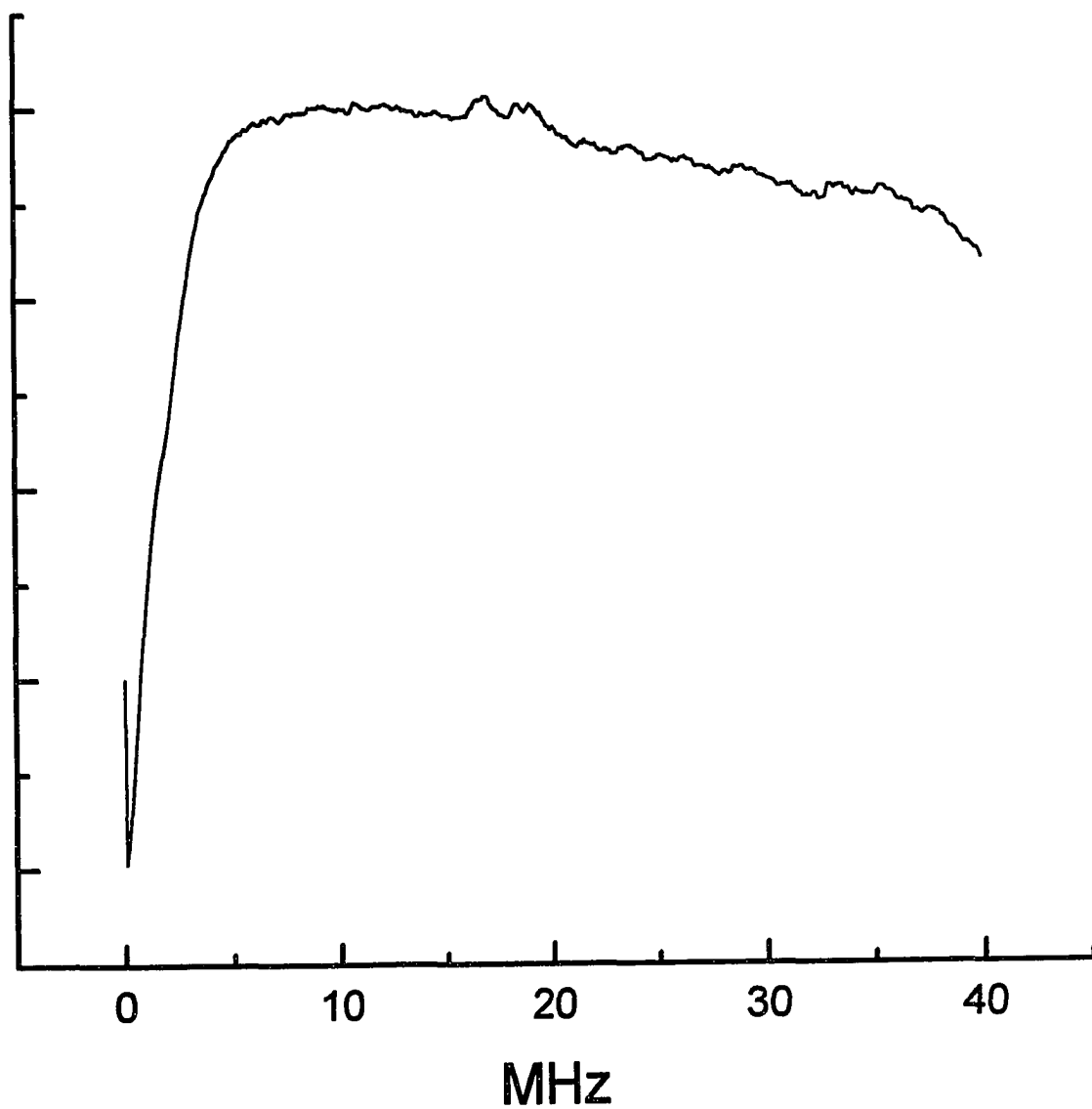


Figure 3.9: Field modulation ENDOR background signal from 0-40 MHz. Experimental conditions: microwave power = 0.5 mW, MA = .1 G, RG = 5, other conditions are the same as that in Figure 3.8. (File name: 051795b.plt)

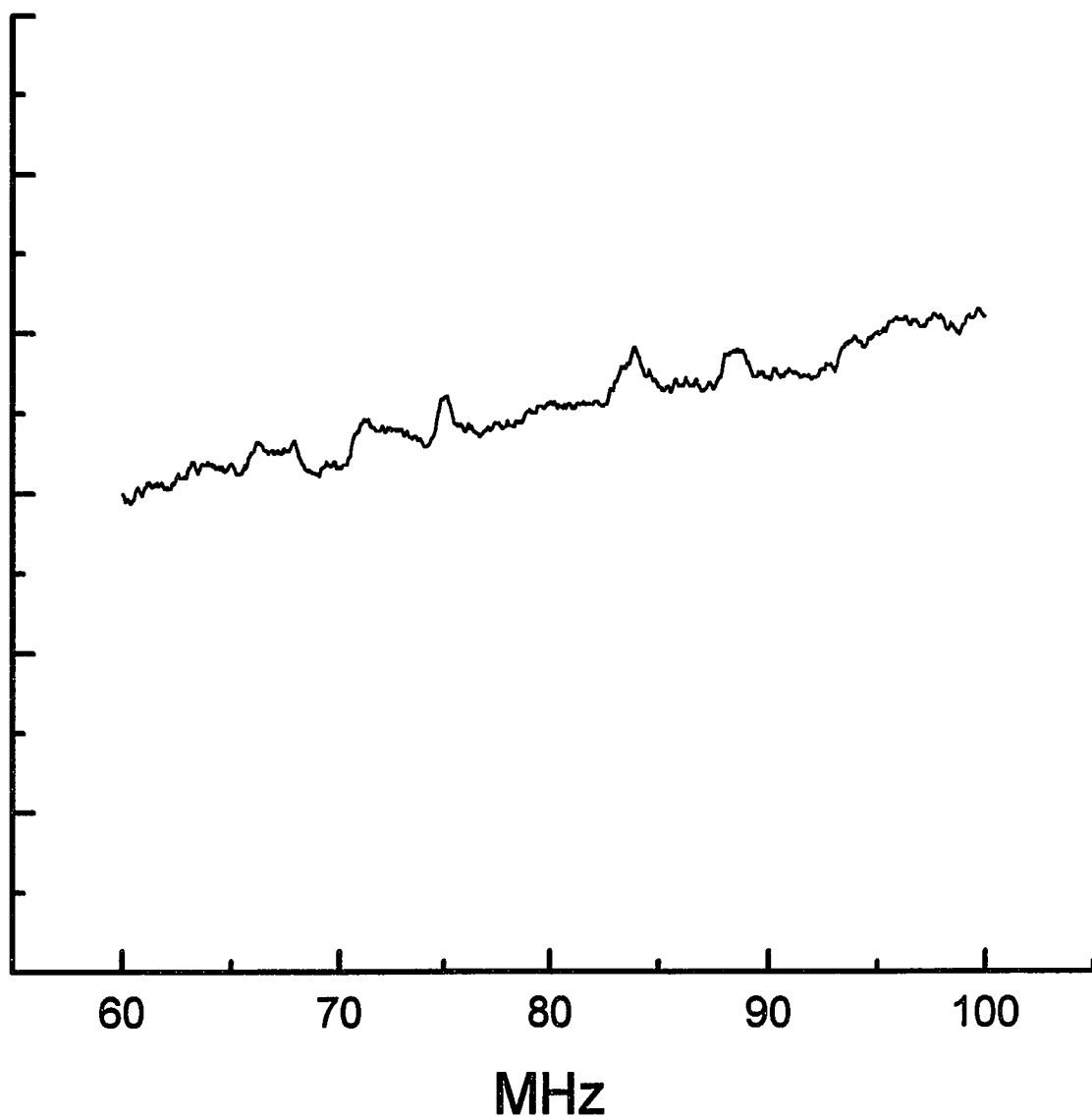


Figure 3.10: Field modulation ENDOR background signal from 60-100 MHz. Experimental conditions: same as in Figure 3.8. (File name: 051795c.plt)

background subtraction, however, an acceptable spectrum (Fig. 3.11 c) was obtained with a S/N ~ 145.

No direct correlation was observed between the RF power output variation and the background signals, which implies that the impedance mismatch is not the cause of the baseline artifacts. The background signals are believed to be due to the variation in coil-cavity capacitance when sweeping the RF frequency. In discussing background signals, it is of importance to distinguish between detection mechanisms for absorption and dispersion modes (52,53). As has been described in Chapter 1, both the real part (dispersive) and the imaginary part (absorptive) of the sample's magnetic susceptibility change during resonance. The former manifests itself in a change in the Cavity Q which can in turn be detected by the crystal detector. The latter produces a change in the resonance frequency of the cavity, which can be detected by a AFC detector. The background signals in ENDOR experiments are to a large extent, if not all, caused by the effects of the applied RF field on the cavity Q and resonant frequency. Our results show that the baseline artifacts are much more severe in frequency modulation ENDOR than in field modulation ENDOR. This is not surprising since one would think the coil-cavity capacitance variation will have a larger effect on the cavity Q than on the resonance frequency. Yet, this argument lacks rigorous justification at this stage.

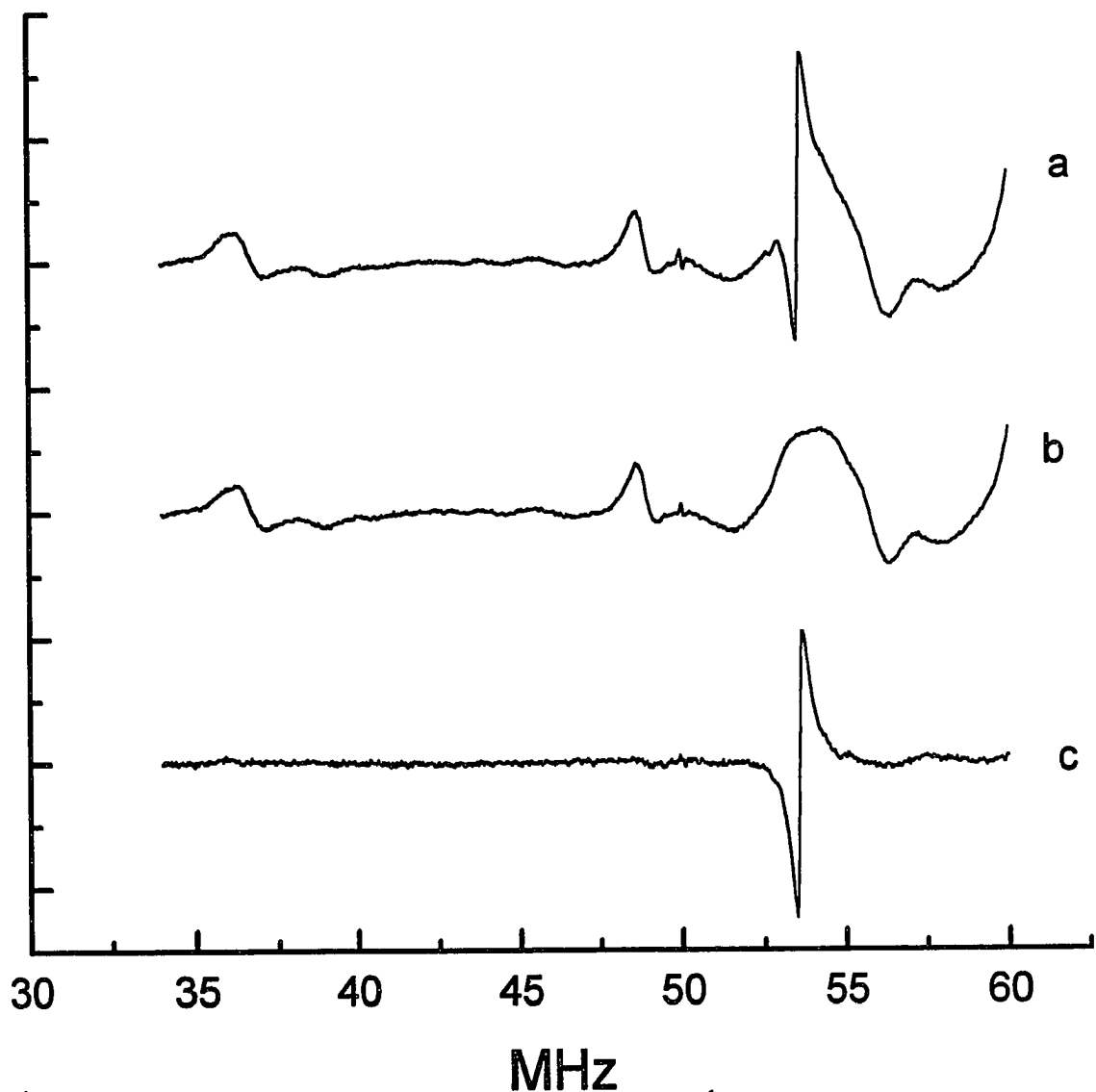


Figure 3.11: Frequency modulation Q-band  $^1\text{H}$  ENDOR of irradiated sucrose radical (a), background spectrum (b), and spectrum after background subtraction (c). Experimental conditions: Field Set = 12572 G (a), 13572 G (b); Microwave Frequency, 34.988 GHz; Microwave power, 0.25 mW; Modulation Frequency, 100 kHz; Modulation Amplitude, 1 G; Receiver Gain, 160; Temperature, 100 K; Time Constant, 0.03 s; radio frequency power, 50 W; radio frequency scan rate, 0.5 MHz/s; number of scan(s) 1. (File name: 041194c4.flr) (041194c4.sem)

To test the sensitivity of the ENDOR spectrometer, the sucrose radical is diluted in KCl by a factor of 50. Figure 3.12 shows the Q-band field modulation ENDOR spectrum of such a sample after signal averaging of 10 scans. The proton ENDOR signal is still quite distinguishable, indicating a high sensitivity of the spectrometer.

Figure 3.13 (a) and 3.13 (b) show the Q-band proton ENDOR spectra of 20 mM  $\text{VO}(\text{Im})_4^{2+}$  obtained with the magnetic field set on the  $m_l = -3/2 \perp$  and  $m_l = -7/2 \parallel$  peak marked by xy and z, respectively, in Figure 2.4. Figure 3.13 (c) illustrates the background ENDOR spectrum obtained with the magnetic field off resonance. The hyperfine couplings of the protons on the imidazole rings obtained from the spectra are (a): 3.06 MHz (3.37 MHz), 2.42 MHz (2.51 MHz), 0.48 MHz (< 0.8 MHz), and (b): 2.52 MHz (2.73 MHz), 1.08 MHz (1.04 MHz), 0.4 MHz (0.75 MHz). In the parallel spectrum ( $H \parallel z$ ) a hyperfine splitting of 6 MHz (6 MHz) due to protons of an axially solvent coordinated water molecule is also observed. A splitting of 5.5 MHz is seen in the perpendicular spectrum ( $H \perp z$ ) which was not detected in the X-band ENDOR experiment (43). Only the  $\nu_-$  branch ( $\nu_+ = \nu_H + A/2$ ;  $\nu_- = \nu_H - A/2$ ) is seen for the  $\text{H}_2\text{O}$  proton ENDOR lines presumably due to the spin cross-relaxation mechanism (16). The hyperfine couplings are well resolved and generally in good agreement with those observed by Mulks et al. (43) in an X-band ENDOR experiment on the same complex (data shown

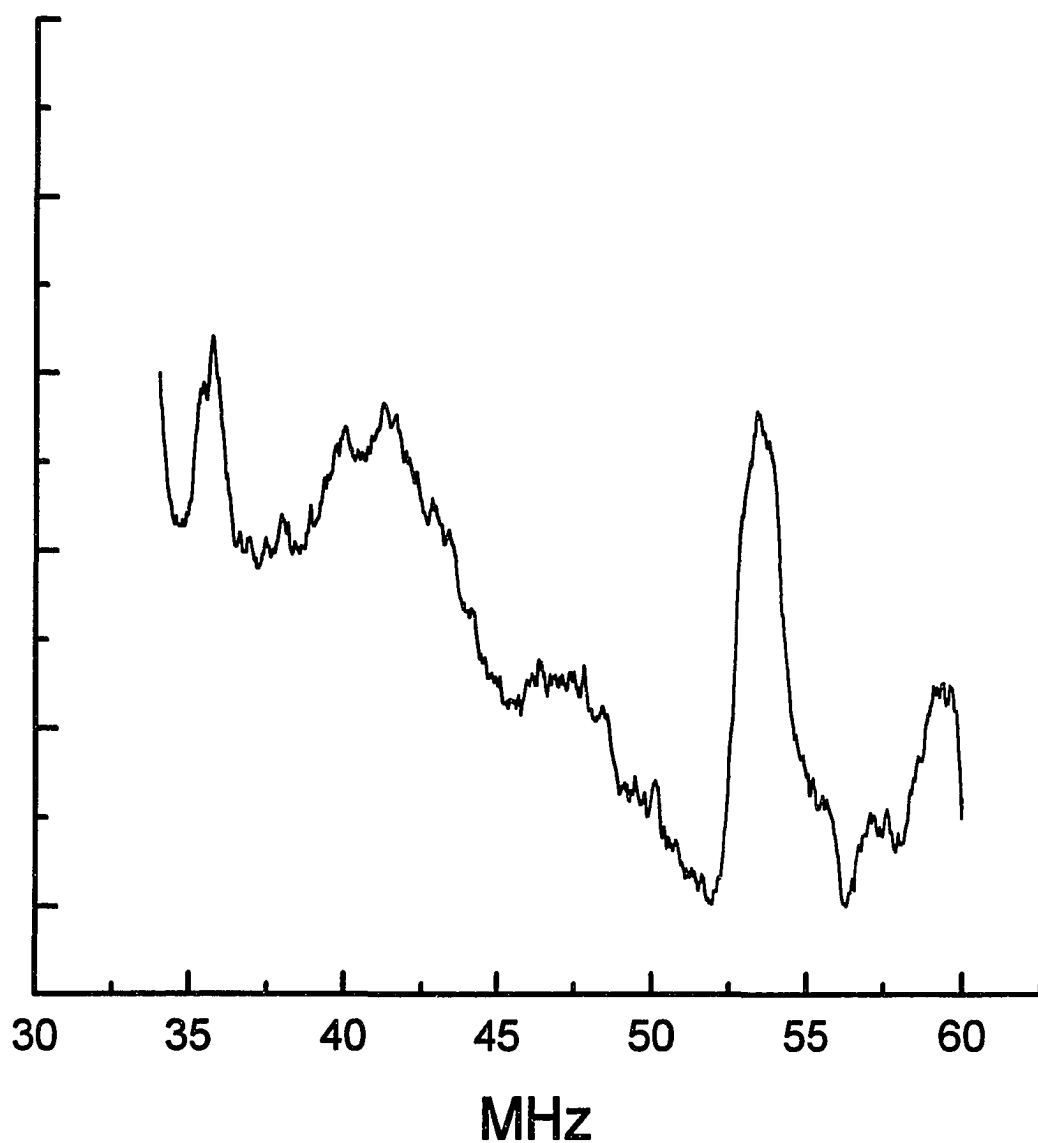


Figure 3.12 : Field modulation Q-band <sup>1</sup>H ENDOR of irradiated sucrose radical 50:1 diluted in KCl. Experiment conditions: Field Set = 12510 G, microwave power = 1 mW; Modulation Amplitude = 2 G, Receiver Gain = 200; Time Constant = 0.3 s, Number of scans = 10. (File name : 041994g3.plt)

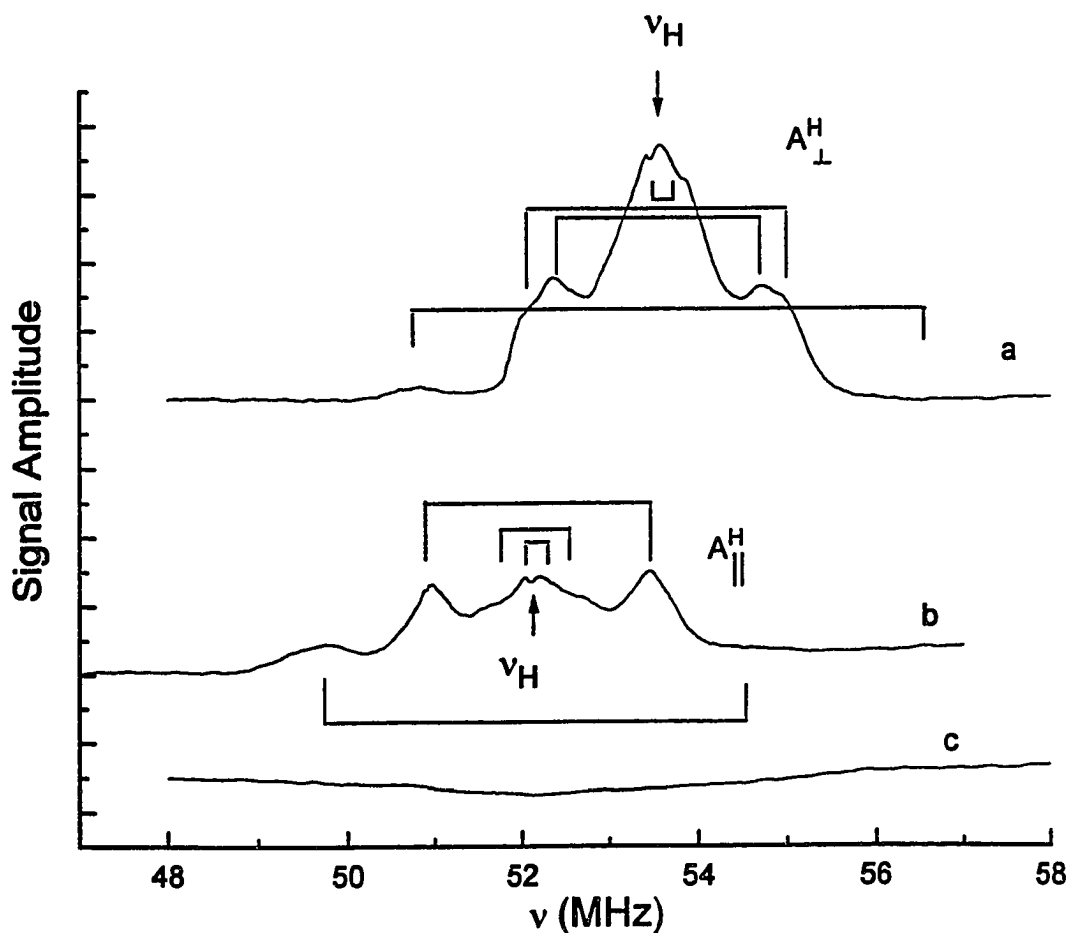


Figure 3.13: Field modulation Q-band  $^1\text{H}$  ENDOR of 20 mM  $\text{VO}(\text{Im})_4^{2+}$  in  $\text{H}_2\text{O}/\text{glycerol}$  solution at  $\text{pH} = 7$  with the magnetic field set on the peak marked xy (a), z (b) of Figure 2.3 and off resonance (b). Experimental conditions: Field Set, (a) 12548 G, (b) 12224 G, (c) 13548 G; Temperature, 5.8 K; Microwave Frequency, 34.910 GHz; Microwave power, 1 mW; Modulation Frequency, 100 kHz; Modulation Amplitude, 0.1 G; Receiver Gain, 125; Time Constant, 0.3 s; radio frequency power, 50 W; radio frequency scan rate, 0.5 MHz/s; number of scans, 8. (File name: 032195a.plt)

in the parentheses), indicating that the ENDOR cavity assembly performs acceptably well.

The RF power dependence of the  $^1\text{H}$  ENDOR signal amplitude of  $\text{VO}(\text{Im})_4^{2+}$  is shown in Figure 3.14, indicating that saturation occurs at about 100 W. Figures 3.15 and 3.16 are the plots of proton ENDOR signal amplitudes vs microwave power and temperature, respectively. All the above ENDOR measurements are made on a  $[\text{VO}(\text{Im})_4]^{2+}$  complex sample (20 mM) in field modulation with the microwave bridge in dispersion mode. Figure 3.15 shows that the proton ENDOR signal reaches a maximum at a microwave power of 0.5 mW and decreases rapidly at higher powers. The proton ENDOR signal decreases monotonically as temperature increases from 6 K to 46 K as indicated in Figure 3.16. Based on these results, the optimum conditions for proton ENDOR measurement would be the following (allowing some variations between different samples): microwave power, 0.5 mW - 2 mW; RF power, about 100 W; temperature, 6 K - 10 K.

We also explored the use of the brass ribbon as the RF coil in an ENDOR experiment as has been done previously with a wire-wound  $\text{TE}_{014}$  cavity. The ribbon of the wall is taped at 4 turns from the bottom, and is soldered directly to the inner conductor of the semirigid coax cable via an enameled copper wire. The top of the ribbon is connected to the outer conductor of the cable in the same fashion, with 12 turns of ribbon between connections.



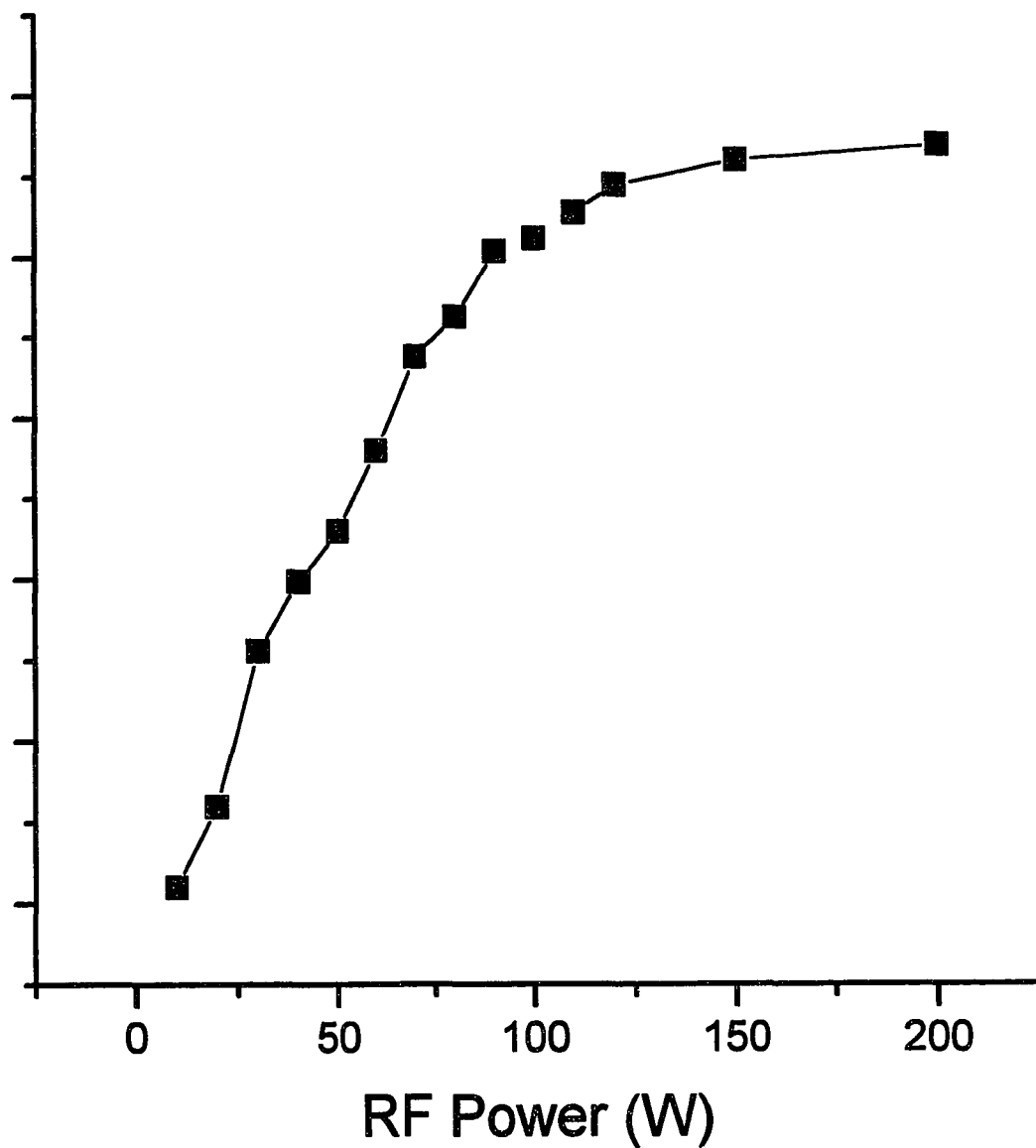


Figure 3.14: 20 mM  $\text{VO}(\text{Im})_4^{2+}$  (pH = 7)  $^1\text{H}$  ENDOR signal amplitude vs. RF power. Conditions: Temperature = 9 K, Time constant = 0.03 s, Modulation Amplitude = 0.5 G, Receiver Gain = 200, Scan Rate = 0.5 MHz/s. (File name : 072295a.plt).

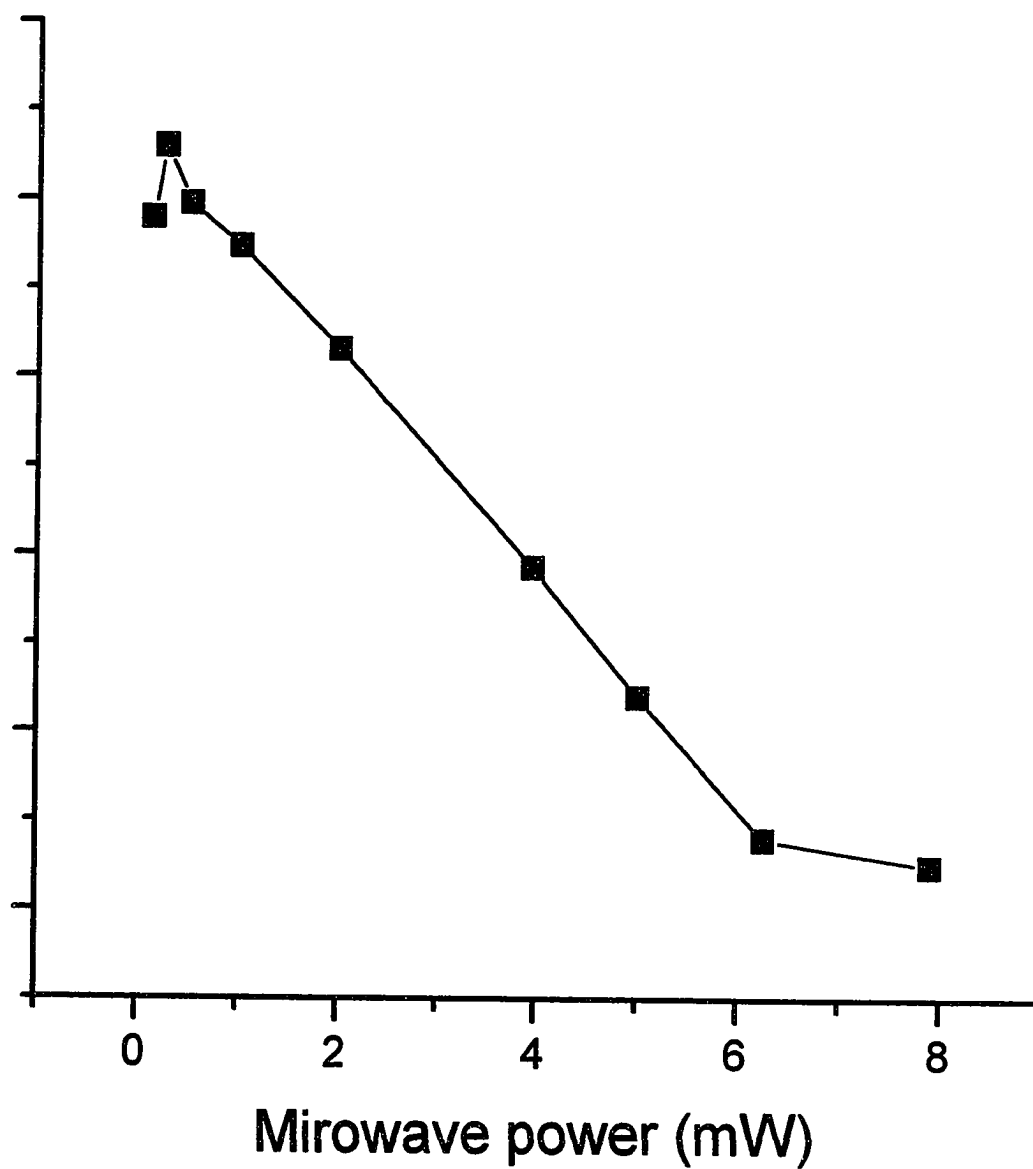


Figure 3.15: 20 mM  $\text{VO}(\text{Im})_4^{2+}$   $^1\text{H}$  ENDOR signal amplitude vs. Microwave power. RF power = 90 W. Other conditions are the same as in Figure 3.14. (File name : 072295b.plt)

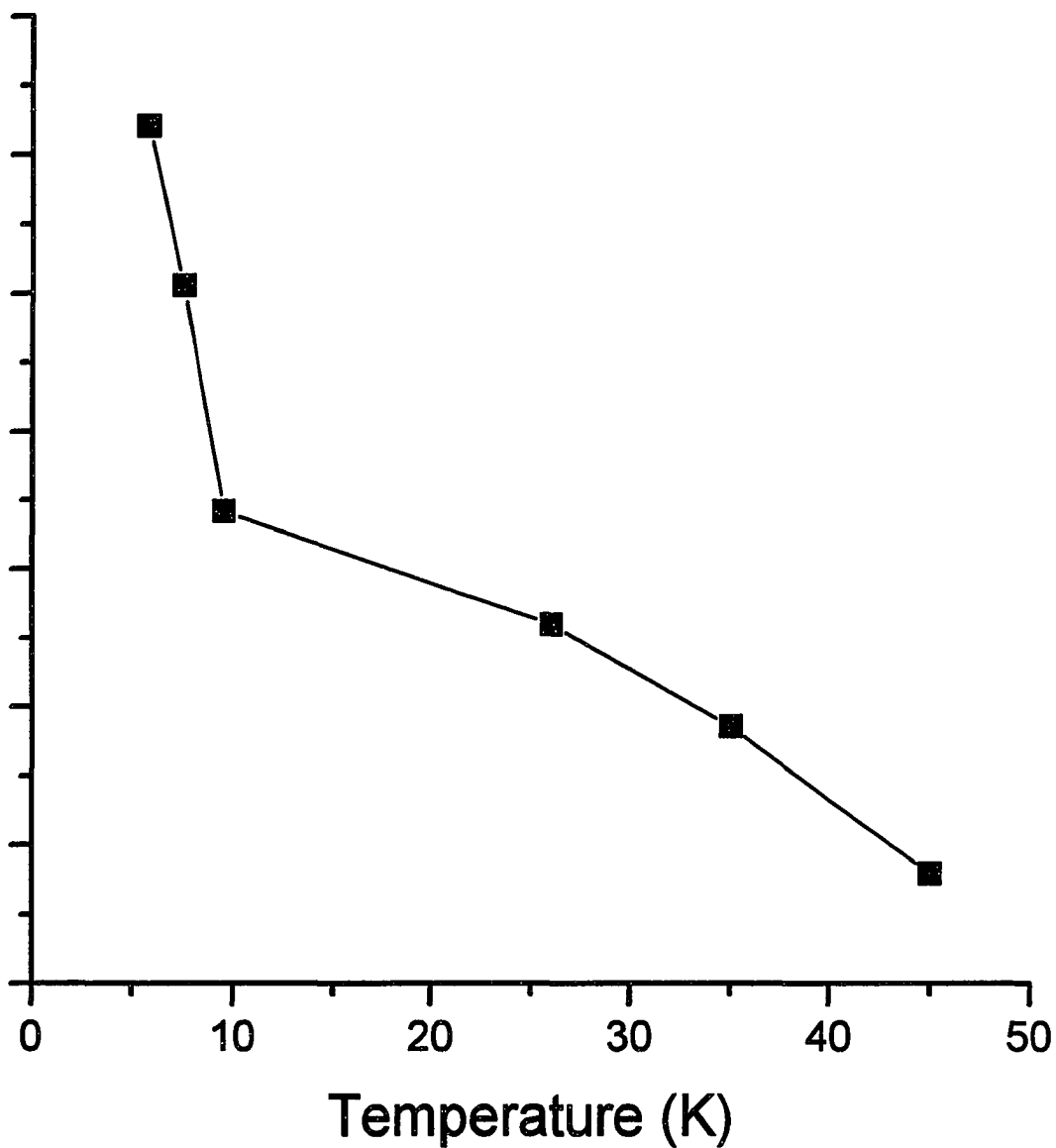


Figure 3.16: 20 mM  $\text{VO}(\text{Im})_4^{2+}$   $^1\text{H}$  ENDOR signal amplitude vs. Temperature. RF power = 90 W, microwave power = 1 mW. Other conditions are the same as in Figure 3.14. (File name : 072295c.plt).

The ENDOR signal of a gamma irradiated sucrose radical sample at 100 K (not shown) obtained with the ribbon RF coil was only 1/10 of that obtained with the parallel posts configuration of Figure 3.1. The limited number of ribbon turns and the large distance between the cavity wall and the sample is not very conducive to ENDOR, probably because of insufficient  $H_2$  field at the sample. While not very useful in the present experiments, the ribbon may be a useful ENDOR coil with higher frequency ribbon-wound cavities having smaller inner diameters or with other  $TE_{01n}$  ( $n > 1$ ) Q-band cavities which have longer cavity walls (54).

## CHAPTER IV

### EPR and ENDOR STUDIES OF DINITROSYL IRON MODEL COMPOUNDS

#### Introduction

In the past few years, increasing attention has been drawn to a simple yet biologically significant molecule: nitric oxide (NO) (56-66). It has been shown that NO is essential to many physiological functions such as digestion, blood pressure regulation, neurotransmission and antimicrobial defense (67-71). In most instances, however, functions attributed to NO are actually carried out in the form of its derivatives, in particular, the complexes formed with transition metal ions (72-76). Among those, dinitrosyl iron complexes are probably the most important and well-studied systems (77-81). They are believed to be possible NO carriers in many biological processes (82). Thus the chemical form of NO as well as the structure of the complexes formed is very important in understanding its transport process and functionality.

Rhombic and axial EPR signals have been observed with small molecule and protein iron nitrosyl complexes and have been attributed to the coordination of iron at histidine and cysteine residues, respectively (78). In recent work with the iron nitrosyl complexes of ferritin it has been demonstrated that the rhombic and axial signals from this

protein are due to iron binding at His-128 and Cys-130 in the vicinity of the 3-fold channels of the protein (83). It has been suggested that ferritin may store NO and Fe in the form of nitrosyl iron complexes (83). However the detailed structures of the iron nitrosyl complexes formed in ferritin are unknown. Nor are they known in any other nonheme protein. The total coordination number, the identity of *all* the protein ligands as well as the number of coordinating NO groups need to be established. Previous studies have shown that dinitrosyl iron complexes have a tetrahedral geometry with four ligands, including two NO and two other Lewis base ligands (L) (60). The central Fe atom has a +1 formal charge and is in its high spin,  $d^7$ , electronic configuration, giving an electron spin  $S = 3/2$ . Each NO molecule has one unpaired electron in its antibonding  $2p\pi^*$  orbital, giving  $S = 1/2$ . This unpaired electron will antiferromagnetically couple with another electron from the Fe during bond formation, resulting in a total electron spin  $S_{total} = 3/2 - 1/2 - 1/2 = 1/2$ . The complex thus formed has a  $g$  value of about 2.02 ~ 2.04 at room temperature (60). In solution, dinitrosyl iron complexes are believed to be in equilibrium between a monomer and dimer form, which is best illustrated by the following equilibrium (60):



The dimer formed is diamagnetic due to the antiferromagnetic

electron exchange interaction between the two spin centers in the complex and thus only the monomer accounts for the observed EPR signal.

Because of the radical nature of NO complexes, EPR and ENDOR spectroscopy can be used to detect the formation and elucidate the structure of dinitrosyl iron complexes. However, the analysis of experimental results requires a database of relevant model complexes. Dinitrosyl iron complexes with a large number of small organic and inorganic ligands have been studied extensively using the EPR technique (77,78,81-83). Recently, Mullins and coworkers have performed ESEEM (Electron Spin Echo Envelope Modulation) measurements on dinitrosyl iron complexes with proteins and low molecular weight molecules (79). However no ENDOR work has been published. Furthermore, no rigorous analysis regarding the structure of the complexes has been provided. The objective of this work is to further examine the structure of dinitrosyl iron complexes through a combination of EPR and ENDOR studies on some model compounds.

The ligands employed in these studies include cysteine (Cys), mercaptoethanol (Mer), penicillamine (Pen), ethanethiol (Eth), thioglycolic acid (TGA) and imidazole (Im) (Fig. 4.1). This chapter is devoted to EPR and ENDOR studies on dinitrosyl iron model complexes with these

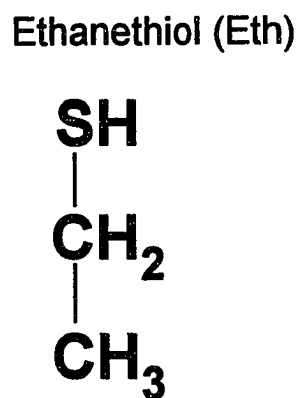
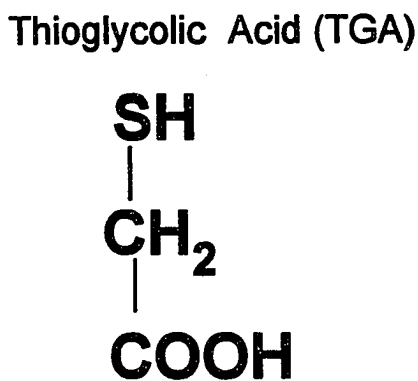
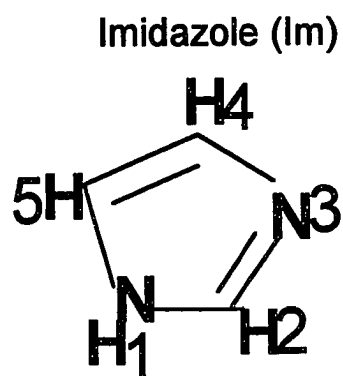
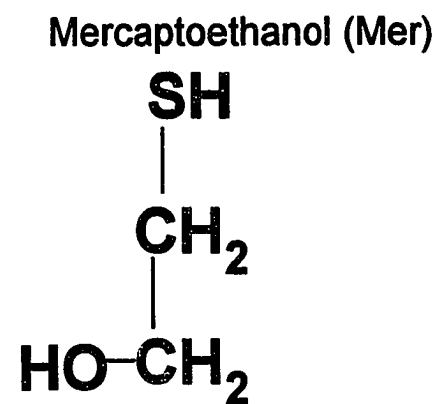
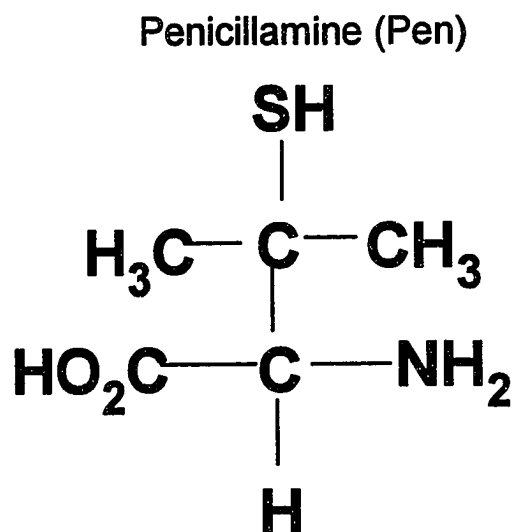
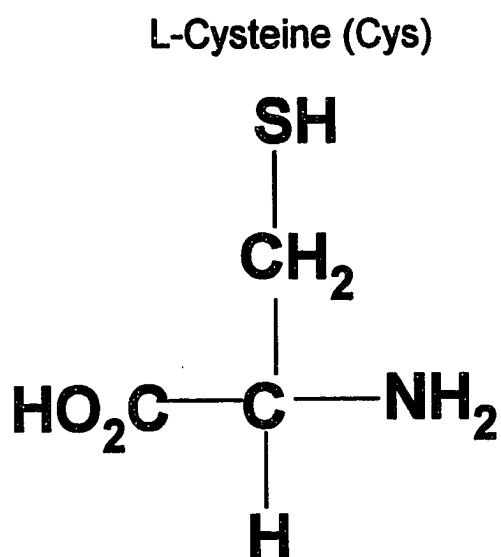


Figure 4.1 Schematic diagram of the structures for the ligands in dinitrosyl iron complexes. (ligand.the)



ligands. Experimental results will be presented along with discussion and some tentative conclusions.

### Experimental Methods

Dinitrosyl iron complexes were prepared according to the prescription given in reference 78. In short, 20-30 mg of the ligand, i.e., L-cysteine and L-penicillamine (Fluka Chemical Corp., Ronkonkoma, New York), imidazole (Aldrich Chemical Company, Inc., Milwaukee, WI), thioglycolic Acid (TGA) (Aldrich), ethanethiol (Aldrich) and mercaptoethanol (Eastman Organic Chemicals, Rochester, New York), was dissolved in 1 mL neutralized ascorbic acid (Aldrich) (30 mg/ml). About 6 - 8 mg of  $\text{FeSO}_4 \cdot 7\text{H}_2\text{O}$  (Aldrich) was added to the above solution to make a final concentration of 20 - 30 mM Fe. The pH was adjusted to 6 or slightly higher with HCl or NaOH. Finally 20 mg of  $\text{NaNO}_2$  (General Chemical Division, Morristown, N.J.) was added and the mixture was allowed to react for about 5 minutes at room temperature.  $^{15}\text{N}$  isotope substituted samples were prepared using  $\text{NaNO}_2$  enriched with  $^{15}\text{N}$  (99%) (Cambridge Isotope Laboratories, Inc., Andover, Massachusetts).  $\text{D}_2\text{O}$  exchange samples were prepared in the same manner except that  $\text{D}_2\text{O}$  (99% purity, Cambridge Isotope Laboratories) was used as the solvent and the pD was adjusted to the equivalent pH according to  $\text{pD} = \text{pH} + 0.4$

using DCl or NaOD (Cambridge Isotope Laboratories).

The resulting mixture was allowed to react for about 5 minutes, then transferred to a standard EPR tube (3mm i.d., 4 mm o.d.) for X-band or a capillary tube (1.3 mm i.d., 2.15 mm o.d.) for Q-band measurement and stored in liquid nitrogen. For room temperature EPR measurements, freshly prepared samples were transferred into a 1.15 mm i.d., 3.15 mm o.d. capillary tube, which was in turn placed into a 3.25 mm i.d., 3.60 mm o.d. EPR tube, and measured immediately. Small sample size is required for room temperature measurement because of dielectric losses in liquid samples. The extra layer of quartz tube helps to focus the microwave energy at the sample.

X-band EPR measurements at both room temperature and liquid nitrogen temperature were carried out on either a home constructed (FRED) or a Varian E-4 EPR spectrometer. ENDOR spectra were recorded with a home constructed ENDOR spectrometer equipped with a prototype variable temperature liquid helium cryostat (CRYO Industries of America, Inc., Atkinson, New Hampshire). Temperature was monitored and controlled by a 330 autotuning temperature controller (Lake Shore Cryotronics, Inc., Westerville, Ohio). The ENDOR accessory for both X-band and Q-band measurements is the same as described in Chapter 3.

Spectra simulation was done by using EPRPOW FORTRAN

program package, which was originally developed by Drs. L. K. White and R. L. Belford (School of Chemical Sciences of the University of Illinois) and modified by L. K. White , N. F. Albanese, and N. D. Chasteen (University of New Hampshire).

The theoretical geometry of the model complexes was obtained by building the molecule in the SPARTAN molecular builder on an SGI work station followed by a structure minimization using the Molecular Mechanics minimizer incorporated into the SPARTAN Electronic Structure Program. The minimization is based on the Tripos 5.2 force field, which includes additional bonding arrangements.

## **Results and Discussion**

### ***EPR Studies of Dinitrosyl Iron Complexes***

The power saturation curves of one of the dinitrosyl iron complexes, dinitrosyl iron penicillamine ( $\text{Fe-}^{14}\text{NO-Pen}$ ), were measured for different concentrations at liquid nitrogen temperature as shown in Figure 4.2 a. Figure 4.2 b represents the saturation curves after correction for the concentration differences. Results show that the EPR signals are approximately proportional to the sample concentrations and there is no obvious trend in saturation

behavior with sample concentrations. So relaxation effects through the spin-spin interaction normally encountered for high concentration samples is not a problem up to 20 mM concentration for dinitrosyl iron complex samples at liquid nitrogen temperature. However, the samples of 5 mM concentration do saturate more readily than 20 mM samples at 2 K, based on the observation that the former reach its maximum EPR signal amplitude at 0.5 mW, while the latter at 1 mW at this temperature. The proton ENDOR results obtained from samples of both concentration show no noticeable differences, however.

#### Dinitrosyl Iron cysteine complex (Fe-NO-Cys)

The proposed structure of Fe-NO-Cys is shown in Figure 4.3, where two cysteine molecules are bound to the Fe via the thiol groups. This hypothesis is based on the X-ray structure of dinitrosyl iron ethyl ester (Roussin's red ethyl ester), which is illustrated in Figure 4.4 (77). The dinitrosyl iron cysteine complex in solution is then considered to closely resemble the dissociated form of the ethyl ester complex. The room temperature spectrum of Fe-<sup>14</sup>NO-Cys is illustrated in Figure 4.5 a, which shows 13 well resolved hyperfine lines with a g value of  $2.030 \pm 0.001$ , as has been observed by McDonald and coworkers (77). The inset is the corresponding frozen solution spectrum (78) which

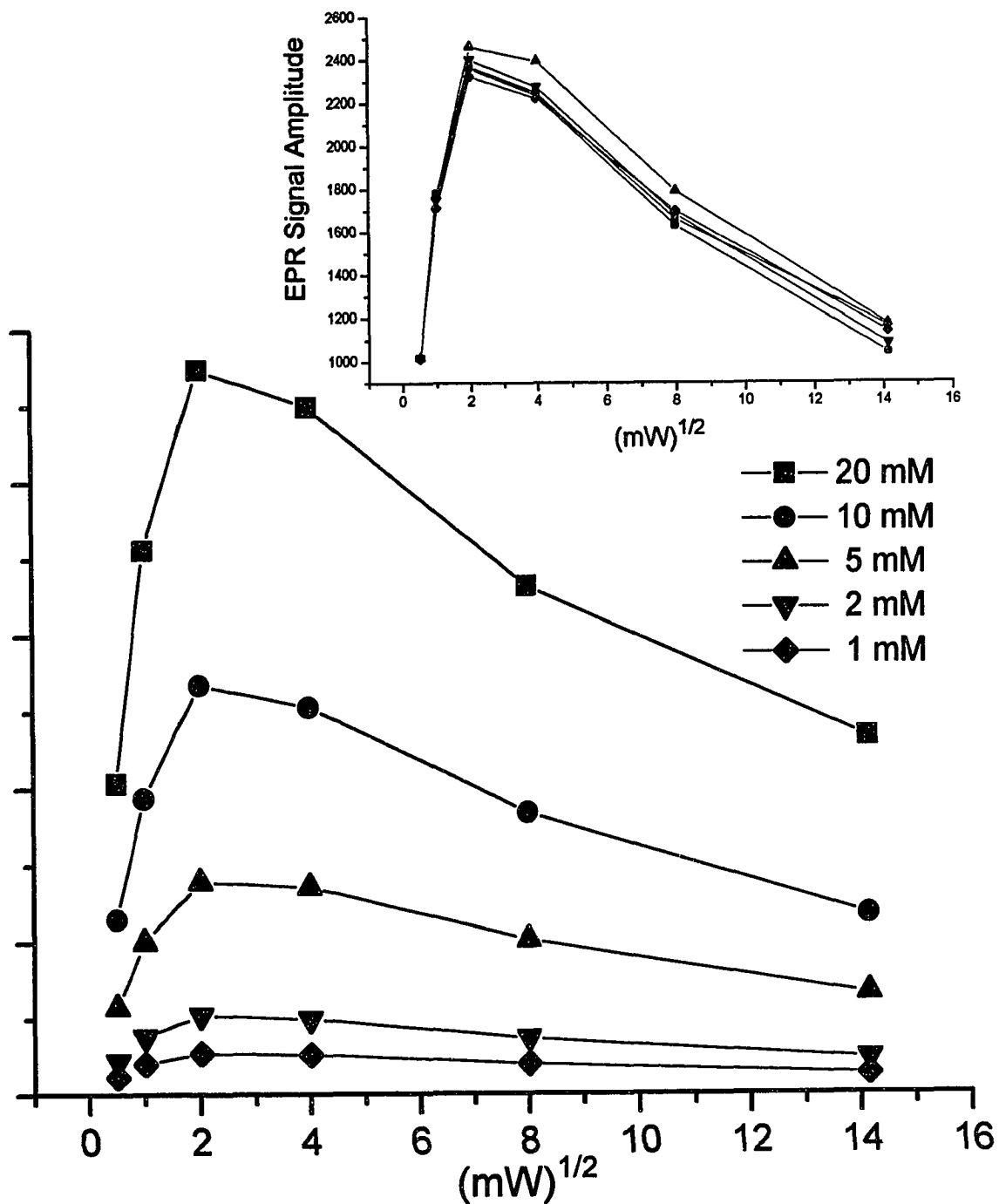
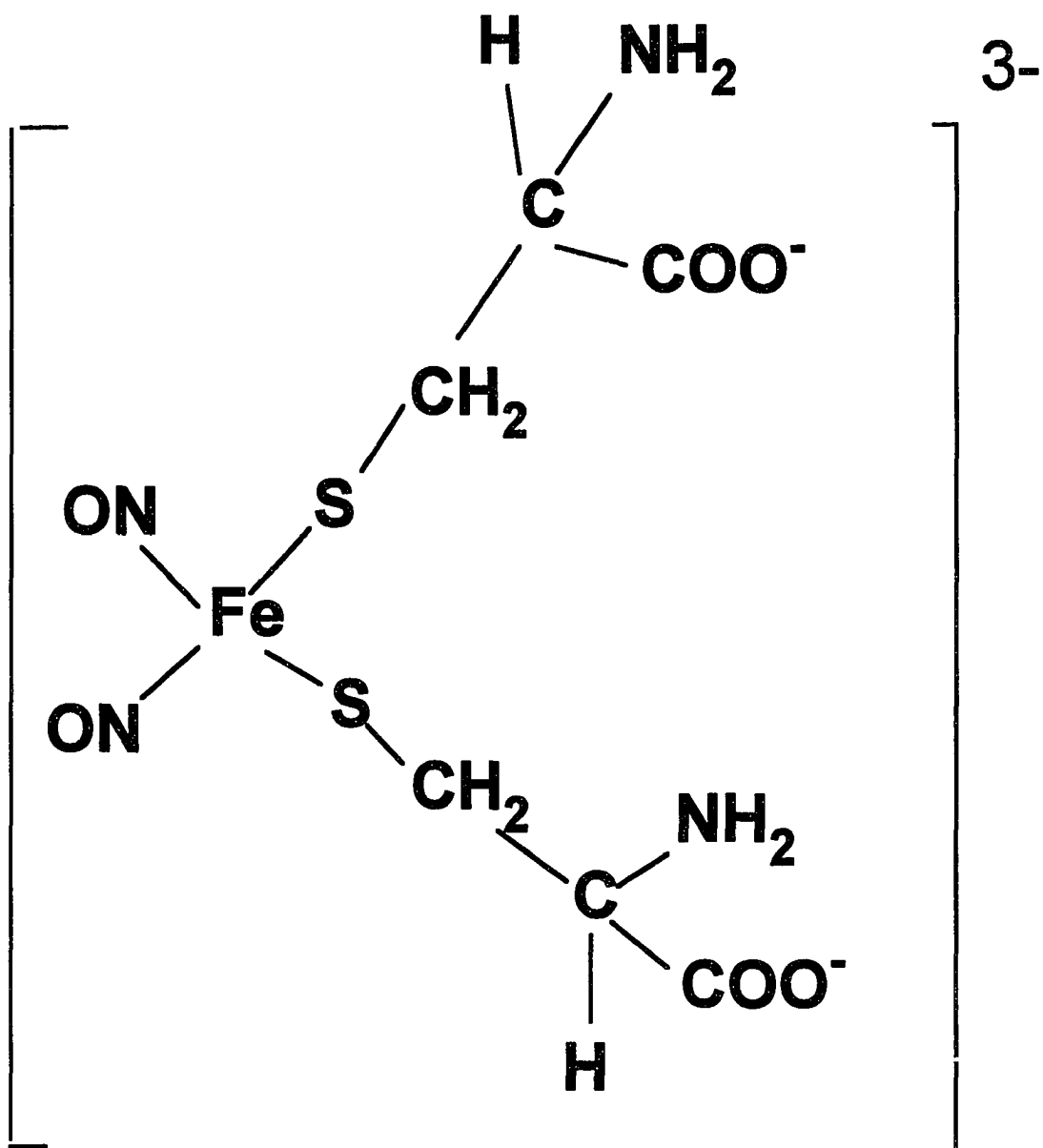
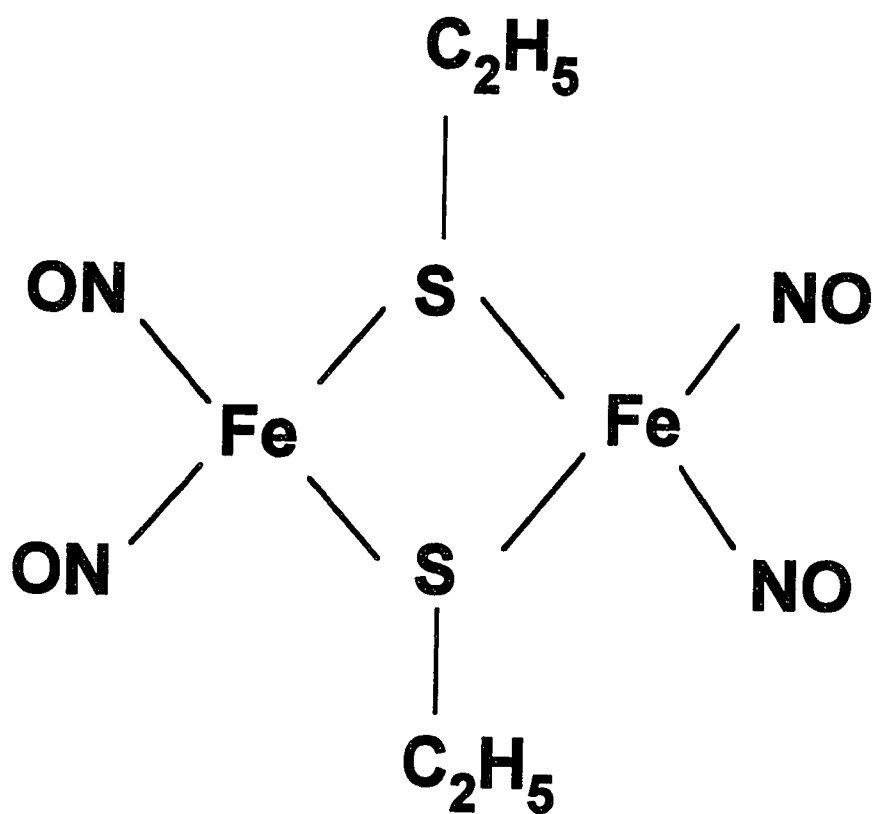


Figure 4.2 Saturation curves of Fe-<sup>14</sup>NO-Pen at different concentrations. Inset: Saturation curves of Fe-<sup>14</sup>NO-Pen after correction for concentration differences. Experimental conditions: Temperature: 77 K; Modulation Amplitude: 2 G; Time Constant: 0.3 s. (pensat.the)



Fe-NO-Cysteine complex

Figure 4.3 Proposed structure of dinitrosyl ion cysteine.  
(Fecys.dia)



## Roussin's red ethyl ester

Figure 4.4 X-ray structure of Roussin's red ethyl ester.  
(ester.the) (77)

shows an axial symmetry with  $g_{\perp} = 2.035 \pm 0.001$  and  $g_{\parallel} = 2.016 \pm 0.001$ . EPR spectrum of Fe-<sup>14</sup>N O-Cys made in D<sub>2</sub>O (data not shown) shows no observable changes in the hyperfine pattern or line width, indicating that the hyperfine structure does not come from solvent exchangeable protons, such as H<sub>2</sub>O and/or amino protons. Thus the observed couplings in the room temperature spectrum are believed to be due to the nitrogen from two NO molecules and non-solvent exchangeable protons, i.e. protons from CH<sub>2</sub> group adjacent to the S atom of cysteine, as has been pointed out by McDonald and coworkers (77). The room temperature spectrum of Fe-<sup>14</sup>N O-Cys (Fig. 4.5 b) is simulated assuming that the hyperfine structure arises from two identical nitrogen and four identical hydrogen nuclei with splitting constants being  $2.2 \pm 0.2$  G and  $1.15 \pm 0.2$  G, respectively. The simulation results for Fe-<sup>15</sup>N O-Cys from previous work gave a 3.0 G and 1.5 G hyperfine coupling constant for two identical <sup>15</sup>N and four identical protons, respectively (77). In principle, the proton hyperfine splittings for the two complexes, Fe-<sup>14</sup>N O-Cys and Fe-<sup>15</sup>N O-Cys, should be the same. The discrepancy of the proton hyperfine splittings could be due to the different accuracy of the field sweep range for different instruments. The <sup>14</sup>N splitting constant (2.2 G), however, is in correct ( $g_{14N}/g_{15N}$ ) with the literature value



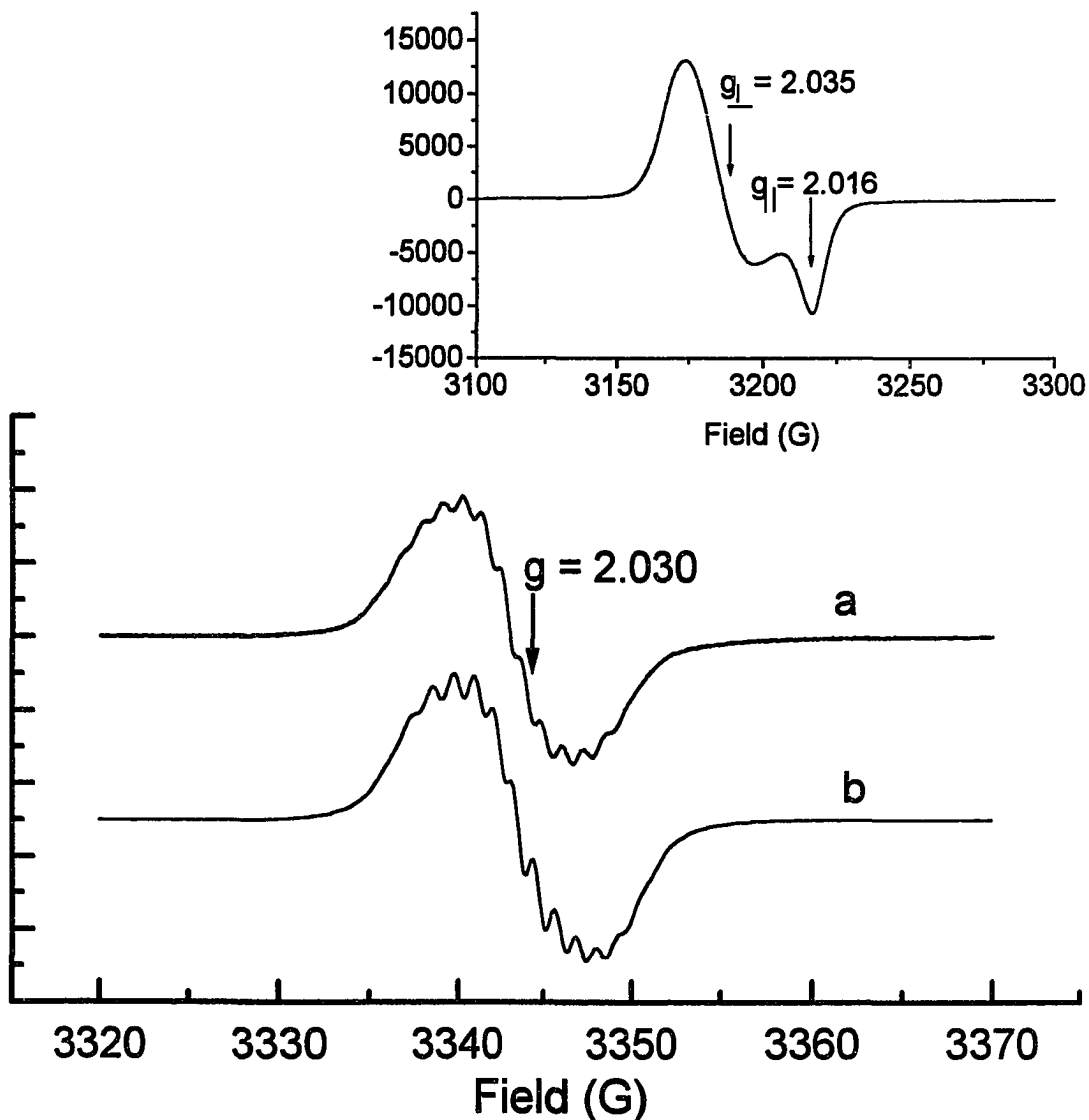


Figure 4.5 (a) Room temperature EPR spectrum of 20 mM dinitrosyl ion cysteine complex at pH = 6. Experimental conditions: Field Set, 3345 G; Scan range, 50 G; Microwave Frequency, 9.5 GHz; Microwave power, 5 mW; Modulation Frequency, 100 kHz; Modulation Amplitude, 0.1 G; Receiver Gain, 100 mV; Time Constant, 0.3 s; Scan time = 500 s (042095a2.fls). (b) Computer simulation of EPR spectrum of Fe-<sup>14</sup>NO-Cys complex at room temperature. Simulation parameters: Line Shape, Lorentzian; Field range: 3225 -3370 G; Field intervals, 0.15 G; Microwave frequency, 9.500 GHz; Line width, 1.2 G; Isotropic g value, 2.019; Hyperfine coupling constant, 2.2 G, 1.15 G; Effective nuclear spins, 2 (2 equivalent I=1 nuclei), 2 (4 equivalent I=1/2 nuclei); Intensity weighing factors, 1:2:3:2:1 and 1:4:6:4:1.(cysn.dua). Inset: EPR spectrum of the same sample at 100 K. Experimental conditions: Field Set, 3350 G; Scan range, 200 G; Microwave Frequency, 9.5 GHz; Microwave power, 1 mW; Modulation Frequency, 100 kHz; Modulation Amplitude, 1 G; Receiver Gain, 1 V; Time Constant, 0.3 s; Scan time = 500 s. File name: 042095a2.fls. (cys.sem)

of  $^{15}\text{N}$  (3.0 G) The results are best accounted for by a structure in which Fe binds to two NO molecules and two cysteine ligands via the thiol groups in accord with the proposed structure in Figure 4.3.

#### Dinitrosyl Iron Mercaptan Complexes

In support of the structure assignment for the dinitrosyl iron cysteine complexes, analogous studies were also done on a number of model complexes with mercaptan ligands, i.e., mercaptoethanol (Mer), ethanethiol (Eth) and thioglycolic acid (TGA). Figure 4.6 a illustrates the room temperature spectrum of dinitrosyl iron mercaptoethanol (Fe- $^{14}\text{NO}$ -Mer) (77) with a g value of  $2.029 \pm 0.001$ . The spectrum has a hyperfine pattern nearly identical to that of Fe- $^{14}\text{NO}$ -Cys in Figure 4.5 a, indicating the same binding structure for the two, i.e. thiol group binding in these two complexes at room temperature. The EPR spectrum was also taken with the a Fe- $^{15}\text{NO}$ -Mer sample and is shown in Figure 4.6 b. The appreciable difference in the hyperfine lines from that of  $^{14}\text{NO}$  sample leaves little doubt about the contribution of NO ligands to the hyperfine structure. The simulations of both the Fe- $^{14}\text{NO}$ -Mer and Fe- $^{15}\text{NO}$ -Mer spectra are shown in Figures 4.7 and 4.8, respectively, along with the corresponding experimental spectra for comparison. The simulation results

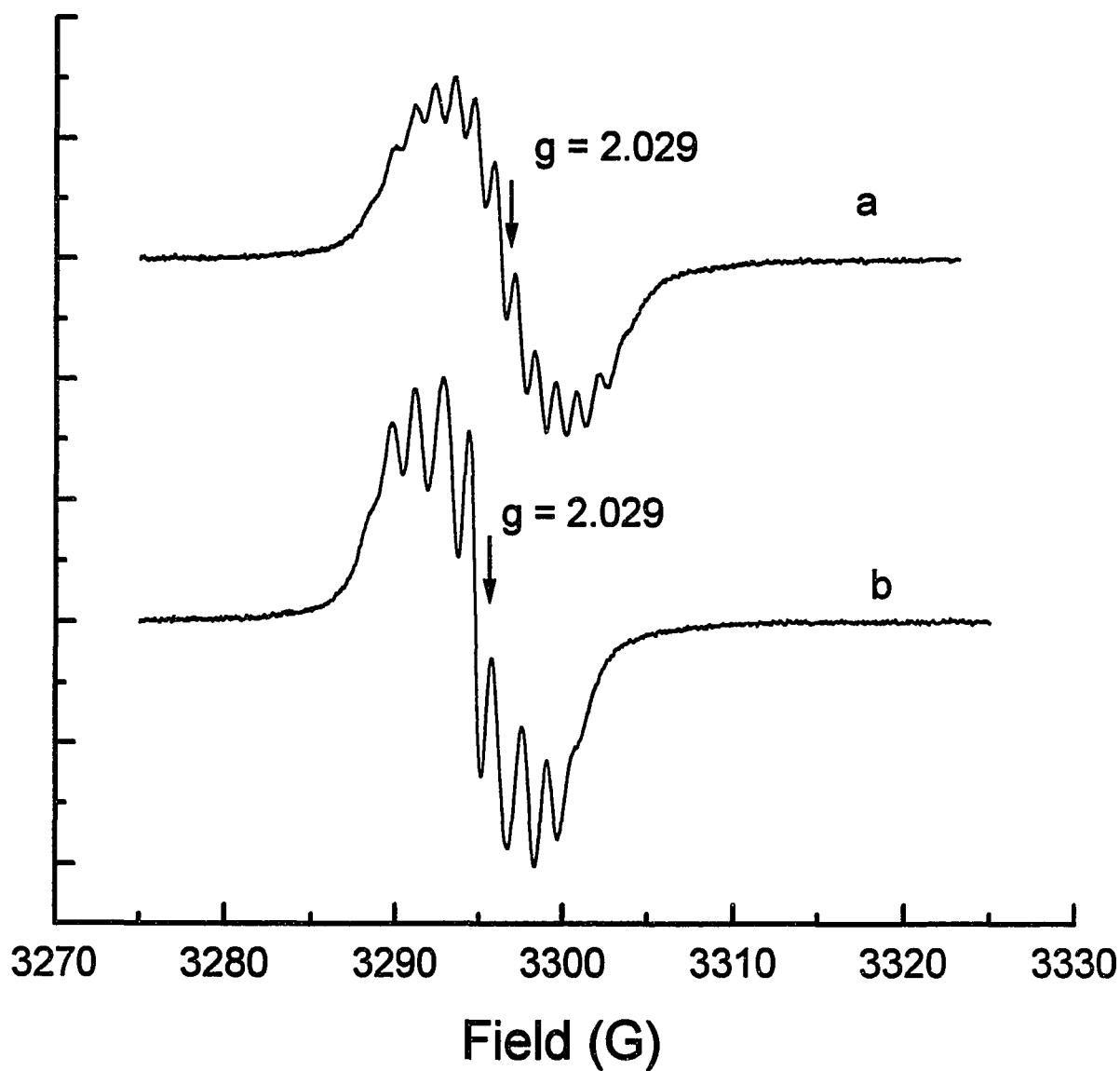


Figure 4.6 Room temperature EPR spectrum of Fe-<sup>14</sup>NO-Mer (a) and Fe-<sup>15</sup>NO-Mer (b) (pH = 6). Experimental conditions: Field Set, 3300 G; Scan range, 50 G; Microwave Frequency, 9.31 GHz; Microwave power, 5 mW; Modulation Frequency, 100 kHz; Modulation Amplitude, 0.1 G; Receiver Gain, 0.01 V; Time Constant, 0.03 s; Scan time = 500 s. File name: 082995a1.flc (a), 090695b1.flc (b). (merrt.the) (77)

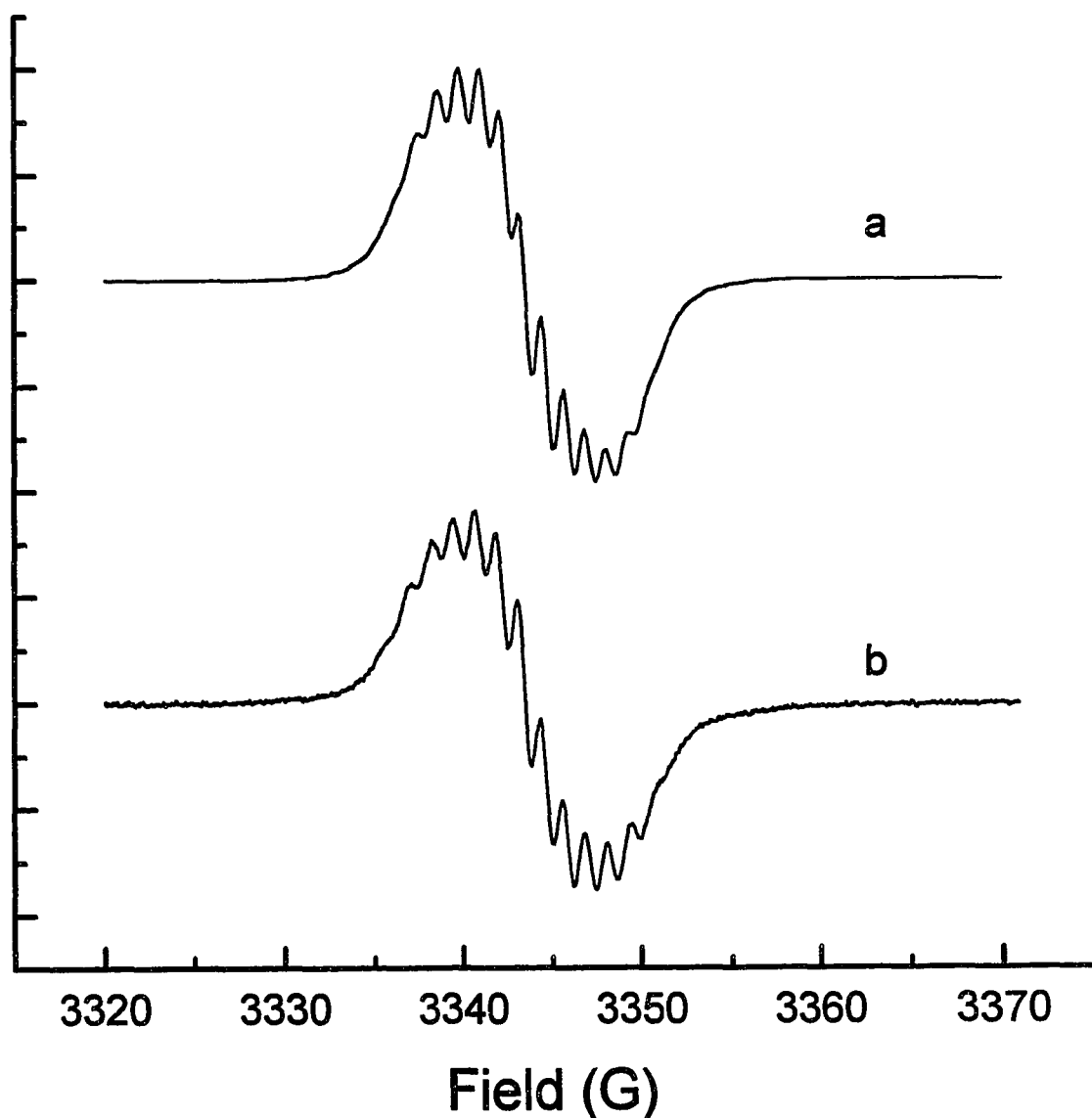


Figure 4.7 Computer simulation (a) and experimental (b) EPR spectrum of Fe-<sup>14</sup>N<sub>2</sub>O-Mer complex at room temperature. Simulation parameters: Line Shape, Lorentzian; Field range: 3320 - 3370 G; Field intervals, 0.15 G; Microwave frequency, 9.500 GHz; Line width, 1.0 G; Isotropic g value, 2.019; Hyperfine coupling constant, 2.1 G, 1.1 G; Effective nuclear spins, 2 (two equivalent I = 1 nuclei), 2 (four equivalent I = 1/2 nuclei); Intensity weighing factors, 1:2:3:2:1 and 1:4:6:4:1. File name: mer14.ida, 082995a1.flc. (mer.sim)

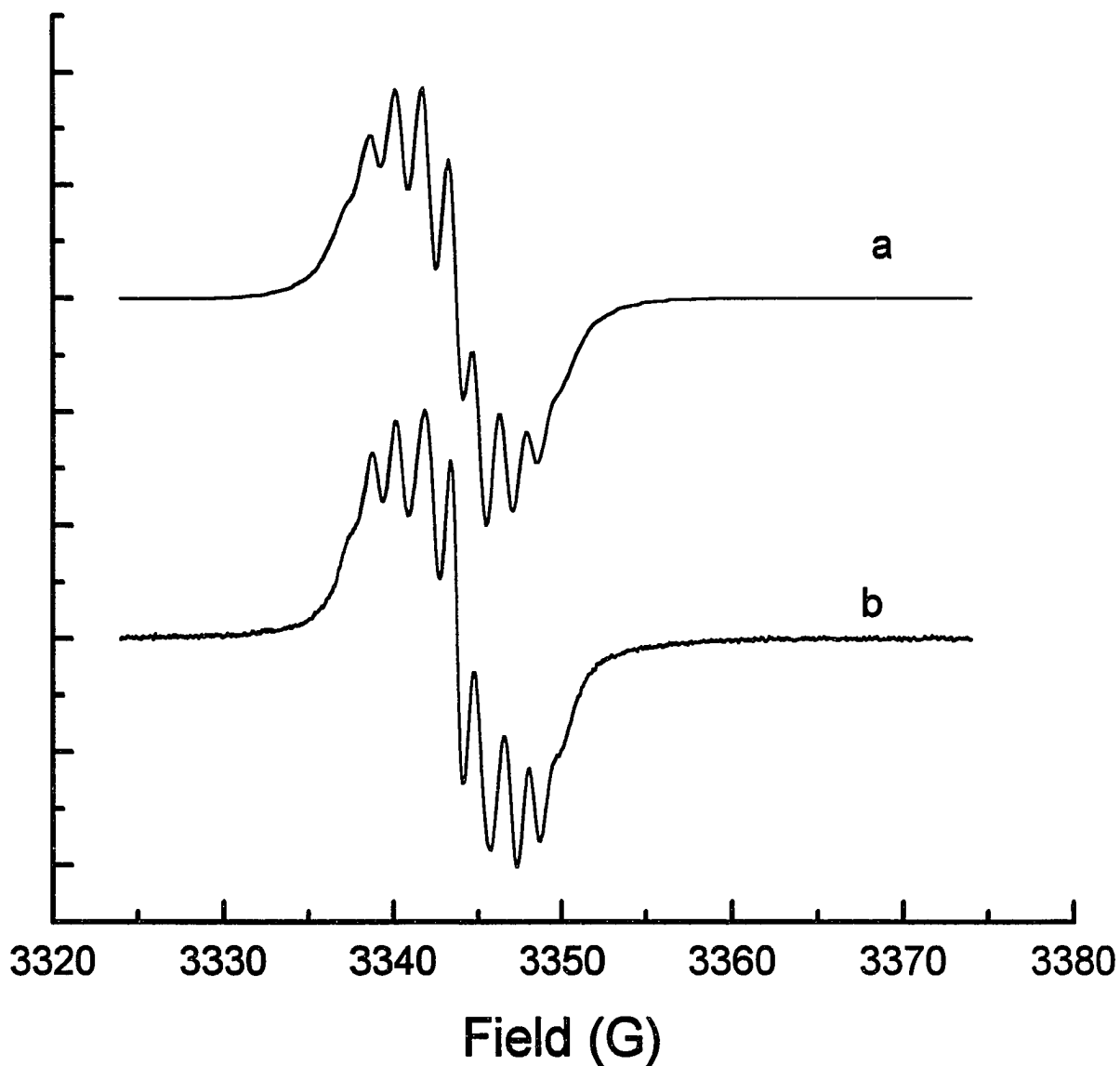


Figure 4.8 Computer simulation (a) and experimental (b) EPR spectrum of Fe-<sup>15</sup>NO-Mer complex at room temperature. Simulation parameters: Line width, 1.2 G; Hyperfine coupling constant, 2.9 G and 1.4 G; Effective nuclear spins, 1 (two equivalent  $I = 1/2$  nuclei), 2 (four equivalent  $I = 1/2$  nuclei); Intensity weighing factors, 1:2:1 and 1:4:6:4:1, other parameters are the same with that for Figure 4.7. File name: mer15.ida (a), 090695b1.flis (b). (mer15.sim)

show splittings from four identical H's and two identical N's. The proton hyperfine splittings for the two complexes,  $1.1 \pm 0.2$  G for Fe-<sup>14</sup>NO-Mer and  $1.4 \pm 0.2$  G for Fe-<sup>15</sup>NO-Mer, are in reasonable agreement. A hyperfine splitting of  $2.1 \pm 0.2$  G was obtained for <sup>14</sup>N and  $2.9 \pm 0.2$  G for <sup>15</sup>N. They are in correct ratio with respect to their nuclear moments. Both splitting constants are in accordance with those for Fe-<sup>14</sup>NO-Cys and Fe-<sup>15</sup>NO-Cys complexes, respectively.

The frozen solution spectrum of Fe-<sup>14</sup>NO-Mer, however, reveals a feature with a nearly isotropic g value as indicated in Figure 4.9 a. The striking difference in the frozen solution spectrum of Fe-<sup>14</sup>NO-Mer from that of Fe-<sup>14</sup>NO-Cys (c.f. Figure 4.5 inset) suggests that the structure for these two complexes in the frozen state is different. One of these two complexes must undergo a structural rearrangement upon freezing the sample. Figure 4.9 b shows the EPR spectrum of Fe-<sup>15</sup>NO-Mer at liquid nitrogen temperature. Because of the pronounced change in the EPR line pattern upon <sup>15</sup>NO substituting in the complex, the hyperfine pattern in the frozen solution spectrum of Fe-NO-Mer is in part, if not entirely, due to the NO ligands.

Although it is generally accepted that the above mentioned mercaptan and cysteine ligands bind to Fe via thiol groups, experimental evidence for this hypothesis has

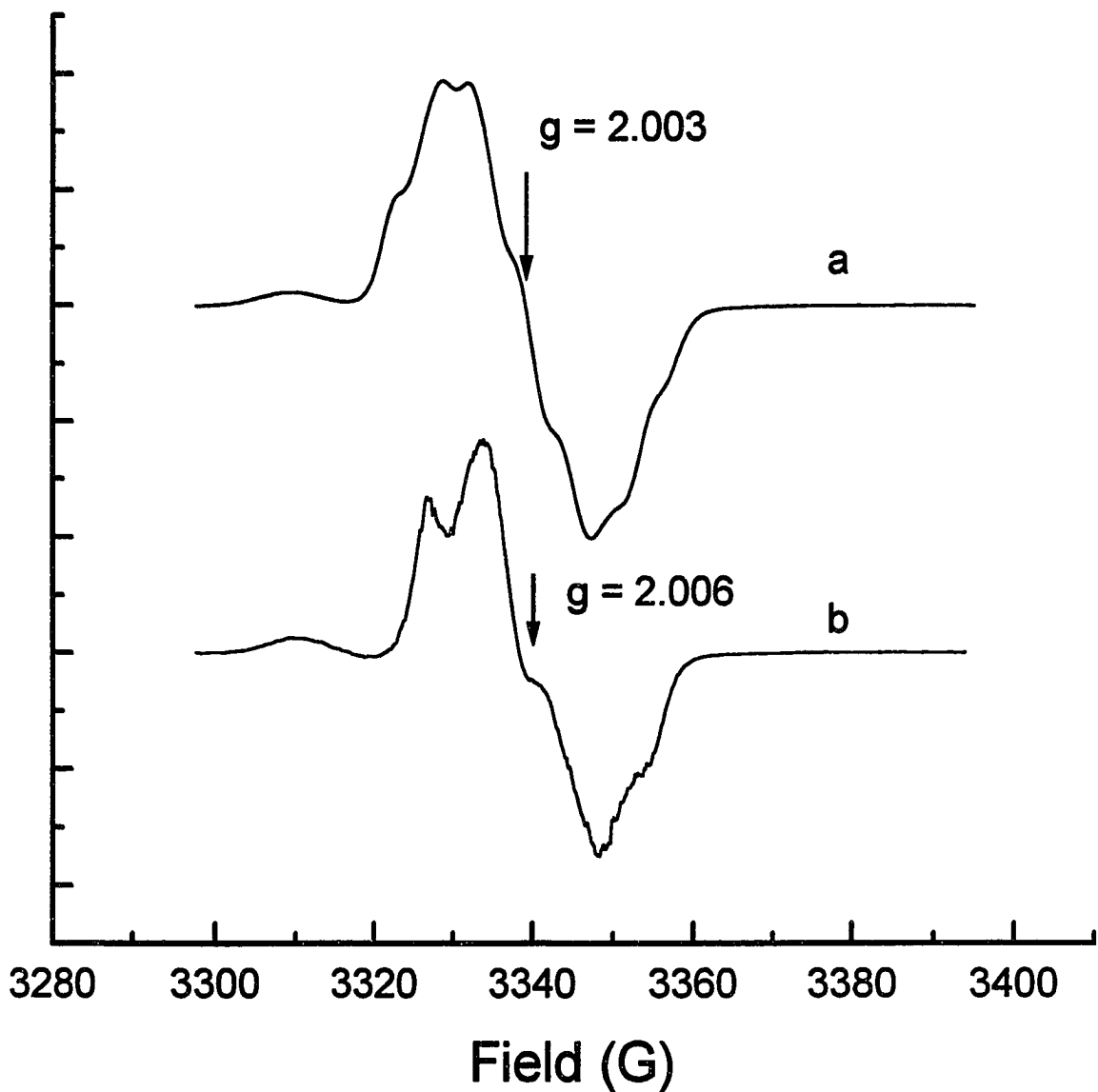


Figure 4.9 EPR spectrum of Fe-<sup>14</sup>NO-Mer (a) and Fe-<sup>15</sup>NO-Mer (b) (pH = 6) at 77 K. Experimental conditions: Field Set, 3300 G; Scan range, 200 G; Microwave Frequency, 9.31 GHz; Microwave power, 2 mW; Modulation Frequency, 100 kHz; Modulation Amplitude, 1 G; Receiver Gain, 0.1 V; Time Constant, 0.03 s; Scan time = 200 s. File name: 082995b2.flc (a), 090695d2.flc (b). (77) (merln.the)

not been unequivocally demonstrated. Thus we investigated another ligand, ethanethiol. In this molecule only the thiol group can provide binding to the Fe center, and therefore dinitrosyl iron ethanethiol complex (Fe-NO-Eth) can serve as an excellent reference for the identification of thiol binding in dinitrosyl iron complexes with other mercaptan ligands. However, apart from its being volatile and a smelly chemical, ethanethiol is nearly insoluble in water, making it difficult to obtain a sample of sufficiently high concentration for EPR measurements at room temperature. Fortunately, due to the larger sample size and lower temperature, the frozen solution spectrum of Fe-NO-Eth (Fig. 4.10) with a same  $g$  value of  $2.003 \pm 0.001$  and EPR lineshape as that observed for Fe-NO-Mer (Fig. 4.9 a) was readily obtained. Based on this observation combined with the foregoing results, it can be concluded with certainty that Fe-NO-Cys, not Fe-NO-Mer, undergoes a structural rearrangement upon freezing the sample, in which case amino group and/or carboxyl group binding may take place. The results thus far confirm the thiol binding structure at room temperature for Fe-NO-Cys, Fe-NO-Mer and Fe-NO-Eth as depicted in Figure 4.3 for cysteine. The significance of these results is that NO molecules may be stabilized and stored as dinitrosyl iron complex with low molecular weight thiols and protein thiols; the thiol groups can be easily



oxidized by molecular oxygen, thus releasing iron and NO, as pointed out by Vanin in their study of endothelium derived relaxing factor (EDRF) (82).

Similar EPR studies have been done on the dinitrosyl iron complex with thioglycolic acid (Fe-NO-TGA). The unique feature of the TGA ligand comes from its bidentant property. Figure 4.11 and inset show the room temperature and frozen solution EPR spectra of Fe-<sup>14</sup>NO-TGA, respectively. The most likely structure for this molecule is the one shown in Figure 4.12, where TGA binds to Fe via both the thiol group and carboxyl group. The reason that resolved hyperfine structures in the room temperature spectrum of Fe-<sup>14</sup>NO-TGA (Fig. 4.11) is not seen could be due to a combination of overlapping fine structure and broad EPR lines. According to the structure of Fe-NO-TGA, the CH<sub>2</sub> group is not free to rotate around the S-C bond as in the ligands of other thiol dinitrosyl iron complexes, thus the two protons contribute differently to the hyperfine structure. This may also contribute to the complexity of the hyperfine pattern of the spectrum, hindering its resolution.

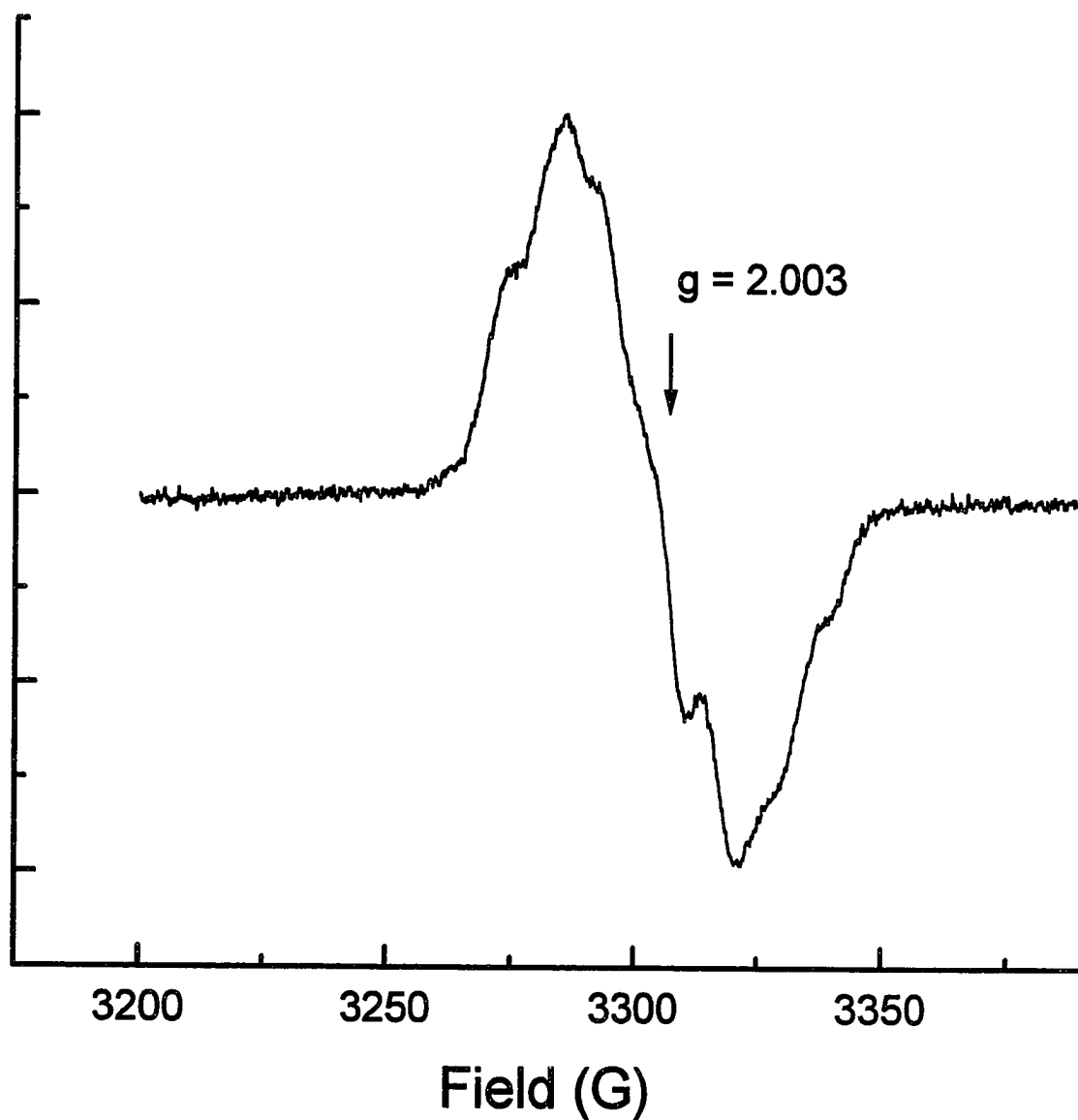


Figure 4.10 EPR spectrum of Fe-<sup>14</sup>NO-Eth (pH = 6) at 77 K. Experimental conditions: Field Set, 3300 G; Scan range, 200 G; Microwave Frequency, 9.31 GHz; Microwave power, 2 mW; Modulation Frequency, 100 kHz; Modulation Amplitude, 1 G; Receiver Gain, 0.1 V; Time Constant, 0.03 s; Scan time = 200 s. File name: 090895a3.fls. (thiol.the)

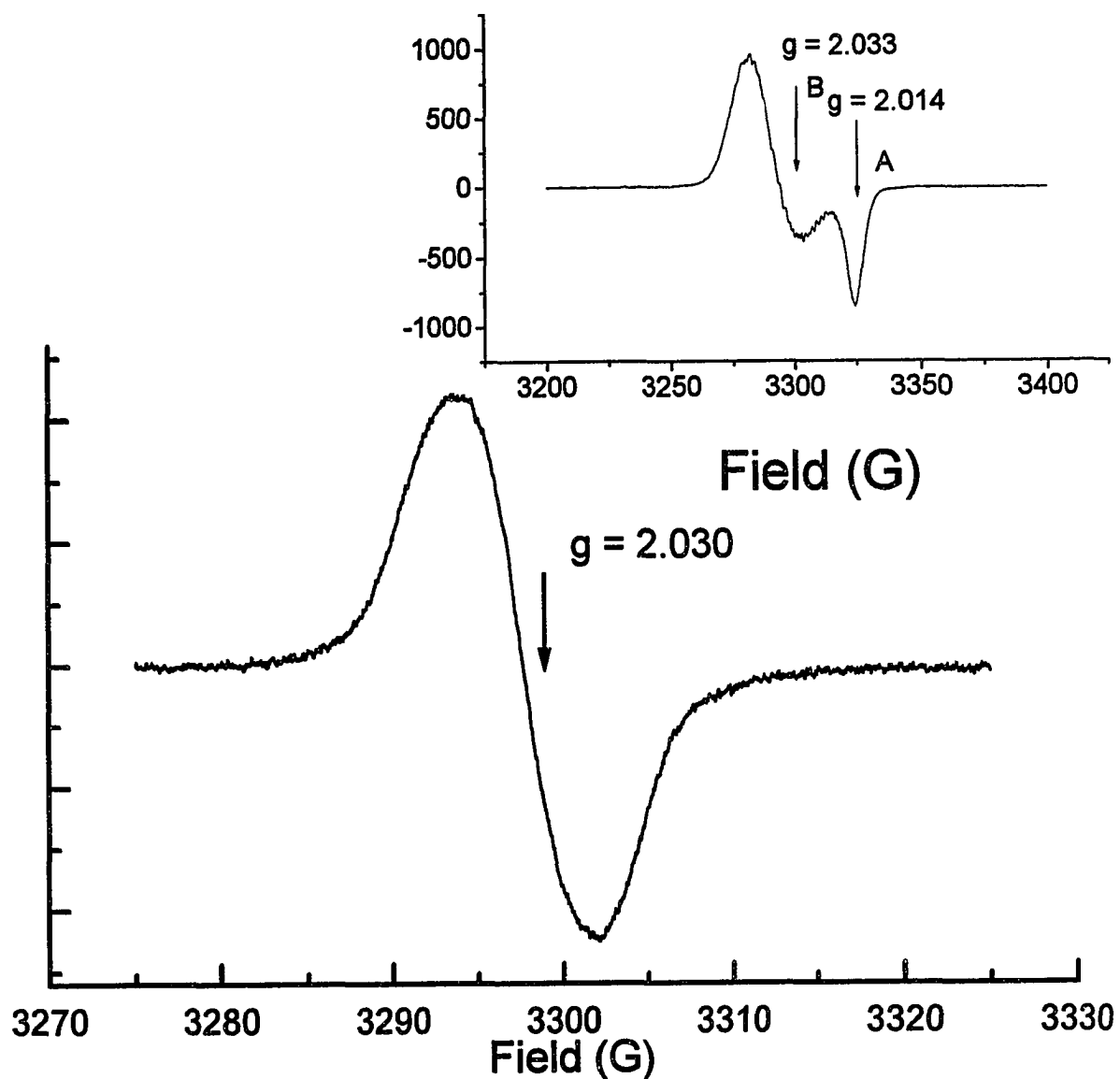


Figure 4.11 Room temperature EPR spectrum of 20 mM Fe-<sup>14</sup>NO-TGA complex at pH = 6. Experimental conditions: Microwave Frequency, 9.31 GHz; Microwave power, 5 mW; Modulation Frequency, 100 kHz; Modulation Amplitude, 0.1 G; Receiver Gain, 0.01 V; Time Constant, 0.03 s; Scan time = 200 s (File name: 082995a2.fls) (tga.the). Inset: EPR spectrum of the same sample at 77 K. Experimental conditions: Receiver Gain, 0.1; other conditions are the same as in the room temperature spectrum. File name: 082995a4.fls. (TGA.the)

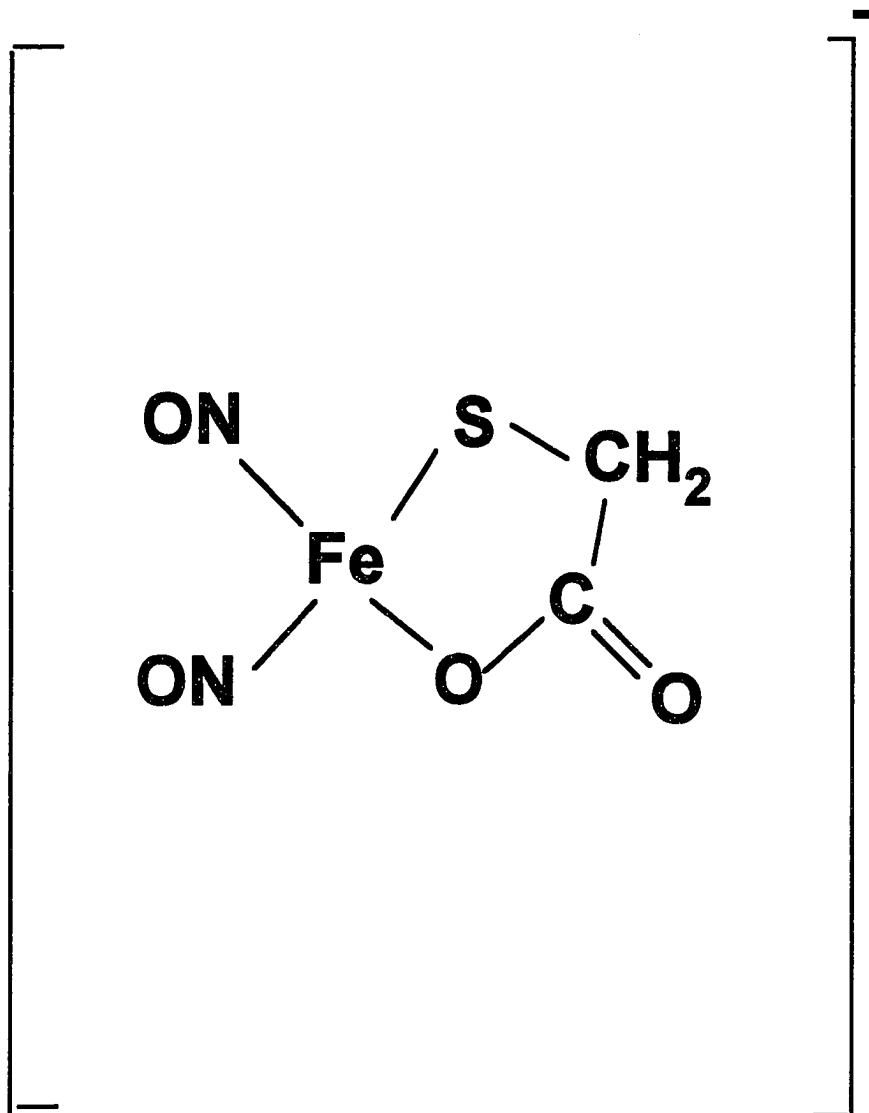
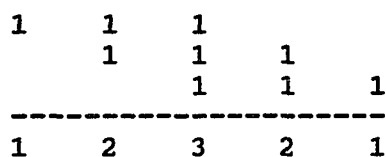


Figure 4.12 Proposed structure of Fe-NO-TGA.

### III Dinitrosyl Iron penicillamine complex (Fe-NO-Pen)

The room temperature EPR spectrum of Fe-<sup>14</sup>N-NO-Pen complex (Fig. 4.13) consists of five hyperfine lines with spacing of 2.5 G (86). The EPR spectrum of this complex in frozen solution obtained at liquid nitrogen temperature is illustrated in the inset, and exhibits axial symmetry with  $g_{\perp} = 2.034 \pm 0.001$  and  $g_{\parallel} = 2.015 \pm 0.001$  similar to those of Fe-<sup>14</sup>N-NO-Cys, suggesting bidentant binding may take place in the frozen samples of Fe-NO-Cys complexes. The hyperfine splittings observed in the room temperature spectrum are primarily due to the NO ligands. For nuclei with spin  $I = 1$ , as in the case of <sup>14</sup>N, has three spin orientations with their  $m_I$  values being +1, 0, and -1 in the direction of the external magnetic field. Thus the interaction of an unpaired electron with one <sup>14</sup>N will result in three EPR lines with equal intensity and spacing. Interaction with a second <sup>14</sup>N will split further each of the three lines into another triplet, resulting in a total of nine EPR lines of equal intensity and spacing. However, if the second nucleus is equivalent with the first one, the splittings overlap, as is shown by the following diagram,



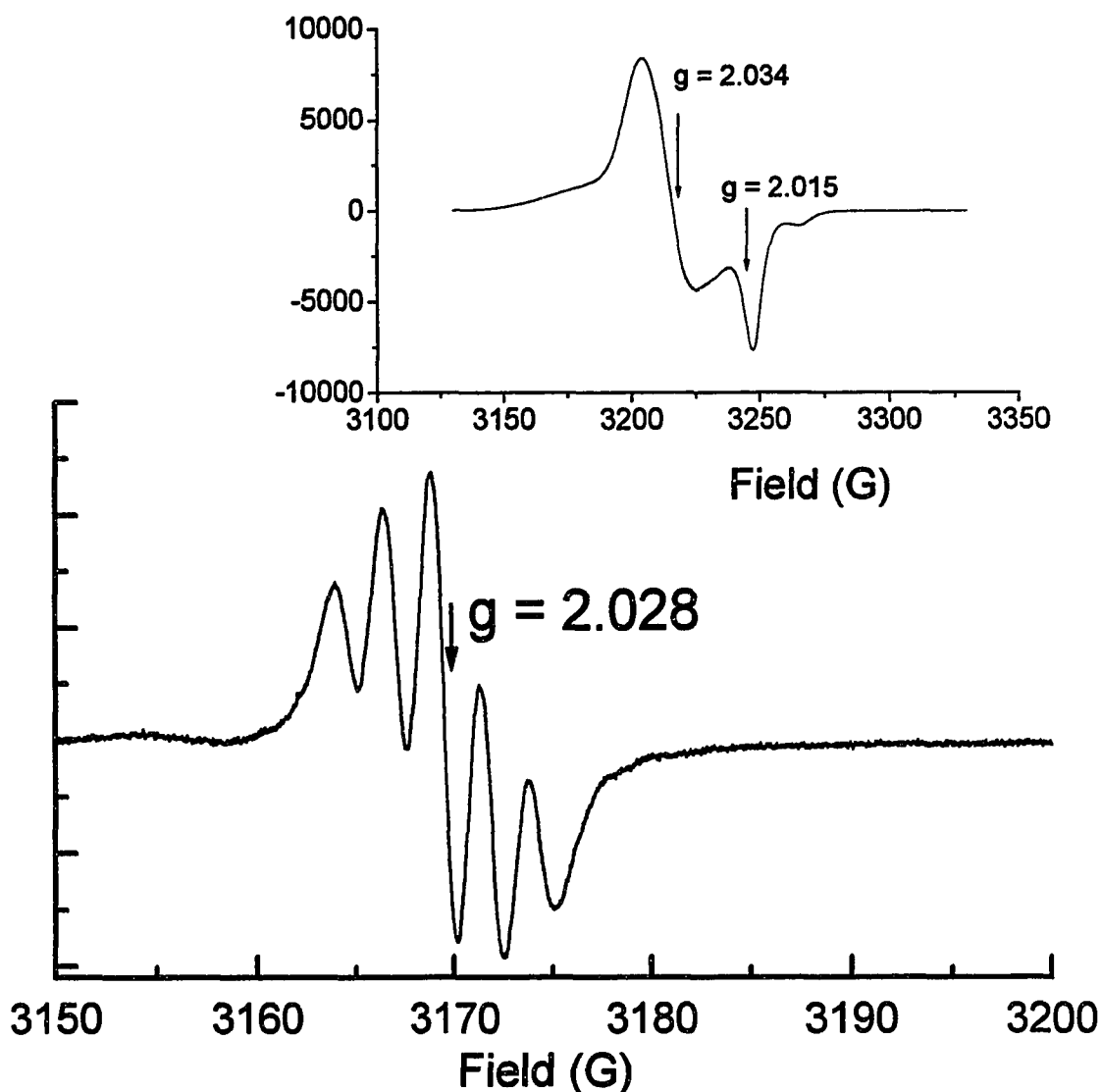


Figure 4.13 Room temperature EPR spectrum of 20 mM Fe-<sup>14</sup>NO-peni at pH = 6. Experimental conditions: Field Set, 3200 G; Scan range, 100 G; Microwave Frequency, 9.11 GHz; Microwave power, 5 mW; Modulation Frequency, 100 kHz; Modulation Amplitude, 1 G; Receiver Gain, 400; Time Constant, 0.03 s; Scan time = 4 min (File name: 051095a3.fls). Inset: EPR spectrum of the same sample at 100 K. Experimental conditions: Field Set, 3225 G; Scan range, 200 G; Microwave Frequency, 9.11 GHz; Microwave power, 5 mW; Modulation Frequency, 100 kHz; Modulation Amplitude, 1 G; Receiver Gain, 125; Time Constant, 0.1 s; Scan time = 4min (File name: 081095a3.fls) (77). (peni.the)

As a result, only five lines are observed with their relative intensities indicated above. The number and intensity ratios of the hyperfine lines observed in the room temperature EPR spectrum clearly demonstrate two identically bound  $^{14}\text{NO}$  molecules in the complex. Further support for this assignment is provided by a room temperature measurement of the same complex with  $^{15}\text{NO}$  ligands (Fig. 4.14) (77). Since the interaction of an unpaired electron with two identical  $I = 1/2$  nuclei will result in a triplet EPR signal with relative intensities of each peak being 1:2:1. The spectrum (Fig. 4.14) shows 3 hyperfine lines with intensity ratio of 1:2:1 and a splitting constant of 3.5 G. The ratio of the hyperfine couplings between the two samples is that expected from the ratio of the nuclear moments of  $^{14}\text{N}$  and  $^{15}\text{N}$ , providing unambiguously assignments to two identically bound  $^{15}\text{NO}$  molecules. The extra peak at lower field in Figure 4.14 is believed to be due to a complex of one iron, two chelate type penicillamine ligands and one nitric oxide (78). No proton hyperfine couplings are observed in the room temperature spectrum, probably because the  $\text{CH}_3$  protons are too distant from the iron spin center. The similarity between the frozen solution spectra of  $\text{Fe-}^{14}\text{NO-Pen}$  and  $\text{Fe-}^{14}\text{NO-Cys}$  (as well as  $\text{Fe-}^{14}\text{NO-TGA}$ ) suggests similar structures of these two complexes in the solid

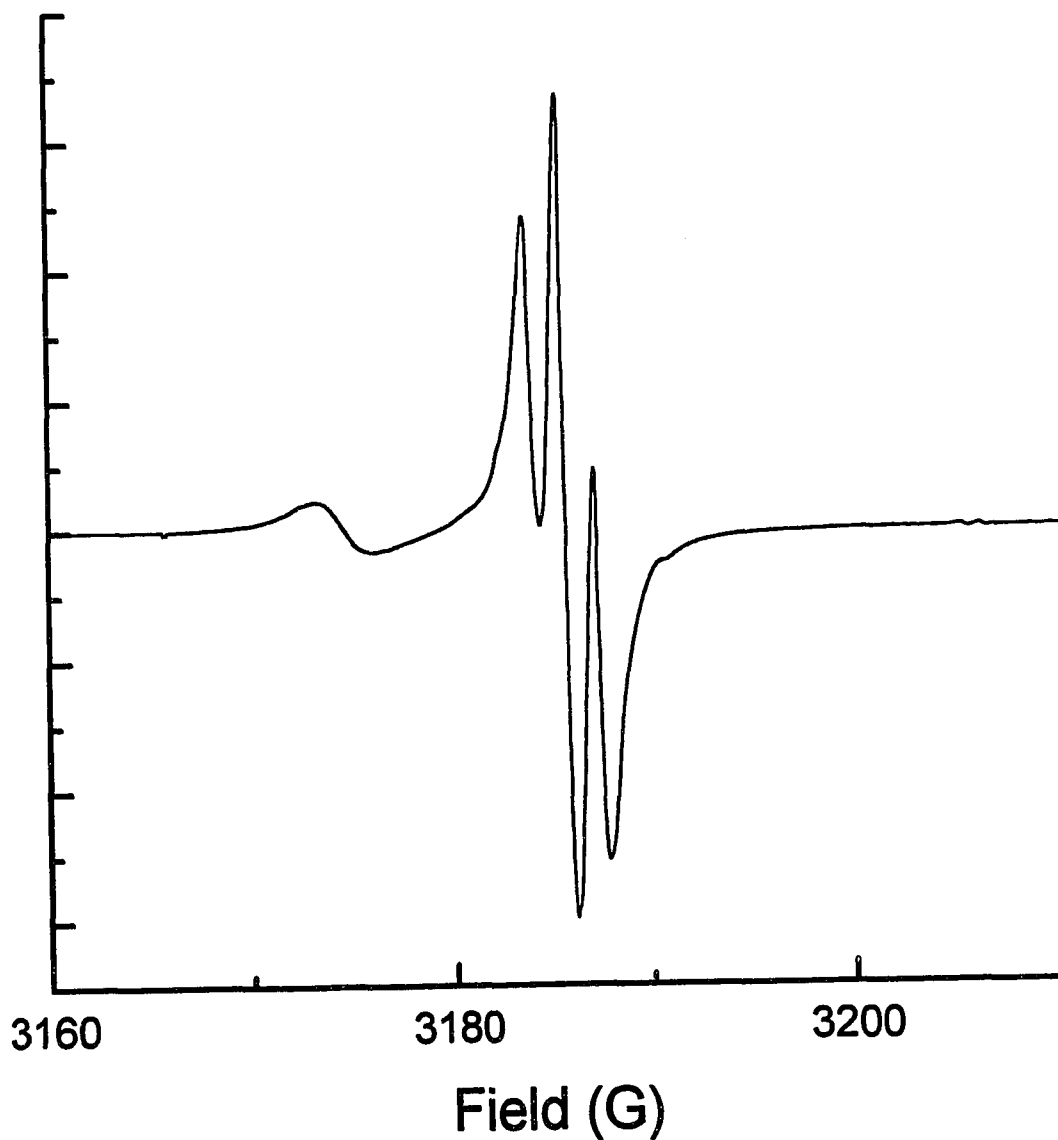


Figure 4.14 Room temperature EPR spectrum of 20 mM Fe-<sup>15</sup>NO-peni complex at pH = 6. Experimental conditions: Field Set, 3225 G; Scan range, 200 G; Microwave Frequency, 9.035 GHz; Microwave power, 5 mW; Modulation Frequency, 100 kHz; Modulation Amplitude, 1 G; Receiver Gain, 400; Time Constant, 0.03 s; Scan time = 4 min (File name: 062195a6.flis) (15nopeni.the).



state. Further investigation of this possibility is provided by the H ENDOR of the complexes made in both H<sub>2</sub>O and D<sub>2</sub>O (see below).

#### IV Dinitrosyl Iron Imidazole complex (Fe-NO-Im)

Figure 4.15 illustrates the room temperature spectrum of Fe-<sup>14</sup>N<sub>2</sub>O-Im complex with a  $g = 2.035 \pm 0.001$ . Fine structure is not well resolved in the room temperature spectrum, as also observed by Woolum and coworkers (78). One possible explanation is that there are four N's bound to the iron center, two from NO and two from imidazole molecules. Each set of nitrogens give five hyperfine lines, resulting in a total of 25 hyperfine lines, which are too many to be well resolved in a regular EPR spectrum. This hypothesis is confirmed by the room temperature EPR measurement of the Fe-<sup>15</sup>N<sub>2</sub>O-Im complex (Figure 4.16 a) which shows clearly resolved hyperfine splittings (78). This can be rationalized by considering that the <sup>15</sup>N hyperfine coupling constant for <sup>15</sup>NO ( $a_{15N}$ ) and the <sup>14</sup>N coupling constant from imidazole ring ( $a_{14N}$ ) are about the same, thus greatly reducing the number of total hyperfine lines. Based on this assumption, a simulation of the room temperature spectrum is constructed (Fig. 4.16b), which is in substantial agreement with the experimental spectrum (Fig.4.16a). The hyperfine

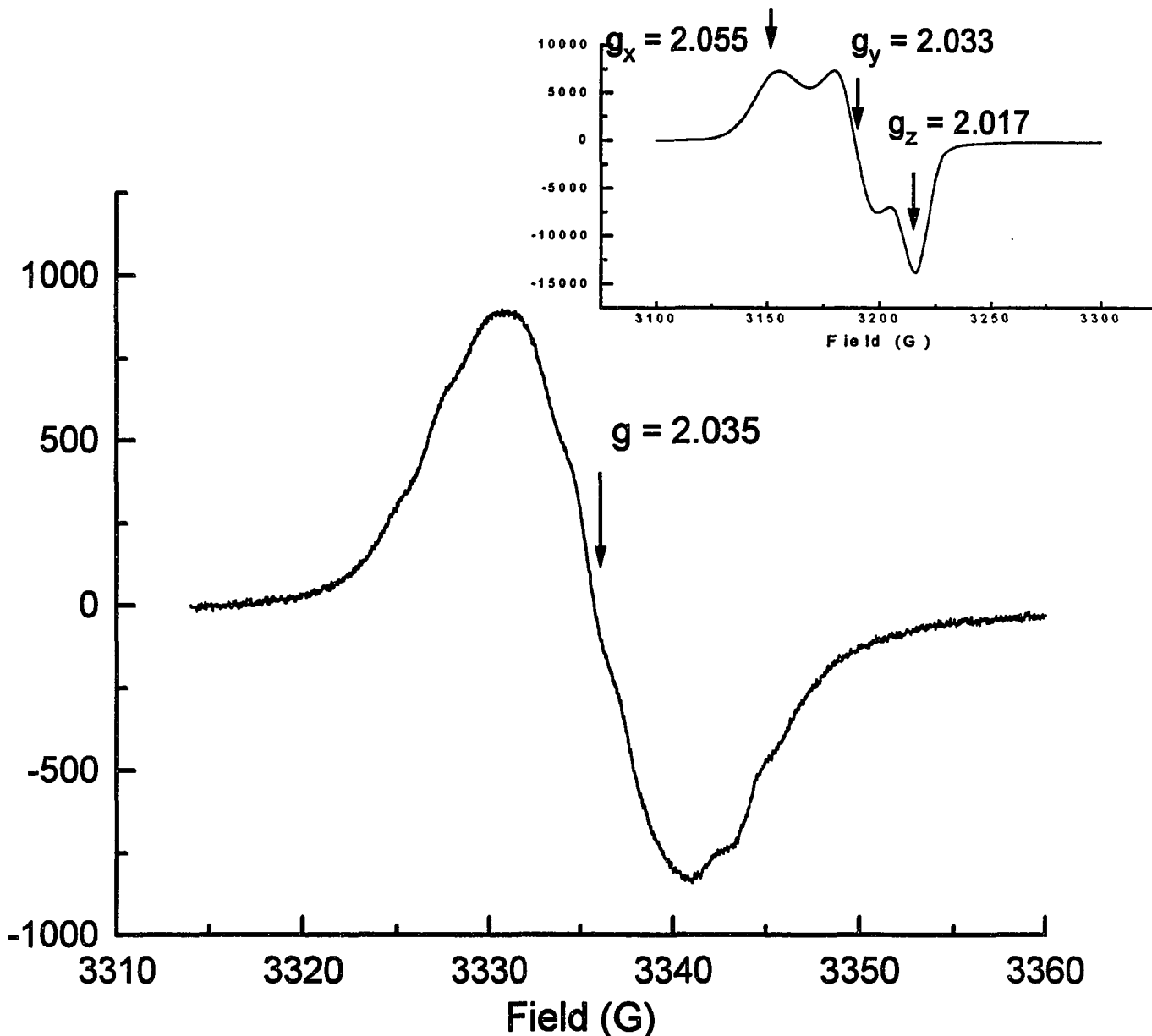


Figure 4.15 Room temperature EPR spectrum of 20 mM Fe-<sup>14</sup>NO-Im complex at pH = 6. Experimental conditions: Field Set, 3345 G; Scan range, 50 G; Microwave Frequency, 9.11 GHz; Microwave power, 5 mW; Modulation Frequency, 100 kHz; Modulation Amplitude, .5 G; Receiver Gain, 100 mV; Time Constant, 0.3 s; Scan time = 500 s (File name: 042095a3.fls). Inset: EPR spectrum of the same sample at 100 K. Experimental conditions: Field Set, 3200 G; Scan range, 200 G; Microwave Frequency, 9.022 GHz; Microwave power, 2.5 mW; Modulation Frequency, 100 kHz; Modulation Amplitude, 1 G; Receiver Gain, 125; Time Constant, 0.1 s; Scan time = 4min. File name: 061495a6.fls. (78). (14nim.the)

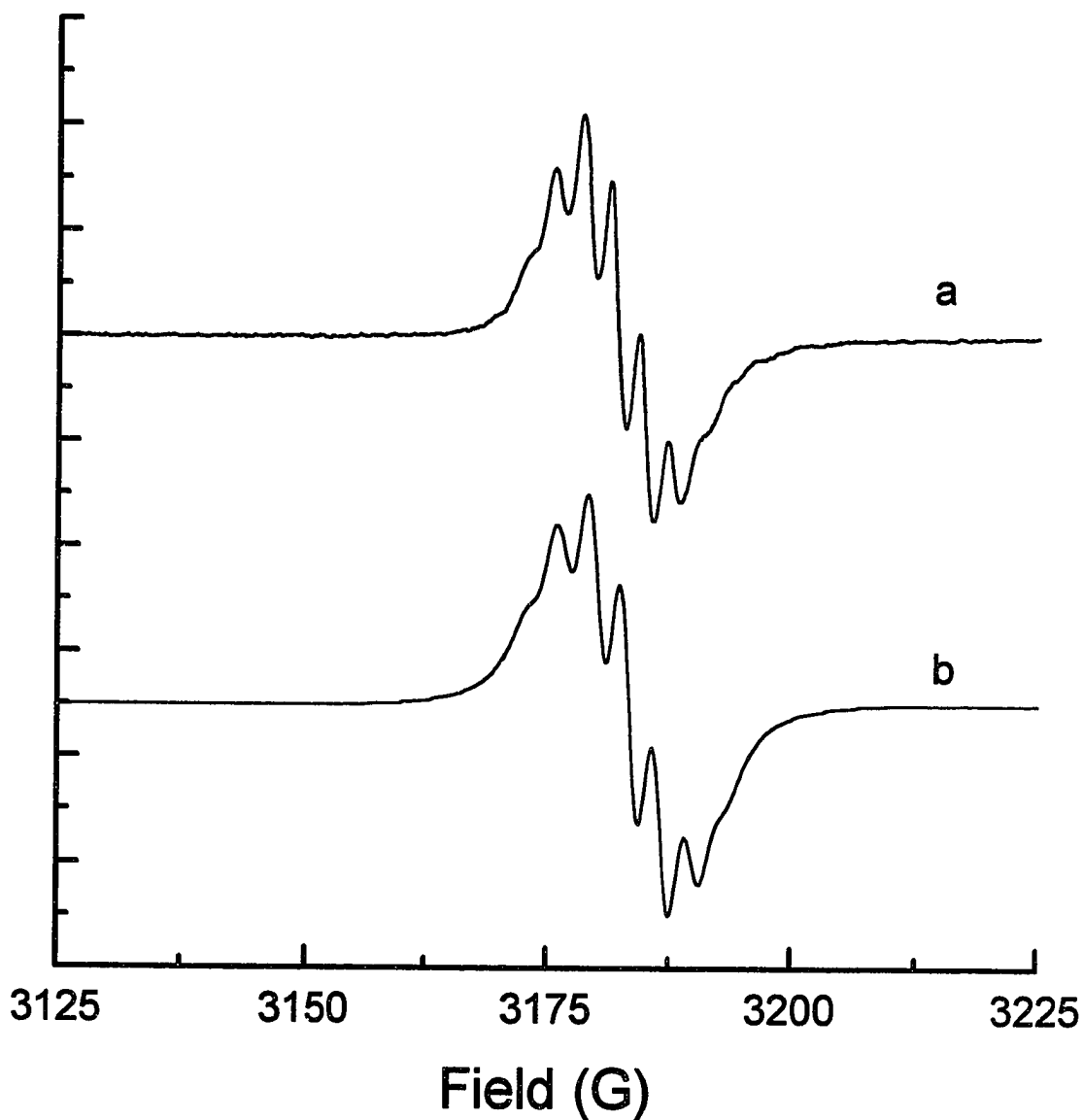


Figure 4.16 Experimental (a) and computer simulation (b) EPR spectrum of Fe-<sup>15</sup>NO-Im complex. Simulation parameters: Line Shape, Lorentzian; Field range: 3100 - 3300 G; Field intervals, 0.15 G; Microwave frequency, 9.022 GHz; Line width, 2.5 G; Isotropic g values, 2.035; Hyperfine coupling constant, 3.0 G, and 3.0 G; Effective nuclear spins, 1 (two equivalent I = 1/2 nuclei) and 2 (two equivalent I = 1 nuclei); Intensity weighing factors, 1:2:1 and 1:2:3:2:1. (feim15.sim)

splitting constants obtained from the simulation are  $a_{15N}(NO) = a_{14N}(Im) = 3.0 \pm 0.2$  G. No proton hyperfine couplings are resolved which is likely a consequence of low electron spin density on the imidazole ring.

Also unlike all the other complexes in this study, the frozen solution spectrum (Fig. 4.15, inset) (78) reveals a rhombic signal with  $g_x = 2.055 \pm 0.001$ ,  $g_y = 2.033 \pm 0.001$  and  $g_z = 2.017 \pm 0.001$ . It should be noted that the EPR spectrum of dinitrosyl iron complexes with histidine (data not shown) also shows a rhombic signal with similar g values ( $g_x = 2.052 \pm 0.001$ ,  $g_y = 2.029 \pm 0.001$ ,  $g_z = 2.013 \pm 0.001$ ). Thus the observation of a rhombic EPR signal could be used to identify Fe binding to histidine moieties of proteins as confirmed by work with the ferritins (83).

### *Proton ENDOR of Dinitrosyl Iron Model Complexes*

Previous and present EPR studies have provided valuable information for the structure analysis of dinitrosyl iron complexes. However, the proposed structure assignments deduced from EPR data for some of the complexes need more rigorous support. Moreover, most of the information have been obtained from room temperature spectra. The structures of these complexes at room temperature are not necessarily the same as those of the corresponding frozen samples, as has been demonstrated by the EPR studies of Fe-NO-Cys and Fe-NO-Mer complexes. Since the frozen samples of the model complexes more closely resemble the complexes seen in proteins (in both cases, molecular tumbling is restricted), the structure of the complexes at frozen state are actually more important in terms of determining the complex structures in proteins. Unfortunately, most of the frozen solution EPR spectra for the dinitrosyl iron complexes in this study did not show resolved nuclear hyperfine interactions, which are needed to establish the binding nuclei of the ligands. Thus the study remains incomplete.

ENDOR spectroscopy has been often used as a powerful structure probe for metalloproteins (90-92). The major advantage of ENDOR comes from its enhanced spectral resolution as well as its ability to directly determine the

identities of the interacting nuclei. The possible interacting nuclei in dinitrosyl iron complexes are nitrogen and hydrogen atoms from the ligands. Nitrogen ENDOR spectra are most needed to unequivocally establish the structures; however, to date we have been unable to see any  $^{14}\text{N}$  or  $^{15}\text{N}$  CW-ENDOR signals for reasons which are unclear but possibly are related to the relaxation properties of these nuclei. The use of pulsed ENDOR is currently being explored in an attempt to observe hyperfine interactions from these nuclei. In the next section, only  $^1\text{H}$  ENDOR results will be presented along with some tentative conclusions regarding the origin of the ENDOR signals and the structure of the complexes.

Since no ENDOR work has been reported on dinitrosyl iron complexes, the ENDOR data shown here will not only provide further insight into the coordination environment of the Fe center in the complexes, but may also prove useful in future studies of more complex protein systems. To facilitate the proton ENDOR data analysis, molecular modeling structures for the dinitrosyl iron complexes are also presented along with the Fe-proton distances for comparison with those calculated from the hyperfine coupling constants via point dipole-dipole interaction approximation (Appendix H).

Fe-NO-Mer, Fe-NO-TGA and Fe-NO-Cys

Figure 4.17 shows the  $^1\text{H}$  ENDOR spectrum of Fe- $^{14}\text{NO}$ -Mer at various field positions along the frozen solution EPR envelope (Figure 4.18). Table 4.1 contains the numerical values of the observed proton hyperfine couplings along with the estimated proton Fe distances under the point dipole-dipole interaction approximation (Appendix H). Since it was suggested by the EPR experiments that the structure of Fe-NO-Mer complex does not change upon freezing the sample, the isotropic hyperfine coupling observed in the room temperature EPR measurement was also taken into account in the proton iron distance calculation using ENDOR data from the frozen solution (Appendix H).

Table 4.1 Proton hyperfine couplings (MHz) of Fe- $^{14}\text{NO}$ -Mer

Spectrum	Field (G)	A (MHz)	
A	3245	0.22	2.72
B	3256	0.22	2.66 (3.75/4.8)**
C	3263	0.22	2.66
D	3270	0.22	2.66
E	3275	0.22	2.66
F	3280	0.22	2.66
G	3290	0.22	2.46
H	3300	0.22	2.22 (3.84/4.5)**
I	3310	0.22	1.87 (3.92/4.2)**
		(7.2/9.0)*	

\*Estimated proton-electron distances in Å under the point dipole interaction approximation assuming the couplings correspond to  $A_{\perp}$  or  $A_{\parallel}$ , respectively.

\*\*Estimated proton-electron distances, which also has taken into account the isotropic hyperfine coupling contributions (Appendix H).

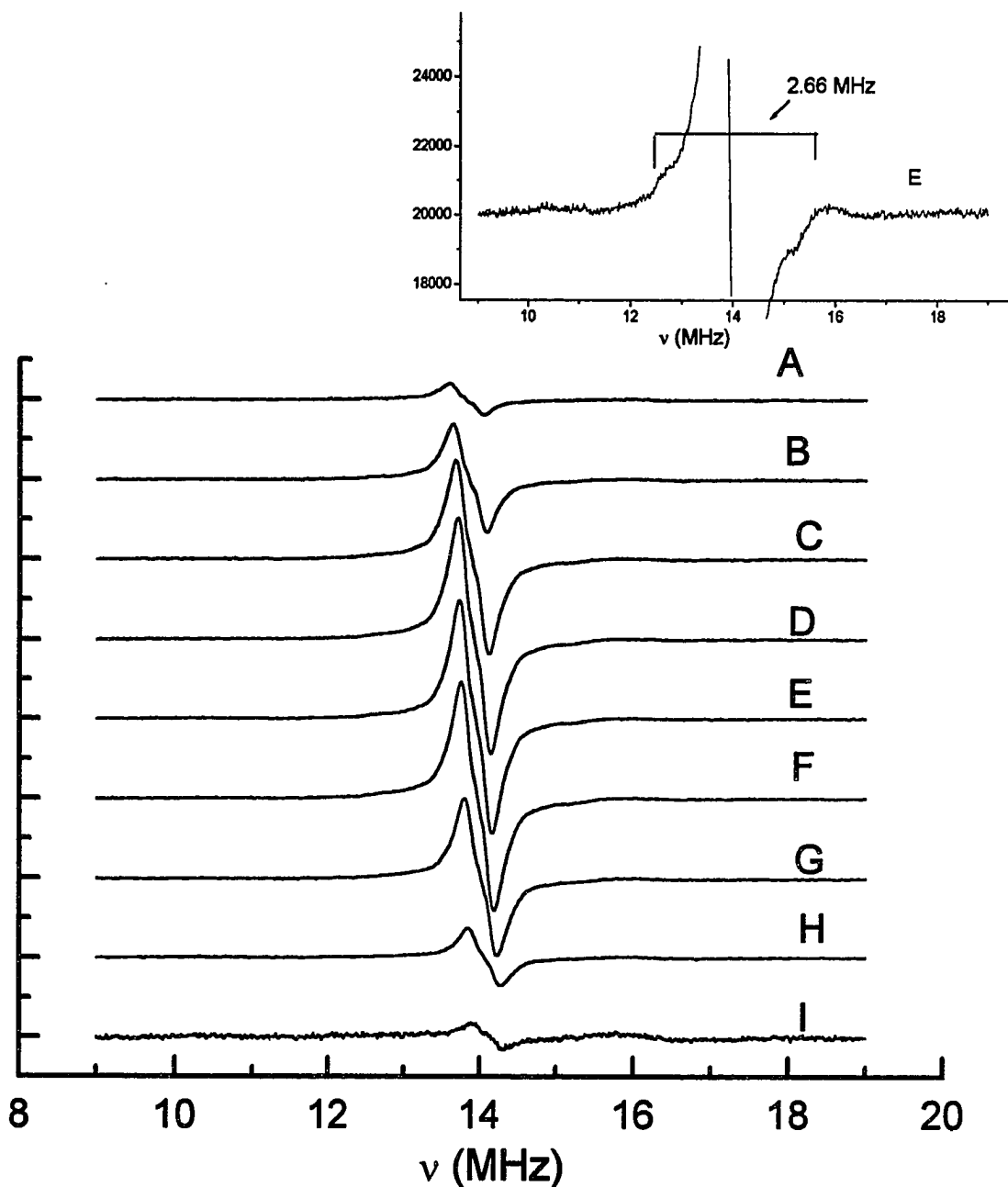


Figure 4.17 Frequency modulation X-band  $^1\text{H}$  ENDOR of 20 mM  $\text{Fe-}^{14}\text{NO-Mer}$  complex at pH = 6. Experimental conditions: Field Set = 3245 G (A), 3256 G (B), 3263 G (C), 3270 G (D), 3275 G (E), 3280 G (F), 3290 G (G), 3300 G (H), 3310 G (I); Microwave Frequency, 9.143 GHz; Microwave power, 5 mW; Modulation Frequency, 10 kHz; Modulation Amplitude, 50 kHz; Temperature, 12 K; Time Constant, 0.03 s; radio frequency power, 100 W; radio frequency scan rate, 0.25 MHz/s. File name: 083095b5.flc (A), b4 (B), b3 (C), b2 (D), b1 (E), b6 (F), b7 (G), b8 (H), b9 (I)) (meren.the).



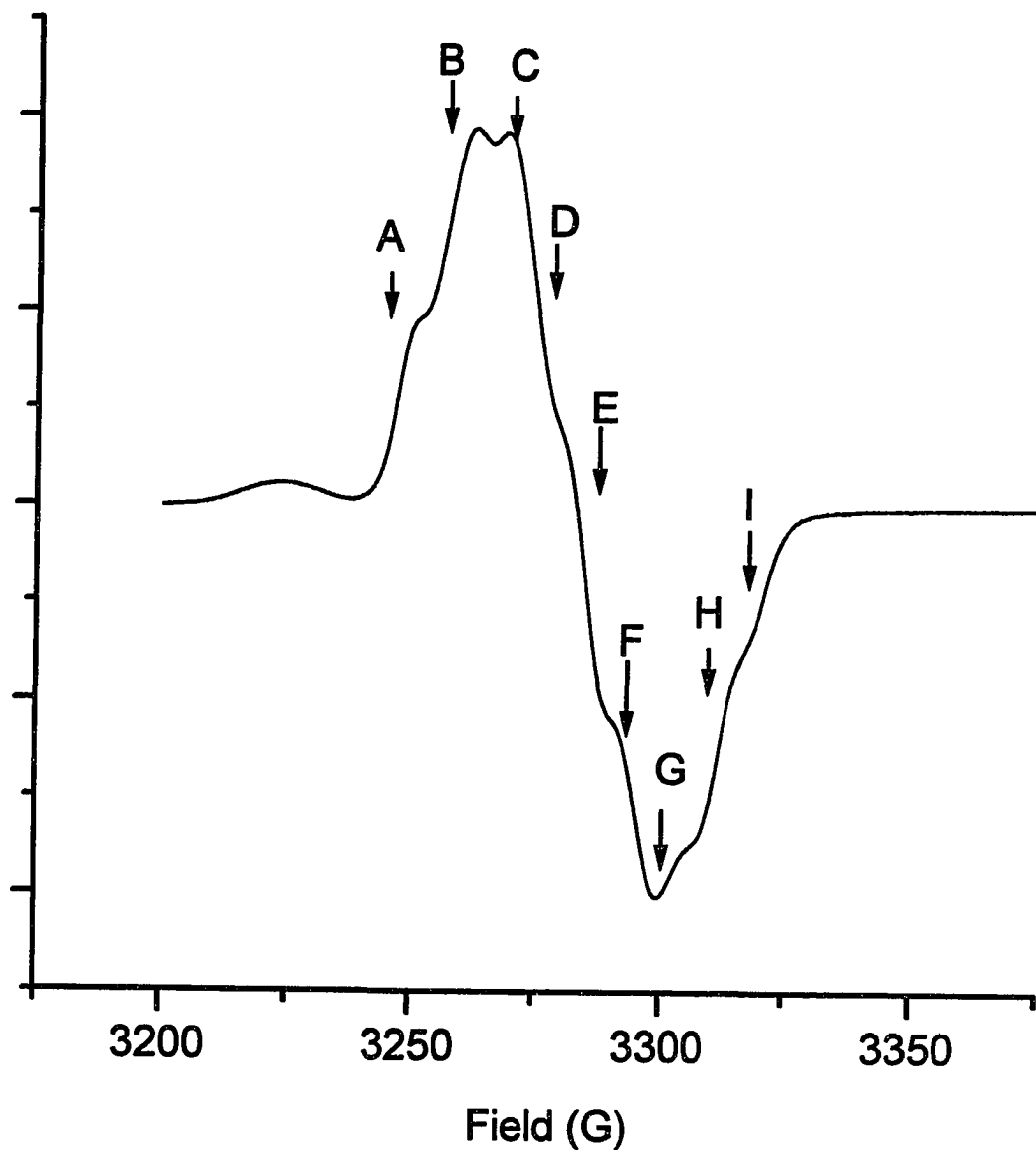


Figure 4.18 EPR spectrum of Fe-<sup>14</sup>NO-Mer (pH = 6) at 77 K. Experimental conditions: Microwave Frequency, 9.31 GHz; Microwave power, 5 mW; Modulation Frequency, 100 kHz; Modulation Amplitude, 0.1 G; Receiver Gain, 0.1 V; Time Constant, 0.03 s; Scan time = 200 s. File name: 082995b2.fls (merlab.the).

Molecular modeling based on the structure deduced from EPR studies results in a geometry shown in Figure 4.19 along with the Fe-proton distances listed at the bottom.

The strong signal in the center of the spectrum, also observed in the  $^1\text{H}$  ENDOR spectra of all of the complexes made in  $\text{H}_2\text{O}$ , is the matrix proton ENDOR signal resulting from dipolar interactions between the spin center and the protons from water molecules of the solvent. There are only two hyperfine couplings resolved in the ENDOR spectrum. The coupling of 0.22 MHz is consistently seen for all the other nitrosyl iron complexes (except for Fe-NO-Im) and it appears to be independent of the magnetic field position. Since it disappears upon  $\text{D}_2\text{O}$  exchange as observed for Fe- $^{14}\text{NO}$ -Pen complex (See below), a remote bound water molecule or OH group might be responsible for this coupling. The larger coupling is likely due to the protons on the  $\text{CH}_2$  groups (H4, H18, H22 and H23 of Figure 4.19) adjacent to the S atom. This coupling is not very well resolved probably because the  $\text{CH}_2$  groups in the complex are free to rotate at room temperature, resulting in a spread of molecular orientations within the molecule upon freezing the sample. The proton assignments basically are in reasonable agreement with the distances calculated from the hyperfine coupling constants and those from molecular modeling results.

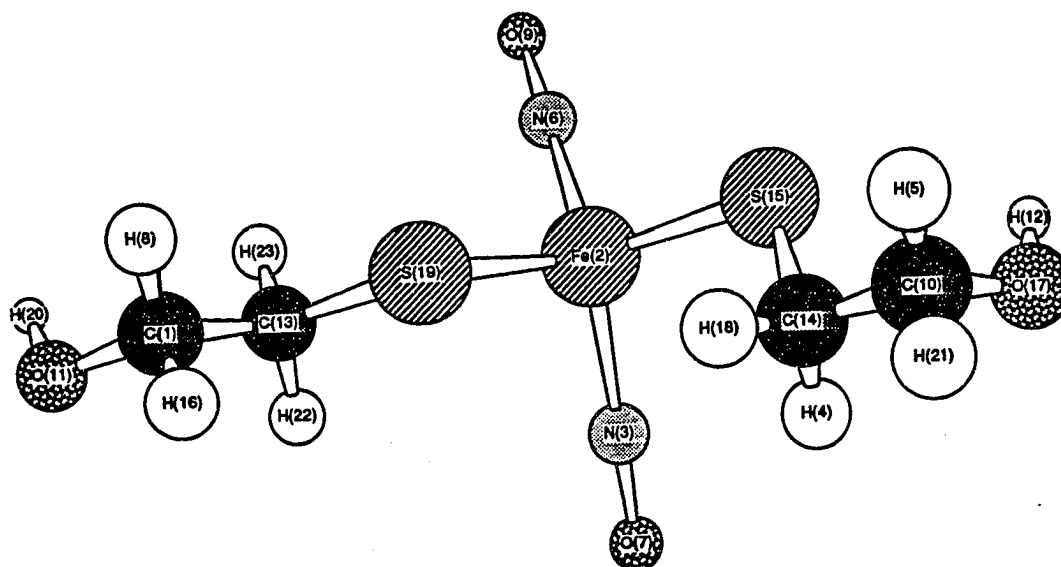


Figure 4.19 Molecular modeling structure of Fe-NO-Mer.  
(Mer.c3d)

Fe-NO-Mer

Proton Number	4, 18, 22, 23	5, 8, 16, 21	12, 20
Iron-proton distances (Å)	3.4	5.0	5.3

Figure 4.20 shows the X-band  $^1\text{H}$  ENDOR spectra of Fe- $^{14}\text{NO}$ -TGA measured at field positions A, B indicated in the frozen solution EPR spectrum of Figure 4.11 inset. The hyperfine couplings obtained from the spectra are listed in Table 4.2.

Table 4.2 Proton hyperfine couplings (MHz) of Fe- $^{14}\text{NO}$ -TGA

Spectrum	Field (G)	A (MHz)*				
A	3253	0.22	1.01	2.07	(3.5/4.2)	2.72(3.0/3.8)
B	3225	0.24	1.07	2.73	(3.0/3.8)	3.5 (2.8/3.5)
		(7.2/9.0)	(4.2/5.3)			

\*Data in parentheses are the estimated proton-electron distances in Å under the point dipole interaction approximation assuming the couplings correspond to  $A_{\perp}$  or  $A_{\parallel}$ , respectively.

According to the structure of Fe-NO-TGA (Fig. 4.12), the two larger couplings observed are presumably due to the  $\text{CH}_2$  protons. The calculated Fe-proton distances from the hyperfine couplings agree reasonably well with that obtained by molecular modeling shown in Figure 4.21. Unlike in mercaptoethanol, the two protons on the  $\text{CH}_2$  group in TGA, namely H8 and H10 (Fig. 21), are not identical in positions relative to the spin center, thus giving different hyperfine coupling contributions. The couplings in the last two columns are thought to be due to the hyperfine interactions from these two protons, although they cannot be unequivocally distinguished at this point. The couplings of about 1 MHz are probably due to a protonated carboxyl

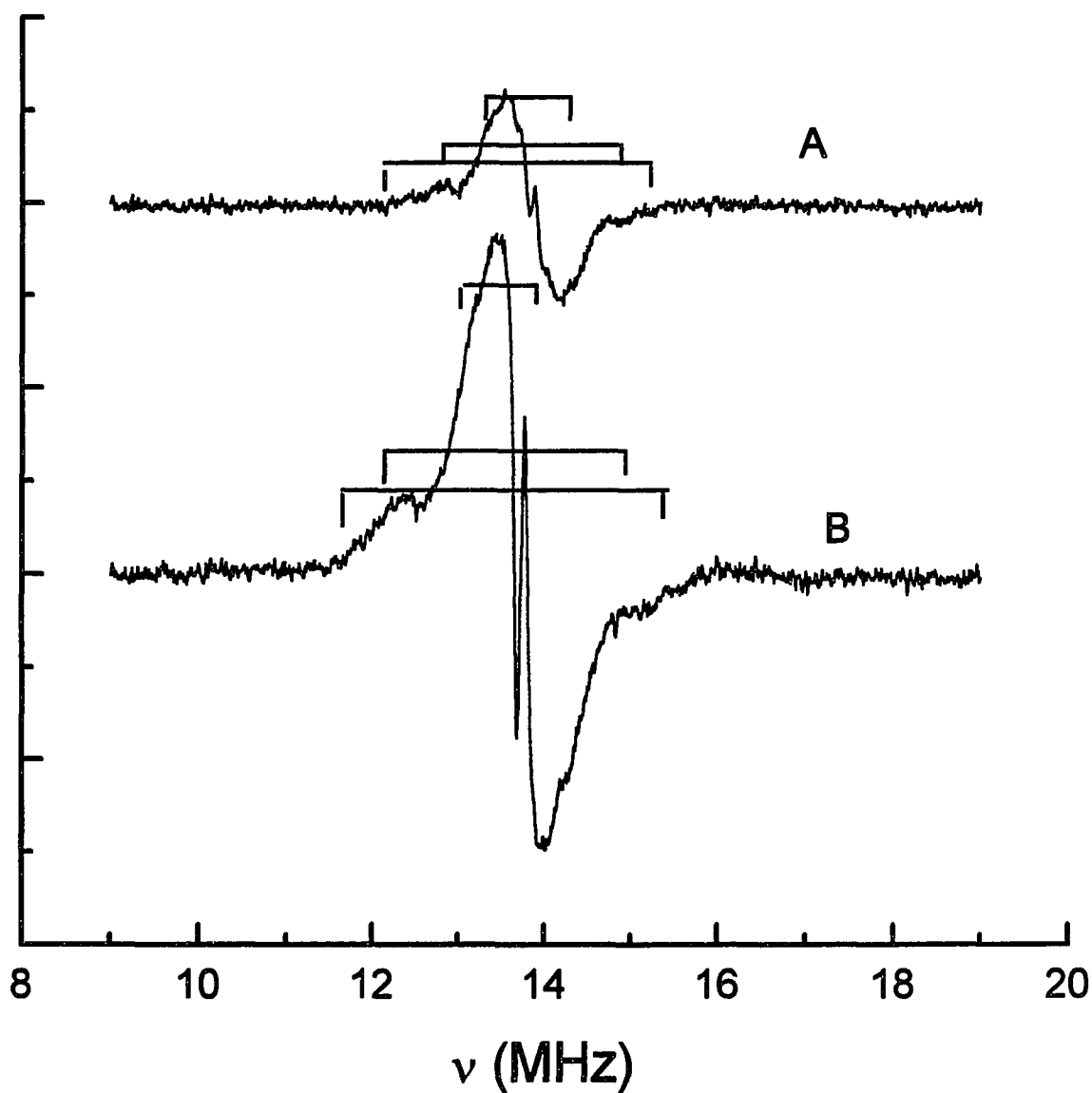


Figure 4.20 Frequency modulation X-band  $^1\text{H}$  ENDOR of 20 mM  $\text{Fe-}^{14}\text{NO-TGA}$  complex at pH = 6. Experimental conditions: Field Set = 3253 G (A), 3225 G (B), 3212 G (C); Microwave Frequency, 9.143 GHz; Microwave power, 5 mW; Modulation Frequency, 10 kHz; Modulation Amplitude, 50 KHz; Temperature, 12 K; Time Constant, 0.03 s; radio frequency power, 100 W; radio frequency scan rate, 0.25 MHz/s. File name: 083095d8.flc (A), d7 (B), d9 (C). (tgaen.the).

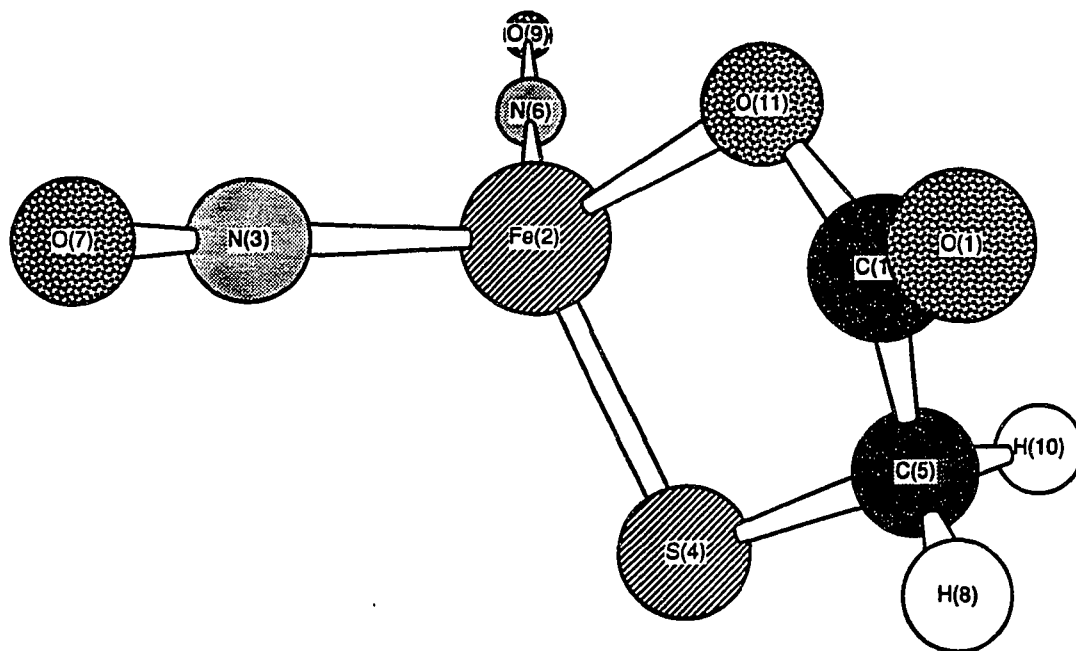


Figure 4.21 Molecular modeling structure of Fe-NO-TGA.  
(tga.c3d)

Fe-NO-TGA

Proton Number	8	10
Iron-proton distances (Å)	3.6	4.0

hydrogen (not shown), or a bound water molecule or an OH group in the complex. Figure 4.22 illustrates the X-band  $^1\text{H}$  ENDOR spectra of  $\text{Fe-}^{14}\text{NO-Cys}$  complex obtained at field positions corresponding to  $g_{\perp}$  (A) and  $g_{\parallel}$  (B), respectively, on the frozen solution EPR envelope (Fig. 4.23). The coupling constants of the ENDOR lines are listed in Table 4.3.

Table 4.3 Proton hyperfine couplings (MHz) of  $\text{Fe-}^{14}\text{NO-Cys}$

Spectrum	Field (G)	A (MHz)*				
A	3215	0.22	0.9		2.0	
B	3246	0.22	1.03	1.44	2.06	3.05
	(7.2/9.0)	(4.6/5.6)	(3.8/4.8)	(3.4/4.1)	(3.0/3.7)	

\*Data in parentheses are the estimated proton-electron distances in Å under the point dipole interaction approximation assuming the couplings correspond to  $A_{\perp}$  or  $A_{\parallel}$ , respectively.

The ENDOR spectrum is very different from that of  $\text{Fe-NO-Mer}$ , indicating a difference in their structures in frozen solutions. This is in accord with the EPR results indicating that  $\text{Fe-NO-Cys}$  complexes undergo a structural rearrangement upon freezing the sample. We assume, therefore, that amino group and/or carboxyl group binding may take place in this instance. Molecular models build under this assumption are shown in Figure 4.24, where (a) is for the structure of amino groups binding, (b) bidentate binding from both amino and sulfur groups and (c) bidentate binding from both amino and carboxyl groups. There are only

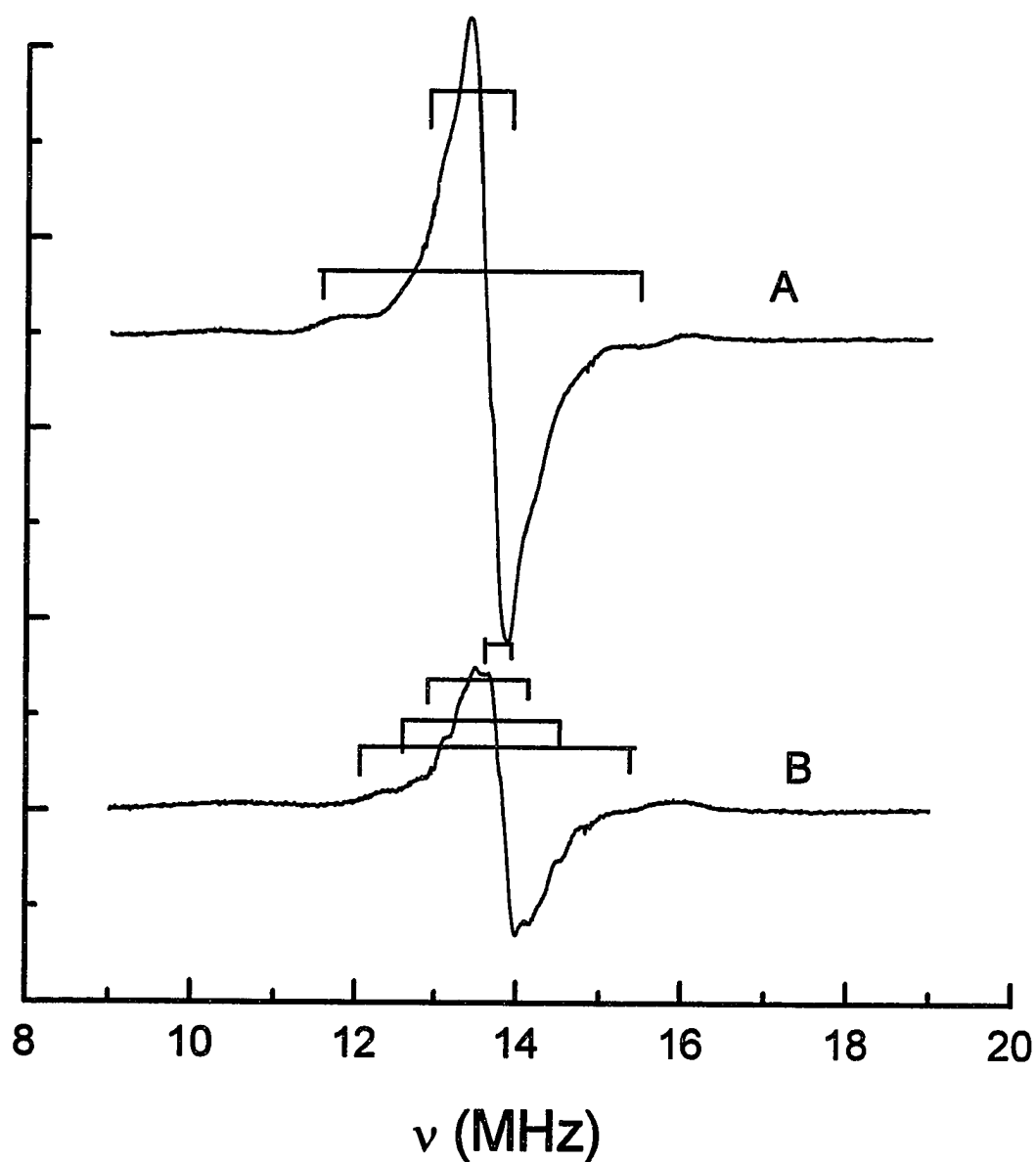


Figure 4.22 Frequency modulation X-band  $^1\text{H}$  ENDOR of 20 mM  $\text{Fe-}^{14}\text{NO-Cys}$  complex. Experimental conditions: Field Set = 3215 G (A), 3246 G (B); Microwave Frequency, 9.143 GHz; Microwave power, 5 mW; Modulation Frequency, 10 kHz; Modulation Amplitude, 100 kHz; Temperature, 26 K; Time Constant, 0.03 s; radio frequency power, 100 W; radio frequency scan rate, 0.25 MHz/s. File name: 083095e1.flc (A), 083095e2.flc (B). (cysen.the)



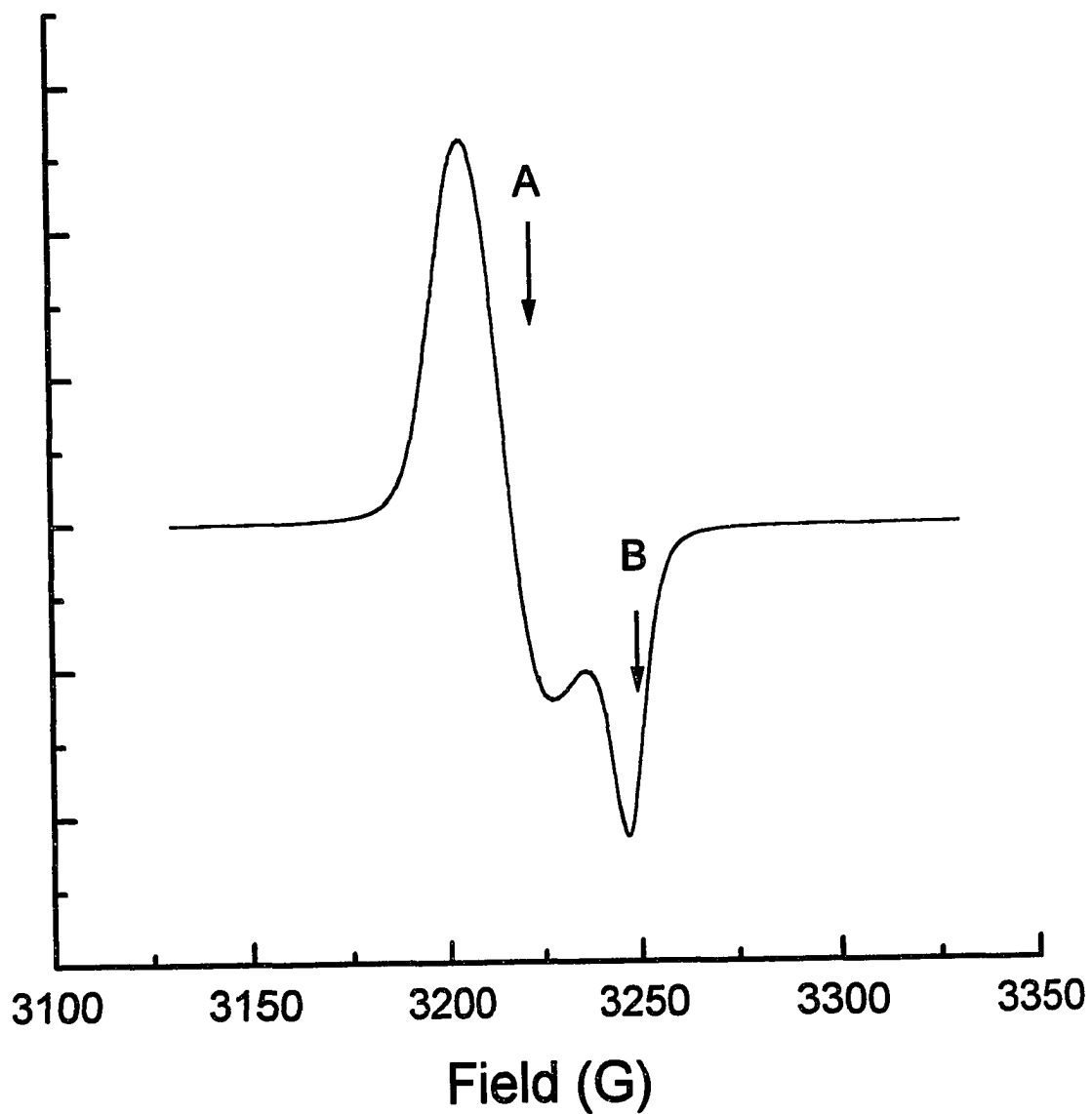


Figure 4.23 EPR spectrum of Fe-<sup>14</sup>NO-Cys (pH = 6) at 77 K. Experimental conditions: Microwave Frequency, 9.31 GHz; Microwave power, 2 mW; Modulation Frequency, 100 kHz; Modulation Amplitude, 1 G; Receiver Gain, 0.01 V; Time Constant, 0.03 s; Scan time = 200 s. (cysl.n.the) (cysl.n.org)

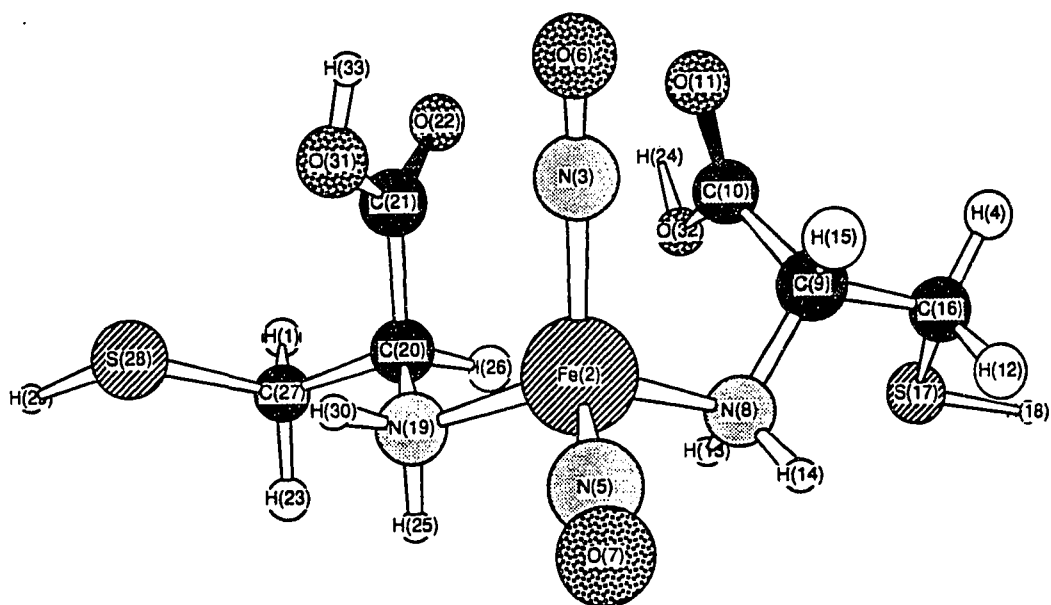


Figure 4.24 (a) Molecular modeling structure of Fe-NO-Cys complex. (cys4.c3d)

Fe-NO-Cys (Amino groups binding)

Proton Number	13, 14, 25, 30	15, 26	12, 23	1, 4	18, 29
Iron-proton distances (Å)	2.6	3.0	4.6	5.1	6.4

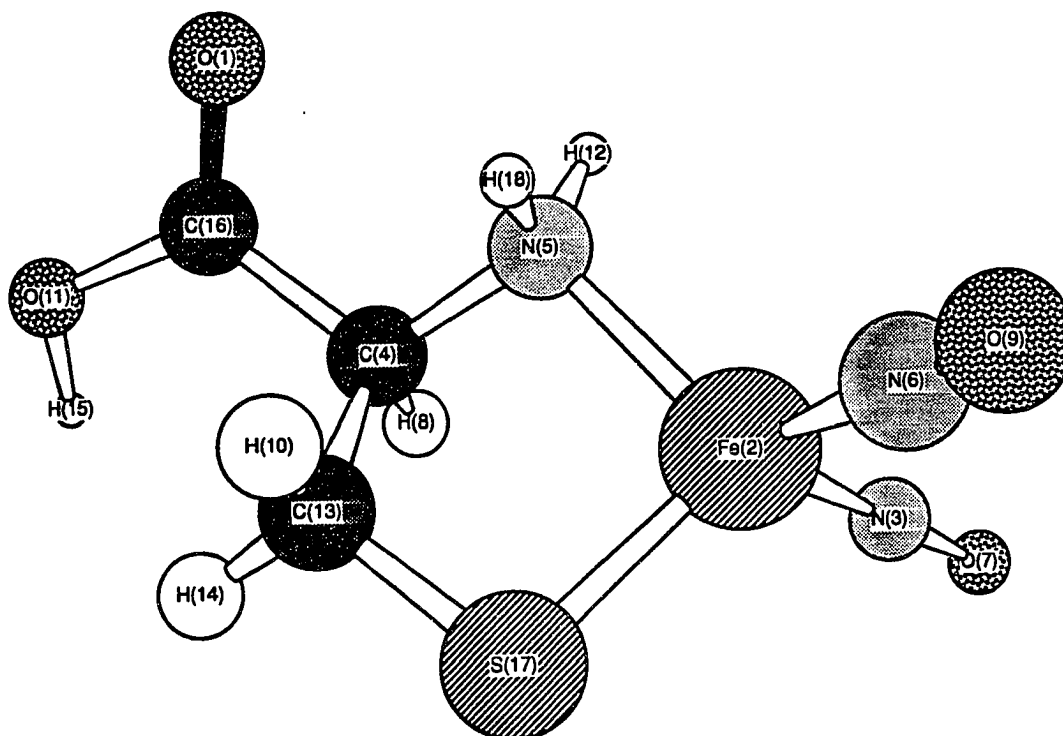


Figure 4.24 (b) Molecular modeling structure of Fe-NO-Cys complex. (cys4.c3d)

Fe-NO-Cys (Amino and sulfur groups binding)

Proton Number	12, 18	8	14	10
Iron-proton distances (Å)	2.6	3.0	3.5	4.0

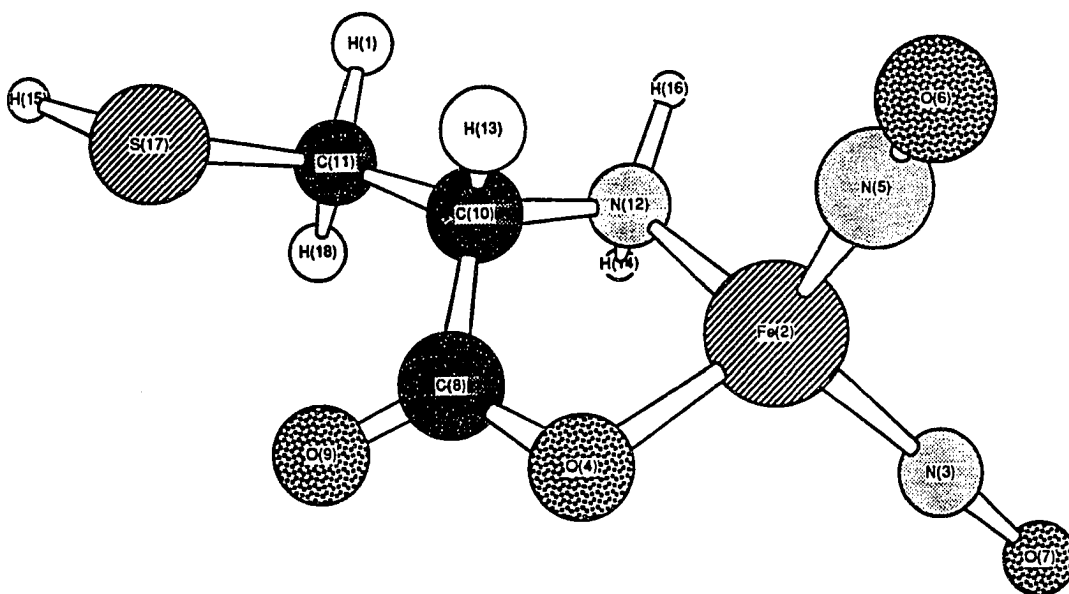


Figure 4.24 (c) Molecular modeling structure of Fe-NO-Cys complex. (cys4.c3d)

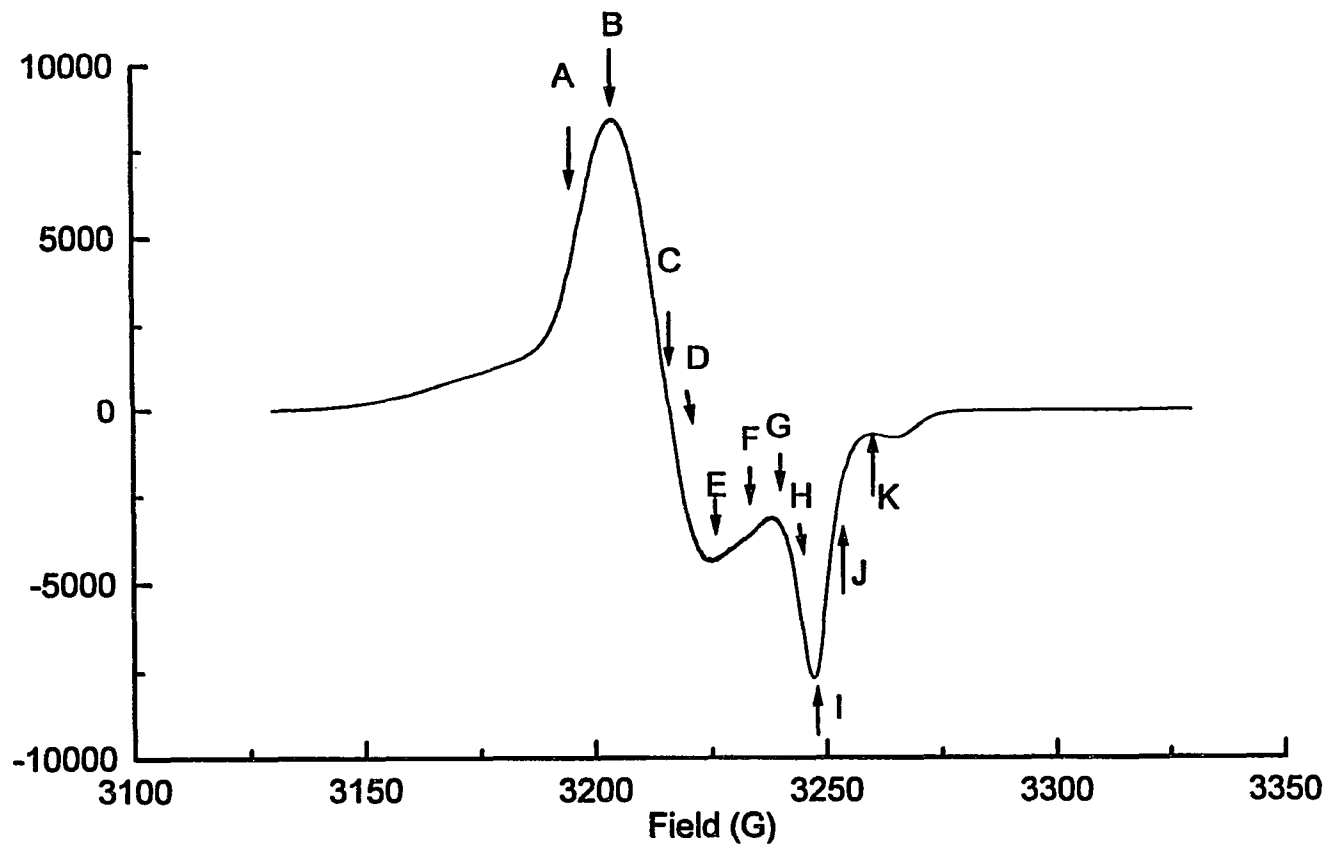
Fe-NO-Cys (Amino and carboxyl groups binding)

Proton Number	14, 16	13	1, 18
Iron-proton distances (Å)	2.6	3.0	4.5

two couplings observed at field setting A, while four couplings become resolved when the magnetic field moves to the low field turning point B, which corresponds to molecules with their  $g_z$  axis parallel to the external magnetic field direction. The coupling of 3.05 MHz resolved at field position B is the largest coupling of all and is therefore assigned to the protons on the amino group (H13, H14, H25 and H30 in (a), H12 and H18 in (b), and H14 and H16 in (c)), which are the closest protons to the Fe center at these structure settings. The coupling of 2.0 MHz is tentatively assigned to the protons on the CH group adjacent to  $\text{NH}_2$  group (i.e. H15, H26 in (a), H8 in (b) and H13 in (c)). The couplings of 1.03 MHz and 1.44 MHz are likely due to the  $\text{CH}_2$  protons adjacent to the amino group. All of the structures presented above are more or less in accordance with the ENDOR data. At the present stage, the  $^1\text{H}$  ENDOR data alone do not enable us to unequivocally identify the structure of Fe-NO-Cys at frozen state.

#### Fe-NO-Pen

X-band proton ENDOR spectra of Fe- $^{14}\text{NO}$ -Pen with magnetic fields set at various places along the EPR envelope (Fig. 4.25) are illustrated in Figure 4.26 and the hyperfine couplings are listed in Table 4.4.



121

Figure 4.25 EPR spectrum of Fe-<sup>14</sup>NO-Pen (pH = 6) at 77 K. Experimental conditions: Field Set, 3225 G; Scan range, 200 G; Microwave Frequency, 9.11 GHz; Microwave power, 5 mW; Modulation Frequency, 100 kHz; Modulation Amplitude, 1 G; Receiver Gain, 125; Time Constant, 0.1 s; Scan time = 4min. File name: 081095a3.flc. (pen100k.the)

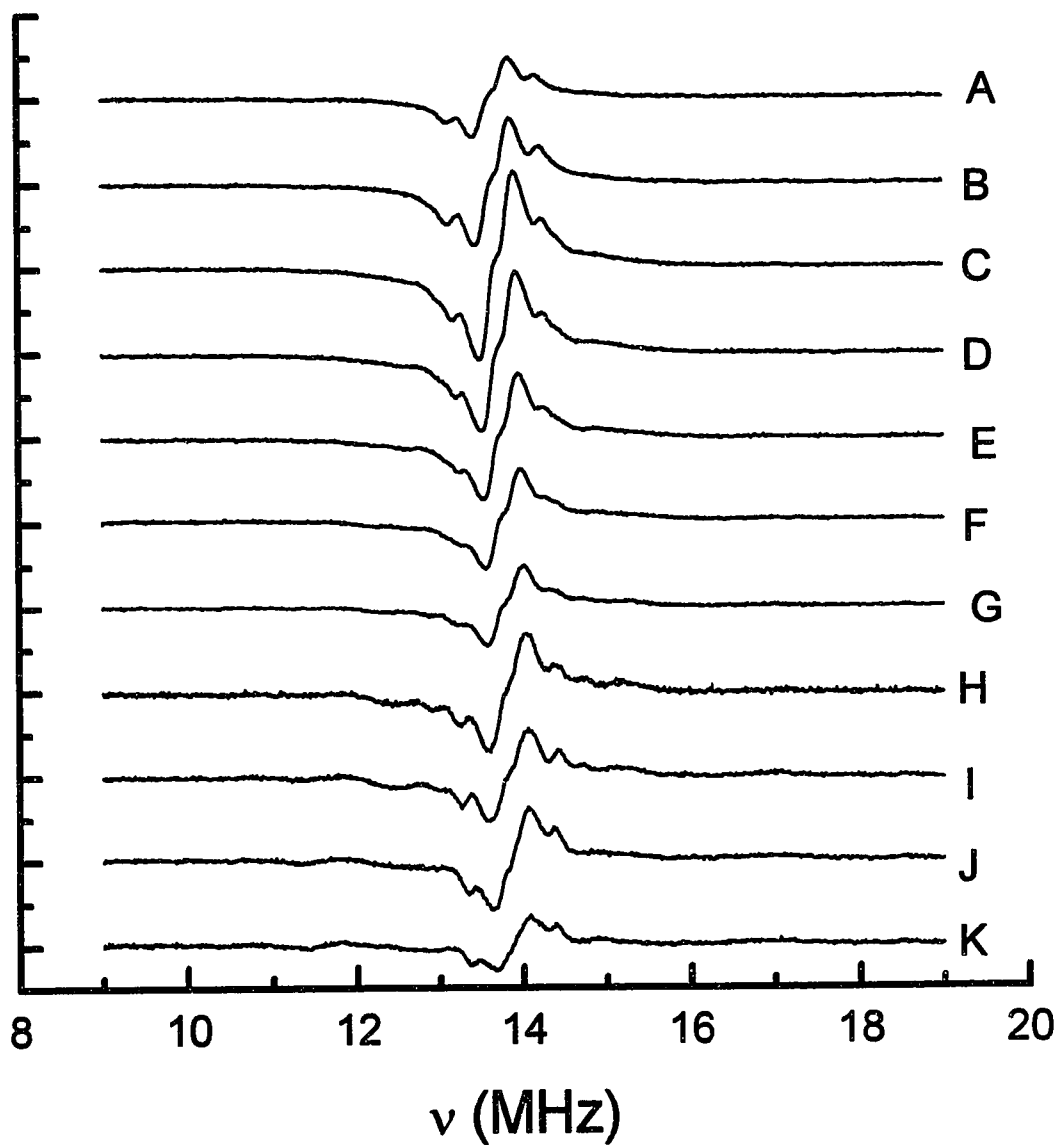


Figure 4.26 Frequency modulation X-band  $^1\text{H}$  ENDOR of 20 mM  $\text{Fe-}^{14}\text{NO-Pen}$  complex at  $\text{pH} = 6$ . Experimental conditions: Microwave Frequency, 9.154 GHz; Microwave power, 2 mW; Modulation Frequency, 10 kHz; Modulation Amplitude, 100 kHz; Temperature, 30 K; Time Constant, 0.03 s; radio frequency power, 100 W; radio frequency scan rate, 0.25 MHz/s. (hendor.pen).

Table 4.4 Proton hyperfine couplings (MHz) of penicillamine.

Spectrum	Field (G)	A (MHz)*		
A	3205	0.21	1.08	
B	3210	0.21	1.14	
C	3220	0.21	1.10	
D	3225	0.21	1.07	2.39
E	3230	0.21	1.04	2.39
F	3235	0.21	1.10	2.01
G	3240	0.21	1.17	1.81      3.09
H	3245	0.21	1.17	1.81      2.69
I	3250	0.21	1.16	1.71      2.74
J	3255	0.21	1.04	(2.94/3.7)
K	3260	0.21	1.03	
(7.18 /9.0) (4.18/5.27) (4.17/3.3)				

\*Data in parentheses are the estimated proton-electron distances in Å under the point dipole interaction approximation assuming the couplings correspond to  $A_{\perp}$  or  $A_{\parallel}$ , respectively.

Well resolved proton hyperfine couplings are observed in all of the spectra. Penicillamine is similar in structure to cysteine, and both Fe-NO-Cys and Fe-NO-Pen complexes show an axial g symmetry with similar g values in frozen conditions. In addition, the  $^1\text{H}$  ENDOR coupling constants of Fe- $^{14}\text{NO}$ -Pen observed here are similar to those of Fe- $^{14}\text{NO}$ -Cys. Thus, it is safe to assume that the structures of Fe-NO-Cys and Fe-NO-pen are similar; amino group binding and/or carboxyl binding may take place in Fe-NO-Pen as well. Figure 4.27 shows the molecular modeling structure based on this assumption, again (a) is for the structure of amino groups binding, (b) bidentate binding from both amino and sulfur groups and (c) bidentate binding



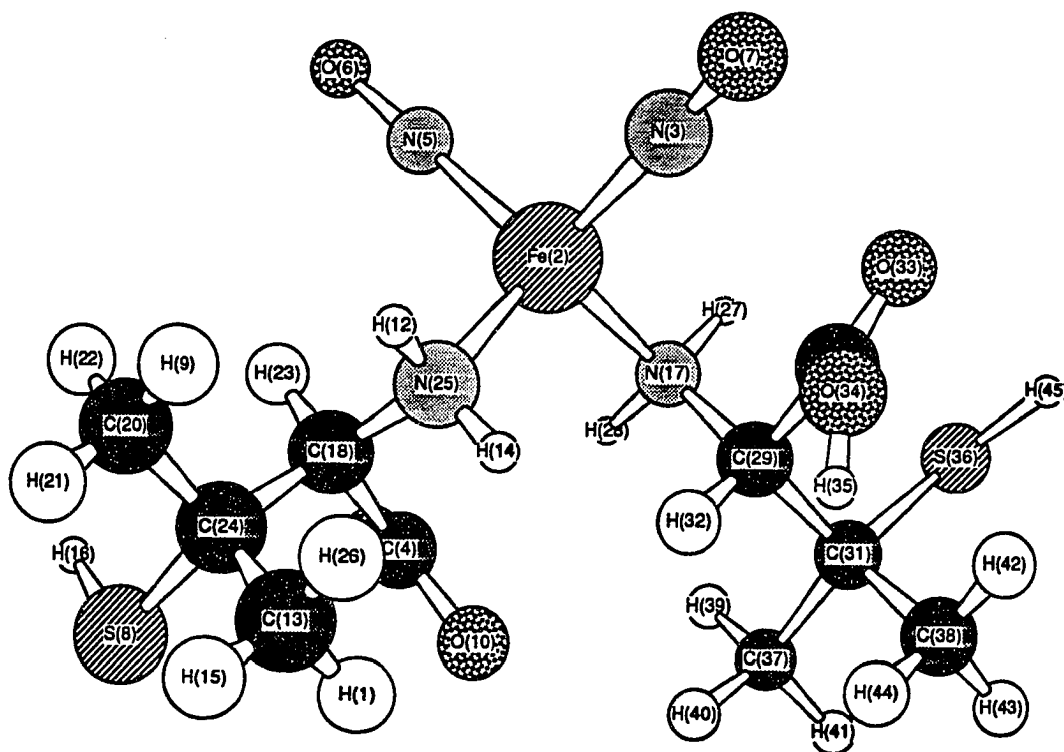


Figure 4.27 (a). Molecular modeling structure of Fe-NO-Pen complex. (Peni2.c3d)

Fe-NO-Pen (Amino groups binding)

Proton Number	12, 14, 27, 28	23, 32	9, 26, 39, 44	1, 22, 40, 42	15, 21, 41, 43, 16, 45
Iron-proton distances (Å)	2.6	2.9	4.6-4.7	4.9-5.0	6.0

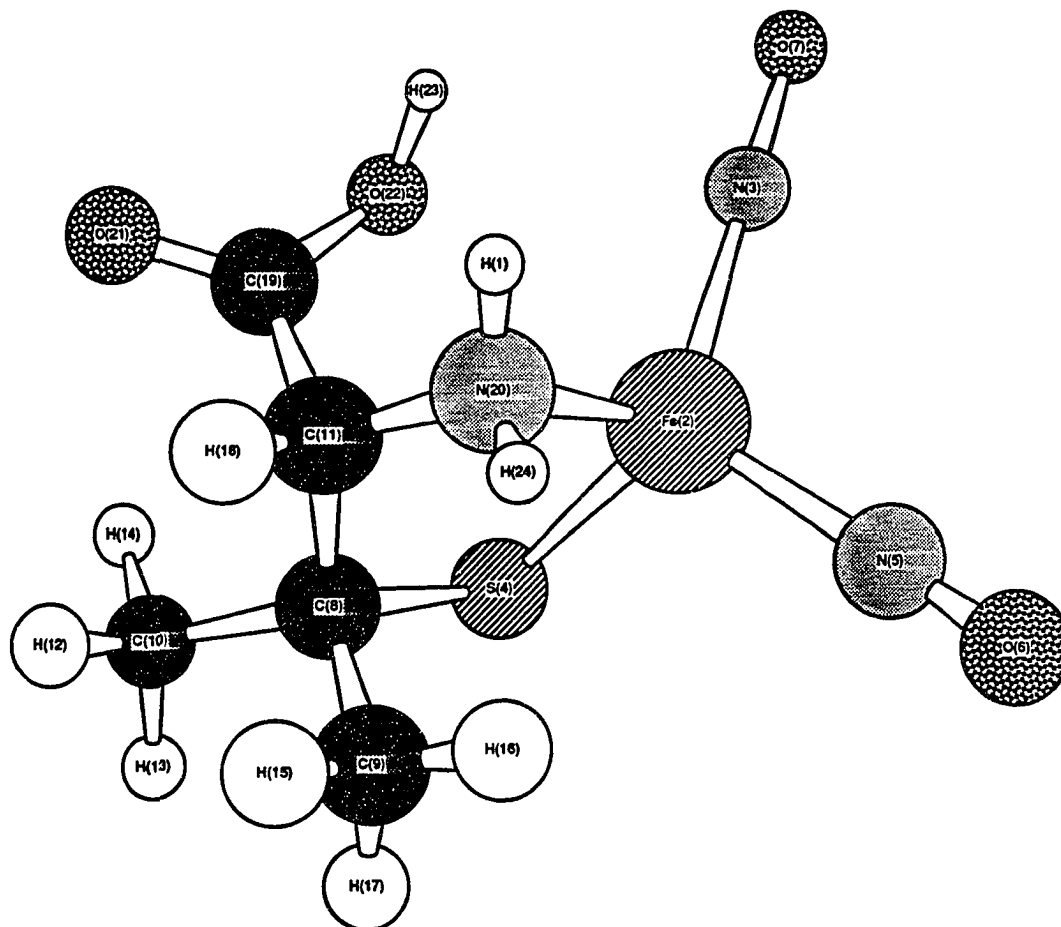


Figure 4.27 (b). Molecular modeling structure of Fe-NO-Pen complex. (Peni2.c3d)

Fe-NO-Pen (Amino and sulfur group binding)

Proton Number	1, 24	18	16	13, 14, 17	12, 15
Iron-proton distances (Å)	2.6	3.9	3.1	4.4	5.0

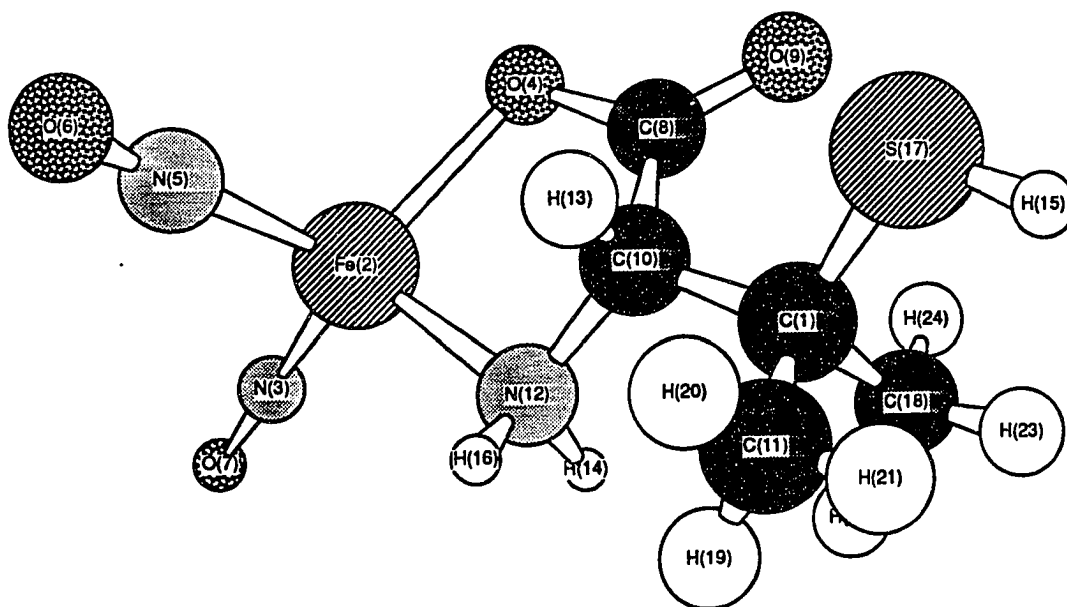


Figure 4.27 (c). Molecular modeling structure of Fe-NO-Pen complex. (Peni2.c3d)

Fe-NO-Pen (Amino and carboxyl group binding)

Proton Number	16, 14	13	19, 20, 22, 24	21, 23
Iron-proton distances (Å)	2.6	2.9	4.8	5.9

from both amino and carboxyl groups. Similarly, we assign the coupling of 2.69-3.09 MHz in the last column in Table 4.4 to the amino group protons (H12, H14, H27 and H28 in (a), H1, H24 in (b), and H14, H16 in (c)). The couplings of 1.71-2.39 MHz (the third column of Table 4.4) are most likely due to the protons on the CH group of penicillamine (H23 and H32 in (a), H13 in (c)). In structure (b), however, both H16 from CH<sub>3</sub> group and H18 from CH group might be responsible for this coupling. Finally, the coupling around 1 MHz can be assigned to protons from CH<sub>3</sub> groups in the complex. Further support for the assignment is also provided by the proton ENDOR measurements on the sample made in D<sub>2</sub>O with magnetic field set at position G (Figure 4.28). If the previous assignment is true, the couplings from the nonexchangeable protons on CH (1.7-2.4 MHz) and CH<sub>3</sub> (~ 1 MHz) group should remain, while the coupling assigned to NH<sub>2</sub> protons (2.7 - 3.09 MHz) should disappear upon D<sub>2</sub>O exchange. This is what is observed in the <sup>1</sup>H ENDOR spectrum of the Fe-<sup>14</sup>NO-Pen sample in D<sub>2</sub>O, in which only couplings of 0.9 MHz and 1.73 MHz are observed. A matrix <sup>1</sup>H ENDOR is also observed in the spectrum; the amplitude of which is about 10 % of that in the H<sub>2</sub>O sample. Since the abundance of H<sub>2</sub>O in D<sub>2</sub>O solvent is about 1%, We therefore conclude that this matrix line in the D<sub>2</sub>O sample is predominantly due to the

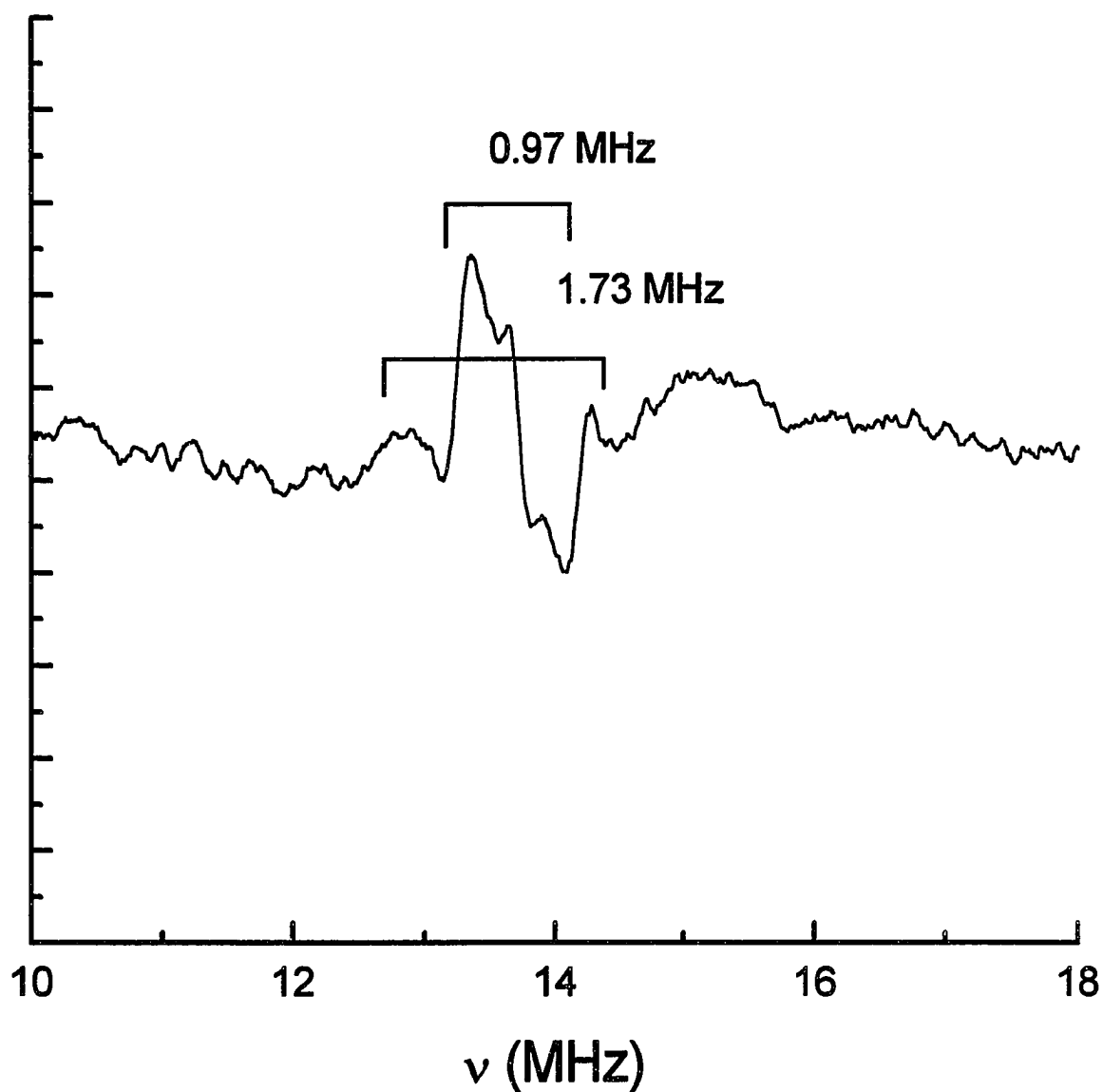


Figure 4.28 X-band 1H ENDOR of Fe-<sup>14</sup>NO-Pen in D<sub>2</sub>O (pD = 6.6). Experimental conditions: Microwave power = 4 mW; Microwave frequency = 9.167 GHz; other conditions are the same as in figure 4.22. File name: 081095c2.fl.s. (dendor.pen)

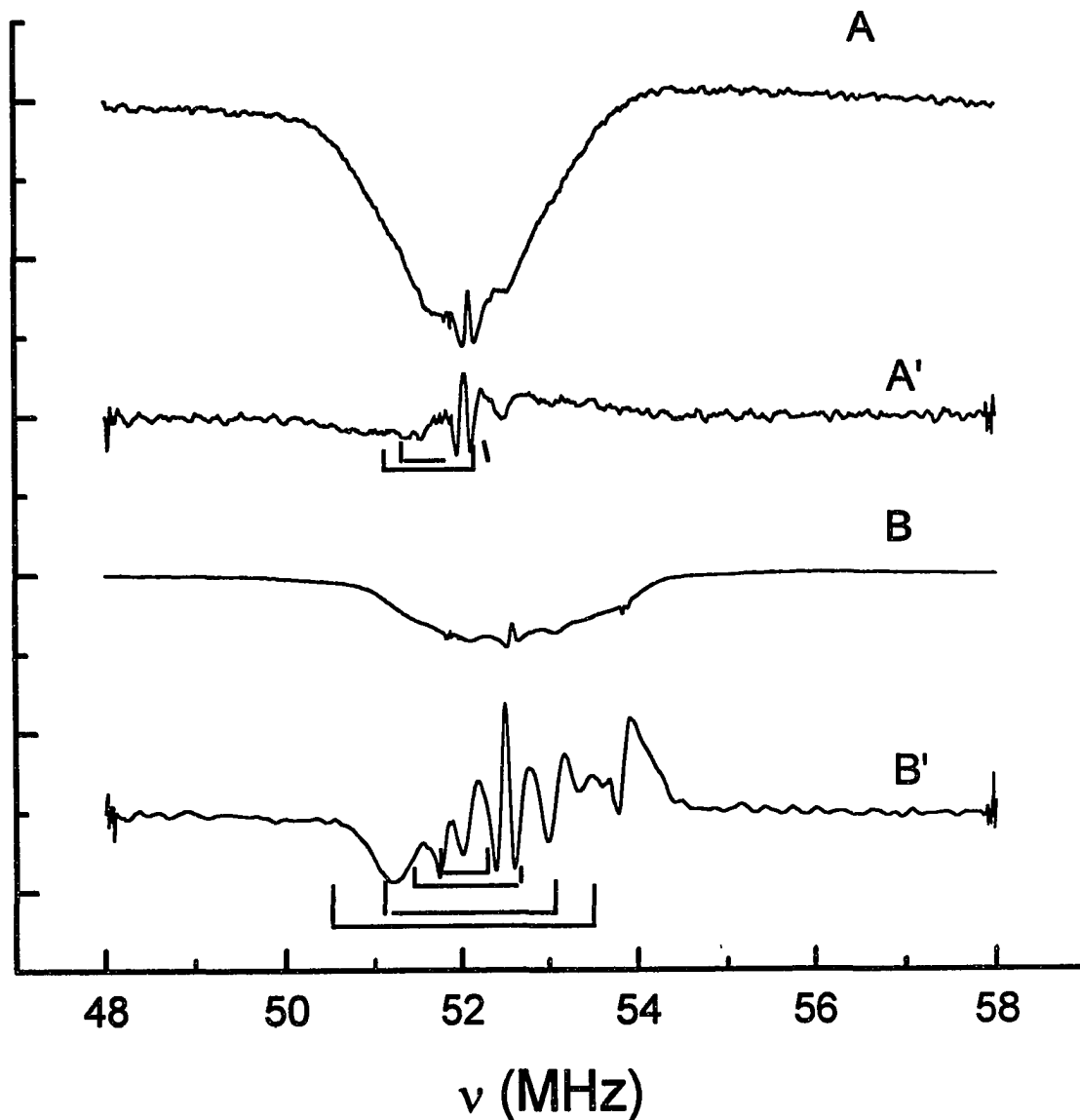


Figure 4.29. Field modulation Q-band  $^1\text{H}$  ENDOR of 20 mM Fe- $^{14}\text{NO}$ -Pen pH = 6 with the magnetic field set at varies positions along the EPR envelope indicated in figure 4.25. Experimental conditions: Temperature, 7.0 K; Microwave Frequency, 34.742 GHz; Microwave power, 1 mW; Modulation Frequency, 100 kHz; Modulation Amplitude, 0.5 G; Receiver Gain, 12.5; Time Constant, 0.01 s; radio frequency power, 50 W; radio frequency scan rate, 0.5 MHz/s; (File name: qendor.the)

nonexchangeable protons in the complex, e.g. protons from  $\text{CH}_3$  protons. The coupling constants expected for these protons, based on their distances from the Fe, are between 0.18 MHz to 0.62 MHz, which are within the line width of the proton matrix ENDOR signal ( $\sim 1$  MHz).

We also performed Q-band proton ENDOR measurement on Fe- $^{14}\text{NO}$ -Pen sample. Figure 4.29 shows Q-band dispersion mode proton ENDOR spectra taken at magnetic field positions A ( $g_{\perp}$ ) and B( $g_{\parallel}$ ), as indicated in the EPR envelope (Figure 4.30). To better resolve the hyperfine structure, the first derivative of each spectra is also taken after doing a 25 point software smoothing of the original spectra and displayed as A' and B', respectively. Again, hyperfine couplings are listed in Table 4.5

Table 4.5 Proton hyperfine couplings (MHz) of penicillamine from Q-band dispersion mode field modulation ENDOR.

Spectrum	Field (G)	A (MHz)			
A	12240	0.22	1.11		
B	12350	0.22	1.13	1.76	2.70

A and B correspond to positions C and I in Figure 4.25, respectively. Our Q-band ENDOR results are in substantial agreement with those of X-band, indicating all the hyperfine couplings observed at X-band are, indeed, solely from protons, since the region of nitrogen hyperfine couplings

should be well below 50 MHz at Q-band.

Fe-NO-Im

Figure 4.31 illustrates a series of X-band <sup>1</sup>H ENDOR spectra of Fe-<sup>14</sup>NO-Im measured at various positions along the envelope of a frozen solution spectrum shown in Figure 4.32.

All the spectra show clearly resolved hyperfine structures and the coupling constants from these spectra were measured and tabulated in Table 4.6.

Table 4.6 Proton hyperfine couplings (MHz) of Fe-<sup>14</sup>NO-Im complex

Field (G)	A (MHz)*			
3185	0.33		2.78	3.5
3190	0.33		2.78	3.5
3195	0.22	0.82	2.87	3.5
3205	0.24	0.82	2.87	3.52
3210	0.24	0.82	2.87	3.52
3215	0.21	0.78	2.78	
3.47				
		(4.6/5.8)		
3220	0.22	1.82	2.63	3.44
3225	0.32	1.83	2.64	3.42
3230	0.33	1.85	2.57	3.42
3235	0.325	1.76	2.57	3.38
3240	0.34	1.72	2.57	3.38
3245	0.34	1.72	2.54	3.32
3250	0.34	1.72	2.54	3.32
3255	0.34		2.48	3.3
	(6.2/7.8)	(3.6/4.5)	(3.0/4.0)	(2.9/3.6)

\*Data in parentheses are the estimated proton-electron distances in Å under the point dipole interaction approximation assuming the couplings correspond to A<sub>⊥</sub> or A<sub>∥</sub>, respectively.



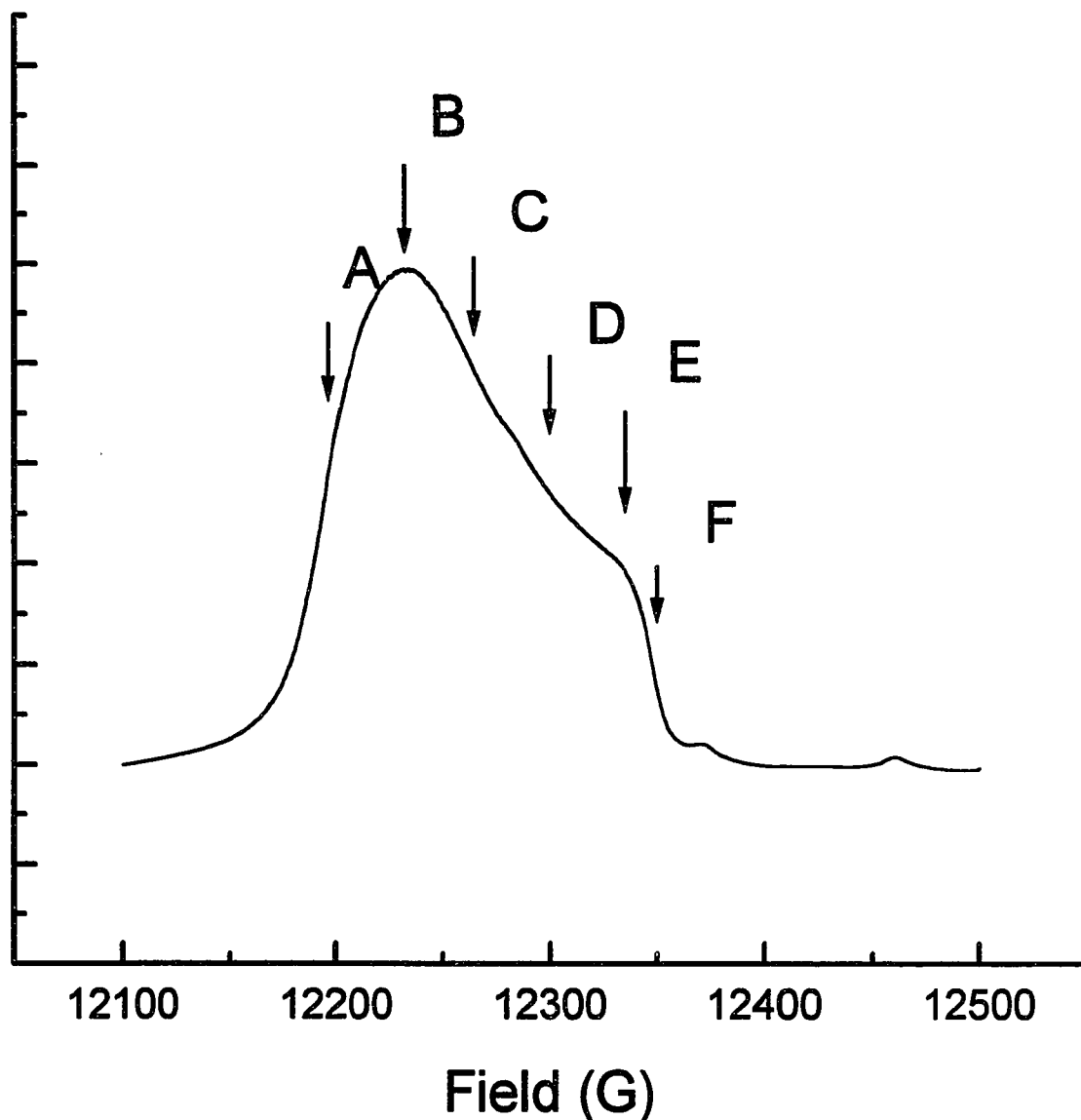


Figure 4.30: EPR spectrum of 20 mM Fe-<sup>14</sup>NO-Pen (pH = 6) at 7 K. Experimental conditions: Field Set, 12300 G; Scan range, 400 G; Microwave Frequency, 34.742 GHz; Microwave power, 1 mW; Modulation Frequency, 100 kHz; Modulation Amplitude, 2 G; Receiver Gain, 2; Time Constant, 0.03 s; Scan time = 4 min. File name: 072095a1.fl.s. (qepr.the).

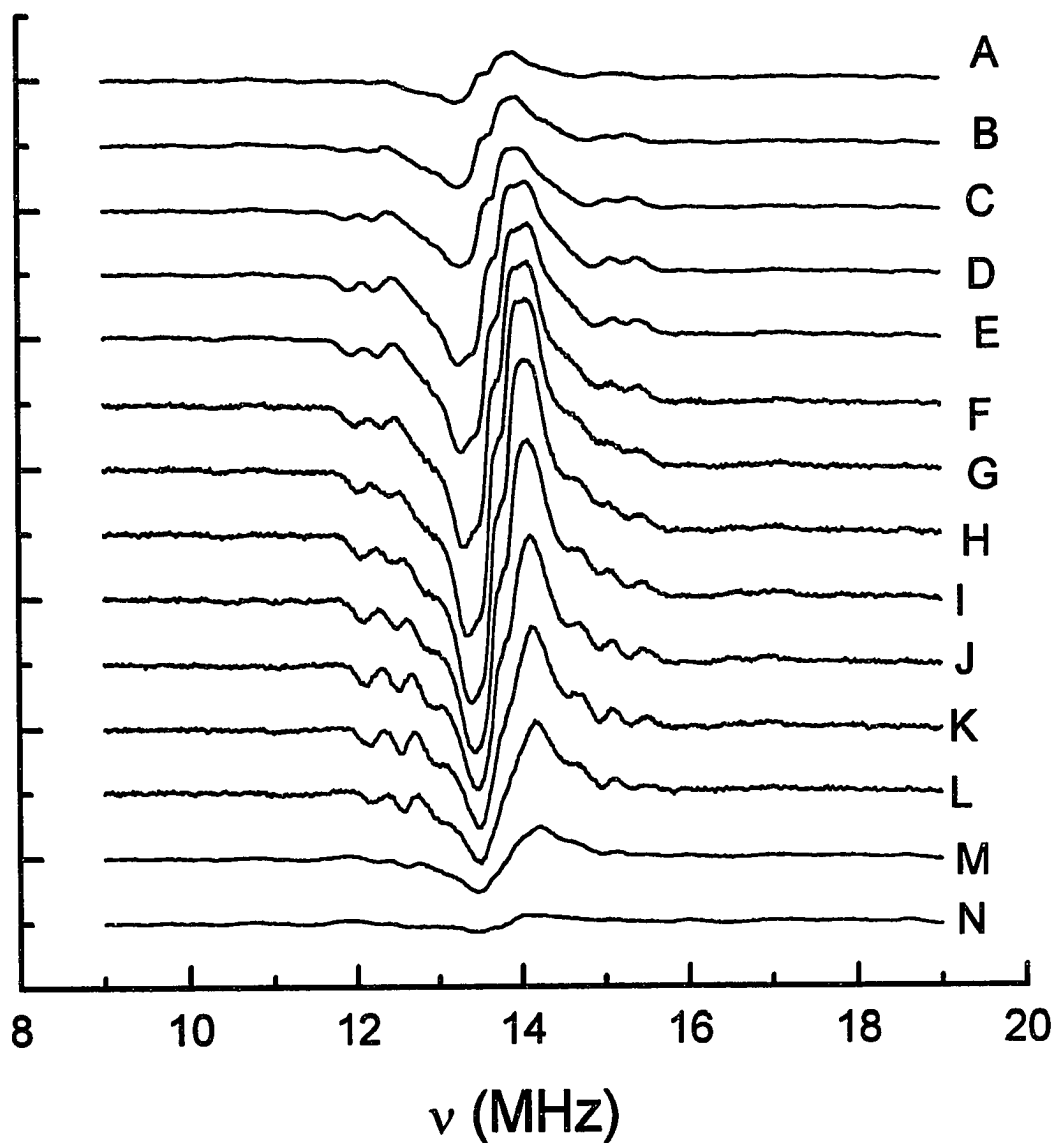


Figure 4.31: Frequency modulation X-band  $^1\text{H}$  ENDOR of 20 mM  $\text{Fe-}^{14}\text{NO-Im}$  (pH = 6) with the magnetic field set at varies positions along the EPR envelope indicated in figure 4.27. Experimental conditions: Temperature, 33 K; Microwave Frequency, 9.156 GHz; Microwave power, 5 mW; Modulation Frequency, 10 kHz; Modulation Amplitude, 100 kHz; Receiver Gain, 5000; Time Constant, 0.01 s; radio frequency power, 50 W; radio frequency scan rate, 0.25 MHz/s; (hendor.im)

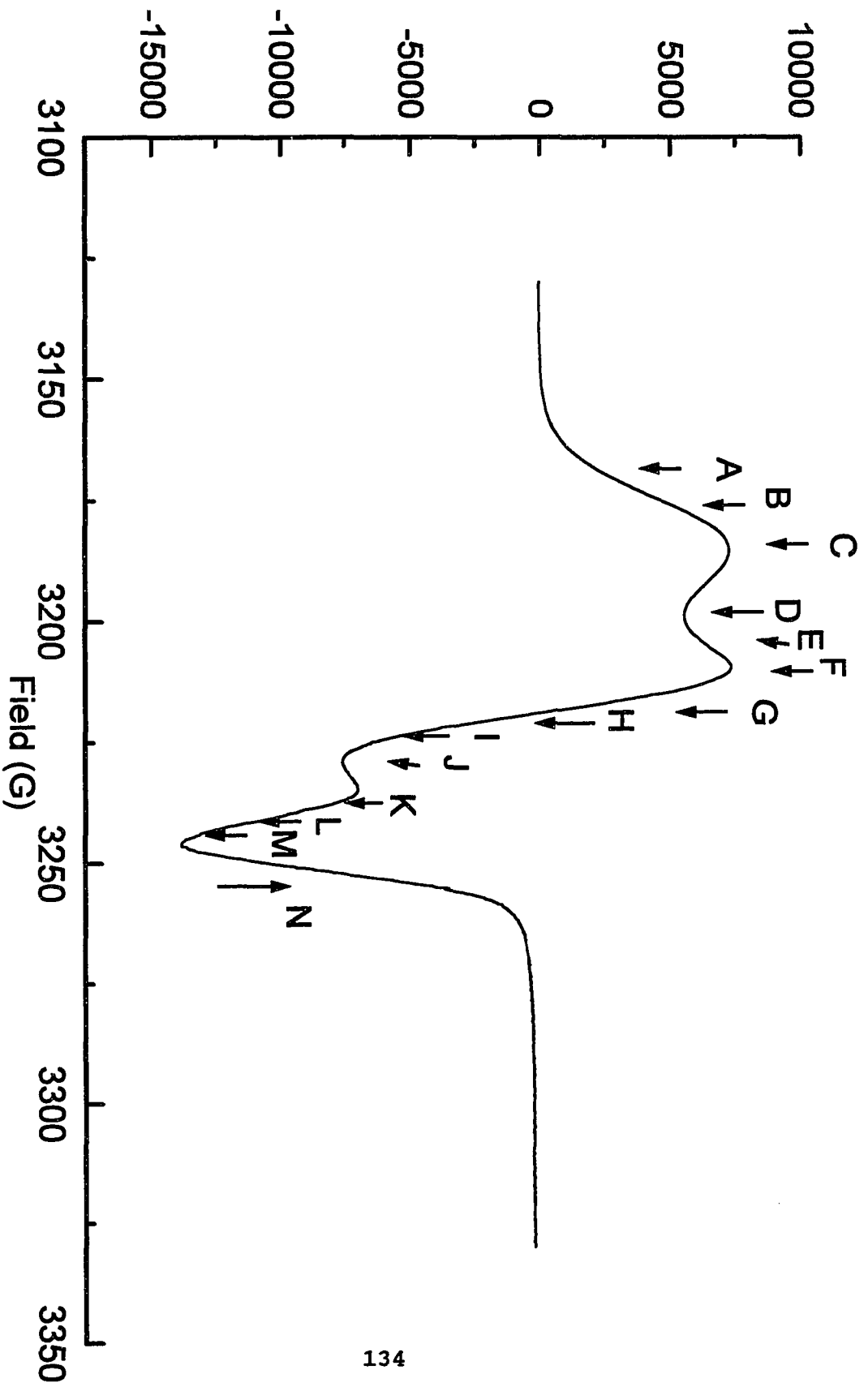


Figure 4.32: EPR spectrum of Fe-<sup>14</sup>NO-Im complex (pH = 6 ) at 100 K. (im100k.the)

Previous EPR studies (77) suggest that in Fe-NO-Im complex the four binding elements are four nitrogen atoms, two from NO molecules and two from imidazole molecules. Thus the four hyperfine couplings observed in the  $^1\text{H}$  ENDOR spectra are presumably due to the four H's on the imidazole ring. This has been confirmed by the ENDOR measurement made on the same sample diluted with  $\text{D}_2\text{O}$  (Figure 4.33), which shows a sharp reduction in intensity of the proton matrix line, and a noticeable decrease in the 1.82 MHz hyperfine line after correction for the dilution. The coupling of 1.82 MHz is most likely due to NH protons on the imidazole rings, based on the calculated distances from the molecular modeling and dipole-dipole interaction calculation. The decrease in intensity of this coupling is presumably due to the partial exchange of H's with  $\text{D}_2\text{O}$  solvent. The rest of the hyperfine lines, which are due to nonsolvent exchangeable protons on the imidazole ring, remain the same as expected. Judging from the fact that only four proton ENDOR lines are observed, we conclude that the N3 atom on the imidazole ring (Fig. 4.1) is the binding site for imidazole in Fe-NO-Im complex. Moreover, it also reflects a high degree of structural order in the complex. In other words, both imidazole ligands appear to have about the same orientation with respect to the symmetry axis of the

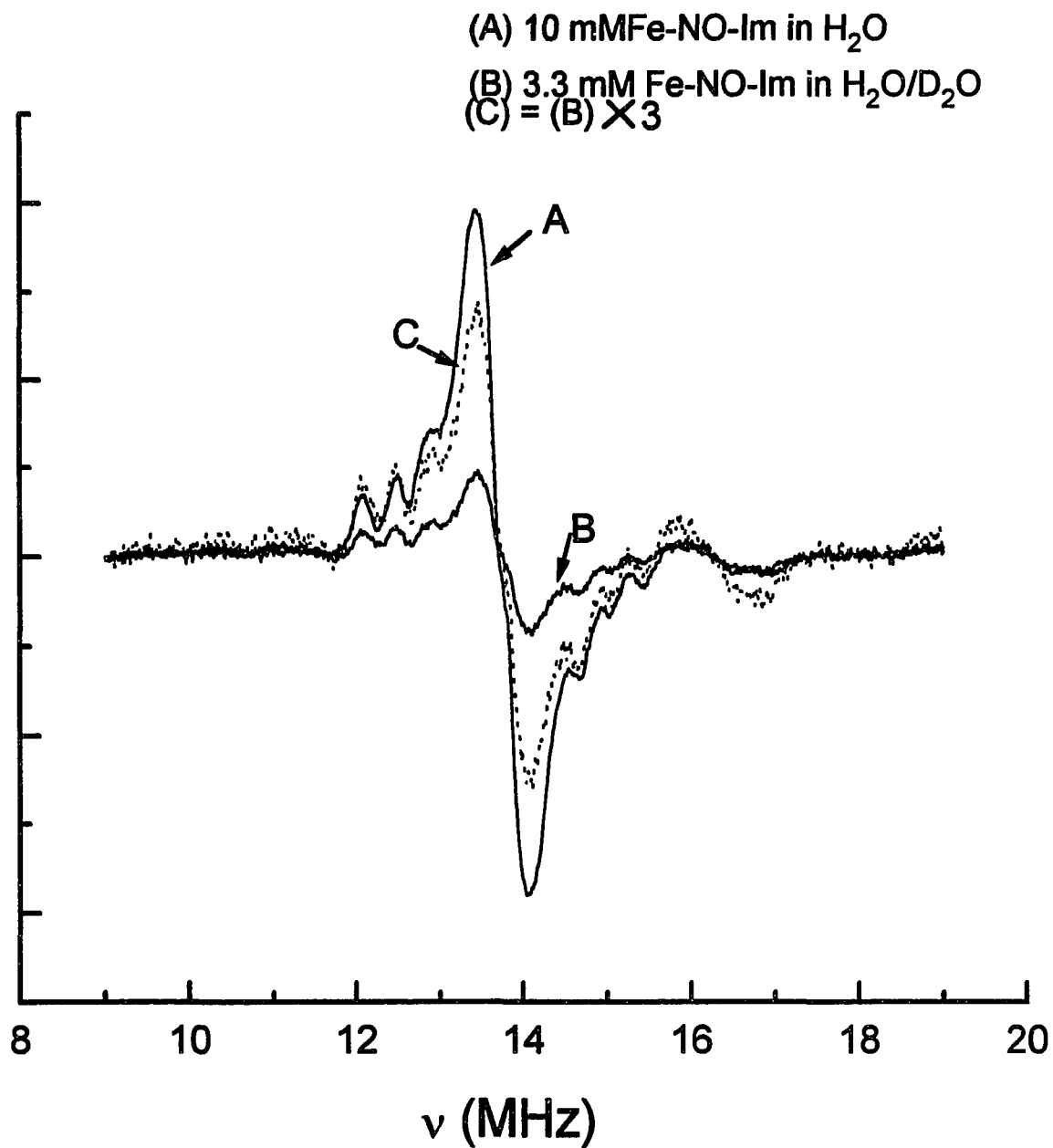


Figure 4.33: X-band <sup>1</sup>H ENDOR of Fe-<sup>14</sup>NO-Im after 3:1 dilution with D<sub>2</sub>O at 30 K. Experimental conditions are the same as in figure 4.26. (imhd.the)

complex, but there might be a small spread of orientations of imidazole ring in the molecular frame of the complex, as suggested by the slightly broadened hyperfine lines in Figure 4.31. Figure 4.34 depicts the molecular modeling structure based on the above conclusions. The proton distances obtained from the dipole-dipole interaction calculation agree reasonably well with that from the molecular modeling results. Also, it is of interest to note that the hyperfine couplings obtained here are similar to those obtained for the vanadyl imidazole sample (Figure 4.35), which suggests that the protons of imidazole in both complexes probably have about the same spin density and/or the same distance from the spin center.

It is noteworthy that the hyperfine couplings of about 0.21 MHz, consistently seen for all the thiol complexes, is not observed for the imidazole complex. This suggests that there are no distal protons, either from H<sub>2</sub>O or a OH group, coupled to the spin center, at least not within the range of proton distance and/or instrumental sensitivity that can be detected with the present ENDOR spectrometer.

### **Conclusions**

We have performed EPR and ENDOR investigations of model

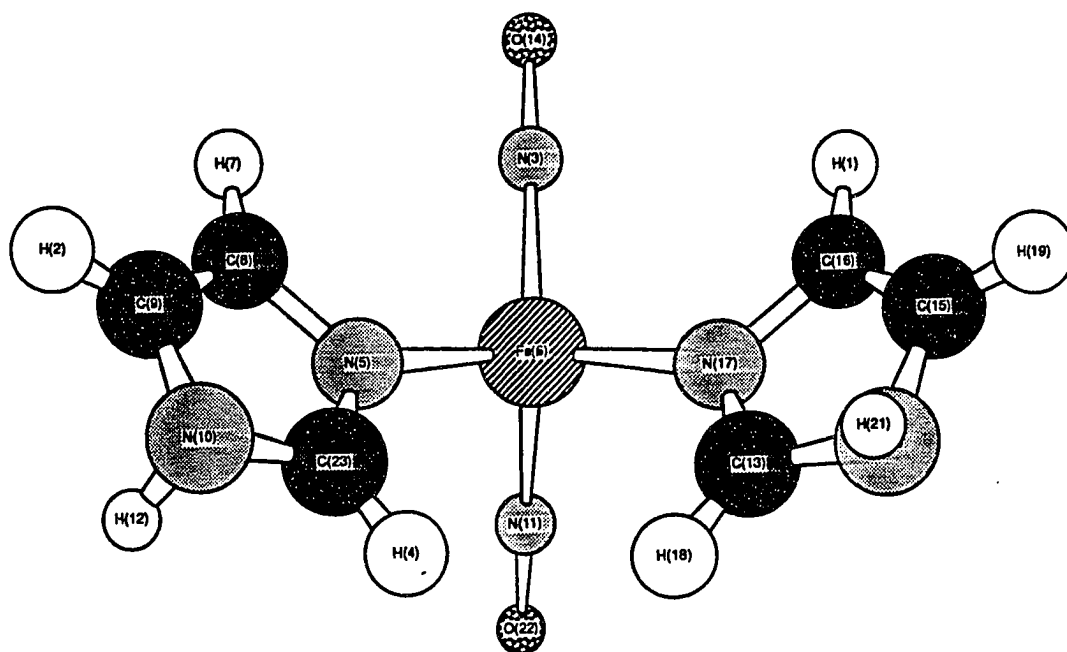


Figure 4.34: Molecular modeling structure of Fe-NO-Im complex. (imidazole.c3d)

Fe-NO-Im

Proton Number	4, 18	1, 7	12, 21	2, 19
Iron-proton distances (Å)	3.2	3.4	4.9	5.2

Summary of proton ENDOR couplings for  $\text{VO}(\text{Im})_4^{2+}$  complex

Proton positions	2	4	1	5
$A_{\perp}$	3.06 (3.37)	2.42 (2.51)	0.48 (<0.8)	0.48 (<0.8)*
$A_{\parallel}$	2.52 (2.37)	2.52 (2.37)	0.4 (<0.8)	0.4 (0.75)

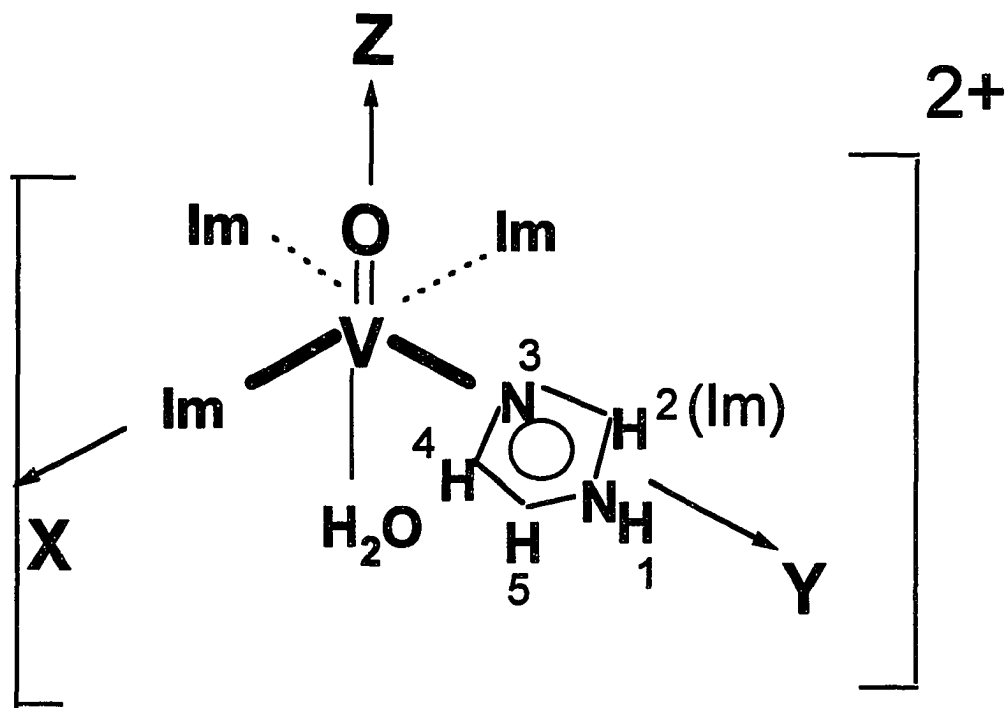


Figure 4.35: Summary of proton ENDOR hyperfine couplings in  $\text{VO}(\text{Im})_4^{2+}$  and the structure of  $\text{VO}(\text{Im})_4^{2+}$  complex. Data in parentheses are the proton hyperfine couplings of the same sample obtained by Mulks and coworkers (43). (coupling.sem)



complexes and have focussed our work on the reexamination of the structure of model compounds studied previously by earlier workers using EPR alone (77,81,83). We also have assigned some of the  $^1\text{H}$  resonances with reasonable certainty. The data indicate that assignment of axial EPR spectra to thiol coordination in every instance cannot be correct. In the case of cysteine and penicillamine, a structural rearrangement occurs upon freezing the sample. According to our later EPR and ENDOR study of dinitrosyl iron complexes with amino ethanethiol (Appendix I), bidentant binding of through the thiol and amino groups appears to take place with cysteine and penicillamine.

Except for the Fe-NO-Pen and Fe-NO-Im complexes, it is still not clear at this stage whether two NO molecules remain bound to Fe for the above nitrosyl iron complexes, and also what is the donor groups from the ligands other than NO in the complexes. Nitrogen ENDOR will be needed to clarify these questions. However, we have not yet been able to obtain CW nitrogen ENDOR for any of these complexes. The observation of low  $\gamma$  nuclei by CW-ENDOR is often difficult and we assume that is the problem here. Pulsed ENDOR (84-88) measurements, which are on the way, should provide the elusive  $^{14,15}\text{N}$  signals of NO and the amino groups of penicillamine and cysteine.

## REFERENCES

1. M. W. Makinen, G. B. Wells, in *Metal Ions in Biological Systems*. Vol.22. *ENDOR, EPR, and Electron Spin Echo for Probing Coordination Spheres*, H. Sigel, Ed. (Marcel Dekker, Inc., New York, 1987), p. 129.
2. J. G. DeWitt, J. G. Bentsen, A. C. Rosenzweig, B. Hedman, J. Green, et al, *J. Am. Chem. Soc.* **113**, 9219 (1991).
3. L. J. Berliner, H. Fujii, in *Biological Magnetic Resonance, Volume 11: In Vivo Spectroscopy*, L. J. Berliner and J. Reuben, Eds. (Plenum Press, New York, 1992), p. 307.
4. S. A. Dzuba, Y. A. Golovina, Y. D. Tsvetkov, *J. Magn. Resonance Ser. B* **101**, 217 (1993).
5. G. R. Eaton, *Biophys. J.* **64**, 1373 (1993).
6. A. Iannone,, A. Tomasi,, V. Quaresima,, M. Ferrari,, *Res. Chem. Intermediates* **19**, 715 (1993).
7. E. Bill,, *Hyperfine Interactions* **90**, 1 (1994).
8. M. W. Makinen, D. Mustafi, in *Metal Ions in Biological Systems*. Volume 31. *Vanadium and Its Role in Life*, H. Sigel and A. Sigel, Eds. (Marcel Dekker, Inc., New York, 1995), p. 89.
9. N. D. Chasteen and P. A. Snetsinger, "ESEEM and ENDOR Spectroscopy" in *Physical Methods in Inorganic and Bioinorganic Chemistry*, L. Que (ed.), University Science Books, Mill Valley, California, in press.
10. N. S. Dalal, D. E. Kennedy, C. A. McDowell, *J. Chem. Phys.* **59(6)**, 3403 (1973).
11. S. P. Greiner, D. L. Rowlands, R. W. Kreilick, *J. Phys. Chem.* **96**, 9132 (1992).
12. J. Rautter, C. Gessner, F. Lendzian, W. Lubitz, J. C. Williams, et al, in *The Photosynthetic Bacterial Reaction Center II*, J. Breton and A. Verméglio, Eds. (Plenum Press, New York, 1992), p. 99.
13. K. Doi, J. McCracken, J. Peisach, P. Aisen, *J. Biol. Chem.* **263**, 5757 (1988).

14. D. J. Lowe, *Prog. Biophys. Mol. Biol.* **57**, 1 (1992).
15. S. P. Greiner, M. Baumgarten, *J. Magn. Reson.* **83**, 630 (1989).
16. L. Keven and L. D. Kispert "Electron Spin Double Resonance Spectroscopy", p. 28, John Wiley & Sons, N. Y., 1976.
17. T. Cole, T. Kushida, and H. C. Heller, *J. Chem. Phys.*, **38**, 2915 (1963).
18. G. J. Gerfen, B. F. Bellew, S. Un, J. M. Bollinger, J. Stubbe, R. G. Griffin., *J. Am. Chem. Soc.*, **115**, 6420 (1993).
19. T. S. Leyh, P. J. Goodhart, A. C. Nguyen, G. L. Kenyon, and G. H. Reed, *Biochemistry* **24**, 308 (1985).
20. M. P. Hendrich, L. L. Pearce, L. Que, Jr., N. D. Chasteen, and E. P. Day, *J. Am. Chem. Soc.* **113**, 3039 (1991).
21. R. Bogumil, R. Kappl, J. Huttermann, C. Sudfeldt, and H. Witzel, *Eur. J. Biochem.* **213**, 1185 (1993).
22. M. M. Werst, C. E. Davoust, and B. M. Hoffman, *J. Am. Chem. Soc.* **113**, 1533 (1991).
23. C. Fan, C. M. Gorst, S. W. Ragsdale, and B. M. Hoffman, *Biochemistry* **30**, 431 (1990).
24. M. M. Werst, M. C. Kennedy, H. Beinert, and B. M. Hoffman, *Biochemistry* **29**, 10526 (1990).
25. A. L. P. Houseman, B. H. Oh, C. Fan, M. M. Werst, M. C. Kennedy, H. Beinert, J. L. Markley, and B. M. Hoffman, *Biochemistry* **31**, 2073 (1992).
26. R. J. Gurbiel, J. T. Bolin, A. E. Ronco, L. Mortenson, B. M. Hoffman, *J. Magn. Reson.* **91**, 227 (1991).
27. R. Bogumil,, R. Kappl,, J. Hutterman, C. Sudfeldt,, *Eur. J. Biochem.* **213**, 1185 (1993).
28. R. G. Bennett, P. C. Hoell and R. P. Schwenker, *Rev. Sci. Instrum.* **29**, 659 (1958).
29. J. Lambe and R. Ager, *Rev. Sci. Instrum.* **30**, 599

(1959).

30. W. Froncisz, T. Oles, and J. S. Hyde, *Rev. Sci. Instrum.* **57**, 1095 (1986).
31. J. E. Wertz and J. R. Bolton, "*Electron Spin Resonance*", McGraw-Hill Book Co., N.Y. 1972, p. 25.
32. Bureau of Naval Personnel, "*Second Level Basic Electronics*", Dover Publications, N. Y. 1984, p134.
33. C. P. Poole, Jr., "*Electron Spin Resonance*", 2nd Ed., John Wiley & Sons, N. Y., 1983, p135.
34. D. P. Dalal, S. S. Eaton, and G. R. Eaton, *J. Magn. Reson.* **44**, 415 (1981).
35. J. P. Hornak, J. H. Freed, *J. Magn. Reson.* **62**, 311 (1985).
36. M. Ono, T. Ogata, K. C. Hsieh, M. Suzuki, E. Yoshida, et al, *Chem. Lett.* 491 (1986).
37. J. S. Hyde, W. Froncisz, in *Advanced EPR: Applications in Biology and Biochemistry*, A. J. Hoff, Ed. (Elsevier, New York, 1989), p. 277.
38. J. S. Hyde, J. -J. Yin, W. Froncisz, J. B. Feix, *J. Magn. Reson.* **63**, 142 (1985).
39. J. S. Hyde, W. Froncisz, A. Kusumi, *Rev. Sci. Instrum.* **53**(12), 1934 (1982).
40. W. L. Hubbell, W. Froncisz, J. S. Hyde, J. Gajdzinski, T. Oles, et al, *National Biomedical ESR Center Inauguration Workshop* (1989).
41. A. J. Estlin, *Rev. Sci. Instrum.* **33**, 369 (1962).
42. A. R. Cook, L. M. Matarrese and J. S. Wells, *Rev. Sci. Instrum.* **30**, 114 (1963).
43. C. F. Mulks, B. Kirste, and H. van Willigen, *J. Am. Chem. Soc.* **104**, 5906 (1982).
44. S. A. Styring and A. W. Rutherford, *Biochemistry* **27**, 4915 (1988).
45. N. D. Chasteen, "*Biological Magnetic Resonance*", L. J.

- Berliner and J. Reuben, 3rd edition, p. 6, Plenum Press, New York, 1981.
46. G. Hurst, K. Kraft, R. Schultz, and R. Kreilick, *J. Magn. Reson.* **49**, 159 (1982).
  47. H. Yagi, M. Inoue, T. Tatsukawa O. Yaeguchi and S. Kato, *Japan. J. Appl. Phys.* **9**, 1534 (1970).
  48. W. T. Doyle, T. F. Dutton, and H. P. Liu, NOTES
  49. H. L. Van Camp and C. P. Scholes, *Rev. Sci. Instrum.* **47**, 516 (1976).
  50. R. B. Clarkson, R. L. Belford, and C. Reiner, *Rev. Sci. Instrum.* **61**, 3356 (1990).
  51. Bureau of Naval Personnel, "Basic Electronics", p.493, Dover Publications, N. Y. 1972.
  52. J. Lambe, N. Laurance, E. C. McIrvine, and R. W. Terhune, *Phys. Rev.*, **122**, 1161 (1961).
  53. G. Feher, *Phys. Rev.*, **114**, 1219 (1959).
  54. H. Yagi, M. Inoue, T. Tatsukawa and T. Yamamoto, *Japan. J. Appl. Phys.* **9**, 1386 (1970).
  55. W. Wang and N. D. Chasteen, *J. Magn. Reson., Ser. A*, **116**, 237 (1995).
  56. M. J. Nelson, *J. Bio. Chem.* **262**, 12137 (1987).
  57. J. M. Nocek and D. M. Kertz, Jr., *Biochemistry*, **27**, 1014 (1987).
  58. J. M. Nocek, D. M. Kartz, Jr., J. T. Sage, P. G. Debrunner, M. J. Maroney, L. Que, Jr., *J. Am. Chem. Soc.*, **107**, 3382 (1985).
  59. R. S. Magliozzo, J. McCracken, and J. Peisach, *Biochemistry*, **26**, 7923 (1987).
  60. J. S. Stamler, D. G. Singel and J. Loscalzo, *Science*, **258**, 1898 (1992).
  61. N. E. Le Brun, M. R. Cheesman, A. J. Thomson, G. R. Moore, S. C. Andrews, J. R. Guest and P. M. Harrison,

- FEBS*, 323, 261 (1993).
- 62 C. Pellat, Y. Henry, J.-C. Drapier, *Biochem. Biophys. Res. Commun.*, 116, 119 (1990)
- 63 M. A. Marletta, M. A. Tayeh, J. M. Hevel, *Biofactors*, 2, 219 (1990).
- 64 L. J. Ignarro, *Hypertension*, 16, 477 (1990)
- 65 S. M. Moncada, R. M. J. Palmer, E. A. Higgs, *Pharmacol. Rev.*, 43, 109 (1991).
- 66 S. H. Snyder, *Science*, 257, 494 (1992).
- 67 E. Culotta, D. E. Koshland, Jr., *Science*, 258, 1862 (1992).
- 68 D. W. Reif and R. D. Simmons, *Arch. Biochem. Biophys.*, 283, 537 (1990).
- 69 J. C. Drapier, H. Hirling, J. Wietzerbin, P. Kaldy, and L. C. Kuhn, *EMBO J.*, 12, 3643 (1993).
- 70 K. Pantopoulos and M. W. Hentze, *Biochemistry*, 92, 1267 (1995).
- 71 J. C. Drapier, C. Pellat, and Y. Henry, *J. Bio. Chem.*, 266, 10162 (1991).
- 72 W. P. Griffith, J. Lewis, and G. Wilkinson, *J. Chem. Soc.*, 3993 (1958).
- 73 A. Dobry-Duclaux, *Biochim. Biophys. Acta*, 39, 33 (1960)
- 74 P. R. Rich, J. C. Salerno, J. S. Leigh and W. D. Bonner, Jr., *FEBS Letters.*, 93, 323 (1978).
- 75 J. M. Nocek and D. M. Kurtz, Jr., *J. Am. Chem. Soc.*, 107, 3382 (1985)
- 76 Y. Zhang, M. A. Pavlosky, C. A. Brown, *J. Am. Chem. Soc.*, 114, 9189 (1987).
- 77 C. C. McDonald, W. D. Phillips, and H. F. Mower, *J. Am. Chem. Soc.*, 87, 3319 (1965).
- 78 J. C. Wollum, E. Tiezzi and B. Commoner, *Biochim. Biophys. Acta*, 160, 311 (1968).

- 79 M. E. Mullins, C. T. Farrar, N. D. Chasteen, J. S. Stamler, J. Loscalzo, D. J. Singel, and A. R. Barron, *Biochem. Biophys. Acta*, submitted.
- 80 K. A. Pearsall and F. T. Bonner, *Inorg. Chem.*, **21**, 1980 (1982).
- 81 B. L. Burlamacchi, G. Martini, and E. Tiezzi, *Inorg. Chem.*, **8**, 2021 (1969).
- 82 A. F. Vanin, *FEBS Lett.* **289**, 1 (1991)
- 83 M. Lee, P. Arosio, A. Cozzi and N. D. Chasteen *Biochemistry.*, **33**, 3679 (1994).
- 84 C. Gemperle, A. Schweiger, *Chem. Rev.* **91**, 1481 (1991).
- 85 M. Hubrich, G. G. Maresch and H. W. Spiess, *J. Magn. Reson. Ser. A.*, **113**, 177 (1995).
- 86 W. A. J. A. van der Poel, D. J. Singel, J. Schmidt and J. H. van der Waals, *Mol. Phys.*, **49**, 1017 (1983).
- 87 C. Fan, M. C. Kennedy, H. Beinert, and B. M. Hoffman, *J. Am. Chem. Soc.*, **114**, 374 (1992).
- 88 C. Gemperle and A. Schweiger, *Chem. Rev.*, **91**, 1481 (1991).
- 89 D. Mustafi and M. W. Makinen, *Inorg. Chem.* **27**, 3360 (1988).
- 90 J. Huttermann, R. Kappl, in *Metal Ions in Biological Systems, Volume 22. Endor, EPR, and Electron Spin Echo for Probing Coordination Spheres*, H. Sigel, Ed. (Marcel Dekker, Inc., New York, 1987), p. 1.
- 91 D. J. Lowe, *Prog. Biophys. Mol. Biol.* **57**, 1 (1992).
- 92 J. W. Pyrz, J. T. Sage, P. G. Debrunner, L. Que, Jr., *J. Biol. Chem.* **261**, 11015 (1986).

**APPENDIX A**  
**HELIUM FLOW CRYOSTAT OPERATION**

Figure A.1 is a schematic drawing of the 8CC Variable Temperature Helium Flow Cryostat used for low temperature Q-band EPR/ENDOR operations. The temperature is monitored and controlled by a T-2000 Cryo controller (TRI research, Inc., St. Paul, Minnesota), which is attached to the 8 pin ELECTRIC FEEDTHRU (F) (Pin A and B go to the C (Carbon) sensor; pin C - F, to the Pt (Platinum) sensor and pin G and H to the heater). The following is a brief description of the operation procedure for liquid helium temperature experiments.

Evacuation

Both the cryostat and the transfer line need to be pumped to vacuum prior to operation. Overnight pumping is highly recommended. A vacuum of  $10^{-5}$  mTorr or less is achieved using a Varian SD-200 diffusion pump. The sample compartment is also evacuated to about 20 Micron by means of a SD-450 mechanical pump through the PUMPING PORT (B) to remove the air inside, thus avoiding ice formation at helium temperature. A 'T' adapter is attached to the pumping arm so that the sample compartment can be either connected to



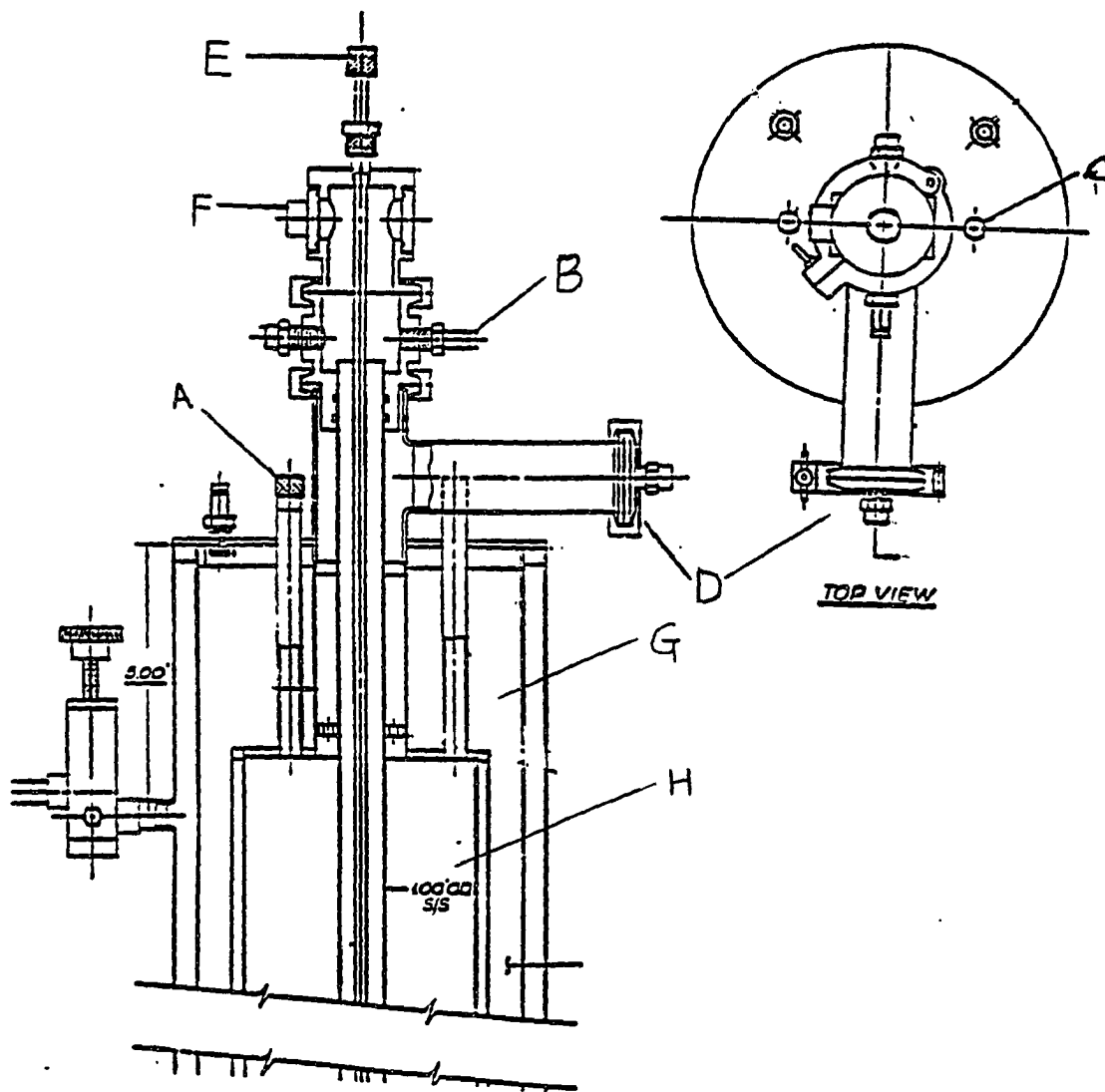


Figure A.1 Schematic drawing of the Cryo Industries 8CC Variable Temperature Helium Flow Cryostat. A - Helium flow valve, B - Pumping port, C - Helium Vent, D - Helium pumping arm, E - Sample cap, F - 8-pin Electric feedthrough, G - Liquid nitrogen reservoir, H - Liquid helium reservoir.

the pump or opened to the air. A pressure window (Model 28-1400 Pres-U-flange, Aerowave Inc., Medford, Massachusetts) which provides a vacuum-tight seal, while passing microwave energy freely has been added to the waveguide system just above the cryostat. It is important that the HELIUM FLOW VALVE (A) is closed before pumping the sample compartment. To check if the HELIUM FLOW VALVE is working properly, adjust the VALVE to about one turn open while pumping; a change of tune on the pump indicates a flow of air through the VALVE into the sample compartment. Close the HELIUM FLOW VALVE immediately afterwards.

#### Cooling down the cryostat

1) Open the HELIUM PUMPING ARM (D), and blow room temperature nitrogen gas through the LIQUID HELIUM RESERVOIR (H) via the HELIUM VENT (C).

2) Fill the LIQUID NITROGEN RESERVOIR (G) with liquid nitrogen and maintain liquid nitrogen level above the LIQUID HELIUM RESERVOIR (H) for maximum efficiency.

3) Blow cold helium gas through one of the HELIUM VENT (C) into the LIQUID HELIUM RESERVOIR. The cold helium, obtained by letting it first go through a copper coil immersed in liquid nitrogen, serves to purge as well as to precool the LIQUID HELIUM RESERVOIR.

4) Keep the HELIUM PUMPING ARM open, fill the helium reservoir with liquid helium through one of the HELIUM VENTS

(C). Do not insert the transfer line into the HELIUM VENT until some cold gas come out of the transfer line to make sure no air is going into the reservoir.

5) The helium level can be read by a MODEL 12 LIQUID HELIUM LEVEL indicator (Cryomagnetics, Inc., Oak Ridge, Tennessee). It reads in cm, and a full tank is about 40 cm. Some white cloud coming out of the PUMPING ARM (F) also indicates that the LIQUID HELIUM RESERVOIR is full.

6) After the tank is full, pull the transfer line out and seal the HELIUM VENT (C) with a rubber septa and the HELIUM PUMPING ARM (D) with the clamp.

#### Cooling down the sample compartment

1) Valve off the SD-450 mechanical pump at PUMPING PORT (B).

2) Open the HELIUM FLOW VALVE (A) at about half turn to let the helium flow through the sample compartment and out from the PUMPING PORT (B). Check occasionally with a flow meter at (B) to make sure a positive flow exists.

3) Temperature then starts to decrease at about 3-5 degrees per minute at the beginning and 8-10 degrees per minute after temperature is close to 100 K. Adjust the HELIUM FLOW VALVE to maintain a cooling rate of about 10 K/min. It usually takes about an hour or so to get to 100 K and another hour or less to reach 4 K. Once the system has been cooled, the HELIUM FLOW VALVE is open typically about 1

turn or less.

4) Use loop function on temperature controller to set and maintain a constant temperature. Typical settings on the controller are GAIN = 50, T INT = 15 sec and T DER = .5 sec. T INT can be lowered for a faster response.

#### Changing samples and cavities

To insert or change samples, close the PUMPING PORT (B); open the SAMPLE CAP (E); insert sample and put SAMPLE CAP back on; open the PUMPING PORT (B) to air again. The flow of helium to the sample compartment should be maintained to prevent air from leaking into the sample compartment.

To change cavities in the middle of the experiment, first take the sample out, then close HELIUM FLOW VALVE (A) as much as possible (to about 1/10 turns), but not all the way (since the sample compartment will be opened later, the helium flow can help to prevent air from getting in). Open PUMPING PORT (B) to air and gradually increase the heater output. After the temperature reaches room temperature, set the heater output to zero. Close PUMPING PORT (B); open the SAMPLE CAP (E); take out the waveguide (the waveguide is still very cold.) and close the sample compartment followed by opening the PUMPING PORT to air. Blow dry the wave guide with nitrogen gas, change the cavity and put the wave guide back into the cryostat. Switch the PUMPING PORT (B) to the

pump. Allow 2-4 minutes to let the air inside the waveguide out, then switch the PUMPING PORT (B) to the air. Open the HELIUM FLOW VALVE to 3/4 turns, and start the cooling process again.

#### Shutting Down

After the experiment is done, take the sample out and blow out the leftover liquid helium by opening the HELIUM FLOW VALVE (about 3 turns or more). After the helium is consumed, close the HELIUM FLOW VALVE and the PUMPING PORT. Let the whole cryostat sit over night. All the helium will vent eventually through the safety pressure relief valve on the PUMPING ARM. Once the system is warmed up to room temperature, open the HELIUM VENT (F) to allow the helium gas escape.

If you want to run the experiment the next day with leftover liquid helium, close all the valves and ports except the PUMPING PORT. Fill up the LIQUID NITROGEN RESERVOIR and keep pumping the sample compartment over night to ensure that no air is leaking in.

## APPENDIX B

### CAVITY Q MEASUREMENTS

The Q of the cavity can be measured by the following methods based on the experimental definition,  $Q = \nu_0/\Delta\nu$ , where  $\nu_0$  and  $\Delta\nu$  have been defined in Chapter 1.

#### Frequency mode (klystron power mode) method

1 The cavity was tuned in the usual way with an empty capillary tube inside. With the dip centered on the frequency mode, the frequency reading on the bridge corresponds to  $\nu_0$  (Fig. B.1).

2 Measure the width ( $w_1$ ) of the mode at the bottom by means of a caliper.

3 Take the empty capillary tube out of the cavity and measure the height ( $h$ ) of the mode on the oscilloscope.

4 Put the capillary tube back into the cavity again and measure the width ( $w_2$ ) of the dip at 70%  $h$  (half power point) from the bottom of the mode.

5 Turn the frequency knob on the bridge to move the dip to the left, then right, until it just disappears on the mode. Take the frequency readings as  $\nu_1$  and  $\nu_2$ , thus  $\Delta\nu$  can be obtained from equation

$$\Delta\nu = (w_2/w_1) * (\nu_1 - \nu_2) \quad (\text{B.1})$$

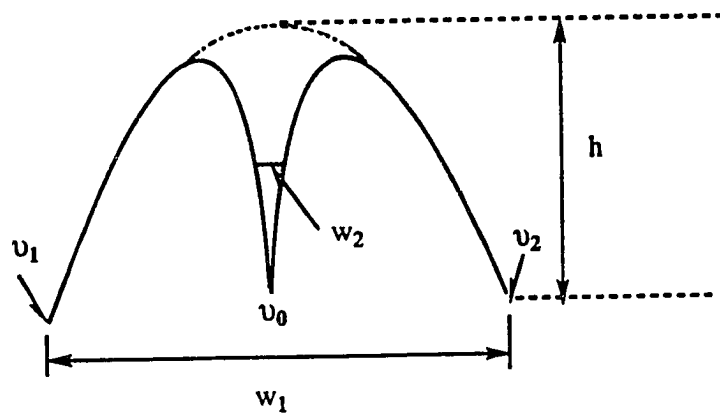


Figure B.1 Klystron power mode. (File name: Q.20, Q.21)

### Hyde's method

1 The bridge is tuned to make the cavity critically coupled, and the REFERENCE ARM and AFC circuits are turned off.

2 Switch to operate and adjust the frequency knob until the detector current reaches a minimum value. The frequency reading under this condition corresponds to  $\nu_0$ .

3 The empty tube was taken out of the cavity to move the cavity out of tune. Set the microwave power to 28 dB. The detector current reading now corresponds to the maximum in the power mode.

4 The power is then reduced to 31 dB, the crystal detector reading is now correspond to the value at half of the previous power.

5 The cavity was brought back to resonance by putting the capillary tube back into the cavity. Set the microwave power back to 28 dB. The microwave frequency is adjusted until the detector current readings are equal to that obtained in step 4.

6 The difference between the two frequencies found in step 5 are thus the width of the cavity dip at half power ( $\Delta\nu$ ).

Both of the above methods have been used in the cavity Q measurement, and the results agree with each other within 10%.



## APPENDIX C

### OPTIMUM DIMENSION FOR THE CYLINDRICAL TE<sub>011</sub> CAVITIES

The unloaded Q ( $Q_u$ ) and the wavelength of the resonance frequency for the TE<sub>mnp</sub> cylindrical cavity are given by

$$Q_u \frac{\delta}{\lambda} = \frac{(1/2\pi) [1 - m/K_{mn}^2] \{K_{mn}^2 + [\rho\pi(d/2z)]^2\}^{3/2}}{K_{mn}^2 + d/z[\rho\pi(d/2z)]^2 + (1 - d/z)[mp\pi(d/2z)K_{mn}]^2} \quad (c.1)$$

$$2\pi/\lambda = [4K_{mn}^2/d^2 + (\pi/z)_2]^{1/2} \quad (c.2)$$

where  $\delta$  (cm) is the skin depth at microwave frequency;  $\lambda$  (cm), the wavelength of the cavity resonant frequency;  $d$ , the inner diameter of the cavity and  $z$  is the length of the cavity at resonance;  $K_{mn}$  is a constant related to cavity operation modes. For TE<sub>011</sub> cylindrical cavity,  $m=0$ ,  $n=1$ ,  $p=1$  and  $k_{01} = 3.832$ . Equation C.1 and C.2 thus become

$$Q_u \delta/\lambda = (1/2\pi) [(3.832^2 + (\pi d/2z)^2)^{3/2} / [3.832^2 + d/z(\pi d/2z)^2]] \quad (C.3)$$

$$2\pi/\lambda = [4 \times 3.832^2/d^2 + (\pi/z)_2]^{1/2} \quad (C.4)$$

The cavity dimension (r and z) for maximum  $Q_u$  value should satisfy the equation  $(Q_u \delta / \lambda)' = 0$ . For simplicity, we set  $3.832^2 = A$ ,  $\pi^2/4 = B$ , and  $d/z = x$ ; equation (C.3) becomes:

$$Q_u \delta / \lambda = (1/2\pi) (A+Bx^2)^{3/2} / (A+Bx^3) \quad (C.5)$$

and

$$\begin{aligned} (Q_u \delta / \lambda)' &= (1/2\pi) [ (3/2) (A+Bx)^{1/2} (2Bx) (A+Bx^3) (A+Bx^2)^{3/2} (3Bx^2) ] \\ &\quad / (A+Bx^3)^2 \\ &= (1/2\pi) Bx^2 (x-1) / (A+Bx^3)^2 = 0 \end{aligned} \quad (C.6)$$

giving  $x = d/z = 1$ . Therefore, a maximum value of  $Q_u \delta / \lambda$  is achieved when the cavity length  $z$  equals the diameter  $d$ . This can be verified by a plot of  $Q_u \delta / \lambda$  vs  $d/z$  ratios (Fig. C.1), which clearly shows a maximum  $Q_u \delta / \lambda$  value at  $d/z = 1$ . At Q-band frequency (e.g. 34.9 GHz),  $\lambda = (34.9 \times 10^9 \text{s}^{-1}) / (3 \times 10^{10} \text{cms}^{-1}) = 1.16 \text{ cm}$ ; and the optimum diameter ( $d_{\text{max}}$ ) and length ( $z_{\text{max}}$ ) for the maximum  $Q_u$  can be calculated from equation c.4:

$$d_{\text{max}} = z_{\text{max}} = 1.13 \text{ cm}$$

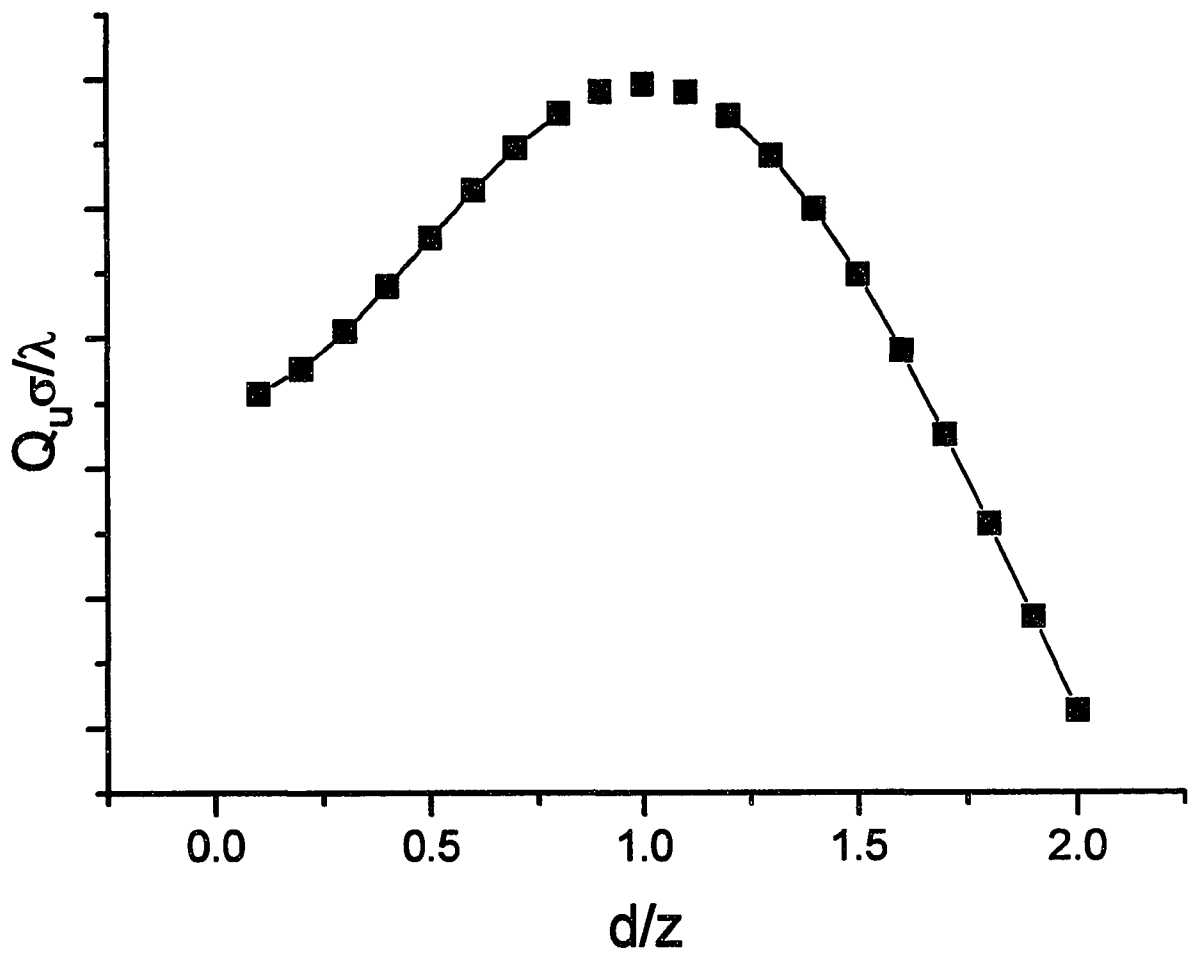


Figure C.1  $Q_u \sigma / \lambda$  vs  $(d/z)$  for cylindrical  $TE_{011}$  cavity. (File name: Q.plt)

**APPENDIX D**  
**SILVER PLATING**

Silver electrolytes of the cyanide type are often employed for both decorative and engineering plating. With proper control of plating conditions and procedure, a smooth and strongly bonded silver layer from several  $\mu\text{m}$  to several mm can be deposited from plating baths on almost any metals and alloys.

Plating bath composition and operating conditions

Potassium cyanide (KCN)	47 g/L
Silver nitrite ( $\text{AgNO}_3$ )	32 g/L
Potassium carbonate ( $\text{K}_2\text{CO}_3$ )	25 g/L
Current density	2 - 5 mA/cm <sup>2</sup>
Operating temperature	70 - 80 °F
pH	8-9

Silver plating apparatus

Figure D.1 shows the schematic drawing of the apparatus for the silver plating. It consists of a plating bath; a

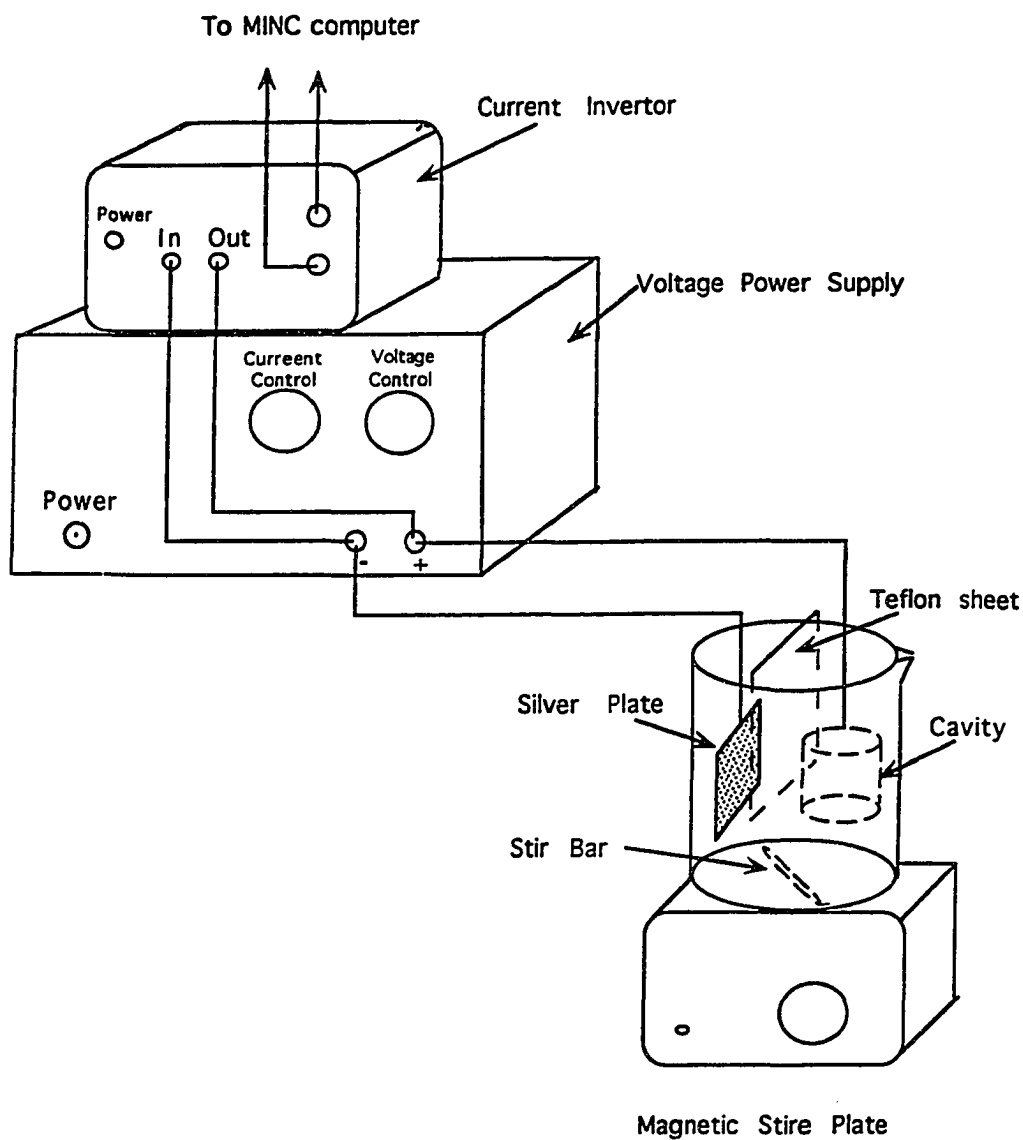


Figure D.1 Apparatus for electro-silver plating of the cylindrical brass ribbon-wound cavity. (plating.21)

voltage power supply (Heath Solid State Low Voltage Power Supply Model EV-41A), which supplies voltage ranging from 0 to 15 V, and current from 0 to 750 mA; a current converter, which serves to change the polarity of the current during plating cycles; a LCD Folding Digital multimeter (MICRONTA, Fort Worth, Texas) (not shown) to monitor the current during plating and a MINC-23 computer (Digital Equipment Corp.) to control both the voltage converter and the plating time using a program (in BASIC) called CAVD.BAS.

#### Calculation of plating time

The desired thickness of the silver layer can be achieved by properly controlled plating time and current. The relationship among the plating parameters is expressed in the following equation:

$$i \times t = (A \times \delta \times d / MW) \times F \quad (D.1)$$

where  $i$  is the plating current,  $t$  the total forward plating time (s),  $A$  the surface area of the part ( $\text{cm}^2$ ),  $\delta$  the plating thickness (cm),  $d$  the density of silver metal ( $10.5 \text{ g/cm}^3$ ),  $MW$  the molecular weight of Ag ( $108 \text{ g/mol}$ ) and  $F$  the Faraday constant ( $9.6 \times 10^4 \text{ C/mol}$ ). The plating area for the ribbon wound cavity is about  $7 \text{ cm}^2$ . To deposit a silver layer of  $5 \text{ }\mu\text{m}$  in thickness under a plating current of  $30 \text{ mA}$ , the total forward plating time needed will be

$$t = (7 \times 5 \times 10^{-4} \times 10.5 / 108) \times 9.6 \times 10^4 = 1089 \text{ (s)} = 18 \text{ (min)}$$

Since the plating is done in a 3 min forward and 1 min reverse plating fashion, the total plating time  $T_{\text{total}} = 2 \times t = 2 \times 18 = 36 \text{ min.}$

### Silver plating procedure

#### Step I : Cleaning

(1) Wear rubber gloves and protective eye glasses during the entire procedure.

(2) Work under the fume hood with exhaust on. CN<sup>-</sup> is given off in this process - be sure that air is flowing properly.

(3) Clean off all oils, grease , etc. from the cavity wall using Sparkleen Laboratory detergent. (Do not use acetone or ethanol. They may dissolve the epoxy body of the cavity.)

(4) Wrap the outermost surface of the cavity with electric tape to minimize the exposure of the epoxy to the solution.

#### Step II : Electropolishing

(1) Obtain a sheet of clean stainless steel foil and set up a beaker (500 mL) with the solution of a phosphoric acid (90 % by volume)/butanol (10 % by volume) mixture.

(2) Make connections as indicated in Figure D.1 except

that the cavity will be connected to '+', and stainless steel foil to '-' on the voltage power supply. (The teflon sheet helps to establish even distribution of current in the plating solution). Turn the current limit to maximum, and the voltage to 6 V or so on the voltage supply.

(3) Start the electroplating program on the computer (Digital VT105) by typing `Run cavd` (Return) at "%". Input the polishing time (in seconds, usually about 300 s) and polishing voltage (9 V) at the prompts.

(4) Lower the parts into the polishing solution at the beep.

(5) "Clean" the part in this solution for approximately 5 minutes or less. Do not over-clean since the acid is actually dissolving the metal of the cavity.

(6) Rinse the part well under hot tap water. Collect the rinsing water in a separate container to be treated later.

\*\*\*\*\*  
**Caution:** Return the phosphoric acid/butanol solution to its container before the next step. Do not use the above beaker for the silver plating solution which contains cyanide.  
\*\*\*\*\*

### Step III : Plating

(1) Fill a 500 mL beaker with ~ 400 mL silver plating solution: KCN (47 g/L), AgNO<sub>3</sub> (31.7 g/L) and K<sub>2</sub>CO<sub>3</sub> (25 g/L).



The plating solution is made by mixing the appropriate amount of KCN and AgNO<sub>3</sub> into water followed by the addition of K<sub>2</sub>CO<sub>3</sub>.

(2) As a primer, dip the part in a HgO (5 g/L)/KCN (50 g/L) solution for 10 seconds. A shiny, mirror coat will result.

(3) Make electrical connections as indicated in Figure 1a. A high purity silver foil (99.9985 %) (Johnson Mathew, Inc.) is used to minimize background signals introduced to the cavity wall during plating.

(4) At the prompt on the computer, input the total plating time (in seconds) needed for the plating procedure (typically about 36 min × 60 s/min for every 5 μm thickness of Ag layer at 30 mA current).

(5) Hit return key on the computer and insert the parts into the plating solution. The current is usually 30 mA under these conditions. (It is important that the electrical contact be made to the cathode and anode before immersing it in the plating bath.)

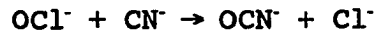
(6) During the plating process, keep the current at about 30 mA by adjusting either the voltage or current control on the voltage power supply.

(7) After the plating is done, immediately take the parts out of solution. Turn off the voltage power supply. Rinse the cavity with hot tap water at least 3 times and let it dry in the hood.

(8) Put the silver plating solution back into its container. Plating solution can be reused 6 - 8 times before disposal.

#### Waste disposal

The cyanide solution used in the plating bath needs to be detoxified before disposal. The most commonly used method is to treat the cyanide salt by adding an oxidizing agent such as sodium hypochlorite to produce non-toxic cyanate. The reaction involved in this process is



**General procedure :** A commercial laundry bleach containing 5.25 % (0.75 M) sodium hypochlorite is put in a ice-water bath, and the cyanide solution is added slowly to the bleach while stirring. The ice-water bath helps to dissipate the heat generated by the reaction. The bleach should be in at least 50 % excess to ensure all of the cyanide be oxidized. As a further test, one drop of the treated solution was added to ferrous sulfate/sulfuric acid solution; a precipitate of Prussion Blue indicates the presence of free cyanide. The resulting cyanate is then stored in a waste bottle and sent to the Coordinator of Hazardous Waste and Health Department for further treatment.

#### Source code for Cavd.bas

10 REM \*\*\*\*\* ELECTROPLATING PROGRAM \*\*\*\*\*

```

11 PRINT "INPUT POLISHING TIME (SECONDS)"
12 INPUT T1
13 PRINT "INPUT POLISHING VOLTAGE"
14 INPUT V
15 D=2047*V/10.24
16 AOUT (,D,1,0,1,1) \ PAUSE (T1)
20 PRINT "INPUT TOTAL FORWARD PLATING TIME (SECONDS)"
30 INPUT T5
40 REM CYCLE PLATE IMMEDIATELY 3 MIN FORWARD, TO 1 MINUTE REVERSE
50 F1 = T5/10
60 T=(T5-F1)*2
70 PRINT "INPUT PLATING VOLTAGE (10.24 V MAX.)"
80 INPUT V
90 D=2047*V/10.24
100 N%=T/240
110 PRINT " THE SAMPLE MUST BE OUT OF THE SOLUTION AT THIS POINT."
120 PRINT " HIT THE RETURN BUTTON AND IMMEDIATELY LOWER THE SAMPLE"
130 INPUT R$
140 FOR Z9=1 TO 5 \PRINT CHR$(7);\ PAUSE (1)\NEXT Z9
150 PRINT "CONTINUOUS FORWARD PLATING BEGINNING."
160 PRINT
170 TZ=0
180 FOR Z9=1 TO 5 \PRINT CHR$(7);\PAUSE (1)\NEXT Z9
190 START_TIME ('LINE')
200 AOUT (,D,1,0,1,1)\PAUSE (F1)
210 PRINT CHR&(7);\PRINT CHR$(7);
220 PRINT "CYCLE PLATING BEGINNING"
230 FOR I=1 TO N%
240 AOUT (,D,1,0,1,1)
250 PAUSE (180)
260 AOUT (,-D,1,0,1)

```

```
270 PAUSE (60)
280 T1=I*240
290 REM PRINT "CYCLE"+STR$(I)+" , TIME= "+STR$(T1)+" SECONDS."
300 NEXT I
310 GET_TIME(Q9)\FOR Z9=1 TO 5\ PRINT CHR$(7) \ NEXT Z9
320 D=0
330 AOUT (,D,1,0,1)
340 PRINT "PLATING FINISHED!"
350 PRINT "ELAPSED TIME SHOULD HAVE BEEN "+STR$(T+F1)+" SECONDS"
360 PRINT "THE ELAPSED TIME WAS -----"+STR$(Q9)+ " SECONDS"
370 END
```

**APPENDIX E**  
**OPERATION OF Q-BAND EPR SPECTROMETER**

The Q-band spectrometer system consists of a Varian E-line console, a E-line/35 GHz microwave bridge, a magnet and a magnet power supply. The microwave bridge provides operations in both the dispersion and absorption mode and can be operated at frequencies from 34.5 to 35.5 GHz. The power output of the bridge has a maximum of 63 mW with 50 dB dynamic range.

X-band to Q-band conversion

**I Microwave bridge**

(1) Disconnect P1201, P1206 and ground from X-band E-line Varian microwave bridge.

(2) Connect P1201, P1207 and ground on the Q-band E-101 Varian bridge.

**II Magnet system**

(1) Disconnect P009 at the back of the console.

(2) Plug red and black leads of field controller cable for the Q-band magnet power supply into pin C and A of J009, respectively. Connect the other end of the cable to the EXTERNAL CONTROL INPUT on the magnet power supply.

(3) Take the hall probe from the holder on the X-band

magnet and slip into that on the Q-band magnet.

### III Modulation system

(1) Connect the back cavity cable from J408 on the console to the Q-band modulation coil.

(2) Pull out the 100 kHz panel. Set MODULATION CALIBRATION to Q and the REFERENCE PHASE to about 130.

(3) Pull out System Function Selector. Set the 100 kHz CAVITY TUNING to 8 (COARSE) and 2 (FINE).

#### Operation procedure (absorption mode)

1 Switch on the transformer for Q-band power supply in Room G226. Turn on the coolant to the microwave bridge and the magnet.

2 Press console POWER switch on

3 Insert the sample capillary tube into the cavity (The cavity can not be tuned without a sample tube or an empty capillary tube inside).

4 Set ABS-DISP switch to ABS position.

5 Set the REFERENCE ARM POWER control to half-scale position and ATTENUATION control to 20 dB.

6 Switch microwave bridge from STANDBY to TUNE, Klystron mode trace will appear on the oscilloscope. (On initial turn-on, there will be about a 30 second delay after turning mode switch to TUNE.)

7 Set the frequency at about the middle of the

frequency range (e.g. 34.9 GHz). Adjust cavity piston position until a dip appears and is centered on the klystron mode trace. To verify that it is the right dip, simply move the sample out of the cavity and the dip should disappear.

8 Adjust the REFERENCE ARM PHASE control to obtain a symmetric dip.

9 Adjust the iris (Figure E.1) (sometimes sample position as well) so that the bottom of the dip reaches its minimum (Increase the microwave power, if necessary, to aid in the observation of the dip position).

10 Switch the bridge to OPERATE, set the desired microwave power (ATTENUATION) and set the detector current value to 50  $\mu$ A or slightly higher by adjusting the POWER knob.

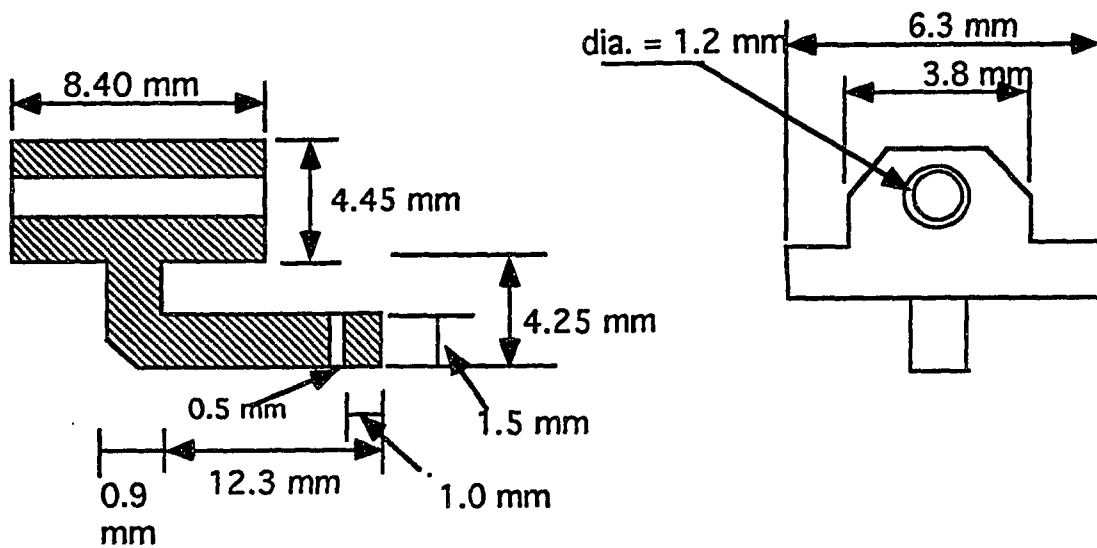
11 Turn on the magnet power supply. Make sure the MODE SELECTOR is on FIELD SET position before pushing the ON bottom (black).

12 Wait about 1 minute for it to warm up, and switch the MODE SELECTOR to FIELD SWEEP.

13 After setting the appropriate parameters (e.g. Field set, Receiver gain, Time constant, Modulation Amplitude, etc.) on the console, the spectrometer is then ready to record EPR spectrum.

#### Operation procedure (dispersion mode)

1 First tune cavity in absorption mode, then set the



(a) Sideview

(b) Front-view

Figure E.1 Schematic drawing of the Q-band cavity coupler. (iris.21).



microwave power to 20 dB, and switch the ABS-DISP to DISP.

2 Increase the microwave power to 6 dB, and adjust the phase to get a symmetric dip on the klystron trace.

3 Set the desired microwave power and turn the bridge to OPERATE. Readjust the POWER knob to obtain a detector current of 50  $\mu$ A.

4 The rest of procedure is the same as in absorption mode.

#### Shutdown procedure

1 After finishing the experiment, reduce microwave power to minimum (50 dB). Switch to TUNE, then STANDBY.

2 Set all the settings on the console to ZERO or OFF. Switch MODE SELECTOR to FIELD SET, and press OFF button (red) on the magnet power supply.

4 Turn off console and coolant water.

#### General notes

1 At low temperatures, it is best not to adjust the iris to avoid possible breakage of the Rexolit holder in the 'iris' arrangement.

2 The microwave frequency increases by about .1 GHz for every 100 K decrease in temperature.

3 The spectrometer needs about 1 hour to warm up to reach its maximum sensitivity and minimum noise condition.

## APPENDIX F

### CAVITY $P_{1/2}$ AND S/N MEASUREMENT ON WEAK PITCH SAMPLE

#### $P_{1/2}$ measurement

$P_{1/2}$  is the microwave power at half saturation of the EPR signal. It gives a good indication of the energy density in the cavity. The lower the  $P_{1/2}$  value, the easier for the sample to be saturated and the higher the energy density inside the cavity. To obtain a saturation curve of the weak pitch sample, the weak pitch spectrum is acquired at different microwave powers, from 0 dB (63 mW) to 50 dB (0.63  $\mu$ W) at an increment of 2 dB. The peak to peak amplitude is measured for each spectrum, and plotted as a function of square root of microwave power (Fig. F.1).  $P_{1/2}$  can then be obtained from fitting the curve with equation  $A = KP^{0.5}/(1+P/P_{1/2})^{.5b}$ , where A is the EPR signal amplitude, K a proportionality constant, P the microwave power, and b the inhomogeneity parameter. The fitting was achieved via a nonlinear least-square curve fitting program (Origin), which uses the Levenberg-Marquardt (LM) algorithm. A typical fitted curve is shown in Figure F.2. The  $P_{1/2}$  obtained from the least-squares fitting is 0.22 mW with a standard deviation of 0.04 mW.

### Signal-to-Noise measurement

The power at the 4th point (A) on the linear nonsaturating portion (Figure F.2 inset) of the curve,  $P_1$  (0.01 mW), was chosen for measuring the signal amplitude. Acquire a weak pitch spectrum at microwave power  $P_1$  (Fig. F.3a), a Modulation Amplitude of 8 G and a Time Constant of 1 s. The digitized signal amplitude, which is 8055 for this spectrum, is taken as the "Signal". To obtain the "Noise", a baseline spectrum was measured at 0 dB attenuation ( $P_0$  nominally 63 mW) with the field off resonance and the scan range off (other instrumental settings are the same with that for the signal measurement) (Fig. F.3b). This tests the stability of the microwave source and other components which contribute to high power noise. A linear regression was applied to the entire baseline and standard deviation (SD), which is the root-mean-square deviation of the baseline (experimental data) from that of the fitting curve (linear regression result), is taken as the "Noise" of the baseline (Fig. F.4). The Signal-to-Noise ratio was then calculated from

$$S/N = (\text{Signal/Noise}) \cdot \sqrt{P_0/P_1} / 1.05 \quad (\text{F.1})$$

where  $\sqrt{P_0/P_1}$  corrects for the power difference in the signal and noise measurements. The factor of 1.05 corrects for the fact that the homemade weakpitch sample has a 5% higher

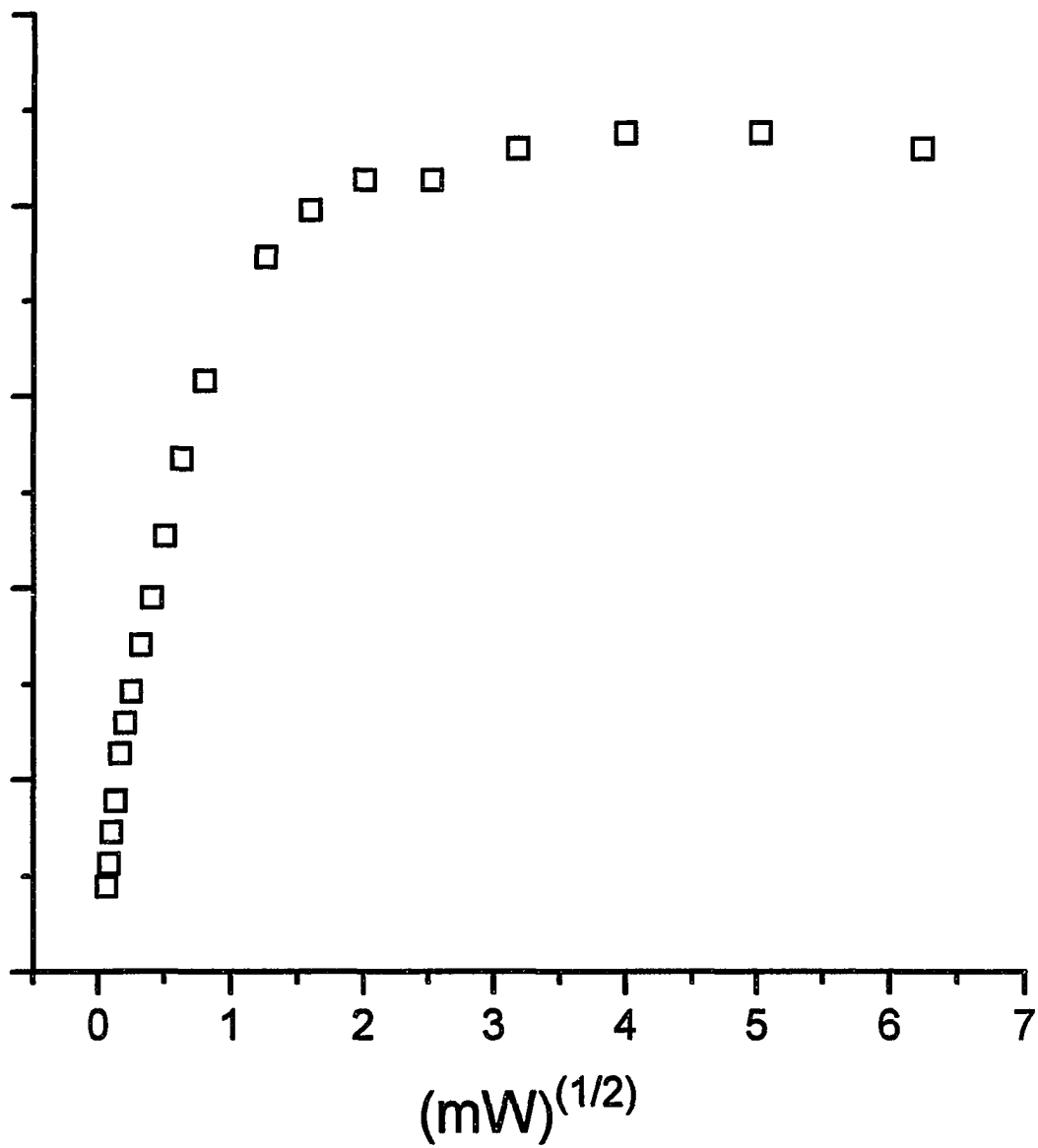


Figure F.1 Power saturation curve of weakpitch sample.  
 Cavity: silver-plated brass ribbon wound cavity.  
 Instrumental conditions: same as in Figure 2.2. (File name: sat.the)

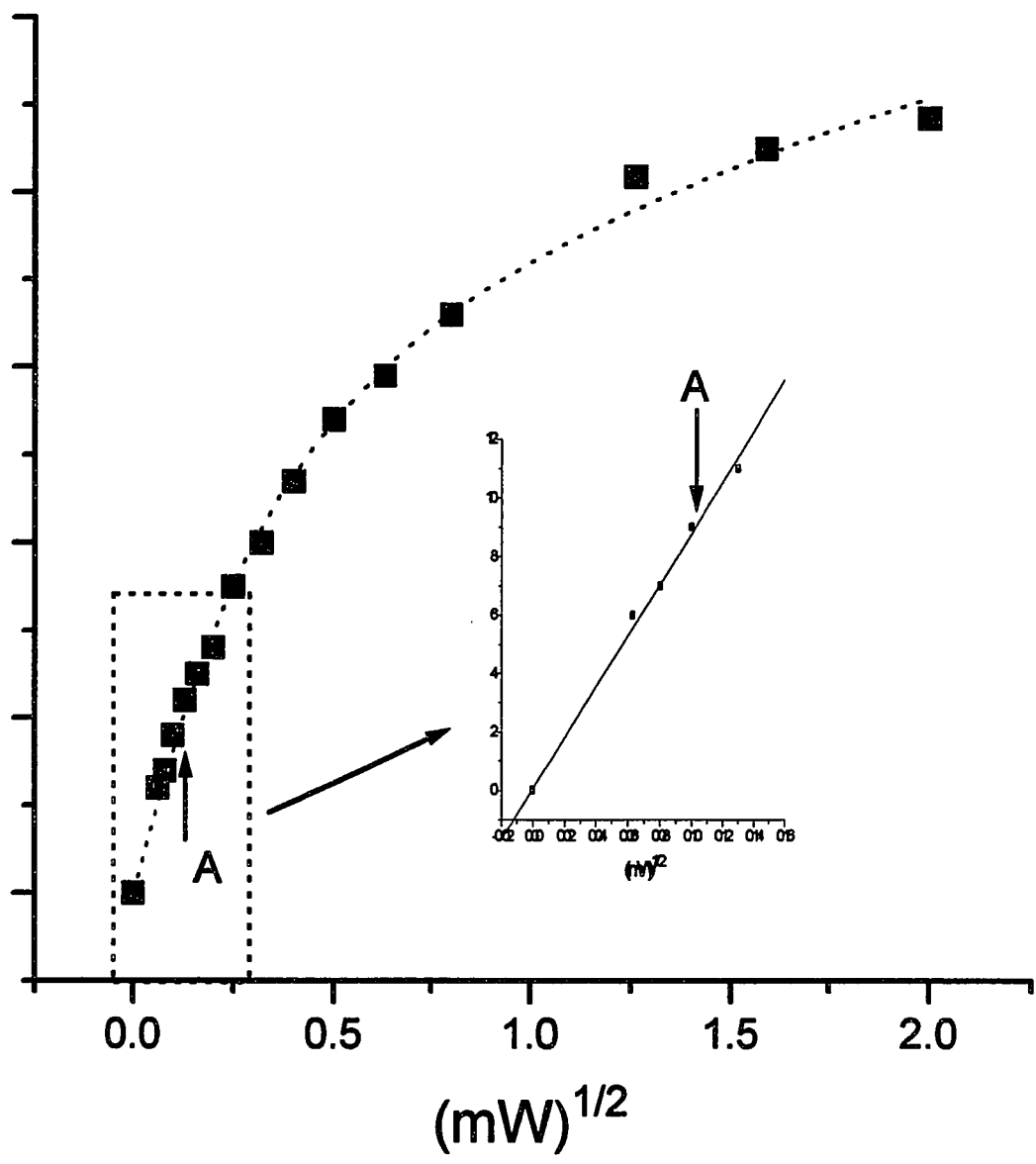


Figure F.2 Curve fitting of the power saturation data in Figure F.1. Inset: The linear part of the saturation curve. (File name: P06.plt)

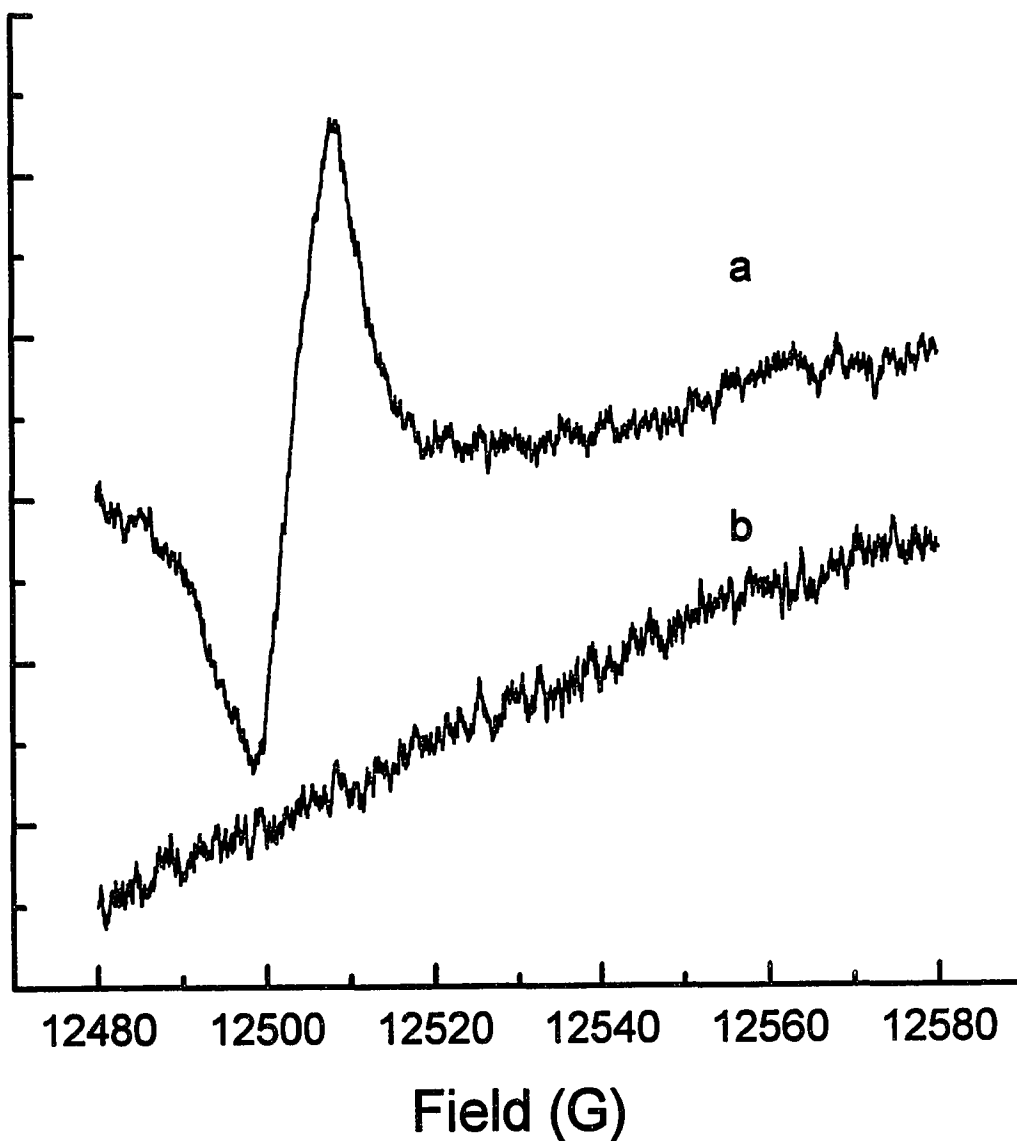
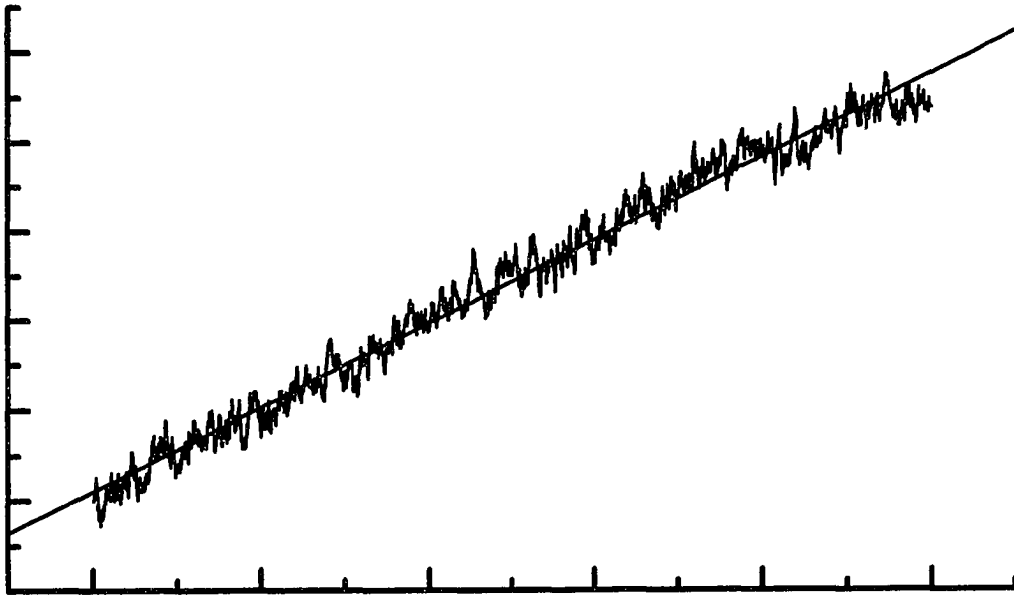


Figure F.3 (a) Weak pitch spectrum at 0.01 mW power. Instrument conditions: Field Scan Range, 100 G; Scan Time, 4 minutes; Room temperature; Microwave Frequency, 35 GHz; Modulation Frequency, 100 KHz; Modulation Amplitude, 4 G; Receiver gain, 1600; Time Constant, 1 s. (File name 062894a6.fls) : (b) Baseline trace at 63 mW microwave power (0 dB). Instrument conditions: same as (a) except for the Scan Range which is off in this case. (File name: 062894a4.fls). (S-N.plt)



Linear Regression for A062894A4.FLS\_A:

$$Y = A + B * X$$

Param	Value	sd
A	113.56487	4.71513
B	0.93032	0.00163

R = 0.99239

SD = 166.68, N = 5000

P = 0

Figure F.4 Linear regression of the baseline in Figure F.3b.  
(n.plt)

signal amplitude than the Varian standard. Plug the values for Signal, Noise,  $P_0$  and  $P_1$  in equation F.1, giving

$$\begin{aligned} S/N &= (8055/167) \cdot \sqrt{63/0.01}/1.05 \\ &= 1150 \end{aligned}$$



## APPENDIX G

### Q-BAND MODULATION COIL CONSTRUCTION

The homemade modulation coil is basically a mimic of the Varian modulation coil except that the inner diameter of the coil holder for the former is slightly larger, thus allowing the tail of the 8CC Variable Temperature Helium Flow Cryostat to get through.

The coil itself (Fig. G.1a) consists of two loops (34 turns each) made out of a single 26 gauge enameled copper wire. A simple device (Fig. G.1b) was made for the purpose of making such a coil. It consists of two polycarbonate plates and a cardboard spacer (cut from the cardboard backing of a notepad) with the shape and dimensions shown in Figure G.1 b. To make the coil, the plates and spacer were first jointed together by two screws in the middle and the copper wire was wound tightly against the spacer in between the plates. After the winding was finished (32 turns), liquid epoxy was applied evenly onto the coil layer between the slots on the plates. After the epoxy had cured, the plates were released and the coil was taken out of the spacer. To ensure mechanical stability, the four corners of the coils were tied with dental floss threads. The other loop was done in the same manner with about 10 cm length of wire left between the loops.

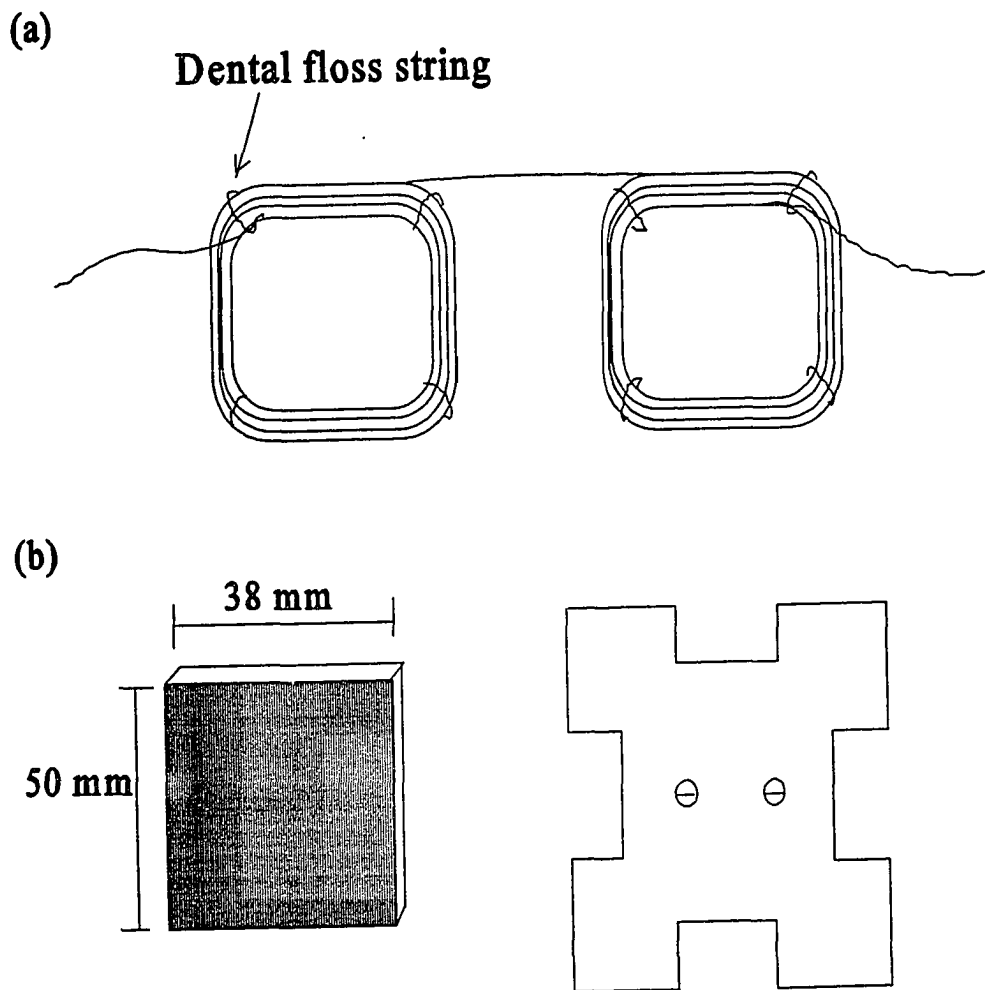


Figure G.1 Schematic diagrams of the EPR Q-band modulation coil (a) and the device for making the coil (b). (coil.dia)

The finished coils were then placed against the outside surface of a polycarbonate cylinder (i.d. 42 mm, o.d. 44 mm) and between the secured by wrapping electrical tape. The coils were carefully positioned so that the cavity was in the center of the two loops. The total length of the coil is about 200 cm with 1.8 ohms resistance. A 3300 pf capacitor was connected in parallel to match the impedance of the console.

## APPENDIX H

### POINT DIPOLE DIPOLE INTERACTION APPROXIMATION

Generally speaking, the experimentally observed hyperfine splitting ( $A_{\text{obs}}$ ) arises from anisotropic dipolar interactions (between the unpaired electron and the protons) and the isotropic coupling. Under the point dipole interaction approximation,  $A_{\text{obs}}$  can be represented by the following (89)

$$A_{\text{obs}} = \beta_e \beta_n g_e g_n (3 \cos^2 \phi - 1) / r^3 + A_{\text{iso}} \quad (\text{G.1})$$

where  $r$  is the distance between the proton and electron,  $\phi$  represents the angle between the  $r$  vector connecting the unpaired electron and the interacting nucleus and the applied field vector  $H_0$ .  $A_{\text{iso}}$  is the isotropic hyperfine contribution, which can sometimes be obtained from room temperature EPR spectra.  $g_e$  describes the effective  $g$  given by  $g_e = (g_1^2 \cos^2 \theta + g_2^2 \sin^2 \theta)^{1/2}$ , where  $\theta$  represents the angle between  $H_0$  and the symmetry axis of the complex.

When  $\phi = 0^\circ$  and  $90^\circ$ , the observed hyperfine coupling ( $A_{\text{obs}}$ ) correspond to  $A_{\parallel}$  and  $A_{\perp}$ , respectively, and Equation G.1 becomes:

$$A_{\parallel} = 2\beta_e \beta_n g_e g_n / r^3 + A_{\text{iso}} \quad (\text{G.2})$$

$$A_{\perp} = -\beta_e \beta_n g_e g_n / r^3 + A_{iso} \quad (G.3)$$

From equations G.2 and G.3, we obtain  $A_{iso} = 2/3A_{\perp} + 1/3A_{\parallel}$ . The distance of the protons from the spin center ( $r$ ) can also be estimated from equations G.2 or G.3, provided  $A_{\parallel}$  or  $A_{\perp}$  and  $A_{iso}$  are known. In many instances, such as for the proton hyperfine couplings, the hyperfine coupling contributed from  $A_{iso}$  is minimal and thus can be neglected.

To calculate the  $r$  for a hyperfine coupling ( $A_{obs}$ ) of 0.22 MHz, for example, we first assume  $A_{obs} = A_{\parallel}$  ( $\phi = 0^\circ$ ).

From eq. G.2 and given  $g_e = 2.0023$ ,  $g_n = 5.585$ ,  $\beta_e = 0.927 \times 10^{-20}$  erg/gauss,  $\beta_n = 0.505 \times 10^{-23}$  erg/gauss, we obtain

$$r^3 = 2\beta_e \beta_n g_e g_n / A_{\parallel} = 2 \times 0.927 \times 10^{-20} \text{ erg/gauss} \times 0.505 \times 10^{-23} \text{ erg/gauss} \times 2.0023 \times 5.585 / (0.22 \times 10^6 \text{ s}^{-1} \times 6.63 \times 10^{-27} \text{ erg}\cdot\text{s})$$

$$r = 9.0 \times 10^{-8} \text{ cm} = 9.0 \text{ \AA}$$

Similarly, if  $\phi = 90^\circ$  (eq. G.3),  $r^3 = \beta_e \beta_n g_e g_n / A_{\perp}$  and  $r = 7.2 \text{ \AA}$ .

So for a observed proton hyperfine coupling constant of 0.22 MHz, the corresponding proton electron distance ranges from 7.2  $\text{\AA}$  to 9.0  $\text{\AA}$ , depending on whether the observed  $A$  value corresponds to  $A_{\parallel}$  or  $A_{\perp}$ .

However, there are some cases that  $A_{iso}$  cannot be neglected, such as in the case of Fe-NO-Mer, where the  $A_{iso}$  of proton is about 1.2 G (3.4 MHz). In this case, the  $A_{iso}$  has to be taken into account in calculating  $r$  values. To illustrate this point for Fe-NO-Mer consider a 2.66 MHz  $^1\text{H}$

hyperfine coupling constant observed in the ENDOR spectrum at field position of 3275 G. This coupling could be either  $A_{\parallel}$  or  $A_{\perp}$ , moreover, since the sign of  $A_{\text{iso}}$ ,  $A_{\parallel}$  and  $A_{\perp}$  can not be obtained from either EPR or ENDOR measurements, we need to consider the each of following cases:

Case I  $A_{\text{iso}} > 0$ , from eq. G.2,  $A_{\parallel} > A_{\text{iso}} = 3.4$  MHz. Thus the observed 2.66 MHz hyperfine coupling cannot be  $A_{\parallel}$ .

(1) If  $A_{\perp} = 2.66$  MHz,  $\beta_c \beta_n g_c g_n / r^3 = 0.74$  MHz,  $r = 4.8$  Å

(2) If  $A_{\perp} = -2.66$  MHz,  $\beta_c \beta_n g_c g_n / r^3 = 6.06$  MHz,  $r = 2.3$  Å

Case II  $A_{\text{iso}} < 0$ , from eq. G.3,  $A_{\perp} < A_{\text{iso}} = -3.4$  MHz. The observed 2.66 MHz hyperfine coupling cannot be  $A_{\perp}$ .

(1)  $A_{\parallel} = 2.66$  MHz,  $2\beta_c \beta_n g_c g_n / r^3 = 6.06$  MHz,  $r = 3.75$  Å

(2)  $A_{\parallel} = -2.66$  MHz,  $\beta_c \beta_n g_c g_n / r^3 = 0.74$  MHz,  $r = 7.6$  Å

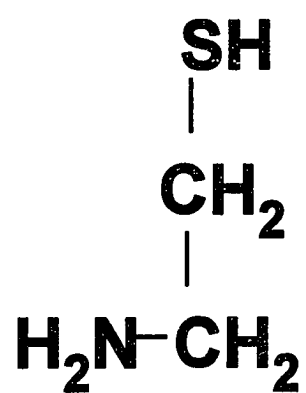
We can basically exclude the possibility of Case I (2) and Case II (2) because the calculated distances are either too small (2.3 Å) or too large (7.6 Å) for the possible proton candidates in Fe-NO-Mer complex. Thus, the coupling constant of 2.66 MHz corresponds to proton-iron distances ranging from 3.75 Å to 4.8 Å.

**APPENDIX I**  
**EPR/ENDOR STUDIES OF DINITROSYL IRON AMINO ETHANETHIOL**  
**COMPLEX**

EPR/ENDOR studies were also done on the dinitrosyl iron complex with amino ethanethiol (AET) ligand (Fig. I.1). Both the room temperature and frozen solution EPR spectra of the Fe-NO-AET complex show the same g value and hyperfine structures as that of Fe-NO-Cys, suggesting that both complexes have the same structures at room temperature and undergo similar kind of structural rearrangement upon freezing. The possible structures for dinitrosyl iron cysteine complex in frozen solution are shown in Figure I.2 (a)-(d). We can first exclude structure (b) and (c), since the carboxyl group is not present in the amino ethanethiol ligand. Structure (d) can also be excluded based on our EPR studies of dinitrosyl iron complex with ethylamine (Fig. I.1), in which case no well defined EPR spectrum was obtained, indicating that the amino groups alone will not give a stable complex. So the most likely structure will be structure (a), where cysteine binds to Fe via both the thiol and amino groups.

Proton ENDOR spectra of Fe-NO-AET made in both H<sub>2</sub>O and D<sub>2</sub>O (Fig. I.3) were also taken with magnetic fields set at

Aminoethanethiol (AET)



Ethylamine

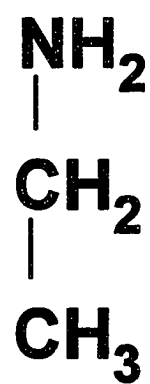


Figure I.1 Structure of aminoethanethiol and ethylamine



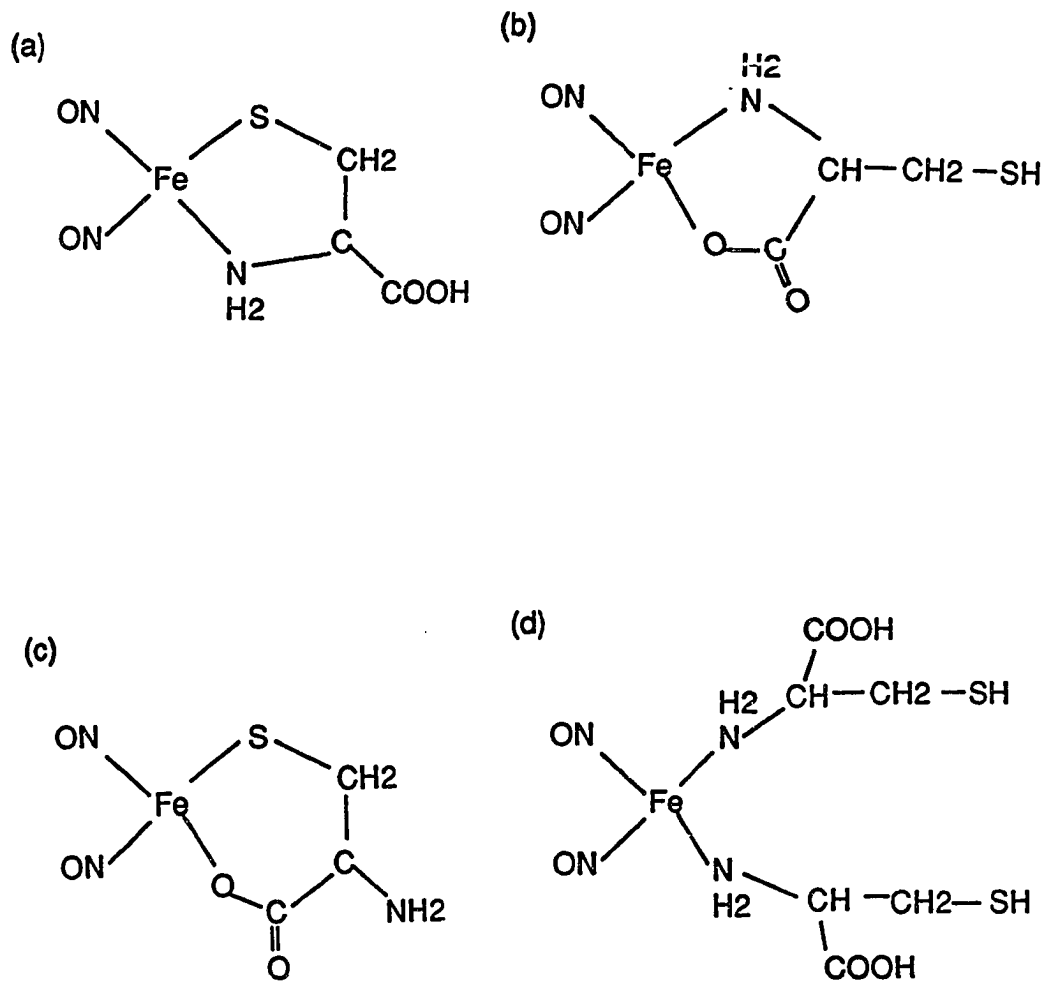


Figure I.2 Possible structures of Fe-NO-Cys at frozen state.

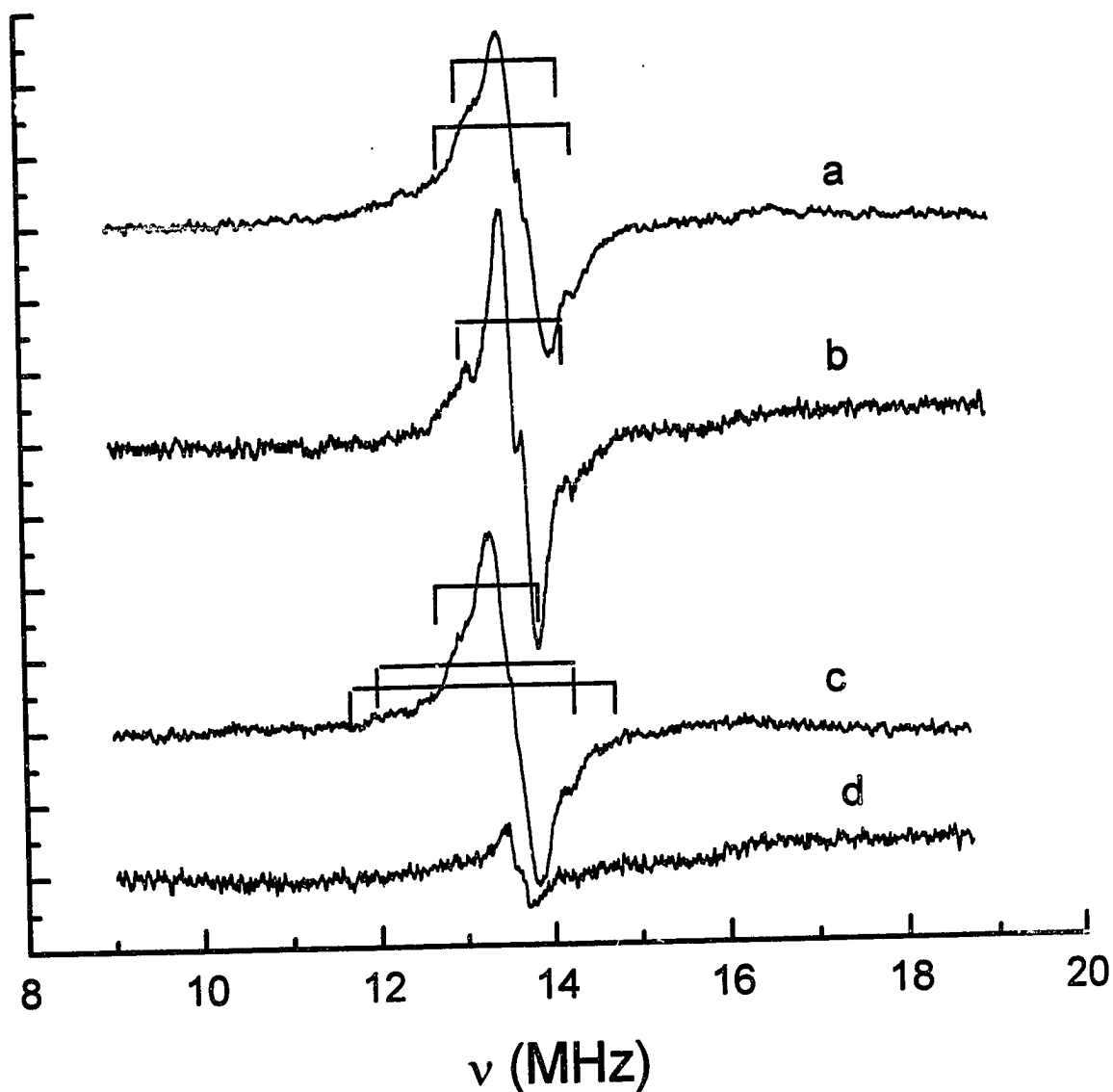


Figure I.3 Frequency modulation X-band  $^1\text{H}$  ENDOR of 20 mM Fe- $^{14}\text{NO}$ -AET complex made in  $\text{H}_2\text{O}$  (a, c) and  $\text{D}_2\text{O}$  (b, d). Experimental conditions: Field Set = 3231 G (a,b), 3254 G (c,d); Microwave Frequency, 9.175 GHz; Microwave power, 2 mW; Modulation Frequency, 10 kHz; Modulation Amplitude, 100 kHz; Temperature, 12 K; Time Constant, 0.03 s; radio frequency power, 100 W; radio frequency scan rate, 0.25 MHz/s. File name: 1130a14.fls (a), 1130b42.fls (b), 1130a46.fls (c), 1130b52.fls (d). (AETEN.the)

both  $g_{\perp}$  and  $g_{\parallel}$  positions and the hyperfine coupling constants are listed in table I.1.

Table I.1 Proton hyperfine couplings (MHz) of Fe-NO-AET complex.

Spectrum	Field (G)	A (MHz)*				
A	3231	0.22	1.12	1.55		
B	3231	0.22	1.12			
C	3254	0.22	1.16	2.03	3.07	
D	3254	0.22	(7.2/9.0) (4.6/5.6) (3.8/4.8) (3.4/4.1) (3.0/3.7)			

\*Estimated proton-electron distances in Å under the point dipole interaction approximation assuming the couplings correspond to  $A_{\perp}$  or  $A_{\parallel}$ , respectively.

The proton ENDOR results are similar to those of Fe-NO-Cys, which gives additional support for the argument that both complexes have the same structure in the frozen state. And the fact that the larger couplings disappeared upon  $D_2O$  exchange provides direct evidence for the hyperfine contributions from solvent exchangeable protons, most likely amino group protons in this case.